

Impacts of indirect photochemistry of Brown Carbon and iron carboxylate complexes on gas and aerosol chemistry

Inauguraldissertation
der Philosophisch-naturwissenschaftlichen Fakultät der
Universität Bern

vorgelegt von
Pablo Corral Arroyo
aus Spanien

Leiter der Arbeit:
Andreas Türler
Departement für Chemie und Biochemie

Von der Philosophisch-naturwissenschaftlichen Fakultät angenommen.

August 29, 2018

Bern, 28.09.2018

Der Dekan:

Prof. Dr. Z. Balogh

Contents

1	Introduction	15
1.1	Atmosphere	15
1.2	Aerosol particles and aerosol aging	15
1.2.1	Sources of atmospheric aerosol particles	15
1.2.2	Composition of atmospheric aerosol particles	17
1.2.3	Aerosol aging	17
1.2.4	Influence on climate, ecosystems and human health	19
1.3	Oxidative radicals in the troposphere	20
1.4	Brown carbon	21
1.4.1	Properties of brown carbon	21
1.4.2	Brown carbon photochemistry and photosensitizers	21
1.5	Iron in atmospheric particles	23
1.5.1	Sources and mobilization	23
1.5.2	Iron speciation	24
1.5.3	Radical chemistry and photochemistry	24
1.6	Halogens in the atmosphere	27
1.6.1	Activated halogen species	27
1.6.2	Feedbacks between photosensitized chemistry and halogen activation	27
1.7	Diffusion, viscosity and chemical reactivity	28
1.8	Motivation and outline	30
1.8.1	Motivation of the project	30
1.8.2	Specific goals of this thesis	32
1.8.3	Outline of the thesis	32
2	Chapter 2	35
2.1	Abstract	36
2.2	Introduction	36
2.3	Experimental section	38
2.3.1	Coated-wall flow tube experiments	38
2.4	Experimental conditions	40
2.4.1	J_{IC} calculations	41
2.4.2	Aerosol flow-reactor experiments	42
2.4.3	Experimental conditions	42
2.4.4	Chemicals	42
2.5	Results and discussion	43
2.5.1	Coated-wall flow tube	43

2.5.2	Aerosol flow tube	49
2.5.3	Proposed mechanism	51
2.6	Atmospheric relevance	51
2.7	Conclusion	52
2.8	Supporting Information	53
2.8.1	NO ₂ actinometry	53
3	Chapter 3	59
3.1	Abstract	60
3.2	Introduction	60
3.3	Experimental	62
3.3.1	Coated-wall flow tube experiments	62
3.3.2	Aerosol flow tube experiments	63
3.4	Results	63
3.4.1	Influence of photosensitizer type and mixing ratio	63
3.4.2	Influence of relative humidity	64
3.4.3	Influence of competing donors	66
3.5	Discussion	67
3.6	Upscaling to atmospheric conditions	70
3.7	Supporting Information	71
3.7.1	Spectra	71
3.7.2	NO loss and conversion to HO ₂ production	71
3.7.3	Experiments performed	72
3.7.4	Laser flash photolysis (LFP) experiments	73
3.7.5	Thickness dependence	75
3.7.6	Radical production from IC/CA aerosol particles in the aerosol flow tube (AFT)	75
3.7.7	Modeling	77
4	Chapter 4	81
4.1	Abstract	82
4.2	Introduction	82
4.3	Experimental section	85
4.3.1	Experimental description	85
4.4	Results	86
4.4.1	HO ₂ production, scavenging and release	86
4.4.2	Iodine activation	88
4.5	Conclusions and atmospheric implications	90
4.6	Supporting Information	91
4.6.1	Spectra	91

4.6.2	NO loss and conversion to HO ₂ production	91
4.6.3	I ₂ O ₅ particles measurements	93
4.6.4	Modelling	93
5	Chapter 5	97
5.1	Abstract	98
5.2	Introduction	98
5.3	Experimental Section	101
5.4	Results and discussion	102
5.5	Conclusions and atmospheric implications	108
5.6	Supporting Information	109
5.6.1	PTR normalization for different <i>RH</i>	109
5.6.2	Modelling	110
6	Chapter 6	113
6.1	Abstract	114
6.2	Introduction	114
6.3	Experimental	117
6.4	Results	118
6.4.1	STXM results	118
6.4.2	HPLC-MS results	121
6.4.3	PTR-MS results	124
6.5	Conclusions	125
7	Conclusions and outlook	127
7.1	Conclusions	127
7.2	Outlook	129
8	References	133
9	Acknowledgements	149

List of Figures

1.1	Overview of AMS datasets of non-refractory PM ₁ . Pie charts show the average mass concentration and chemical composition with the following color code: organics (green), sulfate (red), nitrate (blue), ammonium (orange), and chloride (purple). Colors for the study labels indicate the type of sampling location: urban areas (blue), < 100 miles downwind of major cities (black), and rural/remote areas > 100 miles downwind (pink). Reproduced from Zhang et al. ¹	18
-----	--------------------------------------------------------------------------------------------------------------------------------------------------------------------------------------------------------------------------------------------------------------------------------------------------------------------------------------------------------------------------------------------------------------------------------------------------------------------------------------------------------------	----

1.2	Radiative forcing induced by greenhouse gases, stratospheric water vapour, surface albedo, aerosol particles, between 1750 and 2005. Reproduced from IPCC, AR5 (2013) ²	19
1.3	Catalytic mechanism of a photosensitizer (P). The initial step is the excitation step leading to the singlet state (P*(s)) production followed by the singlet to triplet (P*(t)) intersystem crossing. P*(t) can react with oxygen producing singlet oxygen or with an organic molecule producing an intermediate radical (PH·) which can react the a electron/H atom acceptor leading to the production of P.	22
1.4	Proposed reaction pathways for imidazole formation in the glyoxal/ammonium sulfate system are shown. Green colored compounds were previously described in literature ^{3,4} ; orange colored compounds were identified in this work. Reproduced from Kampf et al. ⁵	23
1.5	Photochemical catalytic cycle of an iron-carboxylate complex in a particle. Fe ^{III} CA (iron citrate) is photolyzed leading to the reduction of iron to Fe ²⁺ and the decarboxylation of the ligand and the production of an organic radical. The latter reacts with oxygen leading to HO _x and a new stable molecule, which can further react with HO _x or by cycling with Fe ³⁺ , leading to the decomposition of citric acid to oxygenated volatile organic compounds (OVOC). HO ₂ reduces Fe ²⁺ back into Fe ³⁺ , which can be complexed again by citric acid.	26
1.6	Classification into solid, semi-solid and liquid states of various substances as a function of dynamic viscosity. For organic liquids the molecular diffusion coefficient D_{org} can be inferred from the viscosity via the Stokes-Einstein relation (eq. 5). In the bottom panel we show the corresponding e-folding times of equilibration for various particle diameters according to Shiraiwa et al. ⁶ . Reproduced from Koop et al. ⁷	29
2.1	Sketch of the photochemical flow tube reactor setups at PSI for (a) Setup 1 in 2013 measuring NO ₂ generation and (b) for Setup 2 in 2014 measuring NO loss.	38
2.2	NO ₂ profile for a 0.025 M IC bulk solution, whose concentration increases to ~ 0.2 M of IC in the film due to the citric acid hygroscopic properties. The gray shaded areas indicate periods where NO was exposed in the dark. The yellow shaded areas indicates the period of irradiation; the decrease in the intensity of yellow represents 2.26×10^{16} , 1.47×10^{16} , 1.14×10^{16} and 3.94×10^{15} photons cm ⁻² s ⁻¹ for seven, five, three and one lamp, respectively. This time series clearly indicates the light dependence production of HO ₂ radicals from the photosensitization of IC in a CA film.	44
2.3	A linear correlation of HO ₂ as a function of IC concentration. The left y axis represents the values for Setup 1, while the right y axis represents the values for Setup 2 (an order of magnitude difference for both scales). The Setup 2 data fall between a factor of 2 and 3 from Setup 1 after accounting for differences between Setup 1 and 2; see Sect. 3.1.1.	45
2.4	HO ₂ fluxes in molecules cm ⁻² min ⁻¹ as a function of actinic flux for a 300 – 420 nm range (solid symbols). The data are plotted as a concentration product of [IC] × [CA] (shown in the legend), which shows the photochemical reaction between IC and CA in H ₂ O matrix and gaseous NO. HONO for 2.441 ([IC] × [CA]) is plotted on the right axis (open circles), showing a ratio of HONO : NO ₂ < 1, which suggests OH as a secondary product.	46

2.5	The indirect flux of HO ₂ in molecules cm ⁻² min ⁻¹ , measured by NO loss and normalized to the film surface area as a function of relative humidity.	47
2.6	The flux of HO ₂ in molecules cm ⁻² min ⁻¹ , measured by NO loss, above a film composed of IC and CA normalized to the film surface area as a function of the O ₂ mixing ratio.	48
2.7	Aerosol flow tube experiments show rapid conversion of NO (solid black line) into NO ₂ (dashed black line) only after the time when limonene (gaseous H donor) is added into the flow tube (vertical dashed line). The gray shaded areas represent the experiment in the dark, and the yellow shaded area represents the experiment under light exposure. The blue line represents the growth of aerosols (right axis).	50
2.8	Proposed mechanism, modified and expanded to photosensitization of IC based on Canonica et al. (1995) ⁸ , George et al. (2005) ⁹ and Aregahegn et al. (2013) ¹⁰ . The reaction in the white square represents the gas-phase, and the blue square represents the aqueous phase. DH is an H donor (e.g., CA, another IC, H ₂ O + CA matrix to be determined from flash photolysis). 51	
2.9	NO ₂ j-values in s ⁻¹ from the bare glass and citric acid blank coated flow-tubes in Setup 1. . .	53
2.10	Determination of the NO concentration in the 2014 PSI flow-tube system. The lifetime of HO ₂ is short enough at 500 ppbv with respect to its reaction with NO. This ensures a 1 NO:1 HO ₂ molecular reaction in our experimental conditions. An IM/AC ratio of 0.088 was fixed for this specific experiment.	54
2.11	Solid line: the cross-section of IC in H ₂ O; the UV-VIS absorption of IC was measured by Kampf et al., 2012 ⁵ and interpolated to more recent molar extinction measurements by Barbara Nozière at IRCELyon (right scale in cm ²). Shaded gray: calculated wavelength dependent photolysis frequencies of imidazole-2-carboxaldehyde, j-values, based on the calculated quantum yield in our flow tube. Dotted line: actinic flux of the UV-light source in our flow-tube system from 300 – 420 nm range, the total flux is 2.26×10 ¹⁶ photons cm ⁻² s ⁻¹ . Dashed line: a solar actinic flux spectrum for a solar zenith angle of 48°, 37° tilt towards the sun and clear skies (~ 2 × 10 ¹⁶ photons cm ⁻² s ⁻¹ between 300 – 420 nm) obtained from the standard spectrum of the American Society for Testing and Materials (ASTM).	55
2.12	Film thickness dependence represented by NO loss. The IC:CA ratio was kept constant to show the classic behavior of reactions governed by reaction and diffusion. At low thicknesses, P _{HO₂} increases linearly and saturates at thicknesses > 2 μm. This shows that the observed HO ₂ is produced from the top few micrometers of the films under study.	56
2.13	The photosensitized uptake coefficient of NO ₂ (blue diamonds, right axis); this graph shows the inefficiency of NO ₂ to compete with O ₂ at atmospheric mixing ratios. The open red circles represent the CA blank measurements, the closed red circles represent a 1.725 [IC] × [CA] film measurements during NO ₂ actinometry experiments (left axis).	56
2.14	NO to NO ₂ conversion from similar CWFT experiments performed in a different photosensitizer, 4-BBA. The top figure shows that NO does react with HO ₂ to produce NO ₂ in the presence of 4-BBA and adipic acid (AA), as the organic aqueous base. The bottom figure shows no conversion in a clean tube.	57

3.1	Photochemical catalytic cycle of a photosensitizer (P) in a particle. a) The P first absorbs light being excited to the triplet state ($P^*(t)$). b) The triplet reacts with an H atom/electron donor to produce the reduced ketyl radical ($PH\cdot$). c) The ketyl radical may transfer an H atom or electron to an acceptor, such as O_2 . HO_2 radicals can then be released into the gas phase or react within the particle. Red reaction arrows indicate aging reactions of condensed phase organic molecules. Acid dissociation of HO_2 is not shown for simplicity.	61
3.2	Measured HO_2 radical release as a function of the ratio of photosensitizer to citric acid (CA) for BPh at 45 % <i>RH</i> , 4-BBA at 45 % <i>RH</i> and IC at 55 % <i>RH</i> (black, red and blue symbols, respectively). Error bars are determined from the standard deviation of several replicate measurements. Solid lines are fits using the model described in the text.	64
3.3	(a) Measured HO_2 release (symbols) as a function of <i>RH</i> at a fixed mole ratio of photosensitizer to CA (0.08 for BPh, 0.08 for 4-BBA, 0.11 for IC). Blue lines show model calculations for the case of IC based on the parameterization of the diffusion coefficient by Lienhard et al. ¹¹ , with and without an assumed water activity dependence of the rate coefficient for the HO_2 self-reaction (dashed and solid line, respectively). The blue dotted line represents the model prediction with adjusted diffusivity. The dashed purple line represents a suspected surface reaction. See text for more details. (b) Quantum yield HO_2 release of versus <i>RH</i> for the same experiments. Error bars are determined from the standard deviation of several replicate measurements.	65
3.4	HO_2 radical release photosensitized by IC in presence of citric acid and Syr (black squares) and SA (red circles) as additional competing donors, respectively, both at constant IC (0.7 M) and CA (6 M) load at 45 % <i>RH</i> . Error bars are determined from the standard deviation of several replicate measurements. Black and red lines represent the HO_2 release returned by the kinetic model described in the text for Syr and SA, respectively. The blue line and dashed lines indicate the measured HO_2 release and the error range, respectively, in absence of any additional donor apart from CA.	66
3.5	Catalytic mechanism and rate coefficients for the photochemistry of photosensitizers IC, BBA, BPh with a CA and the other H atom donors SA and Syr. Labels for photosensitizer and donors are the same as in Fig. 3.1. Reaction rate coefficients are defined in the SI.	68
3.6	Estimated production of IC ketyl radical, singlet oxygen, IC triplet and HO_2 , in the condensed phase film as well as HO_2 release into the gas phase for IC and CA with increasing concentrations of Syr at the same conditions as the CWFT experiments performed with Syr (Fig. 3.4).	70
3.7	Absorption spectra of the three photosensitizers (IC, BPh and 4-BBA) and the donors (CA, shikimic acid and syringol), irradiance spectrum of the UV lamps used and solar actinic flux at 48° zenith angle.	72
3.8	NO concentration raw data from films with lamps on and off.	73

3.9	NO concentration raw data to show NO loss with lights on and HONO trap in line, and w/o the molybdenum converter, to allow differentiating between the NO loss resulting from the reaction with HO ₂ and the secondary loss from the reaction with OH.	73
3.10	NO loss profile when lights on for films load with BPh and CA at 45 % RH.	74
3.11	Decay of the triplet state due to deactivation and reaction with syringol.	74
3.12	Rate coefficients derived from the laser photolysis experiments for the reactions of the triplet excited state of IC with Syr (black) and with SA (red).	75
3.13	HO ₂ release for films keeping IC/CA molar ratio constant at 0.16 but different loads leading to different film thickness at 36 % RH (black circles). Error bars are determined from the standard deviation of several replicate measurements. The corresponding model results with Lienhard parameterization of diffusion ¹¹ (solid blue line) and k_{scav3} reduced (dashed blue line) are shown. The contribution to the surface reaction was added to the latter (cyan dashed line). The prediction of the model using the proposed diffusion parameterization is represented by the dotted blue line.	76
3.14	HO ₂ radical production in aerosol particles of IC/CA (0.5 molar ratio) at 20 % RH compared NO loss coming from the empty reactor and the CA aerosol particles.	76
3.15	Parameterization of oxygen solubility in mixtures of citric acid and water as a function of relative humidity. The black lines indicate the region of oxygen solubility for our experimental conditions.	77
3.16	Diffusion coefficients as a function of relative humidity from the parameterization of Lienhard et al. ¹¹ at 281 K for water (black line), the extrapolated from the latter to 293 K for HO ₂ (red line) and the alternative parameterization (blue line) to achieve a better fit to the measured HO ₂ release under dry conditions.	78
4.1	Photochemical catalytic cycle of IC (box a) and halide radical chemistry induced in a particle. IC first absorbs light leading to the triplet state, which reacts with an H atom/electron donor (DH and X ⁻) to produce the reduced ketyl radical (PH) and halide radicals (X [·]). The halide radicals can produce molecular halogen (X ₂) or X ₂ ⁻ by reacting with X ⁻ . PH may transfer an H atom or electron to an acceptor, such as O ₂ producing HO ₂ radicals. HO ₂ can recycle the halide radicals previously produced into halides or oxidize further the X ₂ ⁻ to produce halogen molecules. HO ₂ radicals can be released into the gas phase or react within the particle with halide radicals or with itself. Solid lines refer to reactions and dashed lines refer to transfer from condensed to gas phase. Red reaction arrows indicate reactions promoting HO ₂ production, green arrows indicate reactions of recycling of halides promoted by HO ₂ and blue arrows indicate reactions of X ₂ promoted by HO ₂ . Rate coefficients are provided in Table 3.	84

4.2	HO ₂ release at 34 % <i>RH</i> from films with 4 mg of IC, 76.8 mg of CA and various concentrations of bromide (red) and iodide (black). Error bars indicate the standard deviation of between 2–6 measurements in the same film. The blue line and dashed blue lines indicate measured HO ₂ production and uncertainty, respectively, from IC and CA films with the same concentration but in absence of halides. Solid lines are fits using the model described in the text below.	86
4.3	Iodine release (black), produced by mixing the experimental flow with O ₃ /O ₂ as described above, and HO ₂ release (blue) into the gas phase versus time while irradiating a film in the CWFT loaded with 2.5 mg of IC, 76.8 mg of CA and 313 μg of NaI and equilibrated at 34 % <i>RH</i> . The blue arrow indicates the HO ₂ release expected for the film in absence of iodide.	88
4.4	Absorption spectra of IC (100 mM) and CA (from NIST Chemistry WebBook), irradiance spectrum of the UV lamps used and solar actinic flux at 48° zenith angle.	91
4.5	NO concentration raw data from films with lamps on and off at 35 % <i>RH</i> and containing 4 mg of IC and 76.8 mg of CA with an iodide concentration of 1.3×10^{-5} M.	92
4.6	NO concentration raw data to show NO loss with lights on and HONO trap in line, and w/o the molybdenum converter, to allow differentiating between the NO loss resulting from the reaction with HO ₂ and the secondary loss from the reaction with OH.	92
4.7	Mass of I ₂ O ₅ particles produced from the I ₂ released for each particle size at different times. The shady zone corresponds to the zone of the distribution we could not measure due to the limitations of the SMPS system.	93
5.1	Chemical mechanism of photolysis of SOM mediated by iron photochemistry and radical chemistry coupled with iron cycling induced by HO _x radical chemistry.	100
5.2	Diagram illustrating SOM preparation and UV exposure steps. SOA particles are produced by mixing a flow of air and O ₂ /O ₃ with limonene in a flow tube. The particles are collected on CaF ₂ windows located in a MOUDI, and the particles are annealed. FeCl ₃ is added for the iron content dependence experiments. After annealing at 40°C, samples are irradiated with a 305 nm UV-LED, and the OVOCs released are analyzed by a PTR-ToF-MS.	101
5.3	PTR-ToF-MS stick spectra of the OVOCs released from SOM before (red) and during (black) irradiation.	103
5.4	(a) Signal of acetaldehyde normalized to the maximum of the signal for each sample upon irradiation (shaded zone) at several values of <i>RH</i> . (b) Signal of OVOCs upon UV irradiation corresponding to the total OVOC flux and multiplied by the flow in mL/min for SOM samples versus relative humidity (%). The error bars represent the standard deviation resulting from 2 or 3 experiments.	104
5.5	(a) Signal of acetaldehyde after irradiation background-subtracted and normalized to the maximum of the signal for each sample upon irradiation (symbols) as a function of <i>RH</i> . Predictions by the diffusion model with upper and lower limits for the diffusion coefficient are shown as dashed and solid lines, respectively. (b) Diffusion coefficients predicted by the model for acetaldehyde as a function of <i>RH</i> , with the upper (blue) and lower (black) limits shown as blue and black symbols, respectively.	106

5.6	PTR-ToF-MS signal of acetic acid released upon UV irradiation for SOM samples versus time under dry conditions (a) and at 55 % <i>RH</i> (b) with varying mole fraction of added FeCl_3 . The shaded zone indicates the irradiation time. Signals from different samples were normalized to the total mass of the sample.	107
5.7	Peak intensities of signals from acetic acid, formic acid, acetaldehyde and acetone normalized to the total mass of the sample for SOM samples versus Fe/SOA molar ratio under dry conditions (a) and at 55 % <i>RH</i> (b). The error bars represent the standard deviation resulting from 2 or 3 repeated experiments.	108
5.8	Model compartments and layers in which the film is divided. The arrows represent the diffusion that occur between different compartments. The dimension of the compartments is represented by dx	110
6.1	Photochemical catalytic cycle of iron-carboxylate complex in a particle. $\text{Fe}^{\text{III}}\text{CA}$ (iron citrate) is photolyzed leading to the reduction of iron to Fe^{2+} and the decarboxylation of the ligand and the production of an organic radical. The latter reacts with oxygen leading to HO_x and a new stable molecule, which can further react with HO_x or by cycling with Fe^{3+} , leading to the decomposition to oxygenated volatile organic compounds (OVOC). HO_2 reduces Fe^{2+} back into Fe^{3+} , which can be complexed again by citric acid.	115
6.2	Spectrum of absorption of Fe(III) citrate and spectrum of irradiation of the lamps used. . . .	116
6.3	C-NEXAFS spectra from 278 eV to 320 eV of particles containing citric acid (black), iron citrate (red) and FeCit/CA (1:1) after 3 hours of UV irradiation in presence (blue) and absence (green) of oxygen. The shady zones correspond with the absorption of double bond, carbonyl and carboxyl compounds at 285.0 eV, 286.8 eV and at 288.6 eV respectively.	119
6.4	6-Energy spectra of particles containing FeCit/CA (1:1) before (black) and after 0.5, 1 and 3 hours of irradiation (red, blue and green respectively) over the same particles. b) Optical density of the carbonyl (black) and carboxyl (red) peak to the optical density in the post edge (320 eV).	119
6.5	Map of FeCit/CA particles (1:1 molar ratio) after illumination with UV light over 15 minutes in an atmosphere of 110 mbar of oxygen and 40 % <i>RH</i> . The color scale indicates $(\text{Fe}(\text{III})/(\text{Fe}(\text{II})+\text{Fe}(\text{III})))$ and is generated by means of the parameterization described in Moffet et al. ¹²	121
6.6	Signal normalized to the vanillin of citric acid before and after several hours of UV irradiation. Error bars indicate the standard deviation of 2–3 replica experiments. The blue line represents the linear decay from 1 hour to 24 hours of irradiation.	122
6.7	Signal normalized to vanillin signal before and after several hours of UV irradiation of a) several products of the decomposition of citric acid in positive mode and b) products bigger than CA.	122
6.8	Proposed mechanism of degradation of citric acid by FeCit photochemistry.	123

6.9	a) Steady state release of acetic acid and acetaldehyde from films loaded with FeCit and CA at 30 % <i>RH</i> while irradiating UV light as a function of FeCit content keeping constant the CA content. b) Steady state release of acetic for films containing FeCit and CA from films loaded with FeCit and CA ($\chi=0.03$) while irradiating UV light as a function of <i>RH</i>	124
6.10	Acetone release from films containing FeCit/CA with different molar ratios as a function of time at 30 % <i>RH</i>	125

List of Tables

1	Compilation of experimental conditions including masses of photosensitizers (P), CA, Syr and SA.	72
2	Chemical reactions and the corresponding rate coefficients used for the model.	78
3	Chemical reactions and the corresponding rate coefficients of halide and HO ₂ radical chemistry ¹³⁻¹⁹	87
4	Chemical reactions and the corresponding rate coefficients used for the model.	94
5	Signal of H ₃ ¹⁶ O ⁺ (derived from the signal of H ₃ ¹⁸ O ⁺) and signal of the H ₃ O ⁺ (H ₂ O) measured at different <i>RH</i>	110

Abstract Atmospheric aerosol particles suffer transformations during their residence time in the atmosphere (10 days on average). These transformations, known as aerosol aging, include physical transformations or chemical processes and are intensely influenced by the physical properties of the particles such as viscosity, diffusivity or absorption. The understanding of these transformations is essential to evaluate their impact on climate, air quality and health. Photochemistry may start aging processes by the presence of chromophores in aerosol particles that act as photocatalysts inducing oxidation of non-absorbing molecules, known as indirect photochemistry. Even though initial photochemical excitation occurs ubiquitously over the whole particle, the diffusion of the reactants plays a key role in the chemical processes that follow. The scope of this thesis is to assess the role of indirect photochemical aerosol aging in the life cycle of aqueous atmospheric aerosol particles including radical production, halogen activation and chemical evolution, to understand the links with the microphysical properties and to provide a sound basis for integration of these processes in atmospheric models. We aim to find out whether indirect photochemical aerosol aging processes are affected by transport limitations and changing photochemical regimes in viscous aqueous particles and to what degree indirect photochemical processes feed back to the microphysical properties.

The two light absorbing species families we are interested in are iron complexes, specifically Fe(III) citrate and aromatic ketone photosensitizers, which are brown carbon (BrC) substances, such as imidazole-2-carboxaldehyde (IC) among others. Iron (Fe(III)) carboxylate complexes absorb light below about 500 nm which leads to reduction of iron to Fe(II) and oxidation of the carboxylate ligands, which initiates the degradation of carboxylate ligands producing a broad spectrum of compounds, including OVOCs. This process represents an important sink of organic acids in the troposphere²⁰. Fe(III) carboxylate complexes are well-known to be photochemically active and they trigger Fenton-like reactions which are the dominant source of OH radicals in aerosol particles^{21,22}. Aromatic carbonyl photosensitizers absorb above 300 nm and form triplet excited states which initiate redox processes with other compounds by H atom abstraction from organics or electron transfer triggering organic and HO_x radical chemistry. Photosensitized processes provide an important contribution to condensed phase radical production and aerosol aging.

Measurements of HO₂ radical release from films containing BrC chromophores and citric acid, which is the matrix and main H atom donor, are performed as a function of chromophore content, relative humidity (RH), gas phase oxygen content and thickness. Experiments with additional donors such syringol, shikimic acid or halides are performed. In addition, iodine release, photochemically induced by IC, is measured as a function of time. We assess the contribution of photochemistry to radical budgets and redox activity, compare the impact on the gas phase versus internal cycling and consumption, as well as the photochemically induced halogen activation and release, and determine the effect of diffusion and water content on these processes. Aerosol growth induced by IC photochemistry by reactive uptake of an organic H atom donor is also assessed.

The evolution of carbon functional groups is followed in single particles containing Fe(III) citrate and citric acid exposed to humidity and oxygen under irradiation by scanning transmission X-ray microscopy (STXM) experiments. Non-volatile organic compounds produced by Fe(III) citrate photochemistry are analyzed with high pressure liquid chromatography mass spectrometry (HPLC-MS) of the extracts of irradiated samples of iron citrate. STXM and HPLC-MS measurements provide us with information about the chemical evolution and the efficiency of functionalization or oligomerization. By means of OVOCs release measured in SOA

with and without iron under irradiation the impact in the gas phase and to the mass loss in SOA due to photochemistry will be assessed.

1 Introduction

1.1 Atmosphere

Atmosphere (from Greek *atmos* "vapor, steam" + *sphaira* "sphere") refers to the gases and particulate matter surrounding a star or planetary body held in place by gravity. A planet's atmosphere shields the planet's surface from harsh radiation from the outer space and it moderates the amount of energy lost to space from the planet's interior. An atmosphere also makes possible features such as the existence of water on a planet's surface by supplying the pressure needed to keep the liquid from boiling away to space or the existence of life on the surface of a planet. The Earth atmosphere is composed mainly of nitrogen gas (78 %), oxygen gas (21 %), Argon (0.934 %), carbon dioxide (0.038 %) and a variable content of water (< 1 %). Other gases present in minor concentration are trace gases such as ozone (O₃), sulfur dioxide (SO₂), nitrogen oxides (NO_x) or methane (CH₄). Besides gaseous components, condensed aerosol particles are also present in the atmosphere. Typically the mass concentration of those near the surface of the Earth is between 5 and 50 μg per cubic meter. Although the concentration is relatively low, they play a key role in climate and human and ecosystem health.

1.2 Aerosol particles and aerosol aging

An aerosol is defined as a suspension of liquid and solid particles in a gas. Different types of aerosol are ubiquitously distributed through the entire atmosphere. The diameter of atmospheric aerosol particles ranges between a few nanometers up to tens of hundreds of nanometers. They can be separated in three modes: nuclei mode (< 0.1 μm), accumulation mode (from 0.1 to about 2.5 μm) and coarse mode (> 2.5 μm). Aerosol particles produced by mechanical processes are generally larger than 0.1 μm in diameter and mostly above 1 μm. Homogeneous nucleation from the gas phase leads to particles in the low nanometer range (nucleation mode). The composition of atmospheric aerosol particles is very diverse because of the large number of sources that exist and all the physical and chemical processes that they are involved with. It has been demonstrated that aerosol particles play an important role in the Earth's climate²³ and they affect air quality and, in turn, human health and ecosystems^{24,25}.

1.2.1 Sources of atmospheric aerosol particles

Atmospheric aerosol particles can either have natural or anthropogenic sources and are either emitted as primary particles (i.e. they are directly emitted into the atmosphere) or formed by secondary processes (i.e. by transformation of emitted precursor gases). The primary sources of aerosol particles comprise wind-blown mineral dust, sea spray, biological particles, biomass burning or volcanic activity. The secondary aerosol particles are generated by nucleation of new particles or by particle growth or aging of the existing particles.

Mineral dust

Mineral dust aerosol refers to the mineral particles emitted into the atmosphere by wind²⁶ from arid regions.

Once emitted, dust particles can be lifted up into free tropospheric regions through turbulent diffusion and vertical advection²⁷. Afterwards, depending on the dynamical situations of the free troposphere, they can be dispersed further away from their source regions. Especially, the finer dust particles can stay in the atmosphere for a week or more²⁸ and can be easily transported over large distances from their source region^{29,30}. Typical sizes of long-range transported mineral dust particles are from some hundreds of nanometers up to 10 micrometers in diameter³¹. Because of the large emissions and transport, mineral dust is an important and dominant component of atmospheric aerosol in many regions of the planet. Ginoux et al.³² attributed the 75 % of the global dust emissions to natural origin, while 25 % are related to anthropogenic (primarily agricultural) activities. The main source of mineral dust is the Sahara desert, which produces about half of the annual mineral dust^{33,34}. Iron compounds in soil dust absorb visible radiation triggering photochemistry and contributing to atmospheric warming, while scattering of mineral dust particles leads to surface cooling. These effects might impact wind circulation and affect climate on a regional scale^{35,36}.

Sea spray aerosols

The marine aerosol constitutes one of the most important natural aerosol systems globally. The primary aerosol production results from the interaction of wind stress at the ocean surface and results in the mechanical production of sea-spray aerosol (sea spray being the combination of inorganic sea salt and organic matter)³⁷. Sea spray is produced via beaking waves and the bubble-bursting process typically resulting from whitecap generation, producing film and jet drops, resulting in sea-spray particles in the submicrometre and few micrometres size range, respectively. The principal constituents of sea-spray aerosol particles are inorganic salts, such as sulfate, ammonium, nitrate or chloride and mineral dust³⁸. Although the nature of sea-spray particles is inorganic, a substantial fraction of organic compounds is normally found in marine aerosols. The organic matter can be incorporated into primary sea spray particles produced³⁹ from the sea surface microlayers by the processes of sea-spray generation mentioned above. The sea surface microlayer results from the accumulation of poorly soluble and often surface active organic material deriving from marine biota⁴⁰.

Biological aerosol particles

Biological aerosol particles include biological components, such as cellular particles lifted up into the atmosphere, including microorganisms, such as bacteria, algae, fungi or viruses, or dispersal material such as fungal spores, pollen, viruses and biological fragments ranging in size from tens of nanometers to millimeters⁴¹. The concentration heavily varies with location, altitude and season. It has been estimated that biological aerosol comprise 25 % of the total aerosol mass globally^{41,42}.

Secondary organic aerosols (SOA)

Atmospheric secondary aerosols originate from gas-particle conversion processes such as nucleation and growth of new particles, condensation of gas phase compounds onto existing particles and heterogeneous and multiphase chemical reactions. The precursors of secondary aerosol are gases such as SO₂, NO_x, NH₃ and VOCs and intermediate-volatility organic compounds (IVOCs). Those compounds are generally oxidized (or neutralized, in case of acids or bases) by gas-phase chemistry or by multiphase chemistry. The resulting compounds such as H₂SO₄, HNO₃ or low volatility organic compounds (LVOCs) have partition coefficients low enough to be able to condense on existing particles or nucleate new particles⁴³. A main contribution to

the secondary aerosols is of inorganic nature but an important contribution comes from organic compounds, which produce the so-called secondary organic aerosols (SOA). It has been found that many kinds of VOCs are able to produce SOA⁴⁴ such as biogenic compounds (alpha-pinene, limonene or isoprene)^{45–47} or anthropogenic compounds (aromatics)⁴⁸. The gas phase composition plays an important role on SOA composition and properties. Surratt and coworkers⁴⁹ found that different NO_x concentrations in the gas phase lead to a different composition of SOA produced by photooxidation of isoprene. This study points out that SOA composition can be different when deriving from the same precursor but under different conditions, e.g., in clean (low NO_x) and polluted (high NO_x). Marine spray aerosol particles can produce SOA by partitioning of oxidized volatile organic compounds such as dimethyl sulfide (DMS), aliphatic amines, isoprene and monoterpenes⁵⁰ by oxidants such as OH and O₃ and BrO.

Biomass burning

Biomass burning particles are the ones emitted by wildfires, combustion in residential fire places and wood stoves, etc. They contain carbon in the form of soot and organic carbon⁵¹. Emissions from biomass burning are often dominated by OC (pyrolysis products of lignin and polysaccharides), especially in wildfires.

Volcanic activity

Volcanic particles are made by fragmentation of magma (ash particles) and entrainment of ash particles^{52,53}. Their elemental composition is identical to that of the magma. Volcanic gases, such as sulfuric acid or metal halides or hydroxides can induce nucleation and partitioning into the existing volcanic particles.

1.2.2 Composition of atmospheric aerosol particles

The composition of aerosol particles in the atmosphere is extremely diverse because of the large number of sources that exist and all the physical and chemical processes that they are involved in. Therefore, the composition is dependent on location and time. Figure 1.1 shows an overview of the content of organics, sulfate, nitrate, ammonium and chloride of non-refractory PM₁ measured by aerosol mass spectrometry (AMS) at different locations¹. The nature of atmospheric aerosol particles is inorganic and organic. According to Zhang et al.¹ the organic fraction comprises between 18 % and 70 % of the measured mass, while the organic fraction can rise up to 90 % in tropical areas⁵⁴. Because of the large number of sources of organic compounds and the transformations of them in the atmosphere, the organic fraction of compounds found in aerosol particles is an extremely wide spectrum of compounds with different properties⁵⁵. Due to the complexity of the organic fraction, it is usual to use bulk properties to classify the organic molecules such as oxygen to carbon (O:C) ratio, (H:C) ratio, volatility, solubility in water or degree of polymerization.

1.2.3 Aerosol aging

The life time of an aerosol particle in the atmosphere is on average about 10 days. During this time an aerosol particle suffers chemical and physical transformations^{56–58}. Aerosol aging refers to all these transformations that alter the physical and chemical properties of the atmospheric aerosol particles. Aerosol aging comprises physical transformations such as growth by uptake of compounds from the gas phase, such as uptake of organics onto mineral dust particles¹², coagulation of several particles⁵⁹ or phase separation⁶⁰.

Aging can also be driven by chemical processes such as condensed phase reactions⁶¹, reactive uptake⁶², cloud processing⁶³, or gas phase reactions followed by partitioning to a particle. Some examples of aging by reactive uptake are ozone reactive uptake⁶⁴ or OH reactive uptake⁶⁵. Aerosol aging driven by reactions within particles can be induced by processes such as photochemistry^{66–68} or radical chemistry⁶⁹. The reactions that induce aging of organic compounds may be classified into fragmentation, oligomerization and functionalization⁵⁷. Regarding photochemistry in the condensed phase, particle phase photochemical processes contribute to aerosol aging by multiple mechanisms. Energy-transfer or charge-transfer reactions driven by triplet states of organic compounds^{10,70,71}, photolysis of nitrate and nitrite resulting in free radicals⁷², photochemistry of iron carboxylate or free iron²⁰, and photolysis of carbonyls^{73,74} are some of the examples of these processes.

Aging can lead to changing optical properties of the particles like scattering and absorption. Aging increases (browning)^{3,75,76} or decreases (bleaching) the absorbance of the condensed phase material⁷⁷ and the molecular mass and nature of the SOA compounds. The production of conjugated systems is usually the reason of enhancement of the absorption⁷⁵.

Aerosol hygroscopicity is another property that aging can change, which influences optical properties, the effectiveness as cloud condensation or ice nuclei and their respiratory track deposition. Due to the competing effects between fragmentation and functionalization, hygroscopicity will increase or decrease as aging occurs⁷⁸. Aging also changes the volatility distribution of the SOA compounds resulting for example from photo-induced fragmentation or oligomerization of SOA compounds (independent of whether this occurs in the gas or condensed phase) into more or less volatile products^{79,80}.

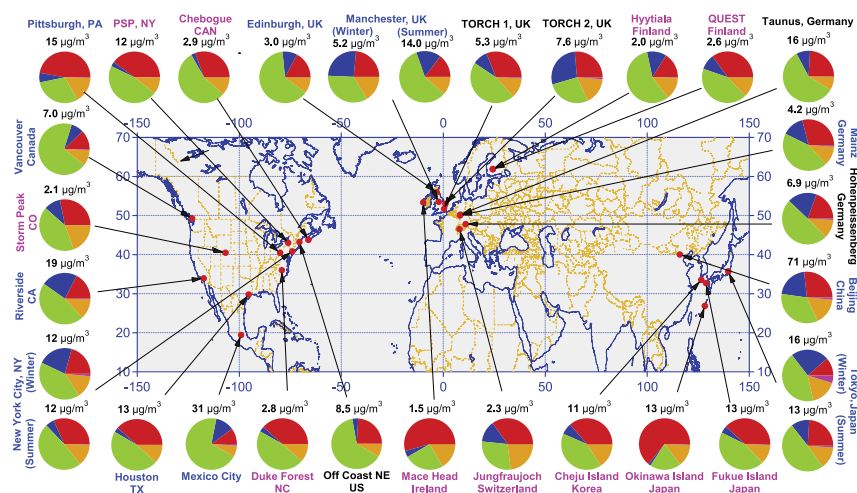


Figure 1.1: Overview of AMS datasets of non-refractory PM₁. Pie charts show the average mass concentration and chemical composition with the following color code: organics (green), sulfate (red), nitrate (blue), ammonium (orange), and chloride (purple). Colors for the study labels indicate the type of sampling location: urban areas (blue), < 100 miles downwind of major cities (black), and rural/remote areas > 100 miles downwind (pink). Reproduced from Zhang et al.¹.

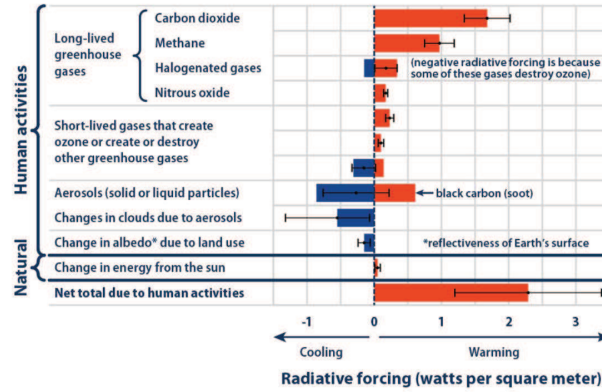


Figure 1.2: Radiative forcing induced by greenhouse gases, stratospheric water vapour, surface albedo, aerosol particles, between 1750 and 2005. Reproduced from IPCC, AR5 (2013)².

1.2.4 Influence on climate, ecosystems and human health

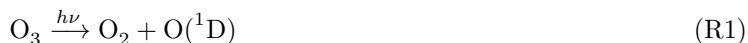
It has been demonstrated that aerosol particles and greenhouse gases play an important role in the Earth's climate, as documented in the reports of the Intergovernmental Panel on Climate Change² (see Fig. 1.2). Atmospheric aerosol particles affect climate in different ways. The direct effect refers to interaction of aerosols with radiation via scattering and absorption, which cause cooling and heating of the atmosphere respectively. The semi-direct effect refers to the heating of the aerosol by absorption of radiation, which reduces the relative humidity and induces the evaporation of the clouds. The indirect effects are related with the increasing number density of atmospheric particles, which leads to higher number density of cloud droplets and to a decrease in the cloud droplet size. This increases the albedo, inducing cooling of the atmosphere, and a decrease in the cloud precipitation efficiency. According to Boucher et al.²³, the current best estimate for the total effective radiative forcing by aerosols is -0.9 W m^{-2} .

Public health is affected by airborne particulate matter exposures that are currently experienced by urban populations in both developed and developing countries²⁵. Government and air-quality monitoring agencies track and regulate $10\text{-}\mu\text{m}$ -diameter (PM_{10}) and $2.5\text{-}\mu\text{m}$ -diameter ($\text{PM}_{2.5}$) particles. The unregulated ultrafine particles (smaller than 100 nm in diameter) are the major component in vehicle emissions and they have the largest surface area and highest content of potentially toxic hydrocarbons among all PM sources^{81,82}. They are potentially the most dangerous because they can also penetrate deeper into lung tissue than fine or coarse particles. The range of health effects that exposure to aerosol has is broad. These effects are related with respiratory diseases including allergies⁸³, cardiovascular diseases⁸⁴ and lung cancer⁸⁵. Since aerosol particles play such an important role in climate and human health, it is very important to understand the processes of formation, growth, aging and deposition as well as the transport through the atmosphere.

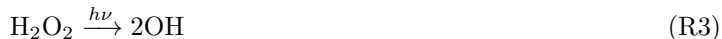
In addition, air pollution contributes to nitrogen deposition above eutrophication limits for large fractions of Europe's terrestrial and marine ecosystems², leading to a substantial loss of biodiversity. Ozone and nitrogen deposition also influence yields of agricultural crops and forest productivity.

1.3 Oxidative radicals in the troposphere

In this section and in the whole thesis radical dots (in species such as HO₂, OH, NO or NO₂) are usually omitted as is common practice in atmospheric chemistry. The sources and sinks of radicals play an important role in the oxidative capacity of the atmosphere. Radicals and other oxidants initiate the chemical degradation of various trace gases, which is key in the troposphere, where these radicals are also considered the cleansing agents to remove pollutants. The hydroxyl (OH) and hydroperoxy (HO₂) radicals belong to the HO_x chemical family and are primarily generated by ultraviolet radiation photochemical reactions (Calvert and Pitts, 1966), like the reaction of O(¹D) (from photolysis of O₃) with H₂O or photolysis of HONO, HCHO, H₂O₂ or acetone. Some secondary gas phase sources are the ozonolysis of alkenes or O(¹D)+CH₄⁸⁶. The oxidation of volatile organic compounds (VOCs) by OH and other oxidants in the presence of NO leads to perturbations in the HO_x, NO_x and RO_x radical cycles that affect O₃ and aerosol formation^{86,87}. The main source of OH radical is started by the photolysis of ozone.



Other sources of OH are the photolysis of H₂O₂.



The main source of HO₂ is driven by these reactions:



Some examples of termination reactions for HO_x radicals are:



The kinetics and photochemical parameters of these reactions are relatively well-known in the gas phase⁸⁸. However, this does not apply to the sources and sinks for HO_x in atmospheric droplets and in aerosol particles⁸⁹. Photolysis of H₂O₂, nitrate, nitrite⁹⁰, hydroperoxides⁹¹ and light-absorbing secondary organic aerosol (SOA)⁹² are the primary photochemical sources for HO_x in the condensed phase²². Other sources of HO_x radicals are the uptake of OH from the gas phase or the chemical reactions of reduced metal ions and H₂O₂, known as Fenton reactions^{93,94}. Other studies have shown that the photochemistry of Fe(III) oxalate

and carboxylate complexes, present in aqueous environments (e.g., wastewater, clouds, fogs, particles), can initiate a radical chain reaction serving as an aqueous source of HO₂ and Fe⁺². Fe⁺² can then regenerate OH starting a new cycle of Fenton reactions^{95,96}. The temperature-dependent rate coefficients in the aqueous phase have been studied for a limited subset of organics⁹⁷. However, there is still a wide gap with respect to understanding the sources, sinks, kinetics and photochemical reaction pathways of HO_x radicals in the condensed phase⁶⁷. A quantification of the OH radical production within atmospheric aerosol particles based on previously established and well characterised radical sources is attempted in the chemical aqueous phase radical mechanism (CAPRAM) model²² leading to an OH production within aerosol particles and uptake from the gas phase of about 15 M per day. It is one of the goals of this thesis to challenge this number by considering indirect photochemical radical sources not well characterized so far.

1.4 Brown carbon

1.4.1 Properties of brown carbon

Most OC compounds in atmospheric aerosol particles absorb strongly in the IR and UV, because of the vibrational modes and electronic transitions from saturated molecules respectively, but their absorption in the visible and near UV is low. Atmospheric brown carbon (BrC) is defined as the fraction of organic compounds in atmospheric aerosol particles that absorb efficiently in the UVA-VIS range^{98,99}. BrC is usually composed of molecules with a π conjugated system such as polycyclic aromatics, humic-like substances, biopolymers, etc. The light absorption in aerosol particles is dominated by three classes of constituents, black carbon (BC), which represents soot-like particulates generated by fossil fuel combustion and biomass burning¹⁰⁰, BrC, which is ubiquitously present in the troposphere^{101–103} and mineral dust. Absorption of solar radiation by BrC has been estimated at 0.1–0.25 W m⁻² globally, which is approximately 25 % of the radiative forcing by black carbon or soot¹⁰³. BrC reaches the aerosol phase of the atmosphere by fossil fuel combustion^{104,105}, biomass burning^{106,107}, gas phase photooxidation of VOCs^{108,109}, aqueous phase radical processes^{110,111} and non-radical aqueous phase processes^{112,113}.

1.4.2 Brown carbon photochemistry and photosensitizers

BrC can also initiate photochemistry resulting in changing composition and physical properties of aerosol particles, being able either to enhance or to reduce light absorption by BrC. For example, aqueous-phase aging of organic material may form light-absorbing oligomeric products, as indicated in studies where increased O/C ratios of OA were found to correlate with enhanced light absorption^{114,115}. On the other hand, direct photolysis of BrC may efficiently photobleach BrC with different photolysis rates highly specific to certain types of chromophores^{77,80,116}. Compositional changes may be partially related to triplet forming BrC species, so called photosensitizers, which may catalyze radical chain reactions. Many known photosensitizers are carbonyls, which absorb above 300 nm especially when attached to an aromatic system. Figure 1.3 illustrates the catalytic cycle of a photosensitizer with an initial excitation step, followed by singlet (P*(s)) to triplet (P*(t)) intersystem crossing. The reason for why triplet states are usually more important than

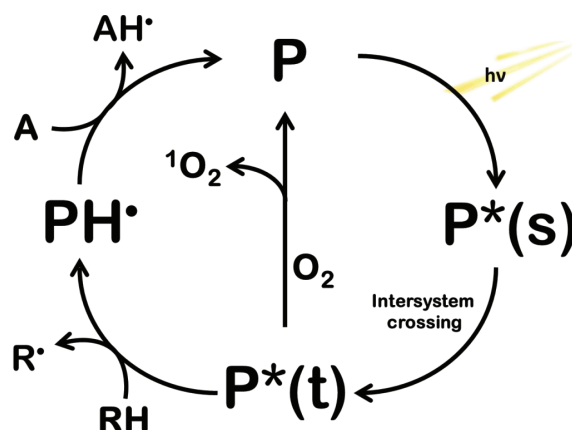


Figure 1.3: Catalytic mechanism of a photosensitizer (P). The initial step is the excitation step leading to the singlet state ($P^*(s)$) production followed by the singlet to triplet ($P^*(t)$) intersystem crossing. $P^*(t)$ can react with oxygen producing singlet oxygen or with an organic molecule producing an intermediate radical ($PH\cdot$) which can react the a electron/H atom acceptor leading to the production of P.

singlet states, even if the reactivity of the singlet is higher, is, because the triplet's steady-state concentration is higher than that of singlets. Normally the production rate is 15 – 100 times faster for singlet states but the decay is around 20000 times faster for singlet states¹¹⁷. The triplet state can either act as an oxidant to partially oxidize organic molecules such as phenols^{118,119} or react by an energy-transfer reaction with oxygen producing singlet oxygen¹¹⁷ and go back to the ground state of the photosensitizer (P). By reacting with organic molecules by hydrogen abstraction, an intermediate radical is produced ($PH\cdot$), called ketyl radical, when the photosensitizer is a carbonylic compound and the radical sits on the carbonyl carbon. This intermediate radical usually reacts with an electron/H atom acceptor (A) reducing it to AH and bringing the photosensitizer back to the ground state (P). O₂ can act as an electron/H atom acceptor producing a superoxide (O_2^-) or hydroperoxy radical ($HO_2\cdot$), respectively. Since photosensitizing BrC compounds absorb in the wavelength range above 300 nm, where direct photolysis of the majority of other organic aerosol components is not possible, the photochemistry initiated by photosensitizer triplets is also called “indirect photochemistry”.

Photosensitized chemistry is well-established in aquatic photochemistry^{117–119} and has been recently recognized as contributors to the oxidant budget in airborne particles^{67,120–123}. This may therefore represent an important contribution to aerosol aging. Imidazole-2-carboxylaldehyde is a well-known photosensitizer present in atmospheric aerosol particles in the range of ng per cubic meter¹²⁴ which together with other imidazole forms are products from the multi-phase chemistry of glyoxal and ammonium sulfate (AS) in aqueous aerosols (Fig. 1.4)^{3,5,10,123}. Glyoxal is an important oxygenated volatile organic compound (OVOC) and some of its sources are the oxidation of VOC such as acetylene, aromatics, or biogenic compounds.

Other examples of photosensitizers are benzophenone and 4-benzoylbenzoic acid¹¹⁹. Those together with other aromatic carbonyls, they may be formed as intermediates in the photooxidation of aromatic compounds in the gas phase^{125,126} or also by condensed phase oxidation of biomass burning products^{127–130}.

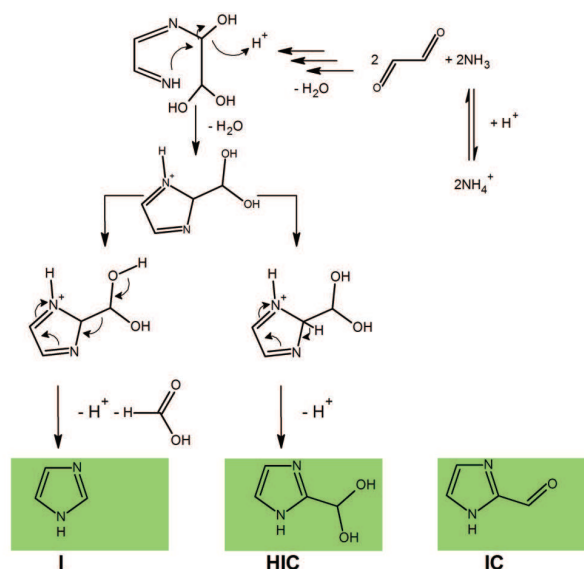


Figure 1.4: Proposed reaction pathways for imidazole formation in the glyoxal/ammonium sulfate system are shown. Green colored compounds were previously described in literature^{3,4}; orange colored compounds were identified in this work. Reproduced from Kampf et al.⁵

1.5 Iron in atmospheric particles

1.5.1 Sources and mobilization

Iron is the most abundant transition metal at the Earth's surface. It is mobilized from mineral structures as well as reaching aquatic atmospheric systems such as aerosol particles. The main sources of iron are wind-blown dust emissions, industrial processes or combustion^{94,131}. Iron reaches the atmospheric aerosol particles mostly as aluminosilicate minerals (either in Fe(II) or Fe(III)), as iron oxides or hydroxides^{94,132,133}, which are mainly hematite (Fe_2O_3), goethite (R-FeOOH)¹³⁴, nanosized amorphous and/or poorly crystalline Fe-oxyhydroxides and clays¹³⁵. In pollution events iron can be found as sulfides (FeS_2 , FeS and Fe_{1-x}S), which are products of coal combustion¹³⁶. Once iron containing mineral particles are in the atmosphere, they start taking part in several chemical processes such as gas-solid heterogeneous chemistry on the surface of solid particles¹³⁷.

Mineral dust takes up acidic gases¹³⁷, which in turn leads to uptake of water on the surface of the solid mineral particle. Iron can then be dissolved, which can happen by two different mechanisms: (i) Acids present in aerosol particles such as H_2SO_4 (from SO_2) or HNO_3 (from NO_x emissions) promote the dissolution of iron cations (Fe^{+2} and Fe^{+3}). The presence of protons adsorbed at the surface of a mineral weakens the O-Al and O-Si bonds, distorting the mineral structure and loosening the O-Fe bond, which facilitates the mobilization of iron cations⁹⁴. (ii) The presence of nucleophilic iron ligands, such as oxylate¹³⁸ or sulfate¹³⁹, induces the dissolution of iron cations and the formation of complexes. The ligands produce coordinate bonds with iron on the surface of the mineral. When the complex formed at the surface is photoactive, the dissolution can be promoted by the photoreduction of Fe(III) to Fe(II), which makes the Fe-O bond

weaker. The solubility of the iron present in particulate matter in the atmosphere varies from 5 % to > 50 % depending on the kind of compound or mineral that is containing iron⁹⁴. Normally anthropogenic iron is more soluble. The range of concentration of soluble iron in condensed phases in the atmosphere is wide going from 10^{-6} M in cloud and rain droplets up to 10^{-2} M in fog or aerosol particles^{94,140,141}.

1.5.2 Iron speciation

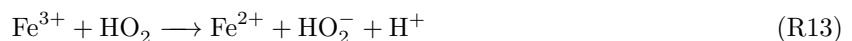
Iron is present in atmospheric aqueous phases mainly as cations with oxidation states (II) and (III). Iron is found producing complexes with inorganic or organic ligands. In the absence of soluble organic compounds, Fe(III) is mainly found in aqueous solution as low molecular weight species complexed with the hydroxide such as $\text{Fe}^{\text{II}}(\text{OH})^+$, $\text{Fe}^{\text{III}}(\text{OH})^{2+}$, $\text{Fe}(\text{OH})^{2+}$ or $\text{Fe}_2(\text{OH})_4^{2+}$. Other ligands that are associated with iron are sulfate (SO_4^{2-}) and sulfite (SO_3^{2-})¹³⁰. Many theoretical studies tried to figure out the importance of each complex that iron forms which concluded that the most probable Fe(III) complexes are formed with hydroxy anion, sulfate and sulfite^{130,142,143}. However, all of these theoretical studies neglect the potential complexing capacity of organic compounds with iron. Some works found high content in oxalate and other carboxylic acids in cloud water^{144,145}. Therefore, complexes with organic ligands are usually found in the atmospheric condensed phase. Siefert et al. calculated the speciation of Fe(III) complexes for the concentrations found in seven fog water samples¹⁴⁶. They show that the predominant Fe(III) species are Fe(III)-oxalate and Fe(III)-hydroxy species. For certain samples characterized by high pH and low oxalate concentrations, calculated Fe(III)-oxalate complexes are insignificant. Weschler et al.¹³⁰ noted that a portion of iron can be strongly complexed with ligands that are bound to the metal by more than one functional group, which are called chelate ligands. Some investigations^{130,147} postulated that a fraction of iron may be linked with humic substances, which can act as chelate ligands. In conclusion, these studies show that the most important Fe(III) complexes in atmospheric liquid water are Fe(III)-hydroxy species and Fe(III)-organic complexes. However, because of the lack of knowledge on the organic compounds speciation in atmospheric liquid phase, it is difficult to draw conclusions on the nature of Fe(III)-organic complexes, even if oxalate complexes seem to be usually observed.

Field campaign measurements show a great variability in the Fe(II)/Fe(III) ratio. Some works have found a greater concentration of Fe(II)¹⁴⁸ during the day which led to the assumption that the photolysis and reduction of Fe(III) complexes was dominating. Measurements of Fe(II)/Fe(III) by X-ray absorption near edge structure (XANES) spectroscopy showed that Fe(III) was more concentrated in the solid phase than in the water soluble fraction, which points out to the importance of the photoreduction of Fe(III) in presence of ligands with which Fe(III) can produce photoactive complexes¹⁴⁹. These results are supported by a work of Moffet et al.¹², where they found a ratio $\text{Fe}(\text{II})/(\text{Fe}(\text{II})+\text{Fe}(\text{III}))$ of 0.33 for particles collected on Okinawa Island during an atmospheric pollution transport event from China.

1.5.3 Radical chemistry and photochemistry

Dissolved iron undergoes a complex redox cycling in atmospheric particles that involves reactions with HO_x radicals and photolysis. One of the most important and interesting reactions that iron undergoes is

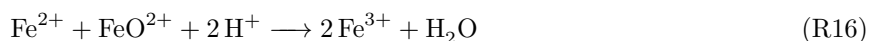
known as Fenton reaction, on the basis of an article by Fenton et al.⁹³ The Fenton reaction of Fe(II) with H_2O_2 is recognized as a significant source of OH radicals in atmospheric particle phases²², even though the reaction rate coefficient is rather low ($50 \text{ M}^{-1} \text{ s}^{-1}$ at 25°C)¹⁵⁰. The mechanism by which hydrogen peroxide is degraded by Fe(II) is still uncertain and under debate. The mechanism was firstly described by Barb et al.¹⁵¹



And/or



An alternative mechanism based on the reaction of Fe(II) with H_2O_2 producing the ferryl ion (Fe (IV))¹⁵² was taken into consideration after the OH radical production via the Fenton reaction was questioned by several studies. The ferryl ion is an intermediate species in the Fenton chemistry.



Many other studies have been performed over decades suggesting different mechanisms for different conditions^{94,153–156} and not all details have been resolved about Fenton chemistry in atmospheric waters^{157,158}. Even so, we know that OH production in the aqueous phase is partly driven by iron reactivity. For continental clouds the sources of OH are numerous²², and the respective contributions of each one depend on the concentrations of chemical species in the aqueous phase, the pH value, the actinic flux, etc^{94,159}.

Additionally to dark radical and Fenton chemistry, iron complexes in atmospheric particles can be excited by light which leads to HO_x and organic radical production. For example $\text{Fe}(\text{OH})^{2+}$ is a photoactive complex in the UV region which contributes significantly to the OH production in cloud water and in the aerosol phase by the following reaction:



As said in the previous section, oxalate and other carboxylic acids are present in environmental systems^{144,145} and, therefore, Fe(III) is usually found forming complexes with those carboxylate ligands in environmental waters and particles^{160,161}. The resulting Fe(III) carboxylate complexes are well-known photoactive compounds^{20,95,162} that absorb radiation in the UV-VIS region and are photoreactive through ligand to metal charge transfer reactions (LMCT)¹⁶³, which is an inner sphere electron transfer from the carboxylate func-

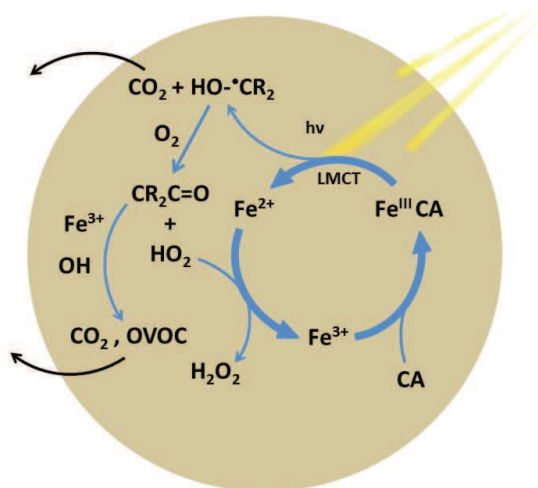
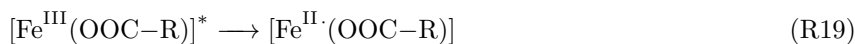


Figure 1.5: Photochemical catalytic cycle of an iron-carboxylate complex in a particle. $\text{Fe}^{\text{III}}\text{CA}$ (iron citrate) is photolyzed leading to the reduction of iron to Fe^{2+} and the decarboxylation of the ligand and the production of an organic radical. The latter reacts with oxygen leading to HO_x and a new stable molecule, which can further react with HO_x or by cycling with Fe^{3+} , leading to the decomposition of citric acid to oxygenated volatile organic compounds (OVOC). HO_2 reduces Fe^{2+} back into Fe^{3+} , which can be complexed again by citric acid.

tionality to iron. $\text{Fe}(\text{III})$ carboxylate complex is initially excited to a long lived radical complex^{164–166} which can dissociate producing Fe^{2+} and R-COO^\cdot radical.



After separation from Fe^{2+} , the R-COO^\cdot radical decarboxylates rapidly producing CO_2 and an organic radical (R^\cdot) and this last radical presumably will react rapidly with oxygen, producing a peroxy radical.



As it is described in figure 1.5, peroxy radicals subsequently might produce oxidants such as $\text{O}_2^{\cdot-}/\text{HO}_2$ and H_2O_2 from the unimolecular or bimolecular decay of peroxy radicals^{166,167}. $\text{O}_2^{\cdot-}/\text{HO}_2$ and H_2O_2 can react in cascade with $\text{Fe}(\text{II})$ oxidizing it back into $\text{Fe}(\text{III})$ and thus additionally produce OH radicals, which by themselves also can react with $\text{Fe}(\text{II})$ to oxidize it back into $\text{Fe}(\text{III})$. Presumably $\text{Fe}(\text{III})$ rapidly again forms a complex with a carboxylate group closing the catalytic cycle of photodegradation of carboxylic acids. The whole catalytic cycle is represented for citric acid in Figure 1.5.

Iron acts then as a catalyst for HO_x radical formation and degradation of carboxylic acids by cycling

between Fe(III) and Fe(II), and thus, in a way, establishes another example of indirect photochemistry. These degradation processes are the major sink of carboxylate groups in the aerosol phase in the atmosphere and produce a change in the chemical composition and also volatile OVOC species^{20,95,168}. It has been suggested that this photochemistry might be an important source of reactive oxygen species (ROS) in atmospheric condensed phases^{94,169,170}. Additionally, ROS such as HO₂ and OH radicals are key to assess the oxidative capacity in aerosol particles²². OH radicals react rapidly with organic compounds in the condensed phase producing a broad spectrum of oxidized compounds^{65,69,171}. Apart of the reactions included in the mechanism shown in Figure 1.5, alternative pathways have been suggested as the reduction of the Fe(III) to Fe(II) by organic radicals or a decarboxylation driven by di-iron complexes that does not include the production of any radical¹⁶⁸.

1.6 Halogens in the atmosphere

1.6.1 Activated halogen species

Volatile halogen-containing species such as CH₃X, CH₂XY, HOX, XY, and X₂ (where X and Y can be Cl, Br and I), also called activated halogen species, are emitted into the atmospheric gas phase by oxidation of halides by ozone in the sea surface¹⁷², or in snowpacks^{173,174} by biogenic emissions of halogen-containing organic species (Org-X)^{175,176}, or by emissions from volcanos, among other processes¹⁷⁷. Halogen activation refers to the production of activated halogen species. These species are direct precursors of reactive halogen species (RHS) such as X atom or XO¹⁷⁸, which trigger oxidative processes in the gas phase¹⁷⁹. In the troposphere the presence of XO shifts the HO_x equilibrium (HO₂ \rightleftharpoons OH) towards OH^{180–185}. It has been observed that RHS of iodine produce ultrafine particles found in coastal areas^{186,187}. This new particle formation takes place by the polymerization of I₂O₅^{188–191}, which is produced by the oxidation of iodine precursor species such as I₂¹⁹² and Org-X¹⁹³. The production and depletion at the sea surface or in suspended condensed matter of activated halogen species are key processes to understand their release into the gas phase and the contribution to their emissions^{172,194}.

1.6.2 Feedbacks between photosensitized chemistry and halogen activation

Halides present in the environmental waters and aerosol particles have influence on photosensitized chemistry. The triplet states of photosensitizers act as oxidants reacting with an electron donor, such as halides (X⁻), producing organic and HO_x radicals. Subsequent to the oxidation of the halide anion by the triplet state of IC, halide radicals (X[·] and X₂⁻) are produced and the ensuing halide radical-radical reactions produce molecular halogen. The oxidized species X₂, X₂⁻ and X[·] are likely recycled into X⁻ by HO₂ radicals, however a fraction of X₂ may be released into the gas phase¹⁹⁵, and these recycling processes are determining the effective efficiency of halogen activation.

1.7 Diffusion, viscosity and chemical reactivity

Atmospheric aerosol particles are solid or liquid or a mixture of both depending on their composition and ambient conditions^{196,197}. Because the large number of organic compounds that are present in organic-rich aerosol particles and the non-crystalline nature of some of them, the organic phases are non-crystalline, i.e. amorphous. The viscosity and therefore diffusion properties of SOA material largely change over different temperatures or humidity^{11,198,199} because water acts as a plasticizer for most aqueous organic mixtures. Viscosity and diffusion are related with each other by the Stokes-Einstein equation:

$$D = \left(\frac{k_B T}{6\pi\eta r} \right) \quad (1)$$

Where D is the diffusion coefficient, k_B is the Boltzmann constant, T is temperature, η is viscosity and r is the apparent radius of the molecule that diffuses. The viscosity of atmospherically relevant mixtures may vary over a very wide range depending on T and RH and composition, going from 5×10^{-3} to 10×10^9 Pa s. We cannot always rely on viscosity measurements to estimate diffusion since it has been found that the Stokes-Einstein treatment cannot relate the diffusivity of water to the particle viscosity when the viscosity exceeds 10 Pa s²⁰⁰. Koop et al.⁷ shows a classification of organic phases sorting them in terms of viscosity and diffusion defining liquids, semisolid and solid phases as shown in Figure 1.6. Virtanen et al. (2010)²⁰¹ showed that SOA particles formed in plant chamber experiments and in new particle formation events over boreal forests can adopt an amorphous semisolid state. In addition, vapor pressure, volatility, and evaporation kinetics experiments also indicate a highly-viscous state^{202,203}. This is in line with the observed presence of oligomers or other organic compounds with high molecular mass and low volatility in SOA²⁰⁴. Depending on viscosity and microstructure, the amorphous phases can be classified as glasses, rubbers, gels or ultra-viscous liquids²⁰⁵. The reduced mobility of aerosol constituents in high viscosity particles has a great impact on multiphase chemistry since the reactive uptake is dependent on diffusion⁶⁴. Changes in viscosity can also induce changes in the photolysis rate of chromophores²⁰⁶ and intersystem crossing efficiencies²⁰⁷. Solid particles such as combustion particles^{208,209} or mineral dust²¹⁰ undergo chemical reactions with gas phase species at the surface. It may be expected that this is also the case for semi-solid states, as suggested in several studies, where in the vicinity of the glass transition, surface processes may become dominant²¹¹⁻²¹³. When this high-viscosity scenario does not apply, reactions may occur in the bulk and in the surface simultaneously^{214,215}. Two different cases are usually considered by comparing the diffusion and reaction rates²¹⁶. In the first case, from the point of view of the incoming trace gas molecule, the diffusion is much faster than the reaction rate, therefore the volatile reactant molecule, which is taken up, diffuses through the entire bulk without significant loss. Then we can treat the reaction as a common second order reaction in a homogeneously mixed bulk phase:

$$\frac{d[Y]_b}{dt} = -k_b^{II} [X]_b [Y]_b = -k_b^{II} H_X P_X [Y]_b \quad (2)$$

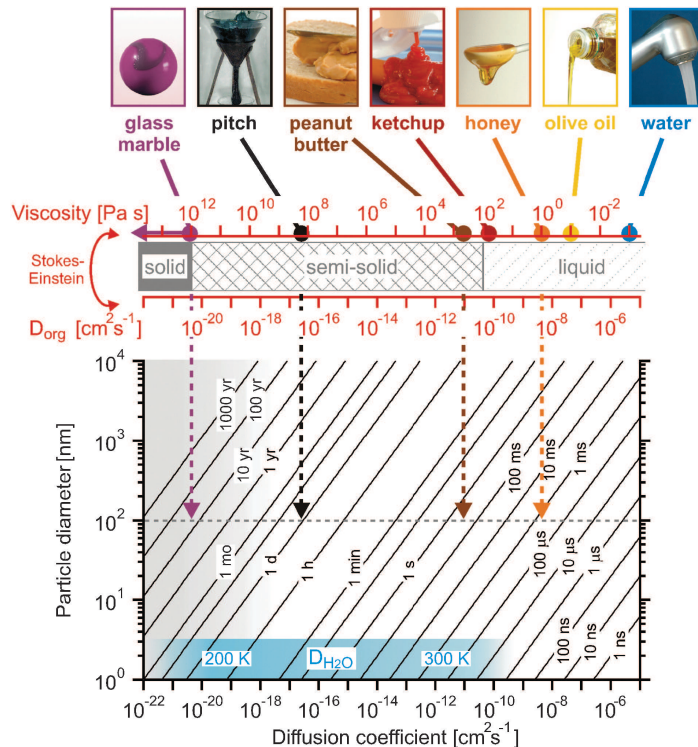


Figure 1.6: Classification into solid, semi-solid and liquid states of various substances as a function of dynamic viscosity. For organic liquids the molecular diffusion coefficient D_{org} can be inferred from the viscosity via the Stokes-Einstein relation (eq. 5). In the bottom panel we show the corresponding e-folding times of equilibration for various particle diameters according to Shiraiwa et al.⁶. Reproduced from Koop et al.⁷

Where $[Y]_b$ is the concentration of the reacting molecule in the condensed phase, $[X]_b$ is the concentration in the condensed phase of the reactant molecule that is being taken up, k^{II} is the second order rate coefficient, H_X is the Henry's law constant of the molecule X and P_X is the pressure of X in the gas phase. In this case, the overall reaction rate scales with the volume of the system; this is the reason why in multiphase chemical kinetics this regime is commonly referred to as volume limited reaction kinetic regime.

The second case applies when the molecule X diffuses slowly in comparison with the reaction rate coefficient. In this reacto-diffusion limited kinetic regime a gradient of the volatile reactant X forms in the condensed phase and the reaction rate depends on the diffusion coefficient of X within the particle bulk. Effectively, reaction occurs only within a layer of thickness l , which is the so-called reacto-diffusive depth, below the surface.

$$l = \sqrt{\frac{k_b^{\text{II}}[Y]_b}{D_X}} \quad (3)$$

Where D_X is the diffusion coefficient. The reaction rate for this case is described with the following equation:

$$\frac{d[Y]_b}{dt} = -H_X RT \sqrt{D_X k_b^{\text{II}} [Y]_b} \left[\coth\left(\frac{r}{l}\right) - \left(\frac{l}{r}\right) \right] \frac{S_p}{V_p} [X]_g \quad (4)$$

Where R is the gas constant, T is temperature, D_x is the diffusion coefficient, l is the reacto-diffusive length, r is the radius of the particle, S_p is the surface of the particle and V_p is the volume of the particle. This equation can be applied for a wide range of reactive trace gas uptake systems²¹⁶ as long as the reactant Y can be considered well-mixed over the time scale of its loss due to reaction with X . In case of intermediate viscosity, the proper kinetic regime, for which either equation (X) or (Y) above apply, needs to be assessed. For instance, in the ozonolysis of shikimic acid, at very high humidity the first regime applies (low viscosity, both reactants well-mixed), while for intermediate humidity, the regime changes to the second, shikimic acid remaining well-mixed but O_3 lost close to the surface²¹². In the same experiments, at lower humidity close to the glass transition, this simple steady state analysis fails due to concomitant diffusion limitation by both reactants. In this case, an explicit depth resolving model needed to be applied to successfully explain the kinetic behavior⁶⁴.

Apart of the effect of viscosity affecting diffusion and thus transport and mixing rates, viscosity can directly affect condensed-phase reaction rates. Lignell and coworkers²⁰⁶ demonstrated that viscosity can drastically enhance the photolysis rate coefficient of 2,4-dinitrophenol changing from water to an organic solvent also suggesting the relation between photochemical rate coefficients and viscosity and/or matrix must be properly assessed. They also reveal differences between the effect of temperature on the photolysis efficiency of 2,4-dinitrophenol trapped in a viscous organic matrix, in a liquid organic solvent, and in an aqueous solution. A study from Nagarajam et al.²⁰⁷ explained that steric congestion induces twisted conformations in aromatic molecules which results in an increase in the yield of triplet excited states. They observed a range of quantum yields from $< 1\%$ in planar conformation up to 30% in twisted conformations. An increase in viscosity results in stronger steric congestions and therefore viscosity affects the intersystem crossing efficiency. The viscosity of SOA material is controlled by the humidity that it is exposed to and therefore the water content. When relative humidity changes, water content and viscosity/diffusion change simultaneously. There is evidence that the water content influences the rate coefficient of radical reactions: hydrogen bonded transition states are involved in electron transfer²¹⁷, proton coupled electron transfer²¹⁸ and hydrogen abstraction reactions²¹⁸. Therefore, changes on rate coefficients by water content will interfere with the changes of rate coefficients by viscosity explained above. In the photochemical systems described above (photosensitized chemistry and iron carboxylate complexes chemistry), oxygen plays an important role since it induces HO_x radical production and deactivates triplet states. Changes in the diffusion coefficient of oxygen indirectly induce changes on HO_x production and on the steady-state concentration of triplet states. Variation of RH induces different diffusion and viscous properties and different water content. In terms of photochemistry, the interplay of these processes makes understanding the feedbacks between photochemistry and physical properties a challenging task for this thesis.

1.8 Motivation and outline

1.8.1 Motivation of the project

Indirect photochemistry is especially relevant in the lower troposphere where UV light intensity with sufficiently low wavelengths to directly photolyze the major organic or inorganic aerosol components is

low. The two light absorbing species families we are interested in are iron complexes and aromatic ketone photosensitizers. Iron (Fe(III)) carboxylate complexes absorb light below about 500 nm which leads to reduction of iron to Fe(II) and oxidation of the carboxylate ligands, which initiates the degradation of carboxylate ligands producing a broad spectrum of compounds, including OVOCs. This process represents an important sink of organic acids in the troposphere²⁰. Fe(III) carboxylate complexes are well-known to be photochemically active and they trigger Fenton-like reactions which are the dominant source of OH radicals in aerosol particles^{21,22}. Aromatic carbonyl photosensitizers absorb below about 600 nm¹⁰⁵ and form triplet excited states which initiate redox processes with other compounds triggering organic and HO_x radical chemistry. Photosensitized processes provide an important contribution to condensed phase radical production and aerosol aging. In the last two decades both systems have been investigated in detail in aquatic systems^{20,118}, but just a few in depth studies have been made under conditions relevant for the aerosol phase. It has recently been recognized that aqueous aerosol particles may attain highly viscous, semisolid or even glassy physical states under a wide range of conditions in the atmosphere²¹⁹. While the impact of reduced mobility of aerosol constituents in high viscosity particles on dark multiphase chemistry has received substantial attention⁶⁴, systematic studies on the effect of high viscosity on photochemical processes are scarce²⁰⁶.

This thesis is embedded in a larger project in collaboration with colleagues at ETH Zürich, in which we study indirect photochemical processes, which catalyze redox processes of non-absorbing molecules, and the impacts the reduced mobility and low water content in highly viscous particles has on them. This includes a comprehensive analysis of a wide range of observables to constrain the many driving variables as much as possible. Mass loss, size, water diffusivity, and optical properties of single levitated particles are measured in an electrodynamic balance at ETH. Spatially resolved O:C ratios, carbon functional group composition, and Fe oxidation state is measured by in situ scanning transmission X-ray microscopy (STXM) at PSI. Measurements of OVOC formation rates and assessment of radical budgets are performed in an irradiated coated wall flow tube (CWFT) at PSI together with offline organic analysis by HPLC-MS of non-volatile organic compounds. In each of these techniques, the model systems will be followed over time as a function of irradiation, *RH* and temperature. The integration of the results will be assisted by kinetic model tools developed within the collaboration. It will provide a sound basis to understand the bidirectional feedbacks between indirect photochemical aerosol aging, optical properties and viscosity for the selected particle system. In this collaborative project we assess the role of indirect photochemical aerosol aging in the life cycle of aqueous atmospheric particles, how it is linked with microphysical properties and provide a sound basis for integration of these processes in atmospheric models. We intend to figure out whether indirect photochemical aerosol aging processes are affected by transport limitations and changing photochemical regimes in viscous aqueous particles and to what degree indirect photochemical processes feed back to the microphysical properties, to the optical and to the photochemical properties. We will link our results with health effects by assessing the contribution of the ROS produced by photochemistry to the oxidative stress suffered by lung cells when particles exposed to light are inhaled by humans.

1.8.2 Specific goals of this thesis

By means of measurements of HO₂ radical release rates in CWFT experiments at different conditions of *RH* or chromophore content, I will assess the contribution of photochemistry to radical budgets and redox activity, compare the impact on the gas phase versus internal cycling and consumption and determine the effect of diffusion and water content on photochemical reaction rates. By measuring the iodine release from mixtures of photosensitizers with iodide and bromide as a proxy for sea water containing chromophoric dissolved organic matter (CDOM), we assess the contribution of photosensitized chemistry to halogen activation and the efficiency of the release versus the internal cycling of halide radicals.

Carbon functional group composition is measured by STXM and non-volatile organic compounds produced are analyzed by analysis with HPLC-MS of irradiated samples of iron citrate. These latter measurements provide us with information about the chemical evolution and the efficiency of functionalization or oligomerization. By means of OVOCs release measured in SOA with and without iron under irradiation I will assess the impact on the gas phase and on the mass loss of SOA due to photochemistry.

The experimental observables are always studied as a function of relative humidity to address kinetic regimes, the role of transport limitations and to partially assess the feedbacks between microphysical properties and photochemistry as set out in the overall project goals.

1.8.3 Outline of the thesis

Chapter 2. Heterogeneous photochemistry of imidazole-2-carboxaldehyde. HO₂ radical formation and aerosol growth. HO₂ release was measured for mixtures of imidazole-2-carboxyldehyde (IC) and citric acid under irradiation by CWFT experiments for several conditions. SOA growth was observed via IC photochemistry by reactive uptake of limonene. The results indicate a potentially relevant contribution of triplet state photochemistry for gas-phase HO₂ production, aerosol growth and aging in the atmosphere.

Chapter 3. Particle phase photosensitized radical production and aerosol aging. We extended the series of photosensitizers including the benzophenone and 4-benzoylbenzoic acid apart of IC measuring the HO₂ release for mixtures of photosensitizers and citric acid under irradiation by for several conditions including in the presence of additional organic donors (syringol and shikimic acid). We developed steady-state model and concluded that photosensitized radical production can be a major contribution to the radical production in aerosol particles when the concentration of triplet-scavenging organic compounds is high enough.

Chapter 4. Halogen activation and radical cycling initiated by imidazole-2-carboxaldehyde photochemistry. HO₂ release was measured for mixtures of imidazole-2-carboxyldehyde (IC) and citric acid under irradiation by CWFT experiments as a function of bromide and iodide content. The iodine release was measured for mixtures of imidazole-2-carboxyldehyde (IC) and citric acid under irradiation as a function of time. Halogen radicals formed in turn scavenge the HO₂ thereby recycling the iodine radicals back into iodide and partially shutting down HO_x

chemistry. Occasionally molecular iodine is produced and released into the gas phase as a still important halogen activation process, specially under dry conditions.

Chapter 5. Influence of humidity and Fe(III) on photodegradation of atmospheric secondary organic aerosol particles. OVOC release from SOA produced by oxidation of limonene by ozone was measured under irradiation as a function of iron content and RH . Low iron concentration increases slightly OVOC release, whereas at high iron concentration OVOC release decreases significantly. Upon increasing RH up to $\sim 50\%$ RH , OVOCs release was up to 4 times greater than the release under dry conditions. The expected fractional mass loss induced by these photochemical processes from limonene SOA particles would be up to 4 % of particle mass per hour.

Chapter 6. Aerosol aging driven by photochemistry of iron citrate. Fe(III) citrate particles and films were exposed to UV light. We assessed the chemical evolution including OVOC and non-volatile organics. The appearance of products from direct iron citrate photochemistry and from HO_x radical chemistry were observed over hours. Oxygen diffusion limitations probably take place under irradiation inducing an anoxic chemistry in the bulk of the particles.

2 Chapter 2

Heterogeneous photochemistry of imidazole-2-carboxaldehyde: HO₂ radical formation and aerosol growth

Laura González Palacios^{1,2}, Pablo Corral Arroyo^{3,4}, Kifle Z. Aregahegn^{6,a},
Sarah S. Steimer^{3,5,b}, Thorsten Bartels-Rausch³, Barbara Nozière⁶,
Christian George⁶, Markus Ammann³, Rainer Volkamer^{1,2}

1. Department of Chemistry and Biochemistry, 215 UCB, University of Colorado, Boulder, CO 80309, USA.
2. Cooperative Institute for Research in Environmental Sciences (CIRES), 216 UCB, University of Colorado, Boulder, CO 80309, USA.
3. Laboratory of Environmental Chemistry, Paul Scherrer Institute, 5232 Villigen, Switzerland.
4. Department of Chemistry and Biochemistry, University of Bern, 2012 Bern, Switzerland.
5. Institute for Atmospheric and Climate Science, Swiss Federal Institute of Technology Zürich, 8092 Zürich, Switzerland.
6. Université Lyon 1, CNRS, UMR 5256, IRCELYON, Institut de recherches sur la catalyse et l'environnement de Lyon, 2 avenue Albert Einstein, 69626 Villeurbanne, France.
 - a. now at: Chemistry Department, University of California, Irvine, California, 92697-202, USA.
 - b. now at: Department of Chemistry, University of Cambridge, Cambridge, CB2 1EW, UK.

The sections from 2.1 to 2.8 are the reproduction of the publication of “Heterogeneous photochemistry of imidazole-2-carboxaldehyde: HO₂ radical formation and aerosol growth” by L. Gonzalez Palacios, P. Corral-Arroyo, K. Z. Aregahegn, S. S. Steimer, T. Bartels-Rausch, B. Nozière, C. George, M. Ammann, R. Volkamer published in *Atmospheric Chemistry and Physics*, Vol. 16, 11823-11836, 2016, with permission from Copernicus Publications on behalf of the European Geosciences Union. The layout of the article as well as the section figures and table numberings have been adapted to match with the thesis structure.

2.1 Abstract

The multiphase chemistry of glyoxal is a source of secondary organic aerosol (SOA), including its light-absorbing product imidazole-2-carboxaldehyde (IC). IC is a photosensitizer that can contribute to additional aerosol ageing and growth when its excited triplet state oxidizes hydrocarbons (reactive uptake) via H-transfer chemistry. We have conducted a series of photochemical coated-wall flow tube (CWFT) experiments using films of IC and citric acid (CA), an organic proxy and H donor in the condensed phase. The formation rate of gas-phase HO₂ radicals (P_{HO_2}) was measured indirectly by converting gas-phase NO into NO₂. We report on experiments that relied on measurements of NO₂ formation, NO loss and HONO formation. P_{HO_2} was found to be a linear function of (1) the [IC] × [CA] concentration product and (2) the photon actinic flux. Additionally, (3) a more complex function of relative humidity (25 % < RH < 63 %) and of (4) the O₂ / N₂ ratio (15 % < O₂ / N₂ < 56 %) was observed, most likely indicating competing effects of dilution, HO₂ mobility and losses in the film. The maximum P_{HO_2} was observed at 25 – 55 % RH and at ambient O₂ / N₂. The HO₂ radicals form in the condensed phase when excited IC triplet states are reduced by H transfer from a donor, CA in our system, and subsequently react with O₂ to regenerate IC, leading to a catalytic cycle. OH does not appear to be formed as a primary product but is produced from the reaction of NO with HO₂ in the gas phase. Further, seed aerosols containing IC and ammonium sulfate were exposed to gas-phase limonene and NO_x in aerosol flow tube experiments, confirming significant P_{HO_2} from aerosol surfaces. Our results indicate a potentially relevant contribution of triplet state photochemistry for gas-phase HO₂ production, aerosol growth and ageing in the atmosphere.

2.2 Introduction

The sources and sinks of radicals play an important role in the oxidative capacity of the atmosphere. Radicals and other oxidants initiate the chemical degradation of various trace gases, which is key in the troposphere (Jacob, 1999). The hydroxyl (OH) and peroxy (HO₂) radicals belong to the HO_x chemical family and are primarily generated by ultraviolet radiation photochemical reactions²²⁰, like the reaction of O(¹D) (from O₃) with H₂O or photolysis of HONO, HCHO, H₂O₂ or acetone. Some secondary gas-phase sources are the ozonolysis of alkenes or O(¹D) + CH₄⁸⁶. The oxidation of volatile organic compounds (VOCs) by OH and other oxidants in the presence of NO leads to perturbations in the HO_x, NO_x and RO_x radical cycles that affect O₃ and aerosol formation^{86,87}. The kinetics and photochemical parameters of these reactions are relatively well-known in the gas phase^{88,221}. However, this does not apply to the sources and sinks for HO_x in atmospheric droplets and on aerosol surfaces⁸⁹. Uptake of OH from the gas phase and H₂O₂ photolysis in the condensed phase are the primary known sources for HO_x in the condensed phase. HO₂ is highly soluble and the concentrations of OH, the most effective oxidant in the condensed phase, depend on HO₂ radicals. Another source of HO_x radicals is from the chemical reactions of reduced metal ions and H₂O₂, known as Fenton reactions^{93,94}. Direct photolysis of H₂O₂, nitrite, nitrate⁹⁰, hydroperoxides⁹¹ and light-absorbing secondary organic aerosol (SOA)⁹² are also sources of HO_x in the condensed phase. Other studies have shown that the photochemistry of iron (III) oxalate and carboxylate complexes, present in aqueous environments (e.g., wastewater, clouds, fogs, particles), can initiate a radical chain reaction serving as an

aqueous source of HO_2 and Fe^{2+} . Fe^{2+} can then regenerate OH starting a new cycle of Fenton reactions^{95,96}. The temperature-dependent rate constants of OH in the aqueous phase have been studied for a limited subset of organics⁹⁷. However, there is still a wide gap with respect to understanding the sources, sinks, kinetics and photochemical reaction pathways of HO_x radicals in the condensed phase⁶⁷.

Our study investigates photosensitizers as an additional HO_x source that may be relevant to further modify RO_x and NO_x reaction cycles in both the condensed and gas phases. It is motivated by the formation of superoxide in terrestrial aqueous photochemistry^{222–224}, by more recent observations that irradiated surfaces containing titanium dioxide generate HO_x radicals in the gas phase²²⁵ and by the generation of OH from metal oxides acting as photocatalysts in mineral dust²²⁶. Past studies have demonstrated the reactivity of glyoxal towards ammonium ions and amines as a source for light-absorbing brown carbon^{3,5,113,227}. One of these products is imidazole-2-carboxaldehyde (IC; Galloway et al., 2009³), which absorbs light at UV wavelengths ($\lambda < 330$ nm)²²⁸. Other imidazole-type compounds and light-absorbing products are formed in minor amounts but can nonetheless impact optical and radiative properties of secondary organic aerosols (SOAs; Sareen et al., 2010²²⁹; Trainic et al., 2011²³⁰). Photochemical reactions by these species are not typically accounted for in models yet but have a possible role for SOA formation and aerosol aging mechanisms²³¹.

Photosensitizers are light-absorbing compounds that absorb and convert the energy of photons into chemical energy that can facilitate reactions, e.g., at surfaces or within aerosols⁶⁷. For example, aerosol seeds containing humic acid or 4-(benzoyl)benzoic acid (4-BBA), two other known photosensitizers, can induce the reactive uptake of VOCs when exposed to light, leading to SOA formation²³². Aregahegn et al. (2013)¹⁰ and Rossignol et al. (2014)²³³ suggested a mechanism for autophotocatalytic aerosol growth, where radicals are produced from the reaction of an H-donor hydrocarbon species, in this case limonene, and the triplet state of IC. The condensed-phase citric acid and the gas-phase limonene are H-atom donors (in this article we refer to them as H donors) rather than proton donors as in the case of a Brønsted acid. In particular, the transfer of the H atom leads to the formation of an alkyl-radical species. The H-atoms transfer thus has the same effect as an H-atom abstraction reaction by Cl or OH radicals.

Field measurements on fog water samples confirmed that triplet excited states of organic compounds upon irradiation can oxidize model samples such as syringol (a biomass burning phenol) and methyl jasmonate (a green leaf volatile), accounting for 30–90 % of their loss²³⁴. There are very few field measurements of imidazoles; a recent study by Teich et al. (2016)¹²⁴ identified five imidazoles (1-butylimidazole, 1-ethylimidazole, 2-ethylimidazole, IC and 4(5)-methylimidazole) in ambient aerosols in concentrations ranging from 0.2 to 14 ng m⁻³. IC, the molecule of interest in this study, was measured in its hydrated form in ambient aerosols in three urban areas with signs of air pollution and biomass burning (Leipzig, Germany; Wuqing and Xianghe, China). The observed quantities of hydrated IC ranged from 0.9 to 3.2 ng m⁻³. The authors claim that these values could be a lower limit due to high losses of IC during sample preparation indicated by low recovery from standard solutions. This suggests that IC and other imidazole derivatives are present in areas with high pollution and biomass burning. Field measurements in Cyprus during the CYPHEX campaign in 2014 detected IC and bis-imidazole in ambient aerosol samples²³⁵. The IC diurnal cycles showed the highest concentrations at night (0.02–0.115 ng m⁻³) and lower concentrations during the day, suggesting that ambient concentrations of IC in aerosols are a balance between photochemical sources and sinks. Im-

idazoles seem to be widespread in polluted and remote areas. However, the atmospheric implications of IC as a photosensitizer, a proxy species of brown carbon light absorption, and as a radical source in ambient aerosols remains unclear.

The existence of such photocatalytic cycles could be of atmospheric significance. Indeed, Canonica et al. (1995)⁸ suggested that the initial carbonyl, triggering the photochemical properties, is regenerated via a reaction with oxygen-producing HO₂. To our knowledge, the production of such radical side products has not been investigated under atmospheric conditions previously. We therefore report here on the HO₂ radical production from IC in the condensed phase.

2.3 Experimental section

A series of flow tube experiments were conducted to investigate the formation of gas-phase HO₂ radicals from IC photochemistry using two different coated-wall flow tube (CWFT) reactors (Sect. 2.1). Section 2.2 describes aerosol flow tube experiments that confirm the photochemical production of HO₂ radicals in the absence of other known gas-phase radical sources in aerosols. All experiments were performed at atmospheric pressure.

2.3.1 Coated-wall flow tube experiments

The CWFT experiments were designed to investigate the gas-phase production of HO₂ radicals from a film containing IC and citric acid (CA) matrix as a function of UV light intensity, IC concentration in the film, relative humidity (RH) and O₂ mixing ratio. Two similar experimental setups were used as shown in Fig. 2.1. Some of the differences, not major, consist in the flow-reactor volume, surface area, flow rates, IC mass loading, NO mixing ratio, temperature inside the reactor and the connected instrumentation.

Setup 1. Experiments were conducted in a photochemical flow system equipped with a Duran glass CWFT (0.40 cm inner radius, 45.2 and 40.0 cm length, 113.6 and 100.4 cm² inner surface, surface-to-volume

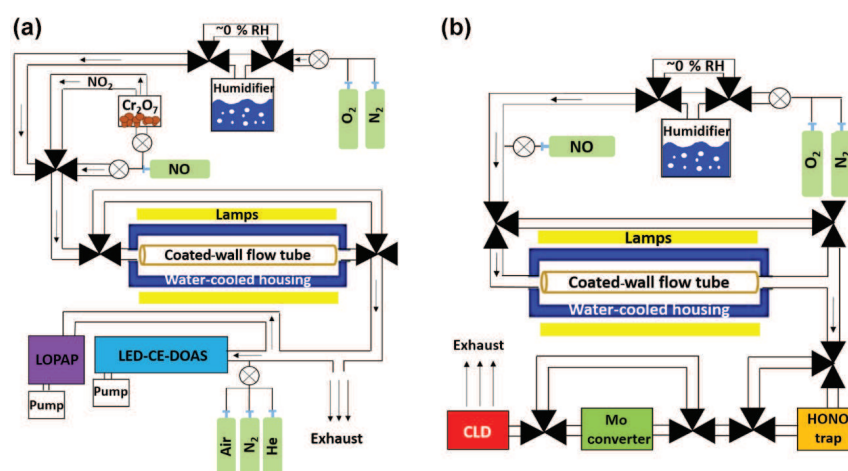


Figure 2.1: Sketch of the photochemical flow tube reactor setups at PSI for (a) Setup 1 in 2013 measuring NO₂ generation and (b) for Setup 2 in 2014 measuring NO loss.

ratio (S/V) = 5.00 cm⁻¹), which was housed in a double-jacketed cell coupled to a recirculating water bath to control the temperature at 298 K; the setup is shown in Fig. 2.1a. A thin film of IC + CA was deposited inside the tubular glass flow tube. The experimental procedure for the preparation of the films is described in Sect. 2.1.2. The system consisted of seven ultraviolet lamps (UV-A range, Philips Cleo Effect 22 W: 300–420 nm, 41 cm, 2.6 cm o.d.) surrounding the flow tube in a circular arrangement of 10 cm in diameter.

Setup 2. The second CWFT (CWFT 0.60 cm inner radius, 50 cm length, inner surface 188.5 cm², S/V = 3.33 cm⁻¹) reactor had a glass jacket to allow water to circulate and maintain temperature control inside the tube at 292 K. The coated-wall tubes were snugly fit into the CWFT as inserts. The CWFT was surrounded by the same seven fluorescent lamps as in Setup 1. The light passed through different circulating water cooling jackets for both setups, thus providing a different light path for each setup.

Setup 1 and 2. The actinic flux in the flow tube reactor, $F_{FT}(\lambda)$, was measured by actinometry of NO₂ (see Supplement for description of J_{NO_2} measurements), independently for both setups. The flows of N₂, O₂, air and NO were set by mass flow controllers. The RH was set by a humidifier placed after the admission of N₂ and O₂ gases but before the admission of NO or NO₂ (see Fig. 2.1), in which the carrier gas bubbles through liquid water at a given temperature. The humidifier could also be bypassed to set a RH of near zero. A typical measurement sequence is described in Sect. 2.1.2.

The J_{NO_2} was measured for both Setup 1 and 2 using NO₂ actinometry. The J_{NO_2} with seven lamps was found to be 2×10^{-2} s⁻¹ for Setup 1 and 1×10^{-2} s⁻¹ for Setup 2 (see Fig. 2.9 for Setup 1 and Supplement text for both Setups). These values were compared to direct actinic flux measurements in the flow tube and thus normalized (see Sect. 3.1.1).

Flow tube instrumentation

The following gas-phase products exiting the flow tube were measured by three different instruments: NO₂ by the University of Colorado Light Emitting Diode Cavity-Enhanced Differential Optical Absorption Spectroscopy (LED-CE-DOAS) instrument²³⁶, HONO by a LOng Path Absorption Photometer (LOPAP, QuMA GmbH,^{237,238} and NO by a chemiluminescence analyzer (Ecophysics CLD 77 AM, also used for NO₂ in Setup 2). HO₂ radicals were indirectly measured by detecting NO₂ with the LED-CE-DOAS (Setup 1) and by the loss of NO with the chemiluminescence detector (Setup 2). The latter was preceded by a molybdenum converter to transform HONO and NO₂ to NO and by an alkaline trap for HONO. Both trap and converter had a bypass to allow sequential measurements, thereby obtaining the concentration of NO₂ and HONO separately. HONO was measured by the LOPAP during some selected experiments^{238,239}.

LED-CE-DOAS

The LED-CE-DOAS instrument²³⁶ detects NO₂ absorption at blue wavelengths. A high-power blue LED light source (420–490 nm) is coupled to a confocal high-finesse optical cavity consisting of two highly reflective mirrors ($R = 0.999956$) peaking at 460 nm that are placed about 87.5 cm apart (sample path length of 74 cm). The absorption path length depends on wavelength, and was about ~ 11 km near peak reflectivity here. A purge flow of dry nitrogen gas is added to keep the mirrors clean. The light exiting the cavity is projected onto a quartz optical fiber coupled to a Princeton Instruments Acton SP2156 Czerny-Turner imaging spectrometer with a PIXIS 400B CCD detector. The mirror reflectivity was calculated by flowing helium and nitrogen gas, exploiting the difference in the Rayleigh scattering cross sections of both

gases as described in Thalman et al. (2014)²⁴⁰. The gas exiting the flow tube was directly injected into the CE-DOAS cavity, and spectra were recorded every 60 s and stored on a computer. For analysis we use broadband cavity enhanced absorption spectroscopy (BBCEAS) fitting at NO₂ concentrations exceeding a few parts per billion by volume²⁴¹ and DOAS least-squares fitting methods at lower concentrations²⁴². The mirror alignment was monitored online as part of every spectrum by observing the slant-column density of oxygen collision complexes, O₂-O₂ (O₄)^{236,243}. The following reference spectra were taken from the literature: NO₂²⁴⁴ and O₂-O₂ collision complexes²⁴³. The detection limit for NO₂ was 50 – 100 pptv.

2.4 Experimental conditions

The IC + CA solutions were prepared by adding IC into a 1 M CA solution in 18 MΩ cm ultrapure water to achieve IC to CA molecular ratios of between 0.026 and 0.127 in the film. The bulk solutions for both setups were prepared by weighing out 384 – 400 mg of CA in 2 mL of water and adding 4 – 20 mg of IC to the solution. The solutions for both setups were freshly prepared for each experiment, and the masses in the film were calculated at 50 % *RH* from the CA hygroscopic growth factors reported by Zardini et al. (2008) for both setups (for Setup 1: 5 – 18 mg of IC and 44 mg of CA; for Setup 2: 1 – 5 mg of IC and 77 mg of CA). The range of concentrations in the films was between 0.148 and 0.671 M of IC and 5.29 and 6.68 M of CA.

The IC + CA solution coatings were produced by depositing 220 – 250 (Setup 1) and 400 μL (Setup 2) of the desired solution in a Duran glass tube, which was then dispersed into a thin and viscous film of 3 – 4 μm. The film was dried with a gentle N₂ stream humidified to a *RH* similar to the experimental *RH* and room temperature. The film was rolled and turned upside down to deposit a homogenous film throughout the entire inner surface of the flow tube. The homogeneity of the film was confirmed by visual inspection. If a bright clear homogenous amorphous film from the supercooled solution was not observed, the film was discarded (e.g., observation of a turbid and cracked crystallized appearance). The carrier gas flows consisted of premixed dry N₂ and O₂ (a ratio of 4.5 / 1 in Setup 1 and a ratio of 2 in Setup 2), and NO was controlled by mass flow controllers. The total flow rates were 500 mL min⁻¹ for Setup 1 and 1500 mL min⁻¹ for Setup 2. In Setup 1, a dilution flow of 1000 mL min⁻¹ was added at the end of the flow tube for a total of 1500 mL min⁻¹ during experiments when HONO was measured along with NO₂. All experiments were conducted at ambient pressure, leading to gas residence times of 2.1 – 2.4 s (depending on flow tube volume, for both setups) under laminar flow conditions. The O₂ flow rate was varied between 0 and 110 mL min⁻¹ to observe the dependence of O₂ while keeping the total flow rate constant. A ratio of 4.5 : 1 of N₂ : O₂ was maintained if any of the other gas flows were changed (e.g., NO and/or NO₂) for Setup 1. For Setup 2, a ratio of 2 : 1 of N₂ : O₂ was also maintained, except for the O₂ concentration dependence studies. The *RH* was kept constant at 50 % *RH* during most experiments and varied between 10 and 60 % *RH* to study humidity effects of the HO₂ radical production. The concentration of NO was ~ 1 ppmv (Setup 1) and varied between 100 and 500 ppbv (Setup 2). Scavenging of HO₂ was achieved by the following reaction:



The lifetime of HO₂ is about 5 ms when 2.5×10^{13} molecules cm⁻³ of NO are present (Setup 1), which ensures efficient conversion of HO₂ molecules into NO₂ ($k = 8.0 \times 10^{-12}$ cm³ molecule⁻¹ s⁻¹ at 298 K;²²¹. As shown in Fig. 2.10, 500 ppbv NO, the concentration used in Setup 2, was sufficient to efficiently convert HO₂ into NO₂; see Sect. 3.1.1. The lifetime of gas-phase HO₂ with respect to loss to the organic film is about 0.1 s, based on a similar formula shown in Eq. 12, where $\gamma = 10^{-3}$ (upper limit by Lakey et al., 2015²⁴⁵). Note that in view of the essentially diffusion-controlled loss of HO₂ to the CWFT and tubing walls, the chosen scheme for determining the production of HO₂ radicals from the films by fast scavenging with NO is superior to a more selective detection method, e.g., laser-induced fluorescence (LIF), which would require passing the HO₂ radicals into a separate setup with substantial losses. For selected experiments, the films were exposed to UV irradiation for over 6 h which showed only a minor change in the decrease in NO₂, leading to the conclusion that the reactivity of the films was stable.

2.4.1 J_{IC} calculations

The absorption cross section of IC and the calculated photolysis rate are shown in Fig. 2.11. The photolysis frequencies of IC were calculated using a similar procedure as described in Schwarzenbach et al. (2002)²²⁴. The spectral actinic flux in the flow tube, $F_{FT}(\lambda)$, was converted to the spectral photon flux density that reaches the film in the flow tube, $F_{film}(\lambda)$, and the photon flux absorbed by IC, F_a^{IC} , as follows:

$$F_a^{IC} = \int_{300}^{420} F_{film}(\lambda) \times [1 - 10^{-\sigma_{IC}(\lambda) \times b \times C_{IC}}] d\lambda, \quad (5)$$

where $F_{film}(\lambda) = \frac{F_{FT}(\lambda) \times SA}{N_a \times V_{film}}$,

where F_a^{IC} has units of Ein L⁻¹ s⁻¹ (1 Ein = 1 mole (6.022×10^{23}) of photons), $F_{film}(\lambda)$ has units of Ein L⁻¹ s⁻¹ nm⁻¹, b is the optical path length taken as the thickness of the film in cm, C_{IC} is the concentration of IC in the film in units of M, and σ_{IC} is the IC absorption cross section. The absorption spectrum of IC in water was based on the measurements by Kampf et al. (2012)⁵ and renormalized to the peak value of 10205 ± 2400 M⁻¹ cm⁻¹ at 284 nm²²⁸. V_{film} is the volume of the film in cm³, calculated from the deposited mass of CA and the hygroscopic growth factors of CA²⁴⁶; SA is the surface area of the film, taken as the geometric area of the inner surface area of the flow tube in cm²; N_a is Avogadro's number in molecules mole⁻¹. The IC photoexcitation rate J_{IC} was about 1.0×10^{-3} s⁻¹ (upper limit).

We have also attempted to calculate an effective quantum yield for the formation of gas-phase HO₂ radicals (ϕ_{HO_2}):

$$P_{HO_2} = \frac{[NO_2] \times flow}{N_a \times V_{film}} \phi_{HO_2} = \frac{P_{HO_2}}{F_a^{IC}}, \quad (6)$$

where P_{HO_2} is the HO₂ production rate in mol L⁻¹ s⁻¹, F_a^{IC} is the calculated mean absorbed photon flux by IC (Eq. 5), $[NO_2]$ is the gas-phase concentration of NO₂ in molecules cm⁻³ assuming a 1 : 1 ratio to HO₂ conversion, flow is the volumetric gas flow at the temperature in the CWFT and atmospheric pressure in cm³ s⁻¹ and V_{film} is in L.

2.4.2 Aerosol flow-reactor experiments

A detailed description of the aerosol flow tube (AFT) is reported elsewhere^{10,232}; therefore, only some principles are given below. The SOA experiments were conducted in a horizontal, cylindrical Pyrex aerosol flow reactor (13 cm i.d., 152 cm length) surrounded by seven UV lamps (Philips CLEO, 80W) with a continuous emission spectrum ranging from 300 to 420 nm (total irradiance of 3.31×10^{16} photons $\text{cm}^{-2} \text{s}^{-1}$). The flow reactor consisted of Teflon stoppers and different flow controllers that maintained the gas–aerosol–UV irradiation contact time between 20 and 50 min. This flow reactor also consisted of an outer jacket that controlled the temperature at 293 ± 2 K by water circulation using a thermostat (Model Huber CC 405).

Seed aerosols (50 nm) were produced by nebulizing a solution (at pH 6) containing ammonium sulfate (AS, 0.95 mM) and IC (1.3 mM), size selected by a DMA and exposed to gas-phase limonene (500 ppbv) in the aerosol flow reactor. The typical aerosol mass loading in the reactor was $2 - 3 \mu\text{g cm}^{-3}$, corresponding to ~ 15000 particles cm^{-3} with a starting diameter of 50 nm. As shown by Aregahegn et al. (2013)¹⁰, limonene is an efficient H-donor VOC that forms SOA via reactive uptake to IC-containing seed aerosol. Due to the excess of limonene and low seed aerosol surface area, the consumption of limonene was below the detection limit. The aerosol growth was measured by means of an ultrafine condensation particle counter (UCPC) and a scanning mobility particle sizer spectrometer (SMPS; both TSI), and similarly to the CWFT experiment, a flow of gaseous NO (from a 1 ppmv cylinder, Linde) was added to the carrier gas, and its conversion to NO₂ was monitored by a chemiluminescence detector with a detection limit of 0.05 ppbv (ECO PHYSICS CLD 88). Due to the long residence time, the NO₂ concentration is affected by its photolysis in the AFT. As discussed below, P_{HO_2} was calculated, in this case, from the growth of the particle diameter measured at the exit of the flow tube; the assumption is that growth was due to reactive uptake of limonene only and that each limonene forms one HO₂ radical. At 30 ppbv NO, the HO₂ radical lifetime is around 2 s.

2.4.3 Experimental conditions

The total flow rate in the aerosol flow reactor was between 400 – 1000 mL min^{-1} , ensuring laminar flow conditions. The RH was varied between 0 and 50 %. The RH of particles in the flow reactor was controlled by saturating the carrier gas via a bubbler containing ultrapure water (Milli Q, 18 M Ω cm). The RH in the flow-reactor system was varied by changing the gas flow rates to the bubbler and the temperature of the circulating water jacket of the bubbler. The RH was measured with a humidity sensor (Meltec UFT 75-AT, Germany) at the exit of the flow reactor. The concentrations for the flow tube experiments were the following: 30 ppbv of NO and 500 ppbv of limonene.

2.4.4 Chemicals

The following chemicals were used without further purification for CWFT studies: IC (97 %, Sigma Aldrich) and CA (Sigma Aldrich). For Setup 1, the Duran glass tubes were soaked in a deconex[®] cleaning solution overnight; the next day they were rinsed with 18 M Ω cm water (Milli Q Element system). These flow tubes were etched with a 5 % hydrofluoric acid solution after the washing procedure and again rinsed

with water before any experimental use. The Duran flow tubes for Setup 2 were not initially etched with any acid but stored in a NaOH solution after washing and lastly rinsed with water; Setup 2 later confirmed that the treatment of flow tube with acids affects P_{HO_2} by rinsing with HCl and etching with HF solutions.

For the aerosol flow-reactor experiments, gas-phase limonene was generated from commercially available limonene (Aldrich, 97 %) by means of a permeation tube. The following chemicals were used without further purification: IC (97 %, Sigma Aldrich) and succinic acid (Sigma Aldrich, ≥ 99.5 %); 4-benzoylbenzoic acid (4-BBA, Aldrich 99 %) and adipic acid (AA, Aldrich, ≥ 99.5 %) were used to expand the CWFT studies to other photosensitizers.

2.5 Results and discussion

2.5.1 Coated-wall flow tube

The following results represent the light-dependent formation of HO_2 indirectly from measurements of NO_2 production and NO loss, measured with Setup 1 and 2, respectively. Figure 2.2 shows a time series of NO_2 measured with Setup 1 as a function of UV-A light, which confirms the light-dependent radical production. This particular film had an IC / CA ratio of 0.026 (0.148 M IC and 5.77 M CA in the film). An evident increase in NO_2 is observed upon UV irradiation, directly reflecting the light-mediated release of HO_2 , as shown in Reaction R1. The NO_2 signal decreases over time with all seven lamps; this was a common feature observed in all films and could be due to HO_2 sinks in the film increasing with time. Thus, the system only slowly evolves into a steady state. A small amount of NO_2 (0.5 – 1.5 ppbv) was observed during experiments that used only CA in the absence of IC; therefore, the data in Fig. 2.2 and all data reported below have been corrected for this NO_2 background, measured routinely in between experiments. Figure 2.2 also indicates a strong correlation with light intensity, which is further discussed in the context of Fig. 2.4. For irradiation, humidity and oxygen dependence experiments, each data point represents a separate experiment using a freshly prepared coated film in the flow tube. The uncertainty for experiments was based on the standard deviation of n , the number of experiments. The total uncertainty was $\pm 6 - 27$ % (propagated error for normalization was $\pm 7 - 29$ %) for the IC mass loading experiments in Setup 1 and up to a factor of 2 for the light dependence experiments. The uncertainty in Setup 2 was 10 – 50 %. As discussed earlier, the lifetime of HO_2 in the system was about 3 orders of magnitude less than the residence time in the flow tube, therefore suggesting that most, if not all, HO_2 reacted with NO to produce the observed NO_2 (Reaction R1). Theoretically, the system was clean of other oxidants such as O_3 (and thus NO_3). The uptake of NO_2 in the film was too small to further produce any nitrate radicals, and the photolysis of NO_2 in the experiments to produce O_3 was insignificant (< 1 %). The recombination of NO and O_3 contributes a negligible (< 0.1 %) NO_2 source under our experimental conditions. RO_2 generation from the reaction between CA and OH from HONO photolysis was also ruled out since it is approximated to account for only 1 % of the NO_2 production if we assume every OH from the photolysis reacts with CA. To our knowledge, the direct photolysis of CA to produce any RO_2 radicals has not been observed. Therefore, we believe that HO_2 is the essential oxidant for NO and refer to the measured NO_2 as HO_2 formation.

Figure 2.3 shows that the HO_2 production fluxes, in molecules $\text{cm}^{-2} \text{min}^{-1}$, increased with IC mass

loading. The CA concentration was kept constant, and results are shown as the product between $[IC] \times [CA]$, since we expect that the production rate of HO_2 is proportional to the concentration of IC, at constant illumination, and to that of the potential H donor, CA. For Setup 1, the HO_2 fluxes were measured as NO_2 mixing ratios and calculated using the following equation:

$$Fluxes_{HO_2} = \frac{[NO_2] \times flow}{SA}. \quad (7)$$

The description of these parameters has been previously explained (see Sect. 2.1.3). For Setup 2, the HO_2 flux was calculated similarly, but only about half of the observed NO loss was considered to account for the loss of NO via the reaction with OH (see Reaction R1 in Supplement), meaning that for each HO_2 scavenged, two NO molecules were lost. In Fig. 2.3, the data from Setup 1 are represented by the black squares and the data from Setup 2 are represented by the gray circles. Setup 1 measurements were taken at about $\sim 50\%$ RH and at room temperature. Setup 2 measurements were taken at 45% RH and at 292 K. Temperature has an effect on the observed gas-phase HO_2 release from the film and thus needs to be accounted for, which is not done in Fig. 2.3, but it is described in detail in Sect. 3.1.1.

Figure 2.4 shows that the HO_2 production exhibited a linear dependence on the actinic flux for various $[IC] \times [CA]$ molar products. From Sect. 2.1.3, we estimated an experimental ϕ_{HO_2} of about 6×10^{-5} , reflecting other probable, unknown quenching processes in our system. Figure 2.4 also shows the formation of HONO from three different IC mass loadings. In all three cases, the HONO : NO_2 ratio is < 1 , confirming HO_2 as a primary product and OH as a secondary product.

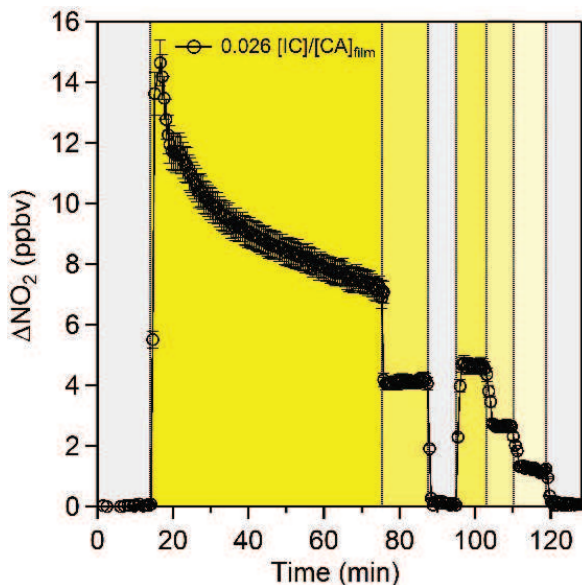


Figure 2.2: NO_2 profile for a 0.025 M IC bulk solution, whose concentration increases to ~ 0.2 M of IC in the film due to the citric acid hygroscopic properties. The gray shaded areas indicate periods where NO was exposed in the dark. The yellow shaded areas indicate the period of irradiation; the decrease in the intensity of yellow represents 2.26×10^{16} , 1.47×10^{16} , 1.14×10^{16} and 3.94×10^{15} photons $cm^{-2} s^{-1}$ for seven, five, three and one lamp, respectively. This time series clearly indicates the light dependence production of HO_2 radicals from the photosensitization of IC in a CA film.

Figure 2.5 shows the dependence of HO₂ production observed via the loss of NO (Setup 2) on relative humidity (0 – 65 %). Water partial pressure is an important parameter in the atmosphere, and it also seems to have an important effect on the photochemical reactions studied here. At *RH* below ~ 10 %, and at high *RH* above ~ 55 %, the yield of HO₂ radicals decreases. The maximum HO₂ radical production is observed at moderate *RH* (20 – 55 %). This is probably due to a combination of factors. In particular, at low *RH* the film may become more viscous, reducing mobility and thus the energy transfer within the film. This may decrease the HO₂ yield as shown in Fig. 2.5. Hinks et al. (2016)²⁴⁷ observed that the movement of molecules in a viscous film at a low *RH* is hindered and thus decreases the photochemical reaction rate of secondary organic material. The reduced diffusivity of HO₂ may also increase the residence time in the film and facilitate the self-reaction in the bulk phase: the diffusivity of H₂O in citric acid is in the range of 10⁻⁷ – 10⁻⁸ cm² s⁻¹ at 50 % *RH*. If the HO₂ diffusivity is between a factor of 10 and 100 lower than that of H₂O due to its larger size (10⁻⁹ cm² s⁻¹), the first-order loss rate coefficient for diffusion out of the film (D / δ^2 , δ denoting the film thickness (4×10^{-4} cm)) becomes about $k_D = 10^{-2}$ s⁻¹. From the observed F_{HO_2} , the steady-state concentration is then about $F_{\text{HO}_2} / k_D / \delta = 4 \times 10^{16}$ cm⁻³ = 10⁻⁷ M. The loss rate coefficient due to HO₂ self-reaction in the condensed phase (7.8×10^5 M⁻¹ s⁻¹) at this concentration would become nearly 0.1 s⁻¹, somewhat higher than that for diffusional loss. Of course these estimates carry a high uncertainty but indicate that at lower humidity, diffusivity gets low enough to effectively reduce the diffusional loss of HO₂ to the gas phase and favor its loss by self-reaction in the condensed phase. The

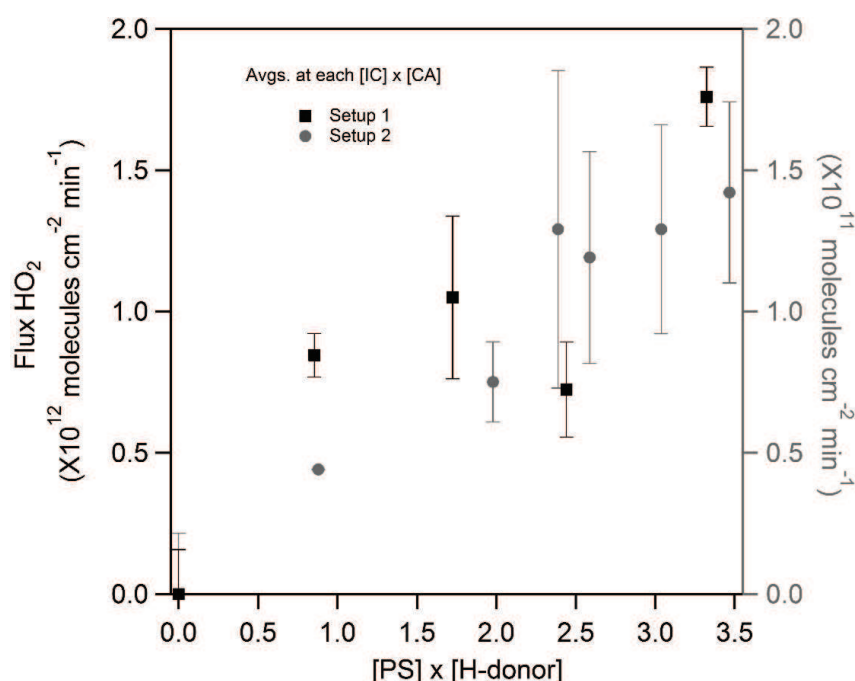


Figure 2.3: A linear correlation of HO₂ as a function of IC concentration. The left *y* axis represents the values for Setup 1, while the right *y* axis represents the values for Setup 2 (an order of magnitude difference for both scales). The Setup 2 data fall between a factor of 2 and 3 from Setup 1 after accounting for differences between Setup 1 and 2; see Sect. 3.1.1.

potential presence of condensed phase sinks, such as RO_2 , formed from secondary chemistry of oxidized citric acid, may add to this uncertainty. Figure 2.12 shows that bulk diffusion can be neglected since any HO_2 produced below the first couple of micrometers at the top of the film is likely lost to self-reaction in the condensed phase. This supplementary experiment studied the thickness dependence of the films keeping the IC : CA ratio constant. The results show that P_{HO_2} increases linearly with thickness up to $\sim 2.5 \mu\text{m}$; however, after this thickness the film saturates, showing that this must happen in our films that are between 3 and 4 μm thick. At high RH ($> 55\%$), the amount of water associated with CA dilutes the reactants, and the quenching of the excited IC triplet states gains in relative importance, consistent with findings in other studies^{248–250}. The RH effect can decrease the HO_2 production by a factor of 3, compared to the plateau of maximum HO_2 production between 20 and 55 % RH .

Figure 2.6 shows the dependence of the HO_2 production based on the observed NO loss on the O_2 mixing ratio (Setup 2). The HO_2 production varied by about 20 % over the range of conditions investigated. A decrease below 15 % O_2 appears to be significant compared to the maximum HO_2 production at $\sim 40\%$ O_2 , indicating that O_2 is needed for HO_2 formation. Sufficient O_2 dissolves in the aqueous phase to produce HO_2 radicals efficiently at atmospheric O_2 mixing ratios. We assume that at 55 % O_2 , the quenching of excited IC triplet states by O_2 has an effect on HO_2 production. This effect may decrease P_{HO_2} based on our results being qualitatively consistent with the observations of decreasing aerosol growth at high O_2 in the autophotocatalytic aerosol growth described in Aregahegn et al. (2013)¹⁰. However, the experimental

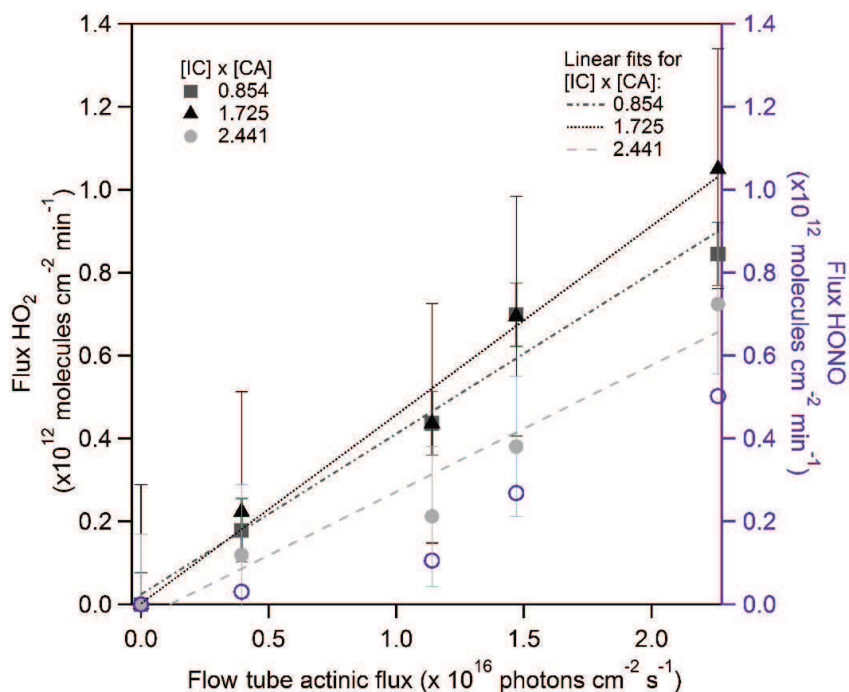


Figure 2.4: HO_2 fluxes in molecules $\text{cm}^{-2} \text{min}^{-1}$ as a function of actinic flux for a 300 – 420 nm range (solid symbols). The data are plotted as a concentration product of $[\text{IC}] \times [\text{CA}]$ (shown in the legend), which shows the photochemical reaction between IC and CA in H_2O matrix and gaseous NO . HONO for 2.441 ($[\text{IC}] \times [\text{CA}]$) is plotted on the right axis (open circles), showing a ratio of $\text{HONO} : \text{NO}_2 < 1$, which suggests OH as a secondary product.

focus of this study was based on atmospheric O_2 mixing ratios, and thus we cannot draw conclusions about the HO_2 production at high O_2 mixing ratios.

In order to test the possibility for excited IC triplet states to react with NO_2 at the surface of the film, experiments were conducted with NO_2 . While we did observe that the uptake of NO_2 on irradiated surfaces scaled with light intensity (see Fig. 2.13), the reactive uptake coefficient of NO_2 to produce HONO at the surface is rather small ($< 2.5 \times 10^{-7}$), corresponding to a k_w of 10^{-3} s^{-1} , and is thus neither a significant loss of NO_2 nor a significant source of HONO. The primary fate of the nitrogen-containing aromatic alkoxy IC radical under atmospheric conditions is reaction with O_2 . However, we have not tested alternative quenching reactions of the triplet state or other pathways of the reduced ketyl radical that do not result in the formation of HONO.

Comparison of data sets

The experimental conditions probed differ in the actinic flux, NO concentration, temperature and acidity. Here, we use the dependencies established in Sect. 3.1 to compare results from both setups. The data from Setup 2 were normalized to conditions of Setup 1. The difference in J_{NO_2} corresponds to multiplying results from Setup 2 with a factor of 2.0 ± 0.1 . HO_2 was measured indirectly by reacting it with NO , and Fig. 2.10 indicates that the minimum NO concentration needed to efficiently scavenge all gas-phase HO_2 is ~ 460 ppbv of NO , indicating efficient conversion for Setup 1 and a conversion efficiency of ~ 0.6 for Setup 2. The

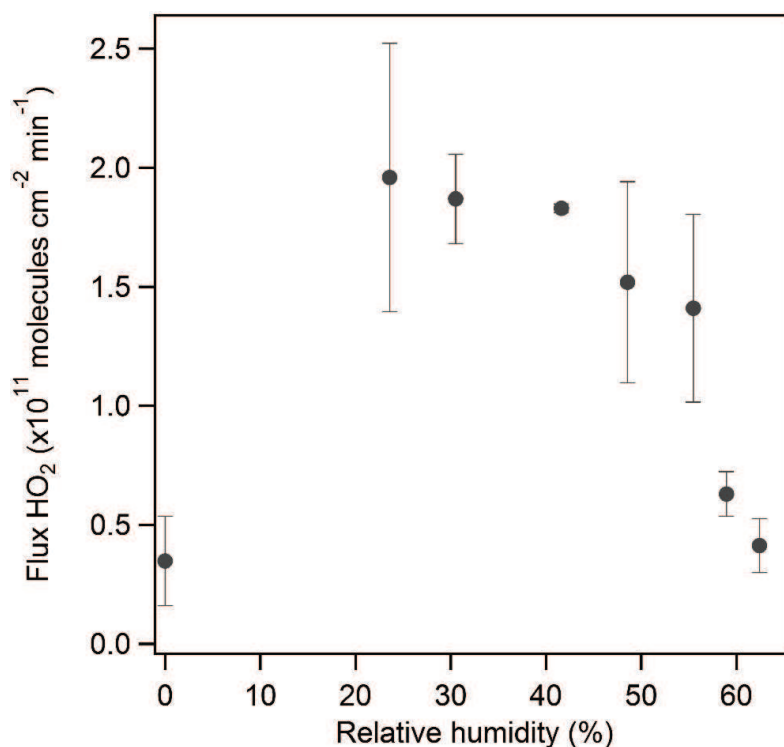


Figure 2.5: The indirect flux of HO_2 in molecules $cm^{-2} min^{-1}$, measured by NO loss and normalized to the film surface area as a function of relative humidity.

data from Setup 2 were multiplied by 1.66 ± 0.10 to normalize for the NO conversion efficiency (Fig. 2.10) and by an additional factor of 1.25 ± 0.10 to match temperatures. We observed some limited variability depending on whether HF or HCl were used to clean the flow tube prior to experiments. A higher P_{HO_2} was observed when cleaning with HF (Setup 1) compared to storing in NaOH and either rinsing with water or HCl (Setup 2); this is accounted for by multiplying data from Setup 2 with a factor of 1.25 ± 0.30 . Notably, the error of the correction for the cleaning procedure that is propagated here is larger than the correction factor. The effect of the pretreatment of the flow tubes was not systematically studied and thus remains a primary uncertainty in the comparison. No further correction was applied for slight differences in RH . The overall correction factor amounts to 5.2 ± 1.4 , with the error reflecting the propagated uncertainty. This explains most of the difference in P_{HO_2} between both setups. The normalized results agree within a factor of 2, which is a reasonably good agreement.

Extension to other photosensitizers

A limited number of experiments were performed using the CWFT approach, using 4-BBA as a photosensitizer, in the presence of 790 ppbv of gaseous limonene (a possible H donor) and NO. The organic thin film contained an organic acid matrix made of 4-BBA with and without adipic acid (AA). A substantial conversion of NO into NO_2 was also observed in this system (see Fig. 2.14). That 4-BBA behaves similar to

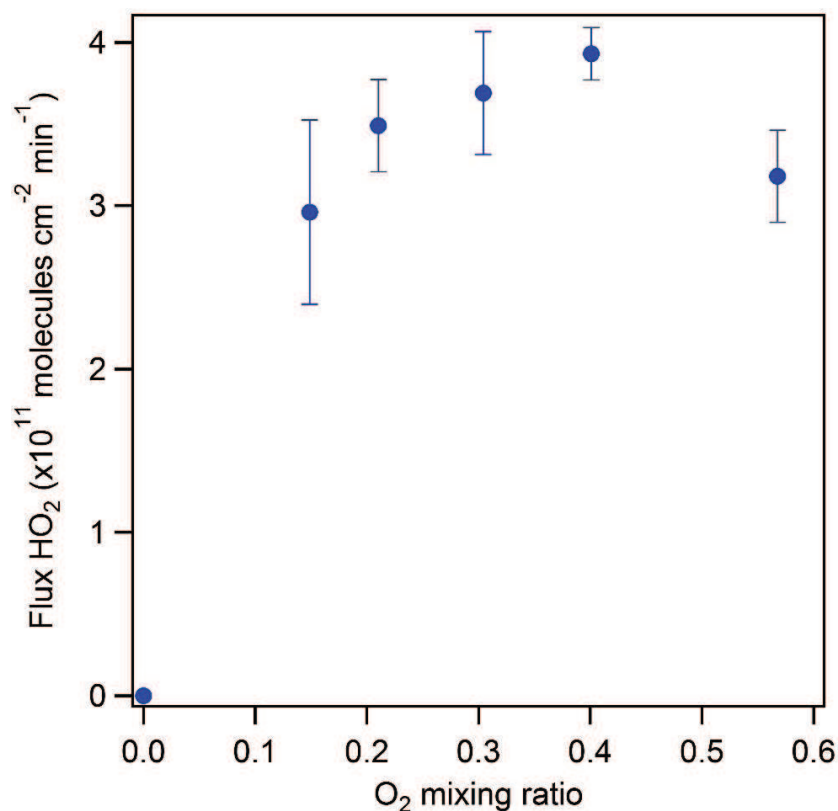


Figure 2.6: The flux of HO_2 in molecules $\text{cm}^{-2} \text{min}^{-1}$, measured by NO loss, above a film composed of IC and CA normalized to the film surface area as a function of the O_2 mixing ratio.

the IC system demonstrates that the chemistry discussed above can occur on different excited carbonyls. It is interesting to note that this photoinduced conversion, and HO₂ production, was observed to be sustained over long times, i.e., more than 15 h, probably due to the catalytic nature of the underlying chemical cycles. However, a fraction of the IC did get consumed by photolysis reactions that do not form the excited triplet state (observed during overnight experiments). The HO₂ flux for the 4-BBA system was estimated to be 2.77×10^{10} molecules cm⁻² min⁻¹ making the same assumption that each HO₂ molecule reacts with NO to generate an NO₂ molecule. The calculation is based on Eq. 7, where it depends on the concentration of NO₂ as well as the surface area and residence time.

2.5.2 Aerosol flow tube

The aerosol flow tube experiments were conducted similarly to the study by Aregahegn et al. (2013)¹⁰, i.e., who demonstrated that in the absence of NO and known gas-phase oxidants, seed particles containing IC can initiate SOA growth in the presence of a gaseous H donor (limonene). Figure 2.7 shows the results from similar experiments when NO was added to the system. No conversion of NO to NO₂ was observed prior to the injection of limonene into the flow tube. The presence of a gaseous H donor and light clearly initiated a series of photochemical processes, leading to SOA growth and gaseous NO₂ production. However, the quantitative interpretation of these experiments is not straightforward due to efficient radical cycling in the VOC-NO_x-light photochemical system and the lack of a blank experiment that did not contain IC as part of the seed particles. Limitations arise from the much longer residence time, which allows NO₂ to be significantly photolyzed. The J_{NO_2} was estimated as $\sim 6.75 \times 10^{-3}$ s⁻¹ and corresponds to a photolysis lifetime of 2.5 min, which is smaller than the actual residence time in the flow tube (~ 40 min). Secondary chemistry can lead, among others, to ozone production (O₃ lifetime at 500 ppbv limonene is ~ 7 min) and secondary OH radical formation from the ozonolysis of limonene. Notably, NO_x is not consumed in Fig. 2.7. The overall effect of this secondary chemistry is an increased SOA growth compared to an experiment without added NO (Aregahegn et al., 2013)¹⁰. As a consequence, the NO₂ yield cannot be used directly to assess P_{HO_2} in the presence of NO.

However, in the absence of NO these secondary processes can largely be avoided and are reduced to a level at which they cannot be identified¹⁰. Under such conditions, the particle growth rates presumably carry information about the photosensitizer cycling and subsequent HO₂ production. If we assume one molecule of limonene reacts to produce one HO₂, the volume change of aerosols is proportional to the overall number of HO₂ produced. For example, a growth of 15 000 particles cm⁻³ from diameter 51.4 to 68.5 nm in 40 min (residence time) is equal to a P_{HO_2} of 1.67×10^{14} molecules cm⁻² min⁻¹. This should be interpreted as an upper limit for the actual P_{HO_2} because water uptake may also be contributing to the volume growth. However, compared to the CWFT experiments the much higher surface-to-volume ratio of nanoparticles is expected to enhance the chemical coupling of a gas-phase H donor and the excited IC triplet state at the aerosol surface. This is at least in part deemed responsible for the 2 orders of magnitude higher P_{HO_2} in the aerosol flow tube compared to the CWFT experiments. Notably, even if ϕ_{HO_2} in the aerosol flow tube was 2 orders of magnitude higher than in the CWFT, it is still significantly smaller than unity.

Primary HO₂ formation from IC

One of the main advantages of the CWFT is that it operates at a much shorter residence time. From Setup 1, we derive a P_{HO_2} of 1.76×10^{12} molecules $\text{cm}^{-2} \text{min}^{-1}$ for IC / CA = 0.1 and $J_{\text{NO}_2} = 8 \times 10^{-3} \text{ s}^{-1}$. This corresponds to 2.9×10^4 molecules $\text{cm}^{-3} \text{ s}^{-1}$ once normalized by aerosol surface area ($1.18 \times 10^{-6} \text{ cm}^2 \text{ cm}^{-3}$) and J_{NO_2} in the aerosol flow tube. Such a primary radical flux is equivalent to the OH radical production rate resulting from photolysis of ~ 1 pptv of HONO in the aerosol flow tube. Conversely, a P_{HO_2} of 1.67×10^{14} molecules $\text{cm}^{-2} \text{min}^{-1}$ is equivalent to the OH radical production rate from ~ 100 pptv HONO in the aerosol flow tube. We conclude that seed particles containing IC contribute significantly (equivalent to 1 – 100 pptv HONO) to the primary HO_x radical production rate in the aerosol flow tube experiments in the presence of NO (Fig. 2.7). Primary HO₂ radicals formed from IC-containing seed particles react rapidly with NO to form OH radicals under the conditions shown in Fig. 2.7. The H-donor species is further expected to form primary RO₂ radicals. These primary HO₂ and RO₂ radicals add directly to the conversion of NO into NO₂ and indirectly by driving secondary NO-to-NO₂ conversion from the RO₂/HO₂ radical chain. The aerosol flow tube experiments thus qualitatively confirm the results obtained from macroscopic surfaces and highlight the potentially important role of surface-to-volume ratio and gaseous H donors to enhance the relevance of H-donor photochemistry as sources for HO_x-RO_x radicals and SOA.

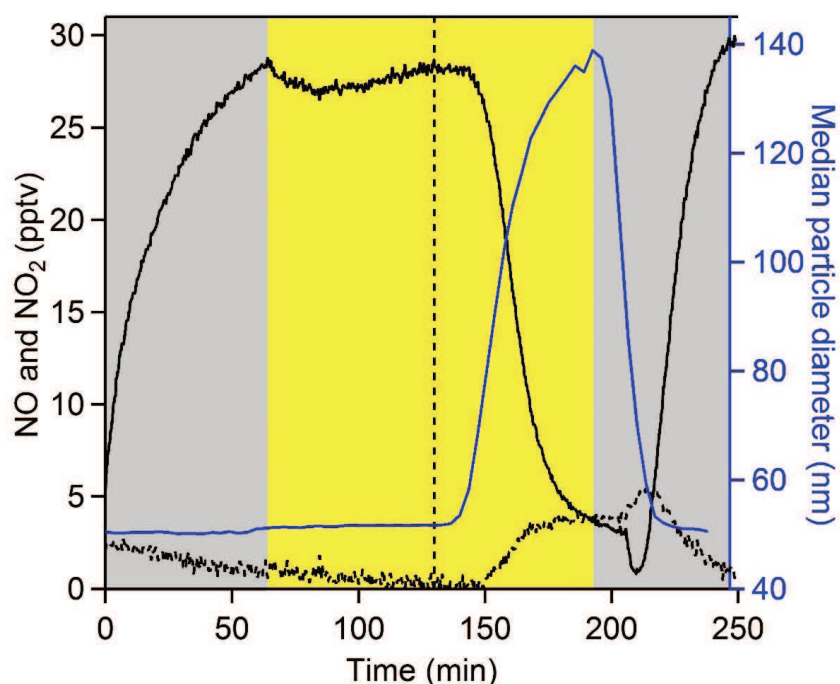


Figure 2.7: Aerosol flow tube experiments show rapid conversion of NO (solid black line) into NO₂ (dashed black line) only after the time when limonene (gaseous H donor) is added into the flow tube (vertical dashed line). The gray shaded areas represent the experiment in the dark, and the yellow shaded area represents the experiment under light exposure. The blue line represents the growth of aerosols (right axis).

2.5.3 Proposed mechanism

A mechanism that can describe the results from the CWFT experiments is shown in Fig. 2.8. It follows the mechanism first proposed by Canonica et al. (1995)⁸. The primary product in our system is the HO₂ radical, which forms from the reaction between a nitrogen-containing aromatic alkoxy IC radical and a ground-state oxygen molecule, recycling the IC molecule. The aromatic alkoxy radicals form from the excited triplet state of IC via transfer of an H atom from an H donor (in our case likely to be CA or the CA / H₂O matrix). While a fraction of the IC will get consumed by photolysis reactions that do not form the excited triplet state (see Sect. 3.1.2.), IC is also continuously produced from multiphase reactions, e.g., of glyoxal^{4,5,228}. Another conclusion is that OH is a secondary product. If OH was a first-generation product, we would have expected HONO : NO₂ ratios larger than 1 : 1. A smaller ratio was observed, as shown in Fig. 2.4, indicating that there was no direct evidence for primary formation of OH radicals. Interestingly, the H-donor species becomes activated as a result of H abstraction and can react further to produce organic peroxy radicals, as evidenced by the aerosol flow tube results.

2.6 Atmospheric relevance

The atmospheric relevance of our findings consists of the possible effect of heterogeneous radical sources to modify atmospheric HO₂ radical concentrations and facilitate aerosol growth and ageing by adding a radical source within aerosol particles. The production of HO₂ from IC photosensitized heterogeneous chemistry is a possible source of gas-phase HO₂ radicals in ambient air. In order to estimate the possible relevance for HO₂ radical concentrations in urban air, we assume P_{HO_2} of 2×10^{12} molecules cm⁻² min⁻¹ (IC / CA = 0.1, Setup 1) as a lower limit and 2×10^{14} molecules cm⁻² min⁻¹ (IC / AS = 0.1, aerosol flow tube) as an upper limit and typical conditions in Mexico City (i.e., $J_{\text{NO}_2} = 8 \times 10^{-3}$ s⁻¹ at noontime in Mexico City, aerosol surface area = 15 cm² m⁻³,²⁵¹). The normalized P_{HO_2} during noontime in Mexico City ranges from 2×10^5 to 2×10^7 molecules cm⁻³ s⁻¹. This corresponds to a rate of new HO_x radical production of 4 to 400 pptv h⁻¹ HONO around solar noon in Mexico City²⁵², where other radical sources produce about 5.9

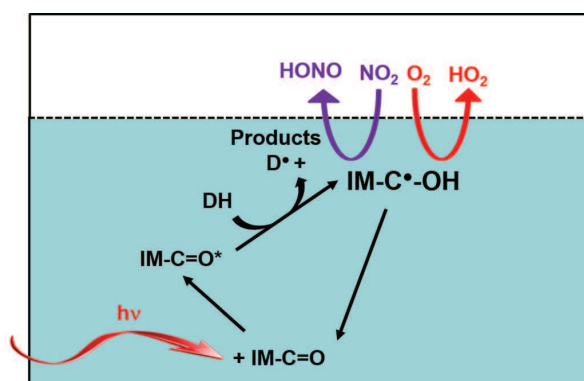


Figure 2.8: Proposed mechanism, modified and expanded to photosensitization of IC based on Canonica et al. (1995)⁸, George et al. (2005)⁹ and Aregahegn et al. (2013)¹⁰. The reaction in the white square represents the gas-phase, and the blue square represents the aqueous phase. DH is an H donor (e.g., CA, another IC, H₂O + CA matrix to be determined from flash photolysis).

$\times 10^7$ molecules $\text{cm}^{-3} \text{s}^{-1}$ at solar noon²⁵³. The upper range value suggests that aerosol surfaces can be a significant source of gas-phase HO_x in places like Mexico City. However, the IC molar ratios used here are likely an upper limit compared to ambient aerosols, yet, in principle other brown carbon molecules (i.e., HULIS and/or other imidazole derivatives) may form additional gas-phase HO_2 . The heterogeneous HO_2 radical source could further be relatively more important in unpolluted regions under biogenic influences, where gas-phase radical production rates are lower. Hence a more comprehensive characterization of the heterogeneous HO_2 source effect on gas-phase HO_2 radical concentrations deserves further investigation.

OH radical uptake from the gas phase is a primary OH source in aerosols²⁵⁴. Assuming a gas-phase OH concentration of 10^6 molecules cm^{-3} , $15 \text{ cm}^2 \text{ m}^{-3}$ aerosol surface area and γ_{OH} of unity, the rate of OH uptake is approximately 2.3×10^5 molecules $\text{cm}^{-3} \text{s}^{-1}$. The above estimated P_{HO_2} is a result from H transfer to form organic peroxy radicals, which is comparable to the rate of OH uptake. The two similar estimates of HO_x suggest that IC is a significant source of radicals in the condensed phase of particles. This is a lower limit due to the unknown radical losses of HO_x to the condensed phase, which have the potential to raise the HO_x source by up to a factor of 10 000 if limited by the IC excitation rate. The unknown amount of HO_2 that remains in the condensed phase is a further source of OH in the same phase; this OH, in the presence of reduced metals, can trigger a cycle of Fenton reactions or other oxidizing pathways that can further age the aerosol.

These results show that IC, and other aromatic carbonyl photosensitizers, are likely a relevant radical source in aerosol particles. Photoinduced radical generation in condensed phases is currently not represented in atmospheric models that describe aerosol ageing and warrants further study.

2.7 Conclusion

Three different experimental setups consistently show that HO_2 radicals are produced from the photochemistry of IC in a CA + H_2O matrix and in seed aerosols containing ammonium sulfate (in the presence of a gas-phase H donor, limonene). The linear correlations of P_{HO_2} (with $[\text{IC}] / [\text{CA}]$ and irradiation) yielded maximum P_{HO_2} under atmospherically relevant irradiation, O_2 and RH but also revealed a complex role of film viscosity and possibly acidity effects (a systematic study of the effect of pH on the IC and CA absorption cross sections and the product yields from the IC photochemistry is desirable). If the H-donor species is in the condensed phase, significant amounts of HO_2 reach the gas phase only for moderately high RH ($\sim 25 - 55\%$ RH) that facilitates H transfer and allows molecules (IC, HO_2) to move freely towards the surface of the film. When the film is too dry, this mobility is inhibited due to enhanced viscosity and significantly decreases the P_{HO_2} . At RH and O_2 higher than 55 %, we observe a decrease in P_{HO_2} probably due to dilution by water and competing quenching reactions in the film. We know from Zardini et al. (2008)²⁴⁶ that pure citric acid does not efflorescence, and thus the film remains homogenous in its aqueous phase under all RH conditions. This supports our conclusion that the P_{HO_2} is RH dependent since it is partially controlled by the diffusivity in the film. On the contrary, if the H-donor species is in the gas phase, significant HO_2 production is also observed under dry conditions. The primary fate of the IC-OH radical at the surface is reaction with O_2 to form HO_2 . NO_2 reactions do not appear to form HONO at the surface. Our results suggest that the radical

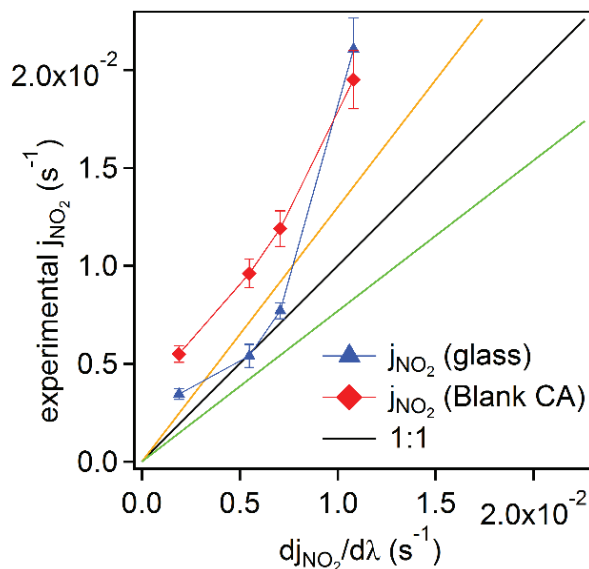


Figure 2.9: NO_2 j -values in s^{-1} from the bare glass and citric acid blank coated flow-tubes in Setup 1.

source from photosensitizers such as IC can help jump-start the photochemistry of VOCs. The effect on the gas-phase HO_2 radical concentration increases for higher surface-to-volume ratio of aerosols and in the presence of gas-phase H donors. The autophotocatalytic growth of aerosols containing photosensitizers via H-donor chemistry is an SOA source also in the presence of NO and adds oxidative capacity inside aerosol particles. Further research on other types of H donors and photosensitizers is necessary to compare different P_{HO_2} and rates of aerosol growth from the reactive uptake of VOC that could potentially have a significant atmospheric relevance for SOA formation and heterogeneous aerosol ageing.

2.8 Supporting Information

2.8.1 NO_2 actinometry

The actinic flux (photons $\text{cm}^{-2} \text{s}^{-1}$) was measured with one, three, five and all seven lamps of the photo reactor turned on using NO_2 actinometry (method A), and independent measurements of the photon actinic flux (method B). With method A, NO_2 in a N_2/O_2 gas mixture was added to the flow-tube under two different configurations: a) a bare glass flow-tube, and b) a blank coated flow-tube consisting of CA only, in the absence of IC. The NO_2 gas was produced from the oxidation of a gas flow of NO through a chromate salt reservoir, shown in Fig. 2.1A. In configuration a), the concentration of NO_2 was about 8 ppbv and in configuration b) it was about 40 ppbv. NO_2 actinometry is based on the following reaction:



The photolysis constant, J , in our case was treated as first-order rate constant, which quantifies the rate of photolysis of NO_2 , J_{NO_2} , in terms of a relative concentration change over time. The decrease in NO_2 was measured by the LED-CE-DOAS (Setup 1) and by the chemiluminescence (Setup 2); the NO_2 signal was

allowed to stabilize, and lights were turned on sequentially. J_{NO_2} was calculated using the measurements and the following equation:

$$J_{NO_2} = \frac{d \ln[NO_2]}{dt} \quad (8)$$

$$-\ln \left(\frac{[NO_2]_t}{[NO_2]_0} \right) = J_{NO_2} \times t \quad (9)$$

With all seven lamps turned on, the J_{NO_2} was about $2 \times 10^{-2} \text{ s}^{-1}$ (Setup 1) and $1 \times 10^{-2} \text{ s}^{-1}$ (Setup 2). This is about 2-3 times the ambient J at mid-latitudes under summer noon-time conditions. The J_{NO_2} for configurations a) and b) are compared in the Fig. 2.10, and agreed within 8 % at 7 lamps and this variability increases as the number of lamps (irradiation) decrease, up to a factor of 2 as a maximum. The J-values of NO_2 were calculated using independent measurements of the photon actinic flux of the UV lamps, which had been determined by B. Bohn at Forschungszentrum Jülich (Germany) with a LICOR 1800 hemispherical, cosine corrected spectro-radiometer (method B). The following equation was used to calculate the first order photolysis rate, J-value:

$$J - value = \int_{300}^{420} F_{FT}(\lambda) \sigma(\lambda) \Phi(\lambda) d(\lambda) \quad (10)$$

where $F_{FT}(\lambda)$ is the actinic flux measured in our flow-tube system, $\sigma(\lambda)$ is the NO_2 cross section at 294 K in $\text{cm}^2 \text{ molecule}^{-1}$ ²⁴⁴, and $\Phi(\lambda)$ is the quantum yield data used from Sander et al., 2011²²¹. The j-values for NO_2 for methods A and B are compared in Fig. 2.10, and agree within a factor of 2 (higher J_{NO_2} for method A). The photon actinic flux shown in the Fig. 2.11 has been adjusted by this factor, and is compared with a typical solar spectral irradiance at the Earth surface (solar zenith of 48° , The American Society for

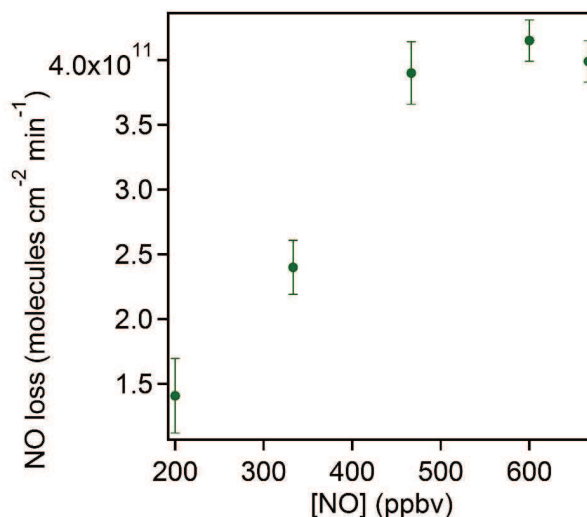


Figure 2.10: Determination of the NO concentration in the 2014 PSI flow-tube system. The lifetime of HO_2 is short enough at 500 ppbv with respect to its reaction with NO. This ensures a 1 NO:1 HO_2 molecular reaction in our experimental conditions. An IM/AC ratio of 0.088 was fixed for this specific experiment.

Testing and Materials, ASTM).

Equation 11 and 12 shows the relationship between the loss of NO_2 , the derived pseudo-first order J_{NO_2} and the uptake coefficient (γ) for a heterogeneous reaction in a cylindrical flow-tube:

$$\frac{dn[\text{NO}_2]}{dt} = J_{\text{NO}_2}[\text{NO}_2] \quad (11)$$

$$J_{\text{NO}_2} = \frac{\gamma \langle c \rangle [s/v]}{4} \quad (12)$$

where $\langle c \rangle$ is the NO_2 mean molecular speed, $(8RT/\pi M)^{1/2}$, and $[s/v]$ is the surface area of the film per gas volume ratio in our flow-tube system. These calculations are represented in Fig. 2.12.

Figure Captions Figure 2.9: NO_2 j-values in s^{-1} from the bare glass and citric acid blank coated flow-tubes in Setup 1.

Figure 2.10: Determination of the NO concentration in the 2014 PSI flow-tube system. The lifetime of HO_2 is short enough at 500 ppbv with respect to its reaction with NO . This ensures a 1 NO :1 HO_2 molecular reaction in our experimental conditions. An IM/AC ratio of 0.088 was fixed for this specific experiment.

Figure 2.11: Solid line: the cross-section of IC in H_2O ; the UV-VIS absorption of IC was measured by Kampf et al., 2012⁵ and interpolated to more recent molar extinction measurements by Barbara Nozière at IRCELYon (right scale in cm^2)²²⁷. Shaded gray: calculated wavelength dependent photolysis frequencies of imidazole-2-carboxaldehyde, j-values, based on the calculated quantum yield in our flow tube. Dotted line: actinic flux of the UV-light source in our flow-tube system from 300 – 420 nm range, the total flux is 2.26×10^{16} photons $\text{cm}^{-2} \text{s}^{-1}$. Dashed line: a solar actinic flux spectrum for a solar zenith angle of 48° , 37° tilt towards the sun and clear skies ($\sim 2 \times 10^{16}$ photons $\text{cm}^{-2} \text{s}^{-1}$ between 300 – 420 nm) obtained from the

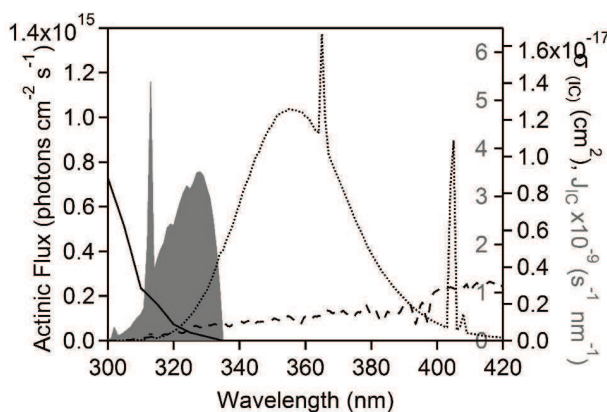


Figure 2.11: Solid line: the cross-section of IC in H_2O ; the UV-VIS absorption of IC was measured by Kampf et al., 2012⁵ and interpolated to more recent molar extinction measurements by Barbara Nozière at IRCELYon (right scale in cm^2). Shaded gray: calculated wavelength dependent photolysis frequencies of imidazole-2-carboxaldehyde, j-values, based on the calculated quantum yield in our flow tube. Dotted line: actinic flux of the UV-light source in our flow-tube system from 300 – 420 nm range, the total flux is 2.26×10^{16} photons $\text{cm}^{-2} \text{s}^{-1}$. Dashed line: a solar actinic flux spectrum for a solar zenith angle of 48° , 37° tilt towards the sun and clear skies ($\sim 2 \times 10^{16}$ photons $\text{cm}^{-2} \text{s}^{-1}$ between 300 – 420 nm) obtained from the standard spectrum of the American Society for Testing and Materials (ASTM).

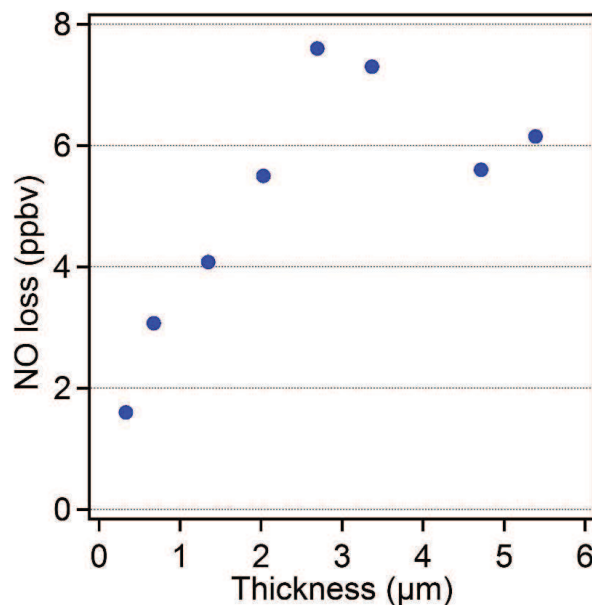


Figure 2.12: Film thickness dependence represented by NO loss. The IC:CA ratio was kept constant to show the classic behavior of reactions governed by reaction and diffusion. At low thicknesses, P_{HO_2} increases linearly and saturates at thicknesses $> 2 \mu\text{m}$. This shows that the observed HO_2 is produced from the top few micrometers of the films under study.

standard spectrum of the American Society for Testing and Materials (ASTM).

Figure 2.12: Film thickness dependence represented by NO loss. The IC:CA ratio was kept constant to show the classic behavior of reactions governed by reaction and diffusion. At low thicknesses, P_{HO_2} increases

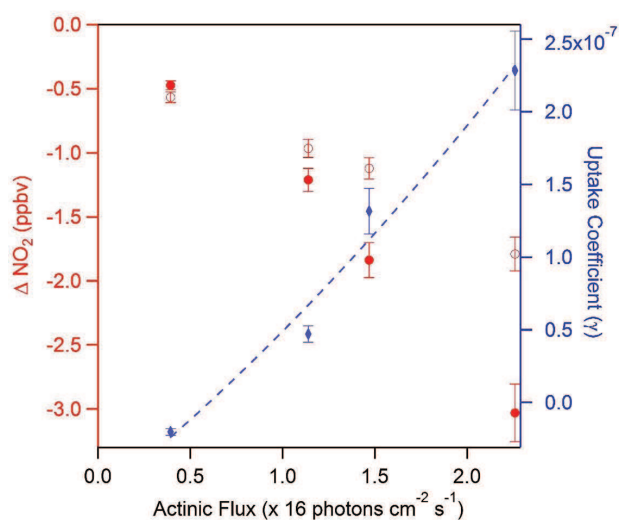


Figure 2.13: The photosensitized uptake coefficient of NO_2 (blue diamonds, right axis); this graph shows the inefficiency of NO_2 to compete with O_2 at atmospheric mixing ratios. The open red circles represent the CA blank measurements, the closed red circles represent a $1.725 [IC] \times [CA]$ film measurements during NO_2 actinometry experiments (left axis).

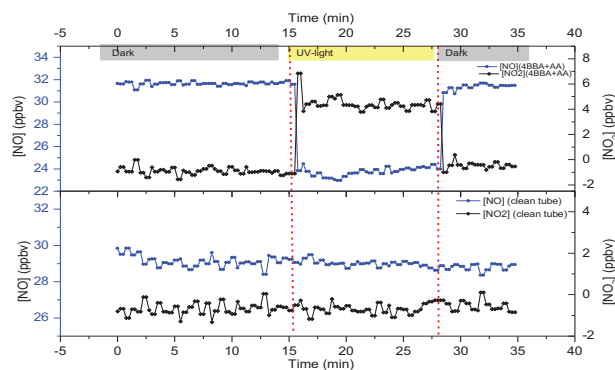


Figure 2.14: NO to NO₂ conversion from similar CWFT experiments performed in a different photosensitizer, 4-BBA. The top figure shows that NO does react with HO₂ to produce NO₂ in the presence of 4-BBA and adipic acid (AA), as the organic aqueous base. The bottom figure shows no conversion in a clean tube.

linearly and saturates at thicknesses $> 2 \mu\text{m}$. This shows that the observed HO₂ is produced from the top few micrometers of the films under study.

Figure 2.13: The photosensitized uptake coefficient of NO₂ (blue diamonds, right axis); this graph shows the inefficiency of NO₂ to compete with O₂ at atmospheric mixing ratios. The open red circles represent the CA blank measurements, the closed red circles represent a $1.725 [\text{IC}] \times [\text{CA}]$ film measurements during NO₂ actinometry experiments (left axis).

Figure 2.14: NO to NO₂ conversion from similar CWFT experiments performed in a different photosensitizer, 4-BBA. The top figure shows that NO does react with HO₂ to produce NO₂ in the presence of 4-BBA and adipic acid (AA), as the organic aqueous base. The bottom figure shows no conversion in a clean tube.

3 Chapter 3

Particle phase photosensitized radical production and aerosol aging

Pablo Corral Arroyo^{1,2}, Thorsten Bartels-Rausch¹, Peter A. Alpert¹,
Stéphane Dumas³, Sébastien Perrier³, Christian George³, Markus Ammann¹

1. Paul Scherrer Institute, Laboratory of Environmental Chemistry, 5232 Villigen PSI, Switzerland.
2. Department of Chemistry and Biochemistry, University of Bern, 2012 Bern, Switzerland.
3. CNRS, UMR5256, IRCELYON, Institut de Recherches sur la Catalyse et l'environnement de Lyon, Villeurbanne F-69626, France.

The sections from 3.1 to 3.7 are the reproduction of the publication of “Particle phase photosensitized radical production and aerosol aging” by P. Corral-Arroyo, T. Bartels-Rausch, P. A. Alpert, S. Dumas, S. Perrier, C. George, M. Ammann published in *Environmental Science and Technology*, Vol. 14, 7680-7688, 2018, with permission from American Chemical Society Publications. The layout of the article as well as the section figures and table numberings have been adapted to match with the thesis structure.

3.1 Abstract

Atmospheric aerosol particles may contain light absorbing (brown carbon, BrC), triplet forming organic compounds that can sustain catalytic radical reactions and thus contribute to oxidative aerosol aging. We quantify UVA induced radical production initiated by imidazole-2-carboxaldehyde (IC), benzophenone (BPh) and 4-Benzoylbenzoic acid (BBA) in the presence of the non-absorbing organics citric acid (CA), shikimic acid (SA) and syringol (Syr) at varying mixing ratios. We observed a maximum HO₂ release of 10¹³ molecules min⁻¹ cm⁻² at a mole ratio $\chi_{\text{BPh}} < 0.02$ for BPh in CA. Mixtures of either IC or BBA with CA resulted in 10¹¹ – 10¹² molecules min⁻¹ cm⁻² of HO₂ at mole ratios (χ_{IC} and χ_{BBA}) between 0.01 and 0.15. HO₂ release was affected by relative humidity (*RH*) and film thickness suggesting coupled photochemical reaction and diffusion processes. Quantum yields of HO₂ formed per absorbed photon for IC, BBA and BPh were between 10⁻⁷ and 5 × 10⁻⁵. The non-photoactive organics, Syr and SA, increased HO₂ production due to the reaction with the triplet excited species ensuing ketyl radical production. Rate coefficients of the triplet of IC with Syr and SA measured by laser flash photolysis experiments were $k_{\text{Syr}} = 9.4 \pm 0.3 \times 10^8 \text{ M}^{-1} \text{ s}^{-1}$ and $k_{\text{SA}} = 2.7 \pm 0.5 \times 10^7 \text{ M}^{-1} \text{ s}^{-1}$. A simple kinetic model was used to assess total HO₂ and organic radical production in the condensed phase and to upscale to ambient aerosol, indicating that BrC induced radical production may amount to an upper limit of 20 and 200 M day⁻¹ of HO₂ and organic radical respectively, which is greater or in the same order of magnitude as the internal radical production from other processes, previously estimated to be around 15 M per day.

3.2 Introduction

Brown carbon (BrC), defined as the fraction of organic compounds in atmospheric aerosol particles that absorb efficiently in the UVA-VIS range, is ubiquitously present in the troposphere^{101–103}. Absorption of solar radiation by BrC has been estimated at 0.1 – 0.25 W m⁻¹ globally, which is approximately 25 % of the radiative forcing by black carbon or soot¹⁰³. Photochemistry initiated by BrC species can change their own chemical composition and both enhance and decrease light absorption over time^{77,116}. These processes may be related to triplet forming BrC species, so called photosensitizers, which may catalyze radical chain reactions. Photosensitized chemistry is well-established in aquatic photochemistry¹¹⁹ and has been recently recognized as contributors to the oxidant budget in airborne particles^{67,120,123}. This may therefore represent an important contribution to aerosol aging, which refers to the chemical transformations induced by uptake of gas phase radicals such as OH, HO₂ or NO₃^{67,68,72}, to cloud droplets or particles²¹, by partitioning of low volatility compounds following the oxidation of the precursors in the gas phase, and by condensed phase chemical processes. Recently, HO₂ release in organic mixtures with imidazole-2-carboxaldehyde (IC) as photosensitizer and citric acid (CA) was determined as a function of relative humidity (*RH*) and IC concentration¹²⁰. Here, we expand to another photosensitizer family and measure photosensitized HO₂ release for IC, benzophenone (BPh) and 4-Benzoylbenzoic acid (BBA). In addition, we quantify the influence of different non-absorbing compounds, shikimic acid (SA) and syringol (Syr) on the IC initiated HO₂ release. Finally, we elucidate chemical cycling using a simple steady-state kinetic model to infer the internal HO₂ and organic radical production. We evaluate the relative importance of internal photochemical radical production

in comparison to oxidant uptake from the gas phase and other internal sources.

Many known photosensitizers are carbonyls, which absorb above 300 nm especially when the carbonyl function is attached to an aromatic system. Figure 3.1 illustrates the catalytic cycle of a photosensitizer (P) with an initial excitation step indicated by the blue box (box a), followed by singlet ($P^*(s)$) to triplet ($P^*(t)$) intersystem crossing (ISC). $P^*(t)$ state is long lived and can act as an oxidant¹¹⁹ towards any organic compound (the “donor”, RH), in the present study represented by CA, SA, and Syr. This leads to an alkyl or phenoxy radical and a ketyl radical (PH^\cdot) as illustrated in the black box b) in Fig. 3.1. PH^\cdot passes on an electron or hydrogen atom to oxygen or another electron acceptor (e.g., NO_2)²⁴⁸ illustrated in the magenta box c) in Fig. 3.1 and leads back to P in its ground state. The efficiency of the catalytic cycle is reduced by several processes involving $P^*(s)$ and $P^*(t)$ such as deactivation of $P^*(s)$, deactivation of $P^*(t)$, i.e. by phosphorescence, non-radiative decay, and reaction with oxygen. Radical reactions of PH^\cdot also influence the efficiency of the catalytic cycle. Overall, formation of $P^*(t)$ leads to the oxidation of RH and to the production of HO_2 . Therefore, this indirect photochemistry may drive oxidation under those daytime tropospheric conditions that are characterized by low flux at wavelengths below 300nm, where direct photolysis of the majority of organic compounds is not possible and HO_x production in the gas phase is not efficient. Imidazoles, which include IC, are BrC compounds formed as products from the multi-phase chemistry of glyoxal and ammonium sulfate (AS) in aqueous aerosols^{5,10,123}. Glyoxal is an important oxygenated volatile organic compound (OVOC) originating from the oxidation of predominantly

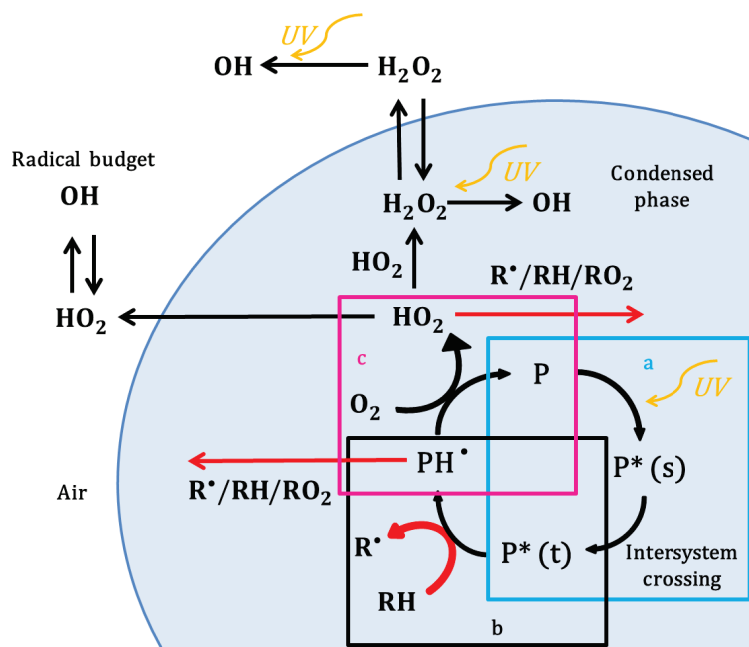


Figure 3.1: Photochemical catalytic cycle of a photosensitizer (P) in a particle. a) The P first absorbs light being excited to the triplet state ($P^*(t)$). b) The triplet reacts with an H atom/electron donor to produce the reduced ketyl radical (PH^\cdot). c) The ketyl radical may transfer an H atom or electron to an acceptor, such as O_2 . HO_2 radicals can then be released into the gas phase or react within the particle. Red reaction arrows indicate aging reactions of condensed phase organic molecules. Acid dissociation of HO_2 is not shown for simplicity.

biogenic precursors. BPh, BBA¹¹⁹ and other aromatic carbonyls may be formed as intermediates in the photooxidation of aromatic compounds in the gas phase^{125,126} or also by condensed phase oxidation of biomass burning products^{127,128}. CA serves as a proxy for non-absorbing, highly oxidized and functionalized secondary organic compounds in the atmosphere. In solution, CA takes up or releases water gradually without phase change over the whole range of relative humidity (*RH*) values studied here^{246,255}, which makes it a good substrate and matrix from an experimental perspective. SA is considered a proxy for reactive oxygenated organic material and has been found in biomass burning aerosol²⁵⁶. Its condensed phase ozonolysis kinetics has been investigated previously^{62,64,212}. Syr is a well-known thermal decomposition product of lignin occurring in biomass burning aerosol from hard woods^{257,258} and known to act as a single-electron reductant with NO₂ and other oxidants^{9,259}

3.3 Experimental

3.3.1 Coated-wall flow tube experiments

The HO₂ release was measured by scavenging HO₂ with an excess of nitrogen monoxide (NO) in an irradiated reactor containing a laminar coated wall flow tube (CWFT). The method has been described in detail in our previous work¹²⁰ and further details, raw data from exemplary experiments and the rationale of the conversion of the measured NO loss to HO₂ release rate are given in the SI. The coated tubes were 1.2 cm inner diameter, 50 cm long (Duran glass) and fitted snugly into the reactor as inserts. The jacketed glass reactor held at $T=20 \pm 1^\circ\text{C}$ was surrounded by 7 fluorescent lamps (UVA range, Philips Cleo Effect 20 W: 300 – 420 nm, 41 cm, 2.6 cm o.d., see SI Fig. 3.7), leading to J_{NO_2} of 0.011 s^{-1} in the flow tube. Flows of N₂ and O₂ were set by mass flow controllers at 1 L/min and 0.5 L/min respectively. NO was added with a third flow of 5 – 10 ml/min of 100 ppm NO in N₂. The NO concentration during CWFT experiments was always in excess of $10^{13} \text{ molecule cm}^{-3}$ to efficiently scavenge 99 % of HO₂ produced by the films within at most 50 ms ($k_1 = 8.0 \times 10^{12} \text{ cm}^3 \text{ molecule}^{-1} \text{ s}^{-1}$ at 298 K⁸⁸; $t_{99\%} = -\ln 0.01 / (k_1[\text{NO}])$). The life time of HO₂ with respect to its self-reaction in the gas phase is about 20 s ($[\text{HO}_2] = 5 \text{ ppb}$ and $k_{\text{HO}_2} = 1.8 \times 10^{12} \text{ cm}^3 \text{ molecule}^{-1} \text{ s}^{-1}$ at 298 K²⁶⁰).



RH from 25 – 65 % at 20°C was controlled using two different humidifier apparatus, in which the carrier gas passed either through a permeable tube immersed in liquid water at $T > 293 \text{ K}$ or over liquid water at $T < 293 \text{ K}$ to a desired dew point. The flow was directed to bypass the reactor to exchange flow tubes without the need to interrupt the flow system and to determine the initial trace gas levels at the entrance of the CWFT. The concentration of NO was measured by a chemiluminescence detector (Ecophysics CLD 77 AM). H₂O₂ was measured by the AeroLaser 2021 analyzer. The preparation of the films composed of IC and CA and their properties are described in our previous work¹²⁰. The IC/CA, BPh/CA and BBA/CA films were produced by depositing 400 μl of aqueous solutions of 0.75M of CA and varying amounts of IC, BPh or BBA in the glass tube inserted. A homogeneous, thin and viscous film in equilibrium with the same *RH* as used later in the experiment was achieved by rolling and turning the tube in all directions at room temperature

under a gentle flow of humidified N_2 . Solutions were prepared prior to each experiment and kept in the dark. The thickness of the film after equilibration with the given RH was estimated from the hygroscopic volume growth factors of CA²⁴⁶, assuming that the water content was dominated by the properties of CA. Final concentrations in the film were 5M of CA, 0.1.6 M for IC and BBA and 0.02 – 0.1 M for BPh at 35 % RH . For CWFT experiments with SA and Syr the mole ratio IC/(CA+SA) and IC/(CA+Syr) was kept constant at 0.15 at 40 % RH while increasing SA and Syr concentrations. Conditions of CWFT experiments are summarized in Table 1. Blank experiments run with non-coated tubes were routinely performed in between experiments with coated tubes and always resulted in NO losses below detection limit. In order to exclude other sources of HO_2 , films composed only of IC were irradiated, which did not result in detectable NO loss. A commercial O_3 analyzer (Photometric O_3 Analyser Model 400E; TELEDYNE Instruments) was used to check the absence of O_3 (detection limit 2 ppb).

3.3.2 Aerosol flow tube experiments

An irradiated aerosol flow tube (AFT) experiment was also used in the exact same configuration as the CWFT experiments to measure HO_2 release from IC/CA particles. The AFT is 156 cm long, 7 cm inner diameter and fabricated with Teflon perfluoroalkoxy copolymer (PFA). Lamps for irradiation (UVA range, Philips Cleo Effect 70 W: 300 – 420 nm, 150.7 cm, 2.8 cm o.d., emission spectrum identical to those of CWFT, Fig. 3.7) resulted in a J_{NO_2} value of $0.011 s^{-1}$. Gas flow in the AFT consisted of 0.8 L/min of N_2 , 0.2 L/min of O_2 and a third flow of NO/ N_2 to maintain the NO concentration at $\sim 2.5 \times 10^{12}$ molecule cm^{-3} . A particle filter downstream of the AFT was used to prevent particles from entering the NO analyzer. More details on the experimental procedure and exemplary raw data are shown in the SI.

Laser flash photolysis experiments The decay rate of the excited triplet state of IC in the presence of SA and Syr was measured in aqueous solution by laser flash photolysis (LFP), as described in detail in the SI.

Chemicals The chemicals used were imidazole-2-carboxaldehyde (> 99 %, Aldrich), benzophenone (> 99 %, Aldrich), 4-benzoylbenzoic acid (> 99 %, Aldrich), citric acid (Fluka), shikimic acid (Alfa Aesar, 98 %) and 2,6-dimethoxyphenol (99 %, Aldrich). The water used was Milli-Q water (18m Ω).

3.4 Results

3.4.1 Influence of photosensitizer type and mixing ratio

Figure 3.2 presents the HO_2 radical release in the CWFT as a function of the photosensitizer/CA mole ratio at constant CA mass (76.8 mg) at a RH of 43 – 47 % for IC and 53 – 57 % for BPh and BBA. The largest HO_2 release of 10^{12} molecule $cm^{-2} min^{-1}$ was due to the BPh/CA mixture at a χ_{BPh} of 0.025 and decreased to 1.6×10^{12} molecule $cm^{-2} min^{-1}$ at a χ_{BPh} of 0.002. The HO_2 release for the mixture of BBA/CA was $0.2 - 0.7 \times 10^{12}$ molecule $cm^{-2} min^{-1}$, while for the mixture of IC/CA the release amounted to $0.1 - 0.3 \times 10^{12}$ molecule $cm^{-2} min^{-1}$ for mole ratios (χ_{BBA} and χ_{IC}) between 0.02 – 0.08 and 0.03 – 0.13, respectively. Despite BPh having the lowest absolute concentration, it resulted in the greatest HO_2 release

reflecting its larger absorbance at wavelengths > 320 nm (Fig. 3.7) and more efficient radical production.

The measurements of the HO_2 release as a function of film thickness (Fig. 3.13, SI)¹²⁰ exhibits an increase until around $3 \mu\text{m}$ and then tends to level off or decrease until $5.5 \mu\text{m}$. This indicates that i) the primary excitation is occurring predominantly throughout the bulk of the film, and ii) the observed HO_2 release is contributed from the upper $3 \mu\text{m}$. The fact that the roughly linear initial increase of HO_2 with film thickness exhibits a small offset may indicate a surface contribution, as discussed below. These results are consistent with the AFT measurements shown in Fig. 3.14 (SI), where we observed two orders of magnitude more HO_2 release per unit mass likely due to the shorter depth, from which HO_2 molecules leave the condensed phase. The absence of O_3 and the fact that the amount of HONO formed was nearly half of the NO loss (see SI) is a strong indication that HO_2 was actually the dominant oxidant. Photolysis of HONO was too slow ($J_{\text{HONO}} = 0.0024\text{s}^{-1}$) to initiate additional gas phase radical chemistry. Measurements were done over 100 hours of irradiation for IC/CA without any significant drop of the HO_2 release, which confirms the photocatalytic nature of the process. We cannot entirely exclude secondary chemistry of the oxidized donor that may lead to elimination of HO_2 and thus contribute to NO loss.

3.4.2 Influence of relative humidity

Figure 3.3 shows the HO_2 release at constant dry masses of CA and constant mole ratio of photosensitizers as a function of RH (Fig. 3.3a). As RH increases from about 40 %, HO_2 release decreases by about 1 order

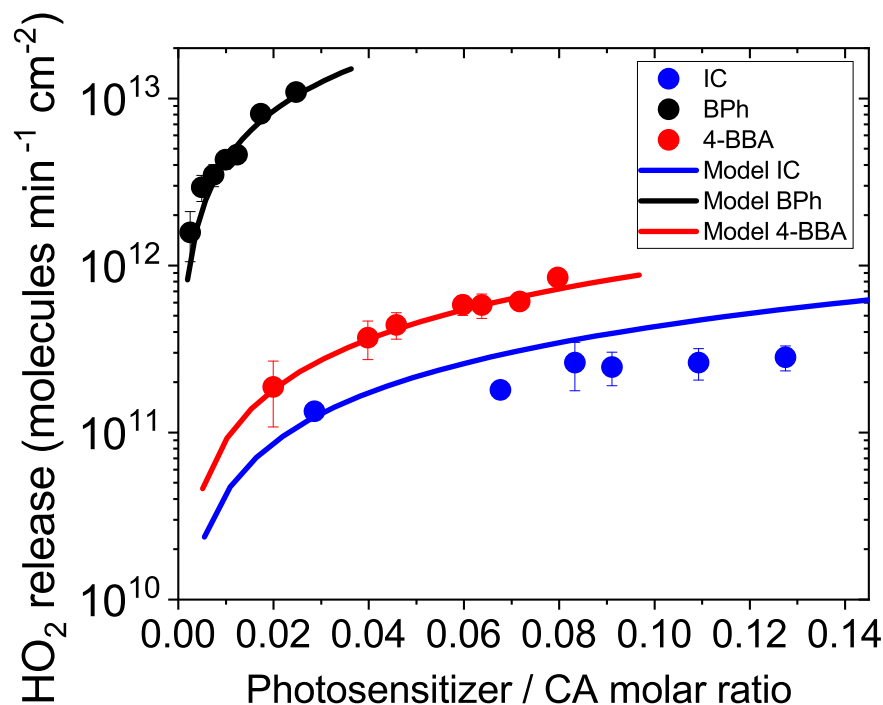


Figure 3.2: Measured HO_2 radical release as a function of the ratio of photosensitizer to citric acid (CA) for BPh at 45 % RH , 4-BBA at 45 % RH and IC at 55 % RH (black, red and blue symbols, respectively). Error bars are determined from the standard deviation of several replicate measurements. Solid lines are fits using the model described in the text.

of magnitude for IC, BBA and BPh. However, the trends of HO_2 release are dissimilar among the three below 40 % RH . For IC/CA and RH increasing from 0 to 20 % the HO_2 release increases to a plateau of 2×10^{12} molecule $\text{cm}^{-2} \text{min}^{-1}$ at RH between 20 and 40 %. In contrast, for BBA/CA and BPh/CA, HO_2 fluxes are much higher for dry conditions and then decrease towards 40 % RH .

Quantum yields of observed HO_2 release per absorbed photon for these experiments calculated based on absorption and lamp emission spectra (SI Fig. 3.7) are shown in Fig. 3.3b. In the high RH region, the quantum yield is highest for IC and lowest for BBA, possibly caused by a lower ISC yield, faster deactivation of $\text{P}^*(t)$, additional sinks for PH^{261} , lower rate of the reaction between $\text{P}^*(t)$ and CA or competing processes such as secondary chemistry of HO_2 . The observed RH dependence (Fig. 3.3a) may be qualitatively understood in the context of RH driven water activity to dilute or concentrate the reactants, to affect the viscosity and thus molecular diffusion, and likely by phase separation occurring at low RH . At RH between 40 – 60 %, where the mixtures with CA are presumably homogeneous solutions, water activity increases which we expected to control the decrease of the HO_2 production for all three photosensitizers due to the decreasing concentrations of donor, triplets, and radical intermediates caused by the dilution by water. At low RH (low water activity) little change in volume and thus donor concentration occurs, but the viscosity of the films increases¹⁹⁹, which we expected to lead to decreasing HO_2 production and release due to low diffusivity of all involved species. The complex interplay of these effects will be examined together with the kinetic model in the discussion section. When different types of organic matter (BBA and BPh mixed with CA) are present in aqueous solution, they may phase separate, which we hypothesize to occur for BBA and BPh between 0 – 20 % RH and 35 – 40 % RH , respectively, due to differences in polarity and solubility, similar to cases of organic solutes mixed with inorganic salts^{262–264} Phase separation may lead to an accumulation of the more surface active photosensitizers at the film-air interface increasing its local

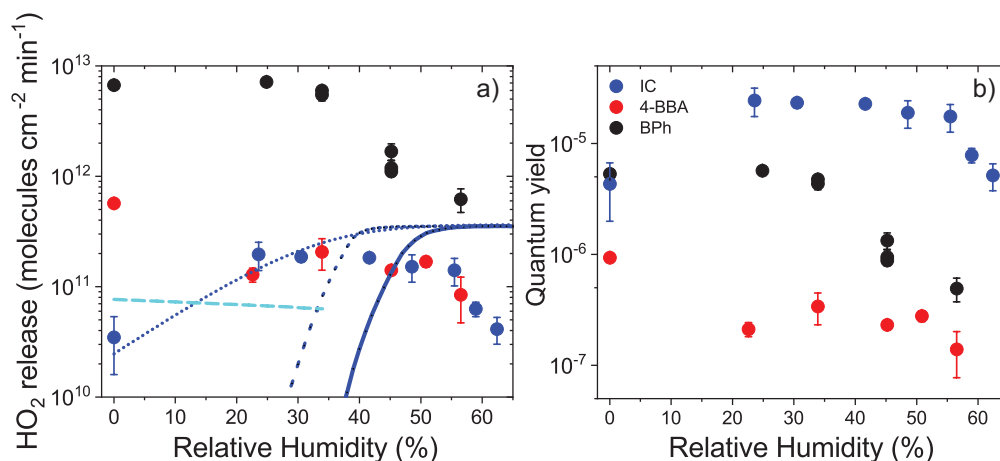


Figure 3.3: (a) Measured HO_2 release (symbols) as a function of RH at a fixed mole ratio of photosensitizer to CA (0.08 for BPh, 0.08 for 4-BBA, 0.11 for IC). Blue lines show model calculations for the case of IC based on the parameterization of the diffusion coefficient by Lienhard et al.¹¹, with and without an assumed water activity dependence of the rate coefficient for the HO_2 self-reaction (dashed and solid line, respectively). The blue dotted line represents the model prediction with adjusted diffusivity. The dashed purple line represents a suspected surface reaction. See text for more details. (b) Quantum yield HO_2 release of versus RH for the same experiments. Error bars are determined from the standard deviation of several replicate measurements.

concentration there and thus increasing reaction rates of $P^*(t)$ or PH^{\cdot} and thereby also the HO_2 release into the gas phase. Due to this complication, we only consider the IC – CA system in our further more quantitative discussion of the behavior under dry conditions.

3.4.3 Influence of competing donors

Figure 3.4 shows the HO_2 release for the two systems IC/Syr/CA and IC/SA/CA as a function of the Syr or SA donor concentration. Experiments employed constant IC and CA concentration at 0.7 M and 6 M, respectively. For comparison, observed HO_2 release for the IC/CA system without any additional donor is shown as the blue line in Fig. 3.4. At a concentration around 10^{-4} M for Syr and 0.5 M for SA, HO_2 release was enhanced compared to experiments using IC/CA. In turn, HO_2 release decreases by about a factor of 5 as the donor concentration increases further by a factor of about 50.

The enhancement of the HO_2 release at low additional donor concentration may result from increased PH^{\cdot} production, i.e., the additional donors compete with CA for oxidation by $P^*(t)$. The concentration at which Syr and SA provide faster PH^{\cdot} production is related to the ratio between the rate coefficient of the $P^*(t)$ with CA and that of the IC triplet with either of the additional donors. These rate coefficients were measured by laser flash photolysis (LFP) as shown in Figure 3.12: $k_{SA} = (2.7 \pm 0.5) \times 10^7 \text{ M}^{-1} \text{ s}^{-1}$ for SA (pH = 7) and $k_{Syr} = (9.4 \pm 0.3) \times 10^8 \text{ M}^{-1} \text{ s}^{-1}$ for Syr (pH = 6.5). The rate coefficient of the reaction between the $P^*(t)$ and CA, $k_{IC/CA}$, was below the detection limit of $10^5 \text{ M}^{-1} \text{ s}^{-1}$. We note that k_{Syr} is about 36 times greater than k_{SA} . Though, the concentration ranges of Syr and SA, at which enhanced HO_2 and

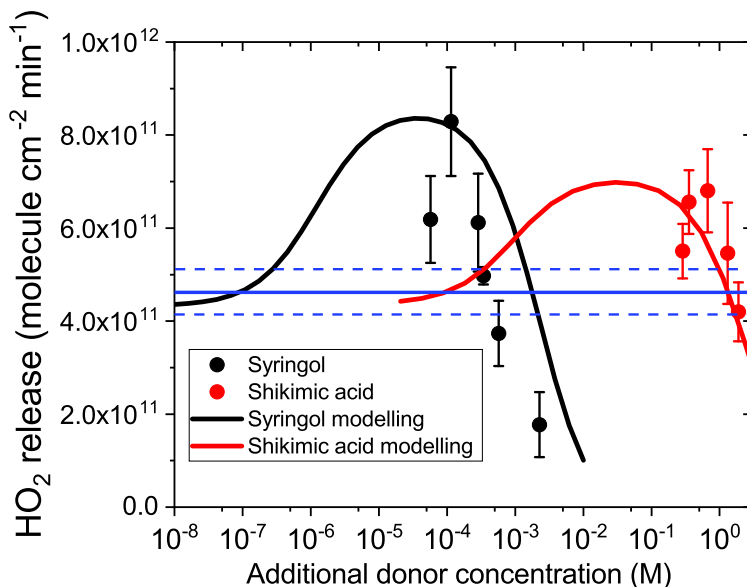


Figure 3.4: HO_2 radical release photosensitized by IC in presence of citric acid and Syr (black squares) and SA (red circles) as additional competing donors, respectively, both at constant IC (0.7 M) and CA (6 M) load at 45 % *RH*. Error bars are determined from the standard deviation of several replicate measurements. Black and red lines represent the HO_2 release returned by the kinetic model described in the text for Syr and SA, respectively. The blue line and dashed lines indicate the measured HO_2 release and the error range, respectively, in absence of any additional donor apart from CA.

its drop was observed, differ by a factor of 1000, implying that additional chemical reactions, such as those of PH^\cdot and HO_2 with the donors or their oxidation products, e.g., peroxy radicals, may also be important, as discussed further below with the kinetic model.

3.5 Discussion

As mentioned above, we expected that the RH dependence would be mainly driven by the water activity changing with RH leading at first to the following two effects: (i) The increasing water activity and thus increasing volume of the film leads to decreasing volumetric concentrations of CA, $\text{P}^*(t)$ and PH^\cdot and thus of resulting reaction rates. (ii) Water acts as a plasticizer for viscous aqueous organic solutions, leading to decreasing viscosity with increasing water content and thus molecular diffusion coefficients increasing by many orders of magnitude from low to high RH ¹⁹⁹. We evaluate the complex interplay of reaction and diffusion with a kinetic model for the overall mechanism shown in Fig. 3.5 to adjust some of the parameters that are not known for the present high solute strength system, to estimate the internal radical turnover and to allow upscaling to atmospheric conditions.

The water activity dependent diffusion coefficient of HO_2 (D_{HO_2}) was first estimated by extrapolating from the data of H_2O diffusion in CA solutions by Lienhard et al.^{11,213} (Figure 3.16, SI). The other parameter values included in Figure 3.5 were obtained or estimated as described in the SI (Table 2). We first tried to adjust the model to the data of Fig. 3.2 at 55 % RH and those for the thickness dependence in Fig. 3.13 with the rate coefficients $k_{\text{IC}/\text{CA}}$, $k_{\text{BPh}/\text{CA}}$, $k_{\text{BBA}/\text{CA}}$, respectively, as the only free variables, because they control PH^\cdot production and strongly influence the calculated HO_2 release, as at 55 % RH the system was not expected to be under diffusion control. The values estimated in this way for $k_{\text{IC}/\text{CA}}$, $k_{\text{BPh}/\text{CA}}$, $k_{\text{BBA}/\text{CA}}$ were 90, 80 and $3.5 \text{ M}^{-1} \text{ s}^{-1}$, respectively. Understandably, they are much lower than for electron rich aromatics in the range $10^5 - 10^9 \text{ M}^{-1} \text{ s}^{-1}$ ^{119,265}. There is not enough literature data to compare the relative reactivities among the three sensitizers. The low value for $k_{\text{IC}/\text{CA}}$ is also consistent with the upper limit obtained from the LFP experiments, $< 10^5 \text{ M}^{-1} \text{ s}^{-1}$. $k_{\text{IC}/\text{CA}}$ was then used to calculate the HO_2 release for the RH dependence data (solid line in Fig. 3.3a). Obviously, the calculated HO_2 release exhibits the expected maximum at intermediate RH in Fig. 3.3a, but completely fails in predicting the observed slopes at low and high RH . The sharp fall-off of the calculated HO_2 release is due to D_{HO_2} dropping by 6 orders of magnitude between 60 % and 20 % RH . Related to that, the model also fails to predict the thickness dependence measured at 36 % RH . On the other hand the model strongly overpredicts HO_2 release at high RH . We note that solubility of O_2 in organic solvents, such as ethanol, propanol or carboxylic acids, is higher than in water²⁶⁶. Thus, O_2 solubility decreases in the transition from a CA rich solution at low RH to a more H_2O rich solution at higher RH (Fig. 3.15). However, the change in O_2 concentration is only about 20 %, and due to the significant rate of triplet scavenging by O_2 , the lower O_2 concentration increases the triplet concentration with higher water activity and thus compensates the dilution effect. Below 50 % RH the decrease in the diffusion controls the decrease of HO_2 , and not oxygen solubility, since D drops several orders of magnitude down to 0 % RH .

The inability of the model to explain the RH dependent reactivity may be related to a dependence of

the many rate coefficients on the activity of the reactants (solute strength effects) and also on viscosity. The first suspect was the self-reaction of HO_2 , k_{scav3} , motivated by the significant dependence of its gas phase rate coefficient with water vapor pressure²⁶⁷. Keeping with the diffusivity as before we parameterized k_{scav3} as a function of RH (see SI) leading to a much lower HO_2 self-reaction rate at lower RH . As a result, the model fits improve with respect to the RH dependence down to around 40 % RH (dashed line in Fig. 3.3a) and with respect to the thickness dependence (measured at 36 % RH , dashed line in Fig. 3.13). Below 50 % RH , diffusion is limiting the HO_2 release, which leads to increasing HO_2 concentration and thus increasing sensitivity to the value of k_{scav3} . At high RH , the self-reaction rate is not relevant enough due to fast diffusion of HO_2 out of the film and thus low steady state HO_2 concentrations, so that the change in k_{scav3} does not improve the fit in that range. Also, below 40 % RH , the drop of D_{HO_2} dominates the fall-off of the modelled HO_2 release. Motivated by the occurrence of rate limiting surface reactions at low RH in many other multiphase reaction systems^{64,211,213}, we added a surface HO_2 production term proportional to the IC concentration adjusted to the thickness dependence in Fig. 3.13 (dashed cyan line). This would provide an explanation for the small offset of the observed linear dependence of the HO_2 release with thickness below $2\mu\text{m}$. The same surface reactivity would then dominate the low RH range in Fig. 3.3a (dashed cyan line). The slight decrease with increasing RH comes from the decrease in IC concentration with increasing water content. Apparently, such a surface process could explain the order of magnitude of HO_2 release at low RH , but in absence of further constraints we refrain from suggesting an explicit RH dependent surface reaction model. We also note that such a surface process could also result from phase separation with higher reactivity than expected for a homogeneously mixed system. As an alternative to suggest a surface process and water activity dependence of k_{scav3} , we also evaluated the effect of an alternative parameterization of D_{HO_2} . (Fig. 3.15, SI, dotted line in Fig. 3.3a, dotted line in Figure 3.13). The results indicate that D_{HO_2} would need

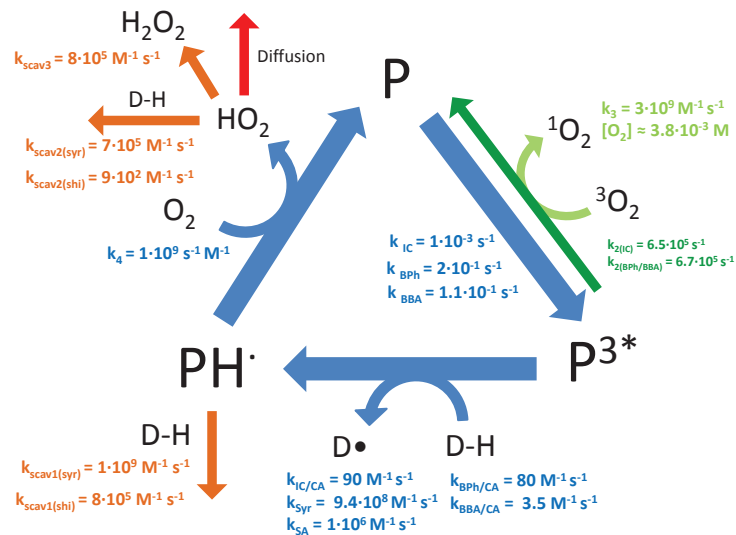


Figure 3.5: Catalytic mechanism and rate coefficients for the photochemistry of photosensitizers IC, BBA, BPh with a CA and the other H atom donors SA and Syr. Labels for photosensitizer and donors are the same as in Fig. 3.1. Reaction rate coefficients are defined in the SI.

to be four orders of magnitude higher than that based on the Lienhard et al.¹¹ data under dry conditions to explain the measured HO₂. In turn, this scenario would be less consistent with the measured thickness dependence of the HO₂ release. In summary, based on the available data and this sensitivity analysis, we are not able to conclusively decide whether the higher than expected HO₂ releases at low *RH* are due to changes in D_{HO_2} , $k_{\text{scav}3}$, the occurrence of a surface process or a combination thereof.

While we do not assume the medium to affect the initial excitation, ISC may be affected by reduced rotational freedom at high viscosity²⁰⁷, leading to increasing ISC yield from low to high *RH*. There is evidence that hydrogen bonded transition states are involved in electron transfer²¹⁷, proton coupled electron transfer²¹⁸ and hydrogen abstraction reactions²¹⁸. This could lead to rates strongly increasing with water activity, not only for $k_{\text{scav}3}$ ²⁶⁷ but also for the self-reaction of PH[•]²¹⁸, their reaction with other organics²⁶⁸ and the quenching reactions between triplets and organics²⁶⁹. As discussed above, while the water activity dependence of $k_{\text{scav}3}$ may help to explain the HO₂ release at 30 – 40 % *RH*, the HO₂ self-reaction is not relevant at high *RH*. Therefore, the strong drop in HO₂ release between 45 % and 65 % *RH* must be the consequence of the water activity dependence of ISC, radical source and radical sink processes, in which the sinks (scavenging reactions of PH[•] and HO₂) are increasing more strongly with water activity than the sources. In absence of reliable information about solute strength effects on these processes, we refrain from using additional ill-constrained parameters in an attempt to fit to the data. We therefore use the parameters valid in the 40 – 50 % *RH* range for the remainder of the discussion.

For the experiments with Syr and SA shown in Fig. 3.4, all parameters were kept fixed, except k_{SA} and k_{Syr} , to reasonably well reproduce the transition from HO₂ release enhancement by Syr and SA into that of HO₂ scavenging towards higher concentrations. The value of k_{SA} had been adjusted downwards from $2.7 \pm 0.5 \times 10^7 \text{ M}^{-1} \text{ s}^{-1}$ as determined in the LFP experiments to $1 \times 10^6 \text{ M}^{-1} \text{ s}^{-1}$. This may be justified by the differences in viscosity for the CWFT (10 Pa s at 40 % *RH*¹⁹⁹) and the LFP experiments (0.001 Pa s), since electron-transfer reactions may slow down from low to high viscosity²¹⁷. Secondly, pH in the CWFT and LFP was 1.2 and 7, respectively. Deprotonated acids may undergo one order of magnitude faster electron transfer reactions²⁷⁰ so that k_{SA} measured at pH = 7 likely overestimates the reactivity for the CWFT experiments. In contrast to SA, Syr neither protonates nor deprotonates at pH conditions between the two experiments and thus, values of k_{Syr} are not expected to be affected by the different pH values. Since no reduction in k_{Syr} compared to its values measured by LFP was required to achieve comparable agreement with observations in Fig. 3.4, pH seems to be the dominant factor affecting the reactivity of the IC triplet with Syr and SA under our conditions. The fate of PH[•] is the reaction with organics (Syr or SA)²³³, self-recombination²⁶⁸ and reaction with O₂ to produce HO₂. This means that PH[•] production is fundamental to explain HO₂ production in the condensed phase. This internal radical turnover in presence of an efficient triplet-state scavenger is substantiated in Figure 3.6 showing the modelled total production rate of HO₂ in the condensed phase and flux to the gas phase for the conditions of the experiments with Syr presented above at 40 % *RH*. Production of PH[•] from the reaction with CA and Syr, singlet oxygen and triplet state of IC are also included in Fig. 3.6. The H₂O₂ release to the gas phase predicted by the model is about $10^9 \text{ molecules cm}^{-2} \text{ min}^{-1}$ (10^{-9} M s^{-1}), unfortunately below the detection limit of the H₂O₂ detector used in our experiments.

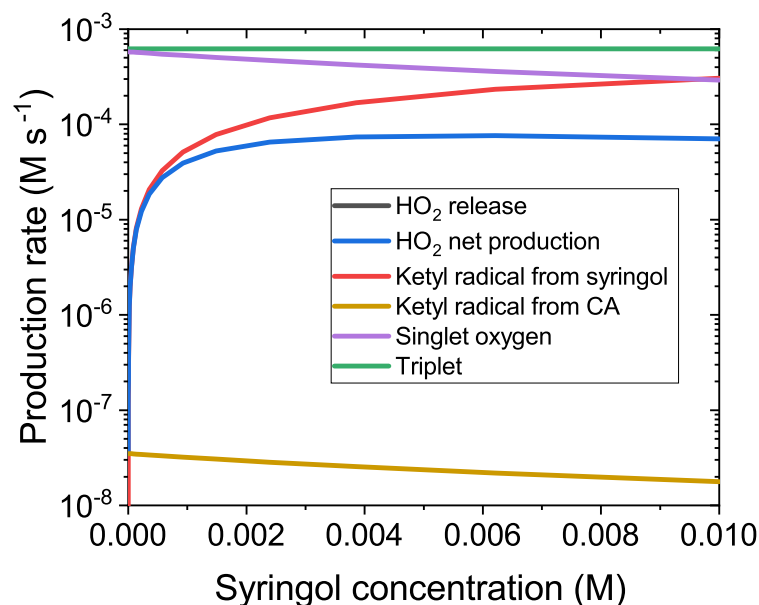


Figure 3.6: Estimated production of IC ketyl radical, singlet oxygen, IC triplet and HO₂, in the condensed phase film as well as HO₂ release into the gas phase for IC and CA with increasing concentrations of Syr at the same conditions as the CWFT experiments performed with Syr (Fig. 3.4).

The internal HO₂ production is predicted to be three orders of magnitude greater than its release (dark blue and black lines, respectively, in Fig. 3.6), mostly due to slowed diffusion and the competing scavenging reactions discussed above. The organic radical production is another factor of 10 higher than that of HO₂. Note that as the Syr concentration increases, PH[•] production increases (red line) while singlet oxygen production decreases (violet line) (Figure 3.6) implying that radicals, both organic radicals and HO₂, may be preserved and lead to an increasing oxidative capacity within the particle at high organic donor concentration. In the sense of an overall uncertainty estimate, we note that when the ISC is reduced to its lower limit of 0.1, the estimated $k_{IC/CA}$ would have to be increased by a factor of 10 to match with the observations, which would lead to a corresponding reduction of radical production. Even so, with either more reactive donors, or higher concentrations of those similar to Syr, the overall radical production may get comparable.

3.6 Upscaling to atmospheric conditions

Photochemistry of triplet forming BrC is an important source of radicals in the condensed phase as clearly demonstrated in this study for IC, BBA, and BPh in combination with different oxidation targets. The mass absorption coefficient (MAC) reported by Zhong and Jan¹⁰⁷ for a biomass burning aerosol indicates that roughly 9000 moles of photons per liter of liquid phase of aerosol are absorbed per day assuming 500 nm diameter particles with chromophore concentrations of 1M. This yields an upper limit for triplet production of 900 M day⁻¹ considering 0.1 as quantum yield for triplet production²⁶¹. The absorbance of the mixtures used in this study would lead to similar MAC values as those reported by Zhong and Jan¹⁰⁷. Mass based upper limits of HO₂ release observed in this study were 4.2×10^{16} , 1.4×10^{17} and 1.4×10^{18} molecule per hour and gram, for IC, BBA and BPh, respectively. We upscale these fluxes by assuming a suspended aerosol

mass of $20 \mu\text{g m}^{-3}$, a 12 hour irradiation cycle with sinusoidal intensity profile at 0° zenith angle and the ratio of the excitation rates of the photosensitizers from the sun spectrum and that used in our experiments ($j_{\text{sun}}/j_{\text{lamps}} = 2.83, 0.51$ and 0.53 for IC, BBA and BPh, respectively). This leads to an HO_2 release of 2.4×10^{12} , 1.4×10^{12} and 1.5×10^{13} molecules $\text{m}^{-3} \text{h}^{-1}$ for IC, BBA and BPh, respectively. These remain far below the full sunlight tropospheric gas phase HO_2 productivity of 1×10^{17} molecules $\text{m}^{-3} \text{h}^{-1}$ ²⁷¹. Though, they may become relevant in heavy pollution episodes¹²⁰ or when not much light $< 300 \text{ nm}$ driving gas phase radical production is available. As demonstrated in Fig. 3.6, depending on the presence of more reactive organic oxidation targets (such as electron rich aromatics occurring in biomass burning particles) the total internal radical turnover may exceed the HO_2 release by four orders of magnitude. The total condensed phase internal radical production was around up to 1×10^{17} molecule $\text{m}^{-3} \text{h}^{-1}$. Considering the same assumed aerosol population and light yields an estimated condensed phase HO_2 production of 10^{16} molecule $\mu\text{g}^{-1} \text{h}^{-1}$, which is about 1×10^{25} molecule $\text{L}^{-1} \text{h}^{-1}$ in the condensed phase or an upper limit of 200 M day^{-1} . For a typical gas phase concentration of 10^6 OH radicals cm^{-3} during the day, its flux into the condensed phase is about 10^{10} molecule $\text{cm}^{-2} \text{s}^{-1}$ or 10^2 molecule s^{-1} into a particle 500 nm in diameter yielding a volume averaged maximum turnover of about 0.2 M day^{-1} . Other radical sources, mainly Fenton chemistry and photolysis of NO_3^- and H_2O_2 contribute about 15 M per day ²². Therefore, the indirect photochemical radical source addressed here may play an important role in aerosol aging. Clearly, the relative importance of triplet oxidation on aerosol aging may depend on the triplet forming efficiency of real chromophores, size and the micro-physical properties of the aerosol particles, and could be clarified by measurements of triplet concentrations in ambient particles²⁷².

3.7 Supporting Information

3.7.1 Spectra

The absorption spectra for the three photosensitizers and the additional organics added to the experiments are shown together with the irradiance of the lamps used and the solar actinic flux for the surface of the Earth at 48° zenith angle (Figure 3.7). The overlap between the absorption spectra of the three photosensitizers and the lamps spectrum is orders of magnitude higher than the overlap between the absorption spectra of the additional donors and the lamps spectrum. This corroborates that the photosensitizers are the primary chromophores in the system.

3.7.2 NO loss and conversion to HO_2 production

NO was added to the gas flow in sufficient excess so that it acts as the scavenger for HO_2 . A clear NO loss is detected upon switching on UV lights (Fig. 3.8) due to the release of HO_2 radicals into the gas phase and reaction of NO with HO_2 to form NO_2 and OH radical. OH is scavenged by NO to produce HONO. The chemiluminescence detector was preceded by a HONO trap with an optional bypass, and a molybdenum converter kept at 360°C , also with an optional bypass, to convert HONO and NO_2 into NO. This configuration allowed determining NO, NO_2 and HONO independently by differential measurements

Table 1: Compilation of experimental conditions including masses of photosensitizers (P), CA, Syr and SA.

Experiment	P mass (mg)	CA mass (mg)	DH mass (mg)	<i>RH</i>
IC/CA	1 – 5 (IC)	76.8		55
BBA/CA	1 – 4 (BBA)	76.8		45
BPh/CA	0.1 – 1 (BPh)	76.8		45
<i>RH</i> dependence	3.4/5.8/7.2 (IC/BPH/BBA)	76.8		0 – 70
IC/CA/Syr	4 (IC)	76.8	$5 \times 10^{-4} - 0.02$	45
IC/CA/SA	4 (IC)	76.8	3.6 – 20	45
IC thickness	0.5-6 (IC)	7.2 – 72		36

(Fig. 3.8 and 3.9). As in previous experiments¹²⁰, the ratio NO_2/HONO was about 1.4. The presence of HONO confirms that HO_2 was indeed the oxidant of NO, rather than another RO_2 species. The fact that the ratio to NO_2 is less than one indicates that some of the OH radicals may be lost at the surface in spite of the large NO concentration or that some HONO may decompose heterogeneously over the film or along tubing downstream of the CWFT. We performed always with NO concentrations above 500 ppb NO, which is sufficient to efficiently scavenge HO_2 ¹²⁰.

The time dependent NO loss for films loaded with BPh and CA for humidities below 50 % (Fig. 3.10) has different behavior than for films loaded with the other two photosensitizers (Fig. 3.8). We assumed that BPh is degraded rapidly in the films by ketyl radical self-reaction or reaction with HO_2 radicals²⁶⁸. A complete steady state was not observed for those experiments. For this reason we take the HO_2 production in the first few seconds of irradiation, for which the concentration of BPh in the films is known.

3.7.3 Experiments performed

Table 1 shows a list of the experiments performed specifying the mass used of the different compounds and the relative humidity.

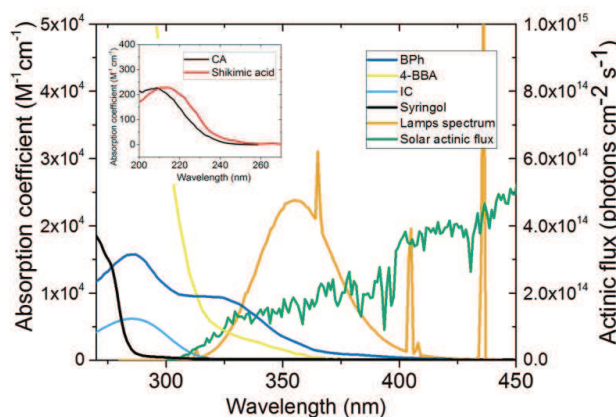


Figure 3.7: Absorption spectra of the three photosensitizers (IC, BPh and 4-BBA) and the donors (CA, shikimic acid and syringol), irradiance spectrum of the UV lamps used and solar actinic flux at 48° zenith angle.

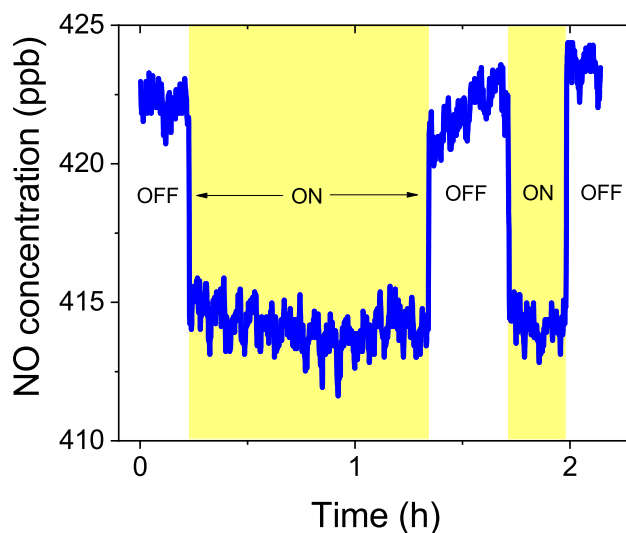


Figure 3.8: NO concentration raw data from films with lamps on and off.

3.7.4 Laser flash photolysis (LFP) experiments

The production of the excited species is driven by a pulse of a laser producing a significant population of the excited species within a few nanoseconds. The kinetic experiments for the reactions between the triplet state of IC with the donors were performed with the third harmonic (266 nm, pulse width ≈ 7 ns) of a Nd:YAG laser (Surelite II 10, Continuum) operated in the single-shot mode. Since the local maximum of absorption for IC is at 280nm, this wavelength was chosen (Figure 3.7). During the experiments, the laser pulse energy was at 12 – 14 mJ per pulse ($31 - 36$ mJ/cm²) to limit as much as possible the photolysis of the photosensitizer and therefore possible interferences of its products on the studied chemistry, but also two-photon excitation. The laser output passed through the aperture in the short axis (4 mm path length) and

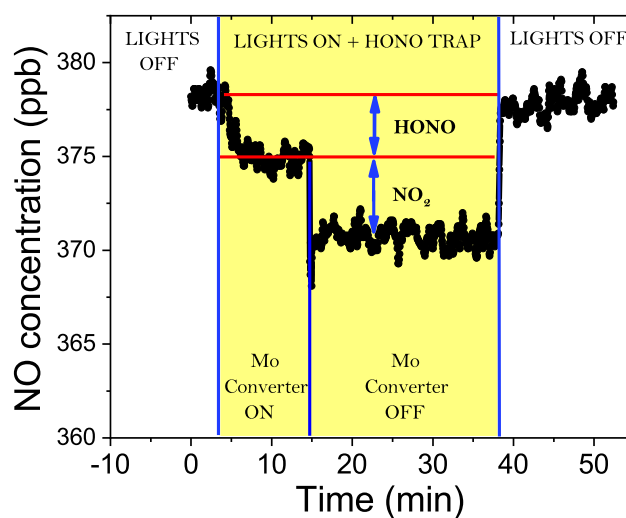


Figure 3.9: NO concentration raw data to show NO loss with lights on and HONO trap in line, and w/o the molybdenum converter, to allow differentiating between the NO loss resulting from the reaction with HO₂ and the secondary loss from the reaction with OH.

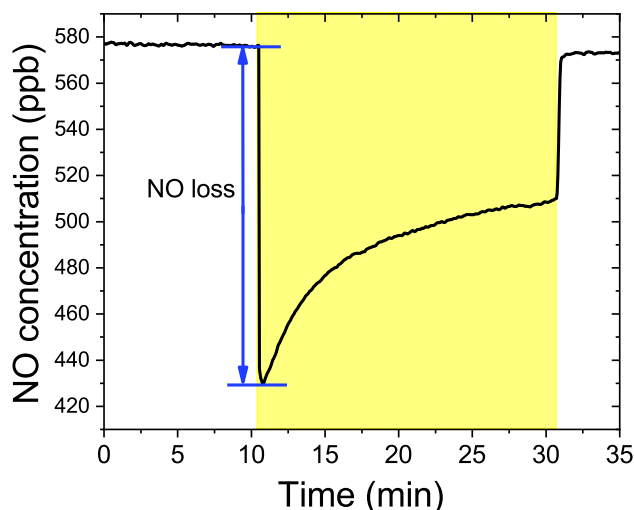


Figure 3.10: NO loss profile when lights on for films load with BPh and CA at 45 % RH.

the beam was led by mirrors to the reaction cell. The solution containing the photosensitizer was introduced in the flow cell of 450 mL by means of a peristaltic pump, with a flow of 1.6 mL/min, ensuring a complete purge of the exposed volume every 17 s. This limited the exposure of the introduced solution to 3 – 4 laser shots and maintained a constant temperature in the flow cell. All connections were made from either glass or PTFE tubing ensuring a clean liquid flow.

Transient species produced by the pulsed laser beam were monitored by means of time-resolved absorption spectroscopy. The analyzing light provided by a 75 W high-pressure Xenon arc lamp (LOT-Oriel) passed through the two apertures of the long axis of the flow cell (1 cm path length). The light was then collected by a 0.25 m monochromator (Spectral Products DK240) equipped with a 2400 grooves/mm grating and detected by a photomultiplier (Hamamatsu H7732-01). The PMT signal was passed through a high-speed current amplifier/discriminator (Femto) and the AC component recorded on a 300 MHz oscilloscope (Tektronix

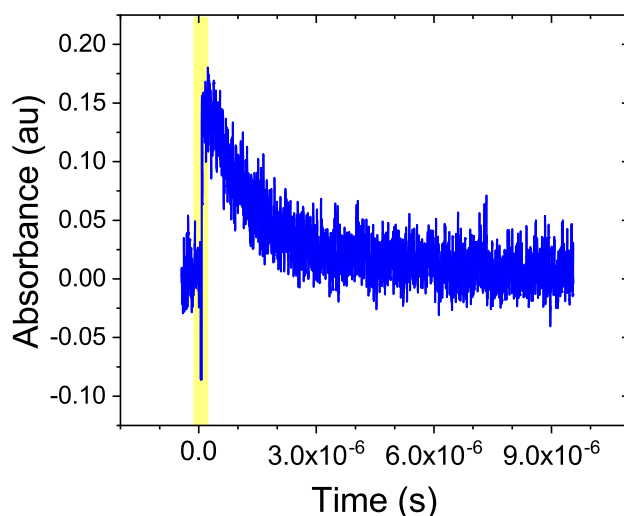


Figure 3.11: Decay of the triplet state due to deactivation and reaction with syringol.

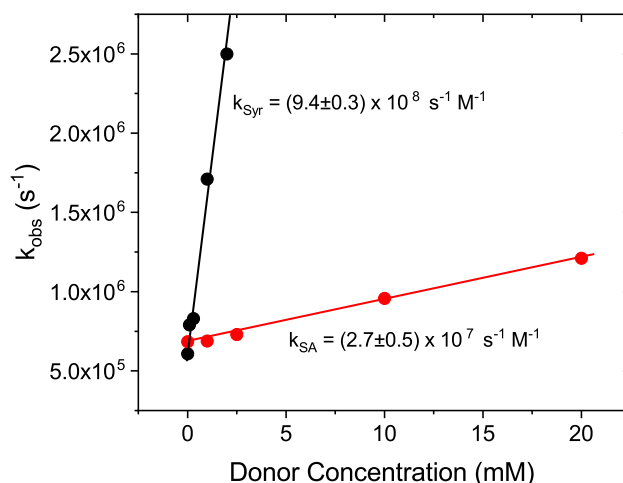


Figure 3.12: Rate coefficients derived from the laser photolysis experiments for the reactions of the triplet excited state of IC with Syr (black) and with SA (red).

TDS3032c). For every experiment we repeated 32 measurements to have an accurate signal of the decay of the triplet (Figure 3.11) excited at 266 nm with the laser by measuring the triplet decay at 330 nm where the spectrum of the triplet state of IC has a maximum²⁷³. We analyzed the mono-exponential decay of the triplet with and without H atom donor (shikimic acid and syringol) in order to evaluate the rate coefficient between the triplet state of IC and the donors.

We determined the rate coefficient of the reaction between the triplet of IC and syringol and shikimic acid in aqueous solution at pH 6.5 and 7 respectively. Measurements at more acidic conditions, which will be closer to the pH of our CWFT experiments, were not possible since the triplet of IC is not detectable by our instrument at low pH. The results are shown in Fig. 3.12.

3.7.5 Thickness dependence

HO_2 production increased with increasing thickness of the film (Figure 3.13) and levels off at thicknesses above about 3 μm . This indicates that HO_2 loss is probed out of the top few μm of the film, indicating that there is a significant HO_2 radical loss within the film by scavenging reactions with organics or by itself. In turn the observed behavior indicates that HO_2 production is not only a surface process.

3.7.6 Radical production from IC/CA aerosol particles in the aerosol flow tube (AFT)

Figure 3.14 displays the behavior of the NO concentration at the exit of the aerosol flow tube while irradiated in presence and absence of pure CA and mixed IC/CA particles. Already in absence of aerosol, a significant light induced NO loss was observed possibly due to indirect photochemical oxidation at the walls of the flow tube. The same NO loss was also observed in presence of pure CA aerosol. In turn, a significantly larger loss was observed when IC was added to the aerosol. The solution from which the particles were generated was made from 260.2 mg of IC and 1005 mg CA in 100 mL (mole ratio 0.5).

The HO_2 production found for aerosol particles is on the same order of magnitude when compared on the basis of surface area (5×10^{12} molecules cm^{-2} min^{-1}) and two orders of magnitude higher when compared

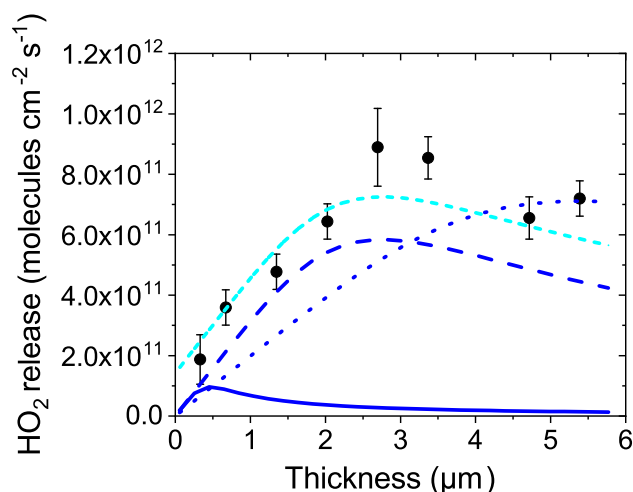


Figure 3.13: HO_2 release for films keeping IC/CA molar ratio constant at 0.16 but different loads leading to different film thickness at 36 % RH (black circles). Error bars are determined from the standard deviation of several replicate measurements. The corresponding model results with Lienhard parameterization of diffusion¹¹ (solid blue line) and k_{scaV3} reduced (dashed blue line) are shown. The contribution to the surface reaction was added to the latter (cyan dashed line). The prediction of the model using the proposed diffusion parameterization is represented by the dotted blue line.

on the basis of mass (4×10^{14} molecules $\text{mg}^{-1} \text{min}^{-1}$) than for the experiments with the films in the CWFT assuming the ratio of IC/CA 0.5. As expected, higher HO_2 release was observed per unit of mass due to the particle diameter being much smaller than the thickness of the films in the CWFT allowing HO_2 release to dominate over self-reaction.

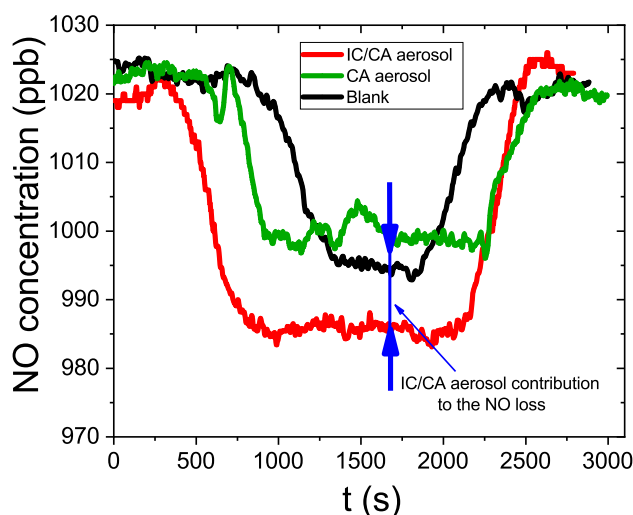


Figure 3.14: HO_2 radical production in aerosol particles of IC/CA (0.5 molar ratio) at 20 % RH compared NO loss coming from the empty reactor and the CA aerosol particles.

3.7.7 Modeling

All the reactions and the corresponding rate coefficients taken into account are shown in Table 2. The excitation rates (k_{IC} , k_{BPh} and k_{BBA}) were obtained by integration of the product of the spectrum of the UV lamps with the absorption spectra of the three photosensitizers (Figure 3.7) and taking into account the fraction of singlet states that turn into the triplet is 0.99 for BPh²⁶¹. We assume an intersystem crossing efficiency of 0.99 for IC and BBA taking into account that all molecules are highly conjugated systems. For IC, the rate coefficients of the deactivation of the triplet ($k_{2(IC)}$) was taken from the laser flash photolysis experiments (Figure 3.12). For the oxidation of syringol (k_{Syr}) and shikimic acid (k_{SA}) by the triplet we took into account the rate coefficients measured by laser flash photolysis experiments but we allowed them to vary to get a better fit and as justified in the main text. The rate coefficient for the deactivation of the triplet of BPh is $6.7 \times 10^5 \text{ s}^{-1}$ ²⁶¹ and we assumed the same for BBA ($k_{2(BPh/BBA)}$). The rate coefficient of the quenching of the triplet by O₂ was taken as an approximation from Canonica et al. 2000¹¹⁹. We assumed a rate coefficient for the reaction between the ketyl radical and the O₂ (k_4) to be $10^9 \text{ M}^{-1} \text{ s}^{-1}$ ²⁷⁴. The HO₂ itself reaction rate (k_{scav3}) was taken from Tang et al.²⁷⁵ The concentration of oxygen in the films was inferred by the study of Battino²⁶⁶, assuming that oxygen solubility in propionic acid (PA) and CA are similar and defining the solubility of oxygen in mixtures of citric acid and water as:

$$s_{O_2, film} = (s_{O_2, H_2O})^w \times s_{(O_2, PA)}^{(1-w)} \quad (13)$$

Where w is the mass fraction of water in the film.

We defined the release due to diffusion (k_{diff}) as:

$$k_{diff} = \left(\frac{D}{Filmthickness} \right) \quad (14)$$

We used the parameterization of D of water in CA from a work of Lienhard et al.¹¹ at 281K to calculate

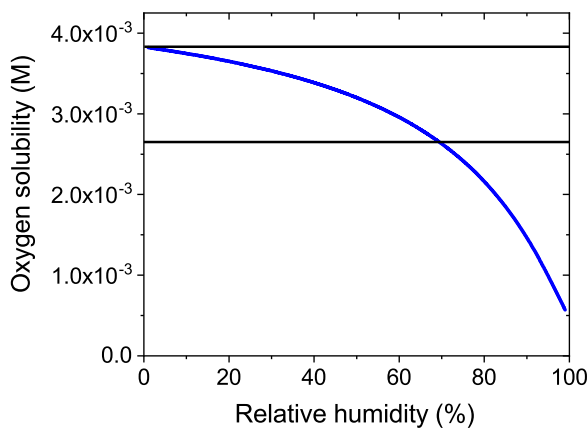


Figure 3.15: Parameterization of oxygen solubility in mixtures of citric acid and water as a function of relative humidity. The black lines indicate the region of oxygen solubility for our experimental conditions.

Table 2: Chemical reactions and the corresponding rate coefficients used for the model.

Rate coefficient symbol	Reaction	Rate coeff. ($M^{-1} s^{-1}$)	Rate coeff. in ref. ($M^{-1} s^{-1}$)	Source/Ref.
k_{IC}	$IC \xrightarrow{h\nu} IC^{3*}$	1×10^{-3}		Calculated ^a
k_{BPh}	$BPh \xrightarrow{h\nu} BPh^{3*}$	2×10^{-1}		Calculated ^a
k_{BBA}	$BBA \xrightarrow{h\nu} BBA^{3*}$	1.1×10^{-1}		Calculated ^a
$k_2(IC)$	$IC^{3*} \longrightarrow IC^{3*}$	6.5×10^5		Measured LFP
$k_2(BPh/BBA)$	$BPh^{3*}/BBA^{3*} \longrightarrow BPh/BBA$	6.5×10^5		Canonica et al. 119
k_3	$P^{3*} + O_2 \longrightarrow P + {}^1O_2$	6.7×10^5	$(6.7 \pm 0.2) \times 10^5$	Canonica et al. 119
$k_{IC/CA}$	$IC^{3*} + CA \longrightarrow ICH. + CA.$	90		Estimated
$k_{BPh/CA}$	$BPh^{3*} \longrightarrow BPhH.$	80		Estimated
$k_{BBA/CA}$	$BBA^{3*} \longrightarrow BBAH.$	3.5		Estimated
k_{Syr}	$IC^{3*} + Syr \longrightarrow ICH. + Syr.$	9.4×10^8	9.4×10^8	Measured LFP
k_{SA}	$IC^{3*} + SA \longrightarrow ICH. + SA.$	1×10^6	2.7×10^6	Measured LFP
$k_{scav1(Syr)}$	$ICH. + Syr \longrightarrow Prod$	1×10^9	$(9.7 \pm 0.4) \times 10^8$	Shi et al. 276
$k_{scav1(SA)}$	$ICH. + SA \longrightarrow Prod$	8×10^5	$(9.7 \pm 0.4) \times 10^8$	Shi et al. 276
k_4	$ICH. + O_2 \longrightarrow IC + HO_2$	1×10^9	$(1 - 5) \times 10^9$	Maillard et al. 274
$k_{scav2(Syr)}$	$HO_2 + Syr \longrightarrow Prod$	7×10^5	$(1.40 \pm 0.03) \times 10^8$	Bielski et al. 16
$k_{scav2(SA)}$	$HO_2 + SA \longrightarrow Prod$	9×10^2	$10^1 - 10^8$	Bielski et al. 16
k_{scav3}	$HO_2 + HO_2 \longrightarrow H_2O_2$	8×10^8	$(8.3 \pm 0.7) \times 10^8$	Bielski et al. 16

^aAssuming intersystem crossing of 1 for all of them (measured for BPh²⁶¹)

D for HO_2 at 293K correcting for different temperatures and molecular size by means of the Stokes-Einstein relation:

$$D = \left(\frac{k_B T}{6\pi\eta r} \right) \quad (15)$$

Where D is diffusion coefficient, k_B is Boltzmann constant, T is temperature. μ is viscosity and R is the radius of the molecule. With the corresponding D , the rate coefficients of the reaction between CA and the triplet state of the photosensitizers ($k_{IC/CA}$, $k_{BPh/CA}$ and $k_{BBA/CA}$) was obtained by adjusting the outcome of the model to the data of HO_2 production for films with the photosensitizers and CA and the thickness dependence experiments (IC/CA) with $k_{IC/CA}$, $k_{BPh/CA}$ and $k_{BBA/CA}$ as free variables. In order to illustrate the response of the model when the diffusion coefficient is higher than expected at low humidity,

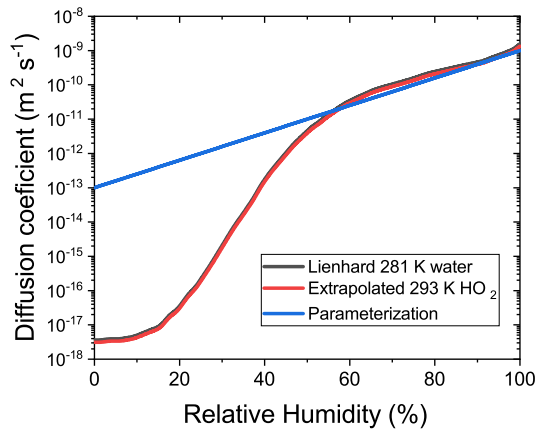


Figure 3.16: Diffusion coefficients as a function of relative humidity from the parameterization of Lienhard et al.¹¹ at 281 K for water (black line), the extrapolated from the latter to 293 K for HO_2 (red line) and the alternative parameterization (blue line) to achieve a better fit to the measured HO_2 release under dry conditions.

an alternative parameterization of $D_{RH}(\%)$ was used as a scenario:

$$\log(D)_{RH(\%)} = \frac{RH(\%)}{25} - 13 \quad (16)$$

For another scenario where HO_2 is poorly scavenged at low RH , we parameterized k_{scav3} as following:

$$\log(k)_{scav3} = \log(8 \times 10^5) + \left(\frac{RH(\%) - 100}{20} \right) \quad (17)$$

The reaction between the ketyl radical and oxygen must compete with the scavenging of the ketyl radical by the donor (k_{scav1}). The competition for the ketyl radical recombining with other radicals is almost inexistent but it might be important for low concentrations of oxygen deep in the film or inside the particle. The ketyl radicals²⁷⁶ and peroxy radical²⁷⁷ can react rapidly with organics, especially with those with conjugated or aromatic functionalities. To simplify the model, k_{scav1} summarizes the reactions of the ketyl radical with the peroxy radical, organics or other radicals preventing HO_2 to be produced and first guesses for their rate coefficients are taken from Shi et al.²⁷⁶ and $k_{scav1(Syr)}$ and $k_{scav1(SA)}$ were adjusted. HO_2 can react rapidly with organic molecules as reported in Bielski et al.¹⁶ As a first guess, we estimated the rate coefficient for the reaction between the HO_2 and the additional organics (k_{scav2}) from the rate coefficient for the reaction of HO_2 with 3,4-Dihydroxybenzaldehyde (similar to syringol), which is $1.40 \pm 0.03 \times 10^7 \text{ M}^{-1} \text{ s}^{-1}$ ¹⁶. From this guess $k_{scav2(Syr)}$ and $k_{scav2(SA)}$ were adjusted. The rate coefficients of the reactions between organics and HO_2 may vary over a broad range from 10^1 to $10^8 \text{ M}^{-1} \text{ s}^{-1}$ while for citrate ion it is $< 0.14 \text{ M}^{-1} \text{ s}^{-1}$ ¹⁶, so we do not consider the reaction between the HO_2 and CA.

Since the release of HO_2 is constant while keeping the lights on, we assumed steady state and calculated the concentrations of the triplet state, ketyl radical and HO_2 , as well as the release of HO_2 to the gas phase.

We set the differential equations shown below based on the mechanism (Table 2) and took the rate coefficients described above. We calculated the concentration of the different chemical species and the production and release of HO_2 for several conditions assuming steady state (shown in the figures in the main text as model lines).

$$\left(\frac{d[IC^{3*}]}{dt} \right) = k_{IC}[IC] - k_2[IC^{3*}] - k_3[O_2][IC^{3*}] - k_{IC/CA}[IC^{3*}][CA] - k_{DH}[DH][IC^{3*}] = 0 \quad (18)$$

$$\left(\frac{d[ICH]}{dt} \right) = k_{IC/CA}[IC^{3*}][CA] + k_{IC/DH}[IC^{3*}][DH] - k_3[O_2][ICH] - k_{scav1}[DH][ICH] = 0 \quad (19)$$

$$\left(\frac{d[HO_2]}{dt} \right) = k_3[O_2][ICH] - k_{scav3}[HO_2]^2 - k_{scav2}[DH][HO_2] - k_{diff}[HO_2] = 0 \quad (20)$$

$$[IC^{3*}] = \frac{k_{IC}[IC]}{k_2 + k_3[O_2] + k_{IC/CA}[CA] + k_{DH}[DH]} \quad (21)$$

$$[ICH] = \frac{k_{IC/CA}[IC^{3*}][CA] + k_{IC/DH}[IC^{3*}][DH]}{k_3[O_2] - k_{scav1}[DH]} \quad (22)$$

$$[HO_2] = \frac{k_{diff} + k_{scav2}[DH] \pm \sqrt{(k_{diff} + k_{scav2}[DH])^2 - 4k_{scav3}k_3[O_2][ICH]}}{2k_{scav3}} \quad (23)$$

4 Chapter 4

Halogen activation and radical cycling initiated by imidazole-2-carboxaldehyde photochemistry

Pablo Corral Arroyo^{1,2}, Raffaele Aellig³, Peter A. Alpert¹, Markus Ammann¹

1. Paul Scherrer Institute, Laboratory of Environmental Chemistry, 5232 Villigen PSI, Switzerland.
2. Department of Chemistry and Biochemistry, University of Bern, 2012 Bern, Switzerland.
3. ETH Swiss Federal Institute of Technology Zürich, Institute for Atmospheric and Climate Science, 8006 Zürich, Switzerland.

The sections from 4.1 to 4.6 are the reproduction of the report of “Halogen activation and radical cycling initiated by imidazole-2-carboxaldehyde photochemistry”

4.1 Abstract

Atmospheric aerosol particles can contain light absorbing organic compounds, also called brown carbon (BrC). Subsequent to UV-VIS light absorption, many BrC species known as photosensitizers, such as imidazole-2-carboxaldehyde (IC), can be excited into triplet states that can initiate catalytic radical reaction cycles within atmospheric aerosol, therefore increasing the reactive oxygen species (ROS) production within atmospheric aerosol particles. Triplet states (or ROS resulting from them) can also react with halides generating halide radicals and additionally molecular halogen, which can be released into the gas phase. In this work we study the influence of bromide and iodide on the photosensitized HO_2 production and release upon UV irradiation of films in a coated wall flow tube (CWFT) containing IC in a matrix of citric acid (CA). Additionally we measured the iodine release upon irradiation of IC/CA films in the CWFT. We use a kinetic model to interpret our results and to assess radical production and iodine release in sea-spray particles. As indicated by the experimental results and confirmed by the model, significant recycling of halogen species occurs via scavenging reactions with HO_2 , to prevent the full and immediate release of the molecular halogen (bromine and iodine) produced, while shutting down partially the HO_x chemistry. The recycling efficiency is higher under the effect of diffusion limitations at high viscosity. Our findings also show that halides can increase substantially the BrC photosensitized HO_2 production promoting radical production by reacting with triplet states affecting the ROS production in sea-spray particles. The iodine production within sea salt aerosol particles due to iodide oxidation by ozone is estimated at $5.9 \times 10^{-5} \text{ M s}^{-1}$. Under diffusion limitation this activation can drop several orders of magnitude (2.7×10^{-8} when D_{O_3}). The estimated iodine production from BrC photochemistry under viscous conditions amounts to $5.4 \times 10^{-8} \text{ M s}^{-1}$. This indicates that BrC photochemistry must be taken into account to correctly predict the iodine activation in sea spray particles under relatively dry conditions where diffusion is slow within particles.

4.2 Introduction

Volatile halogen-containing species such as CH_3X , CH_2XY , HOX , XY , and X_2 (where X and Y can be Cl, Br and I), also called activated halogen species, are emitted into the atmospheric gas phase by oxidation of halides by ozone¹⁷² or by radicals (OH or NO_3 for example)²⁷⁸ at the ocean surface, by dark or photochemical oxidation in snowpacks^{173,174}, by biogenic emissions of halogen-containing organic species (Org-X)^{175,176}, by activation from sea spray aerosols²⁷⁹ or by emissions from volcanos, among other processes¹⁷⁷. Halogen activation refers to the production of activated halogen species. These species are direct precursors of reactive halogen species (RHS) such as X atom or XO ¹⁷⁸, which trigger oxidative processes in the gas phase¹⁸³. RHS were first identified as important catalytic ozone depleting substances by Molina and Rowland²⁸⁰. The related complex chemical cycles explained the loss of stratospheric ozone and specifically also the recurring polar spring time ozone hole over Antarctica²⁸¹. In the troposphere the presence of XO shifts the HO_x equilibrium ($\text{HO}_2 \rightleftharpoons \text{OH}$) towards OH¹⁸⁰⁻¹⁸⁵, especially for the case of IO^{180,279,282,283}. RHS also influence the budgets of nitrogen oxides (NO_x), organic compounds and organic peroxy radicals¹⁷⁷. It has been observed that RHS of iodine produce ultrafine particles found in coastal areas^{186,187}. This new particle formation occurs via polymerization of I_2O_5 ¹⁸⁸⁻¹⁹¹, which is produced by the (photo)oxidation of iodine

precursor species such as I_2 ¹⁹² and Org-X¹⁹³. The production and depletion of activated halogen species at the ocean surface or in sea-spray particles are key processes to understand their release into the gas phase and the contributions to their emission fluxes^{172,194,284}.

Photochemistry can trigger many oxidative processes in the atmosphere which contribute directly to the oxidative budget both in the condensed and gas phases of the atmosphere, by producing oxidizing excited molecular states and radicals such as triplet states, singlet oxygen or HO_x radicals^{67,119}. Brown carbon (BrC) is defined as the fraction of organic compounds in atmospheric aerosol particles that absorbs efficiently in the UVA-VIS range. Some BrC species can undergo direct photolysis, while others may also be photosensitizers, which are species that photocatalyze radical chain reactions, involving organic and HO_x radicals, via excited triplet states as well established in aquatic photochemistry¹¹⁹. Recently, photosensitizing BrC species have been recognized as contributors to the oxidant budget in airborne particles^{67,120,123}. Oxidation of halides by the triplet states of photosensitizers²⁷³ or by chlorophyll²⁸⁵ may precede halide radical chemistry at the sea water surface¹⁹⁵ and likely also in aerosol particles, which contributes to halogen activation. The concentration of organic matter and potential chromophores as precursors for triplets are significant^{39,286–289}, especially at the surface of biologically active oceans and in sea spray particles deriving thereof.

From the concentration of triplet states in fog water of up to 10^{-13} M, the upper limit of the concentration of triplet states in aerosol particles would be around 1×10^{-10} M due to increased concentration at low water activity. The concentration of halides in sea spray aerosol particles goes up to 1×10^{-6} M^{290–292} for iodide and 8×10^{-3} M for bromide²⁸⁴. Assuming a rate coefficient of the reaction between a typical sensitizer triplet state and iodide of 5×10^9 M⁻¹ s⁻¹²⁷³, the upper limit for iodine activation upper limit may get 2.5×10^{-7} M s⁻¹, which leads to a low life time of iodide in the aqueous phase. This indicates that photosensitized chemistry may significantly contribute to the halogen activation in sea-spray particles or at the ocean surface itself.

Typical photosensitizers of interest are carbonyls, which absorb above 300 nm especially when attached to an aromatic system (see absorption spectra in SI Figure 4.4)¹¹⁹. Figure 4.1 illustrates the catalytic cycle of a photosensitizer in an organic aerosol particle in presence of halides. First, the photosensitizer (P) absorbs radiation, and this excitation step is followed by singlet (P*(s)) to triplet (P*(t)) intersystem crossing. The triplet state is long lived and, thus, can act as an oxidant¹¹⁹ reacting with an electron donor, such as a halide ion (X⁻), or an organic H atom donor, producing a ketyl radical (PH·/P·⁻). Oxygen competes with electron/H atom donors for the triplet being able to produce singlet oxygen (¹O₂) from its reaction with the triplet. The ketyl radical passes on an electron or hydrogen atom to oxygen or another electron acceptor (e.g., NO₂²⁴⁸) producing HO₂. The photosensitizer catalytic cycle is enclosed in box a). The efficiency of the catalytic cycle is reduced by deactivation of the singlet, deactivation of the triplet (phosphorescence, non-radiative decay and reaction with oxygen) and other radical reactions involving the reduced ketyl radical. The presence of organics that are highly reactive with triplet states increases the photosensitized HO₂ radical production of imidazole-2-carboxaldehyde (IC) up to 20 M day⁻¹. Subsequent to the oxidation of the halide anion by the triplet state of IC, halide radicals (X· and X₂⁻) are produced and the ensuing halide radical-radical reactions produce molecular halogen compounds (Reactions 1 – 4, Table 3). The oxidized species X₂, X₂⁻ and X· are likely recycled into X⁻ by HO₂ radicals (Reactions 5-9,

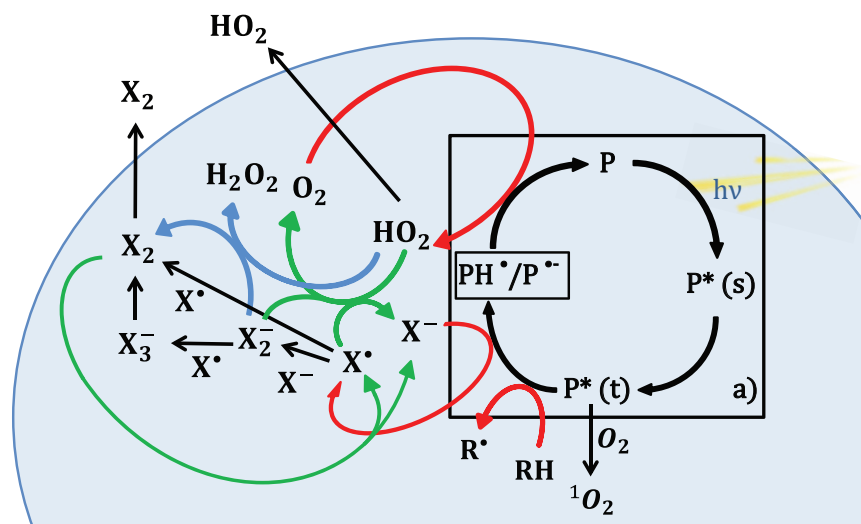


Figure 4.1: Photochemical catalytic cycle of IC (box a) and halide radical chemistry induced in a particle. IC first absorbs light leading to the triplet state, which reacts with an H atom/electron donor (DH and X^-) to produce the reduced ketyl radical (PH) and halide radicals (X^\cdot). The halide radicals can produce molecular halogen (X_2) or X_2^- by reacting with X^- . PH may transfer an H atom or electron to an acceptor, such as O_2 producing HO_2 radicals. HO_2 can recycle the halide radicals previously produced into halides or oxidize further the X_2^- to produce halogen molecules. HO_2 radicals can be released into the gas phase or react within the particle with halide radicals or with itself. Solid lines refer to reactions and dashed lines refer to transfer from condensed to gas phase. Red reaction arrows indicate reactions promoting HO_2 production, green arrows indicate reactions of recycling of halides promoted by HO_2 and blue arrows indicate reactions of X_2 promoted by HO_2 . Rate coefficients are provided in Table 3.

Table 3), however a fraction of X_2 may be released into the gas phase¹⁹⁵, and these recycling processes are determining the effective efficiency of halogen activation. De Laurentiis and co-workers suggested that excited triplet states may oxidize bromide faster than OH radicals in sea water²⁹³. Some modelling studies of aerosol chemistry consider halogen chemistry driven entirely by inorganic halogen chemistry^{178,191}, while Pechtl et al. claim that dissolved organic matter may be included¹⁹⁴. The contribution of photosensitized halogen activation is missing in these models.

Imidazole-2-carboxyldehyde (IC) is a BrC proxy and well-known photosensitizer^{120,294}. Imidazoles, which include IC, are BrC compounds formed as products from the multi-phase chemistry of glyoxal and ammonium sulfate (AS) in aqueous aerosols^{5,10,123}. Glyoxal is an important oxygenated volatile organic compound (OVOC) originating from the oxidation of predominantly biogenic precursors. CA serves as a proxy for non-absorbing highly oxidized and functionalized secondary organic compounds in the atmosphere, which are also ubiquitous in marine air²⁸⁹. In solution, CA takes up or releases water gradually without phase change over the whole range of relative humidity (RH) values studied here^{246,255}.

In this work we quantify the effect of bromide and iodide on the HO_2 production from IC photochemistry and evaluate the iodine activation coming from the consequent condensed phase radical reactions by means of Coated Wall Flow Tube (CWFT) experiments. We measured the iodine and HO_2 release from films loaded with IC, CA and bromide or iodide while irradiating with UV light. Finally, we discuss the relevance of our findings for atmospheric sea spray aerosol.

4.3 Experimental section

4.3.1 Experimental description

The setup to indirectly detect HO₂ production in an irradiated laminar coated wall flow tube (CWFT) by scavenging HO₂ with an excess of nitrogen monoxide (NO) has been described in detail in our previous work¹²⁰ and in the SI (Fig 4.5 and 4.6). Tubes (1.2 cm inner diameter, 50 cm long, Duran glass) coated with mixtures of IC/CA/NaX were snugly fitting into the temperature and relative humidity controlled CWFT as inserts surrounded by 7 fluorescent lamps (UV-A range, Philips Cleo Effect 20 W: 300 – 420 nm, 41 cm, 2.6cm o.d., see SI Fig. 4.4). The flows of N₂ and O₂ were set at 1 L/min and 0.5 L/min respectively. The NO concentration (5 – 10 ml/min of a mix of N₂ and NO at 100ppm) was always high enough ($1 - 2.5 \times 10^{13}$ molecules per cm³) to efficiently scavenge 99 % of HO₂ produced by the films within 20 – 50 ms and thus far less than our residence time of 2 s. NO was measured by a chemiluminescence detector (Ecophysics CLD 77 AM). For experiments with bromide we can assume that the concentration of bromide did not change over the time scale of our experiments and, therefore, the system was in steady-state under irradiation. On the other hand, the concentration of iodide decreased rapidly (within tens of minutes), since the iodine is rapidly released into the gas phase, so we assessed the NO loss from the first few minutes of irradiation for reporting HO₂ production rates.

Halogen release into the gas phase was observed by converting all gas phase iodine compounds to I₂O₅ following a procedure developed by Saunders et al.¹⁹⁰ Part of the flow from the reactor (0.1L/min out of 1.5L/min) was mixed with 0.2 L/min of O₂/O₃ (1 %) and feeding this mixture into a quartz reactor with 0.07 s residence time, which is irradiated with a Hg penray lamp (184 nm) . The O₂/O₃ (1 %) mixture was produced by a discharge in pure O₂ and quantified with a photometric ozone analyzer. All iodine compounds are readily photolyzed and oxidized to I₂O₅, which polymerized and produced particles via homogeneous nucleation^{172,190}. The mass of the I₂O₅ particles was determined from measuring their size distribution with a Scanning Mobility Particle Analyzer (SMPS) consisting of a home-made differential mobility analyzer (DMA, 93.5 cm long, 0.937 cm inner diameter 1.961 outer diam.) and a Condensation Particle Counter (CPC, Model 3775). I₂O₅ particle density was assumed to be 2.3 ± 0.3 g cm⁻³ following Saunders et al.¹⁹⁰ We were confidently able to measure particles < 20 nm in diameter (Fig. 4.7). This method does not distinguish between iodine and any other volatile iodine compound, which can be oxidized up to I₂O₅. HOI might be produced in the films by oxidation of halide radicals or molecular halogen. We rely on our proposed mechanism (Figure 4.1) and assume that iodine activation is dominated by production of I₂.

Aqueous solutions containing halides (10^{-8} M, 10^{-5} M and 0.01 M for iodide and 10^{-5} M and 0.01 M for bromide) were prepared beforehand. For each experiment, 76.6 mg of CA and 4 mg of IC (2.5 mg of IC for the experiments measuring iodine release) were dissolved in different volumes of a halide solution in order to get different halide concentrations in the films. This solution was deposited in the glass tube while rolling and turning the tube in all directions at room temperature under a gentle flow of N₂ humidified to the *RH* later used in experiments. This procedure is necessary to ensure homogeneous thin films. Freshly prepared solutions were used to prepare the films. Concentrations in the film were 6M for CA, 0.7 M for IC, between 10^{-8} M and 0.01 M for iodide and between 10^{-4} and 0.01 M for bromide (0.4 M of IC and 33mM of

iodide for iodine release measurements) at around 35 % *RH* at 20°C. These were calculated assuming that the water content in the film was controlled by the hygroscopicity of citric acid only, as parameterized by Zardini et al.²⁴⁶

Chemicals The chemicals used were imidazole-2-carboxaldehyde (> 99 %, Aldrich), citric acid (Fluka), sodium bromide (Sigma-Aldrich) and sodium iodide (Sigma-Aldrich).

4.4 Results

4.4.1 HO₂ production, scavenging and release

Figure 4.2 presents the HO₂ radical release in the CWFT as a function of halide concentration from films loaded with 4 mg of IC and 76.6 mg of CA and 0.7 – 70 μg of sodium bromide or 10⁻³ – 300 μg of sodium iodide, which equate to 10⁻⁴ – 10⁻² M of bromide and 10⁻⁷ – 3 × 10⁻² M of iodide, respectively. Error bars are the standard deviation of several measurements in the same film. For iodide just two measurements were made for each film, since iodide is consumed rapidly, while for bromide we made 4 – 6 measurements for each film. Experiments employed constant IC and CA concentration at 0.7 M and 6 M, respectively. For comparison, HO₂ production for the IC/CA system without any halides is shown as the blue solid line in Fig. 4.3.

The observed HO₂ production and release is enhanced from 10⁻⁷ M of iodide and 10⁻⁴ M for bromide,

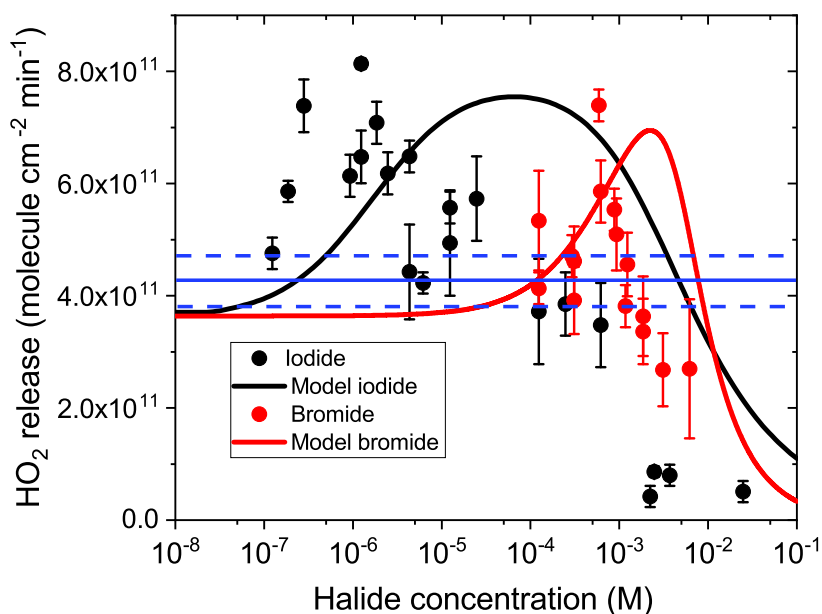


Figure 4.2: HO₂ release at 34 % *RH* from films with 4 mg of IC, 76.8 mg of CA and various concentrations of bromide (red) and iodide (black). Error bars indicate the standard deviation of between 2 – 6 measurements in the same film. The blue line and dashed blue lines indicate measured HO₂ production and uncertainty, respectively, from IC and CA films with the same concentration but in absence of halides. Solid lines are fits using the model described in the text below.

Table 3: Chemical reactions and the corresponding rate coefficients of halide and HO₂ radical chemistry¹³⁻¹⁹.

N ^o	Reaction	Rate coefficient (X=Br) M ⁻¹ s ⁻¹	Rate coefficient (X=I) M ⁻¹ s ⁻¹
R1	IC $\xrightarrow{h\nu}$ IC ^{3*}	1×10 ⁻³	
R2	IC ^{3*} + O ₂ → IC + ¹ O ₂	3×10 ⁹	
R3	IC ^{3*} → IC	6.5×10 ⁵	
R4	IC ^{3*} + CA → ICH [·] + CA [·]	90	
R5	IC ^{3*} + X ⁻ → IC ^{·-} + X [·]	6.27×10 ⁶	5.33×10 ⁹
R6	ICH [·] + O ₂ → IC + HO ₂ [·]	1×10 ⁹	
R7	HO ₂ [·] + HO ₂ [·] → H ₂ O ₂	8×10 ⁵	
R8	X ⁻ + X [·] → X ₂ ⁻	9×10 ⁹	1.1×10 ¹⁰
R9	X ₂ ⁻ + X [·] → X ₃ ⁻	3×10 ⁹	8.4×10 ⁹
R10	X [·] + X [·] → X ₂	1.9×10 ⁹	1.9×10 ¹⁰
R11	X ₂ + X ⁻ ⇌ X ₃ ⁻	2.7×10 ^{4a}	768 ^a
R12	HO ₂ [·] + X [·] → O ₂ + HX	1.8×10 ⁸	
R13	HO ₂ [·] + X ₂ ⁻ → O ₂ + HX	1×10 ⁸	
R14	HO ₂ [·] + X ₂ ⁻ → HO ₂ ⁻ + X ₂	9.1×10 ⁷	4×10 ⁹
R15	HO ₂ [·] + X ₂ → HO ₂ ⁻ + X ₂ ⁻	1.5×10 ⁸	5×10 ⁷
R16	HO ₂ [·] + X ₃ ⁻ → X ⁻ + HO ₂ ⁻ + X ₂ ⁻	<1×10 ⁷	

^aEquilibrium constant (M⁻¹)

which implies a faster rate coefficient for the scavenging of IC triplet by iodide than for bromide and the subsequent increase of the ketyl radical production. Tinel et al.²⁷³ measured the rate coefficients between the triplet state of IC and bromide and iodide as $5.33 \times 10^9 \text{ M}^{-1} \text{ s}^{-1}$ and $6.27 \times 10^6 \text{ M}^{-1} \text{ s}^{-1}$, respectively. The difference is roughly three orders of magnitude. This is in agreement with our results since the ratio of the concentrations at which iodide and bromide provide faster ketyl radical production and thus faster HO₂ release than CA alone (10^{-7} M for iodide and 10^{-4} M for bromide) is comparable to the ratio of these two rate coefficients.

After the oxidation of the halide ion by the triplet state, a cascade of fast reactions takes place leading to the production of X₂⁻ and molecular halogens (X₂). Most of these species, including the molecular halogen compounds, react rapidly with HO₂ (Reaction 5 – 9 in Table 3) leading to the drop of the HO₂ release at higher concentrations of halides (higher concentrations of halides induce higher concentrations of halide radicals). Additionally HO₂ radicals also react with each other meaning that this scavenging pathway is more relevant at high concentrations of halides, where more HO₂ is produced ($8 \times 10^5 \text{ M}^{-1} \text{ s}^{-1}$)¹⁶.

The HO₂ scavenging reactions shown in Table 3 are faster for iodide species than for bromide species which induces a suppression of the HO₂ release at lower concentrations of iodide than for bromide. In this way, HO₂ is mostly scavenged before being released into the gas phase for films with concentrations of iodide above 10^{-3} M . The ratio of the rate coefficients of the triplet with iodide and bromide is higher than the ratio of the rate coefficients of HO₂ with iodide and bromide. We suspect that this is the reason why the HO₂ release drops faster with concentration for bromide than for iodide.

A steady state kinetic model was developed treating IC photochemistry in our recent work²⁹⁴, where we estimated the HO₂ release from films of IC/CA as a function of concentration of IC, relative humidity, film thickness or additional triplet scavengers. In this study, we adapted that model, now including the scavenging of the triplet state of IC by halides²⁷³ (reaction 5) (instead of an additional organic donor) and

the inter-halogen conversion reactions (8 – 11) as well as the set of HO_2 scavenging reactions 12 – 16 (Table 3). We treated I_2 and I_3^- as the same species. Further details of the reactions and rate coefficients are given in the SI. We found that the HO_2 release was underpredicted at middle and high concentrations of halides. We decided to keep the inter-halogen conversion reactions (8 – 11) at their literature values and tune the HO_2 scavenging reactions 12 – 16. To obtain reasonable model results, they were reduced as explained in the SI. The model results allow us to assess the HO_2 release (Figure 4.2), and the efficiency in the cycling of the radicals, which will be explained later below. As apparent from Figure 4.2, important differences between observation and best model output remain. However, we refrained from adding more and ill-constrained processes and parameters to achieve better apparent fit.

4.4.2 Iodine activation

We performed very similar CWFT experiments in which the iodine release was measured as described in the experimental section. The CWFT was loaded with 2.5 mg of IC, 76.6 mg of CA (6.5 % in molar ratio) and 313 μg of NaI, corresponding to concentrations of 0.4 M, 6 M and 33 mM of IC, CA and iodide respectively, and the iodine release into the gas phase at 34 % RH was followed uninterruptedly. The HO_2 release was measured separately with a separate film under the same conditions and within the same range of time. Figure 4.3 shows the release of iodine calculated based on the measurements of I_2O_5 particles by the SMPS versus time. The profile of the release shows a peak after the first ten minutes of irradiation and decays over the following 60 minutes until the release ceases. Figure 4.3 also presents the corresponding HO_2

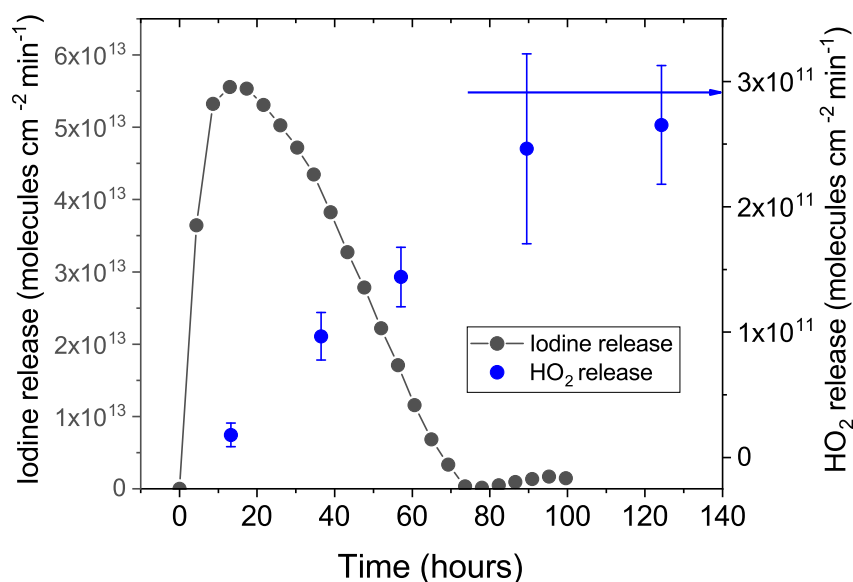


Figure 4.3: Iodine release (black), produced by mixing the experimental flow with O_3/O_2 as described above, and HO_2 release (blue) into the gas phase versus time while irradiating a film in the CWFT loaded with 2.5 mg of IC, 76.8 mg of CA and 313 μg of NaI and equilibrated at 34 % RH . The blue arrow indicates the HO_2 release expected for the film in absence of iodide.

release versus time, which is entirely depleted in the beginning, as expected (see Figure 4.2) for the high iodide concentration, and then increases until 90 minutes and then seems to tend towards a steady state of 3×10^{11} molecules $\text{min}^{-1} \text{cm}^{-2}$, which is the same as that measured in absence of iodide (blue arrow in Figure 4.3). When comparing to Figure 4.2, the evolution of the HO_2 release with time indicates that most likely a drop in the iodide concentration from 33 mM to below 10^{-4} M occurs. The maximum in the iodine release was observed after several minutes of irradiation being about 5×10^{13} molecules $\text{min}^{-1} \text{cm}^{-2}$. The iodine release model prediction is around 10^{11} molecules $\text{min}^{-1} \text{cm}^{-2}$ at the initial concentration of iodide. The difference may be due to the fast initial drop of the iodide concentration and the fact that the model is assuming steady state. The total integrated I_2O_5 mass measured over the whole observation period corresponds to $70(\pm 10)$ % of the iodide added to the film. The synchronized behavior of both releases (HO_2 and I_2) indicates that iodide is significantly consumed after 100 minutes of irradiation and presumably most of iodide is converted into molecular iodine. As indicated in the SI, we could not measure the mass from particles smaller than 20 nm of diameter, so the mass calculated is a lower limit of the real mass released. A possible alternative possible sink of halides in the films is the reaction of halide radicals (I^\cdot or I_2^-) with organics producing Org-X^{295} or further oxidation of iodine to iodate but this is beyond the scope of our study.

The efficiency of the iodine activation depends on the different competing processes occurring in the P catalytic cycle and the ones involving halogen radical chemistry (Figure 4.1). Oxygen and halides will compete for the triplet. Once the triplet oxidizes the halide, the radicals produced can be recycled back to halide (recycling A) or produce the molecular X_2 compounds bromine and iodine. These can be recycled back to X_2^- (recycling B) or escape to the gas phase. For iodine, the model predicts around 50 % of halogen atoms produced to be released to the gas phase as molecular halogen (40 % RH , $D_{\text{HO}_2} = 3.5 \times 10^{-12} \text{cm}^2 \text{s}^{-1}$ and $D_{\text{I}_2} = 2 \times 10^{12} \text{cm}^2 \text{s}^{-1}$) indicating that the fate of around half of iodide radicals is the recycling and the other half is leaving the condensed phase as iodine. This is the overall result of several competing chemical processes. HO_2 , X^\cdot and X^- are competing for X^\cdot , HO_2 and X^\cdot are competing for X_2^- , and finally, after X_2 production, X_2 can diffuse out or react with HO_2 to produce X_2^- . Our model predicts that the ~ 50 % of the I radicals (I^\cdot and I_2^-) produced are recycled back to iodide (around 40 % for bromide) and these numbers do not change significantly with RH . In addition, competition between the release by diffusion and evaporation, and the reduction back to I_2^- is active. Based on the model, the efficiency in the release of molecular iodine or bromine once they are produced is then about 90 – 95 % and > 99 % respectively.

Upon decreasing the diffusion coefficient by two orders of magnitude, the efficiency in the release of molecular iodine or bromine once they are produced is then about 50 % and 97.5 % respectively. On the other hand, upon increasing the diffusion coefficient by two orders of magnitude the efficiency in the release of molecular iodine or bromine once they are produced is then about 97.5 – 99.5 % for iodine and almost 100 % for bromine.

4.5 Conclusions and atmospheric implications

In this work we show the influence of halides on the photochemistry of imidazole-2-carboxaldehyde and its oxidative capacity. Both iodide and bromide can increase significantly the HO₂ radical production in the system IC/CA since the IC triplet scavenging reactions by them are several orders of magnitude faster than the scavenging by CA (when [I⁻] > 10⁻⁶ M then $k_{I^-}[I^-] > k_{CA}[CA]$)^{273,294}. At the same time, the radical species generated in the reaction with the triplet scavenge away the HO₂ produced preventing it to leave the film and keeping the capacity to red-ox cycle with the halide species.

The concentration of halides in sea spray aerosol particles may go up to 10⁻⁶ M for iodide^{194,290,291} and 8×10⁻³ M for bromide²⁸⁴. At the sea surface many kinds of organic compounds are present, including biomolecules, carbonylic and carboxylic compounds (DOM)³⁷, which are uplifted together with sea spray particles^{286,288}. Based on our results, halides are concentrated enough in atmospheric aerosol particles to contribute to the radical production. CA is likely a reasonable proxy for oxidized secondary organic compounds present in aerosol particles after some aging time. Primary organics present in nascent sea spray particles or on the ocean surface may themselves scavenge triplet states with faster rates than CA and in the same order of magnitude as iodide¹¹⁹.

First we calculate the iodine produced internally by reaction between triplets and iodide. Assuming a concentration of 10⁻¹⁰ M for triplet states in sea-spray particles, the first order iodine activation may get 2.5×10⁻⁷ M s⁻¹. Taking the Henry's law constant of ozone (H_{O_3}) of 0.14 M/atm²¹², a diffusion coefficient of ozone (D_{O_3}) of 1×10⁻¹² cm² s⁻¹ in a viscous organic particle⁶⁴ and k_{O_3/I^-} as 4.2×10⁹ M⁻¹ s⁻¹²⁹⁶ the ozone uptake coefficient would be 2.7×10⁻⁸ (eq. 24) under the assumption that the reaction proceeds in the reacto-diffusive regime.

$$\gamma = \frac{4H_{O_3}RT}{\omega_{O_3}} \sqrt{D_x k_b^{II} [I]_b} \quad (24)$$

Where H_{O_3} is the Henry's law constant, R is the gas constant, T is the temperature, ω_{O_3} is the mean thermal velocity of ozone, D_x is the diffusion coefficient, k_b^{II} is the rate coefficient of the reaction between ozone and iodide (k_{O_3/I^-} as 4.2×10⁹ M⁻¹ s⁻¹) and $[I]_b$ is the concentration of iodide in aerosol particles. At 25°C, the mean thermal velocity of ozone is 318 m/s and therefore, for a gas-phase concentration of 100 ppb and a particle 500 nm in radius, the rate of uptake of ozone (U) (eq. 25) and potential iodine activation will be 5.4×10⁻⁸ M s⁻¹.

$$U = \gamma C_{g,O_3} \left(\frac{S_p}{V_p} \right) \frac{\omega_{O_3}}{4} \quad (25)$$

Where C_{O_3} is the concentration of ozone in the gas phase and r is the radius of the particle. On the other hand, when assuming that ozone is equilibrated in the particle at the atmospheric concentrations (100ppb) the iodine activation will be 5.9×10⁻⁵ M s⁻¹. We conclude that photosensitized iodine production is relevant for aerosol sea spray particles containing chromophores under dry conditions or also low temperature when the reactive uptake of ozone is slow due to low diffusivity of ozone in the particle phase. Under humid conditions the activation via reaction with ozone may likely be more relevant. We noted the existence of

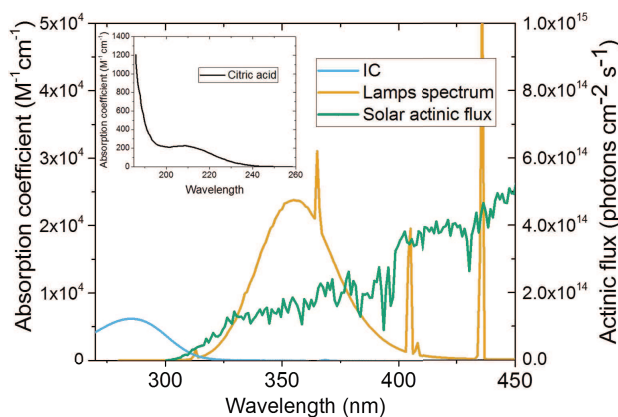


Figure 4.4: Absorption spectra of IC (100 mM) and CA (from NIST Chemistry WebBook), irradiance spectrum of the UV lamps used and solar actinic flux at 48° zenith angle.

a cycling in halide radical chemistry that shuts down the HO_x chemistry and, simultaneously, prevent the release of molecular halogens to the gas phase. Also, this cycling strongly depends on the diffusion properties of the matrix, reaching a greater cycling efficiency when diffusion is low and lower efficiency when diffusion is fast. Even so, the release is unlikely to be completely halted under a wide range of diffusion regimes and a large fraction (50% – 100%) will be released. Based on the model predictions, we suspect that the same processes are happening for bromide. De Laurentiis and co-workers suggested that excited triplet states oxidize bromide faster than OH radicals in sea water²⁹³. This conclusion, together with this work, highlights the role of DOM in halide chemistry in atmospheric aerosol particles.

4.6 Supporting Information

4.6.1 Spectra

The absorption spectra for imidazole-2-carboxaldehyde (IC) and the citric acid (CA) are shown together with the irradiance of the lamps used and the solar actinic flux for the surface of the Earth at 48° zenith angle (Figure 4.4). The overlap between the absorption spectra of IC and the lamps spectrum is orders of magnitude higher than the overlap between the absorption spectra of CA and the lamps spectrum. This corroborates that the photosensitizers are the primary chromophores in the system.

4.6.2 NO loss and conversion to HO₂ production

NO was added to the gas flow in sufficient excess so that it acts as the scavenger for HO₂. A clear NO loss is detected upon switching on UV lights (Fig. 4.5) due to the release of HO₂ radicals into the gas phase and reaction of NO with HO₂ to form NO₂ and OH radical. OH is scavenged by NO to produce HONO. The chemiluminescence detector was preceded by a HONO trap with an optional bypass, and a molybdenum converter kept at 360°C, also with an optional bypass, to convert HONO and NO₂ into NO. This configuration allowed determining NO, NO₂ and HONO independently by differential measurements

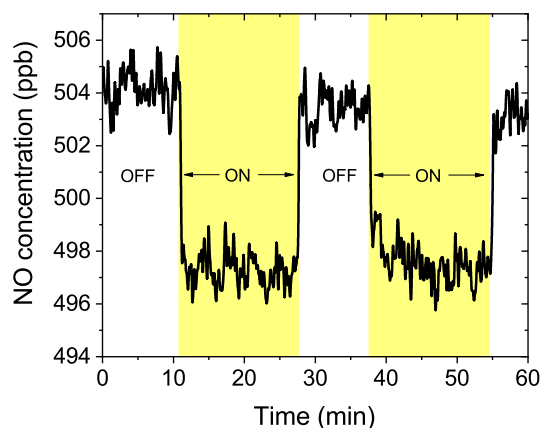


Figure 4.5: NO concentration raw data from films with lamps on and off at 35 % RH and containing 4 mg of IC and 76.8 mg of CA with an iodide concentration of 1.3×10^{-5} M.

(Fig. 4.5 and 4.6). As in previous experiments¹²⁰, the ratio NO_2/HONO was about 1.4. The presence of HONO confirms that HO_2 was indeed the oxidant of NO, rather than another RO_2 species. The fact that the ratio to NO_2 is less than one indicates that some of the OH radicals may be lost at the surface in spite of the large NO concentration or that some HONO may decompose heterogeneously over the film or along tubing downstream of the CWFT. NO was added with a third flow of 5 – 10 ml/min of 100 ppm NO in N_2 . The NO concentration during CWFT experiments was always in excess of 10^{13} molecule cm^{-3} to efficiently scavenge 99 % of HO_2 produced by the films within at most 50 ms ($k_1 = 8 \times 10^{-12}$ cm^3 molecule $^{-1}$ s $^{-1}$ at 298 K¹²⁶; $t_{99\%} = -\ln(0.01)/(k_1[\text{NO}])$).

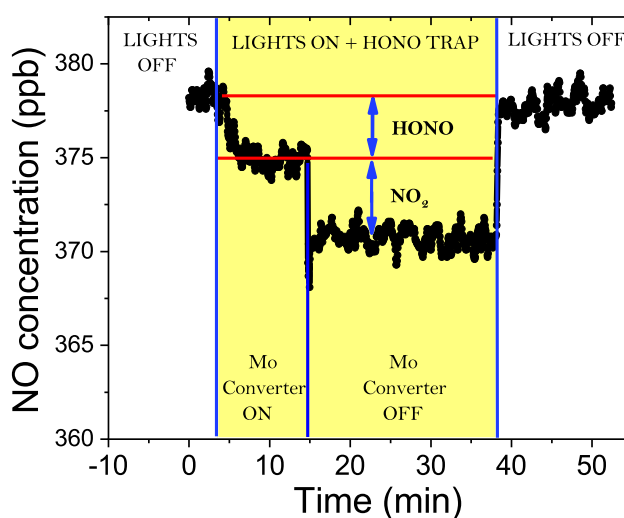


Figure 4.6: NO concentration raw data to show NO loss with lights on and HONO trap in line, and w/o the molybdenum converter, to allow differentiating between the NO loss resulting from the reaction with HO_2 and the secondary loss from the reaction with OH.

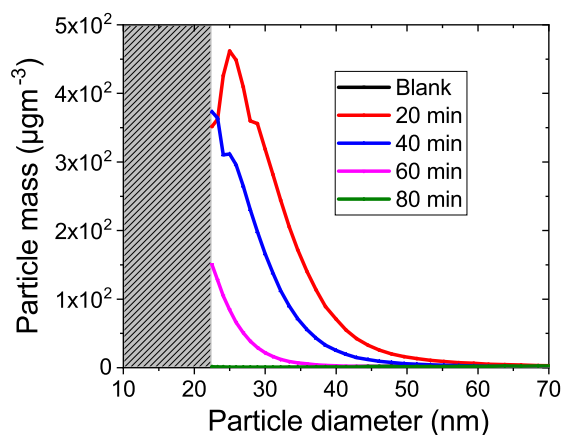


Figure 4.7: Mass of I_2O_5 particles produced from the I_2 released for each particle size at different times. The shady zone corresponds to the zone of the distribution we could not measure due to the limitations of the SMPS system.

The reaction between iodine and OH ($k = 2.1 \times 10^{-10} \text{ cm}^3 \text{ molecule}^{-1} \text{ s}^{-1}$) can interfere with the reaction between OH and NO just at high concentrations of iodide ($> 0.001 \text{ M}$) when iodine concentration can reach levels of $1 \times 10^{11} - 5 \times 10^{12} \text{ molecules cm}^{-3}$.

4.6.3 I_2O_5 particles measurements

The measurement of the mass of I_2O_5 was performed by using a Scanning Mobility Particle Analyzer (SMPS) based of a home-made Differential Mobility Analyzer (DMA) and a Condensation Particle Counter (CPC, Model 3775). The distribution is shown in Fig. 4.7 for different times. The SMPS as used was not allowing us to measure particles below 20 nm of diameter.

4.6.4 Modelling

All reactions considered in the model and the corresponding rate coefficients are listed in Table 4. The excitation rate (R1) was obtained by integration of the product of the spectrum of the UV lamps with the absorption spectrum of IC (Figure 4.7). We took 1 as the intersystem crossing efficiency for IC, which is the upper limit of intersystem crossing in triplet forming chromophores²⁶¹. The rate coefficient of the quenching of the triplet (R3) by O_2 was taken as an approximation from Canonica et al., 2000¹¹⁹. The measurement of R2 and the guess of R4 are explained in our previous work²⁹⁴. The rate coefficients the of the reaction between the triplet of IC and iodide and bromide (R5) were taken from Tinel et al.²⁷³. Maillard et al.²⁷⁴ determined the rate coefficients of reactions between organic radicals and oxygen, finding values around $1 - 5 \times 10^9 \text{ M}^{-1} \text{ s}^{-1}$. Based on this study, we assumed a rate coefficient for the reaction between the ketyl radical and O_2 (R6) to be $10^9 \text{ M}^{-1} \text{ s}^{-1}$. The rate coefficient of the reaction of HO_2 with itself (R7) was taken from Bielski et al.¹⁶ We considered the reaction between HO_2 and X^\cdot with rate coefficients as given in the literature. We took the rate coefficients of the reaction R8 – 10 given in Table 3 available in the literature from several references^{14,17,19}, and we kept them fixed. We took the rate coefficients available in the literature of the reactions involving halide radicals and HO_2 (R11 – 14) and we used them as a first

Table 4: Chemical reactions and the corresponding rate coefficients used for the model.

Reaction number	Rate coefficient	Reaction	Rate coeff. ($M^{-1} s^{-1}$) (Br/I)
R1	k_{1C}	$IC \xrightarrow{h\nu} IC^{3*}$	$1 \times 10^{-3}{}^a$
R2	k_2	$IC^{3*} \longrightarrow IC$	6.5×10^5
R3	k_3	$IC^{3*} + O_2 \longrightarrow IC + {}^1O_2$	3×10^9
R4	k_{CA}	$IC^{3*} + CA \longrightarrow ICH\cdot + CA\cdot$	90
R5	k_{hal}	$IC^{3*} + X^- \longrightarrow ICH\cdot + X\cdot$	$6.27 \times 10^6 / 5.33 \times 10^9$
R6	k_6	$ICH\cdot + O_2 \longrightarrow IC + HO_2$	1×10^9
R7	k_{HO_2}	$HO_2 + HO_2 \longrightarrow H_2O_2$	8×10^5
R8	k_{x1}	$X\cdot + X_2^- \longrightarrow X_2^{\cdot-}$	$9 \times 10^9 / 1.1 \times 10^{10}$
R9	k_{x2}	$X\cdot + X_2^{\cdot-} \longrightarrow X_3^- / X_2$	$8.4 \times 10^9 / 8.4 \times 10^9$
R10	k_{x3}	$X\cdot + X\cdot \longrightarrow X_2$	$3 \times 10^9 / 1.9 \times 10^{10}$
R11	k_{scav1}	$HO_2 + X\cdot \longrightarrow O_2 + HX$	$8 \times 10^3 / 4 \times 10^6$
R12	k_{scav2}	$HO_2 + X_2^{\cdot-} \longrightarrow O_2 + 2 X^- + H^+$	$8 \times 10^3 / 4 \times 10^6$
R13	k_{scav3}	$HO_2 + X_2 \longrightarrow HO_2^- + X_2^{\cdot-}$	$8 \times 10^3 / 4 \times 10^6$
R14	k_{scav4}	$HO_2 + X_2 \longrightarrow HO_2^- + X_2^{\cdot-}$	$8 \times 10^3 / 4 \times 10^6$

^aAssuming intersystem crossing of 1 for all of them (measured for BPh²⁶¹)

guess¹⁶. We assumed that the rate coefficient of the reaction between HO_2 and $I\cdot$ and the reaction between HO_2 and I_2^- to give O_2 and iodide are equal to the one of the reaction between HO_2 and I_2^- to give HO_2^- . We considered the rate coefficient of the reaction between $Br_2^{\cdot-}$ and $Br\cdot$ equals the one of the self-reaction of $Br\cdot$. We assumed that X_3^- has the same reactivity as X_2 .

We observed that our model was underpredicting the HO_2 radical release at middle and high concentrations of halides ($10^{-5} - 10^{-1}$ M). Therefore, to obtain reasonable model results we reduced the values of the rate coefficients of scavenging of HO_2 by halide radicals (R11 – 14) making them equal to each other. There is evidence that hydrogen bonded transition states are involved in proton coupled electron transfer²¹⁸ and hydrogen abstraction reactions²¹⁸. Therefore, scavenging reaction of HO_x radicals can decrease substantially in an organic matrix at low water activity. DHO_2 was set to $3.5 \times 10^{-12} \text{ cm}^2 \text{ s}^{-1}$. The discussion about the diffusion coefficient of HO_2 (D_{HO_2}) can be found in our previous work²⁹⁴. Assuming that D is inversely proportional to the radius of the diffusing molecule (Stokes-Einstein, eq. 26), we made a prediction of D_{Br_2} and D_{I_2} . We set D_{HO_2} to $3.5 \times 10^{-12} \text{ cm}^2 \text{ s}^{-1}$, D_{Br_2} to $3 \times 10^{-12} \text{ cm}^2 \text{ s}^{-1}$ and D_{I_2} to $2 \times 10^{12} \text{ cm}^2 \text{ s}^{-1}$.

$$D = \left(\frac{k_B T}{6\pi\eta r} \right) \quad (26)$$

Equation 26 shows the Stokes-Einstein relation where D is the diffusion coefficient, k_B is the Boltzmann constant, T is temperature, η is viscosity and r is the apparent radius of the molecule that diffuses. As in our previous work²⁹⁴, we defined the release due to diffusion (k_{diff}) as:

$$k_{diff} = \left(\frac{D}{\text{Filmthickness}} \right) \quad (27)$$

We set the differential equations shown below based on the mechanism (Table 4) and took the rate coefficients described above. We calculated the concentration of the different chemical species and the

production and release of HO_2 for several conditions assuming steady state.

$$\left(\frac{d[IC^{3*}]}{dt}\right) = k_{IC}[IC] - k_2[IC^{3*}] - k_3[O_2][IC^{3*}] - k_{CA}[IC^{3*}][CA] - k_{hal}[X^-][IC^{3*}] = 0 \quad (28)$$

$$\left(\frac{d[ICH]}{dt}\right) = k_{CA}[IC^{3*}][CA] + k_{hal}[IC^{3*}][X^-] - k_6[O_2][ICH] = 0 \quad (29)$$

$$[IC^{3*}] = \frac{k_{IC}[IC]}{k_2 + k_3[O_2] + k_{IC/CA}[CA] + k_{DH}[DH]} \quad (30)$$

$$[ICH] = \frac{k_{IC/CA}[IC^{3*}][CA] + k_{hal}[IC^{3*}][X^-]}{k_6[O_2]} \quad (31)$$

$$\begin{aligned} \left(\frac{d[HO_2]}{dt}\right) = & k_6[O_2][ICH] - 2k_{HO_2}[HO_2]^2 - (k_{scav1}[X^\cdot][HO_2] - (k_{scav2} + k_{scav3})[X_2^{\cdot-}][HO_2] \\ & - k_{scav4}[X_2][HO_2] - k_{diff}[HO_2]) = 0 \end{aligned} \quad (32)$$

$$\begin{aligned} \left(\frac{d[X^\cdot]}{dt}\right) = & k_{hal}[IC^{3*}][X^-] - k_{x1}[X^\cdot][X^-] - k_{x2}[X^\cdot][X_2^{\cdot-}] - 2k_{x3}[X^\cdot]^2 - k_{scav1}[X^\cdot][HO_2] \\ & + k_{scav2}[X_2^{\cdot-}][HO_2] = 0 \end{aligned} \quad (33)$$

$$\left(\frac{d[X_2^{\cdot-}]}{dt}\right) = k_{x1}[X^\cdot][X^-] - k_{x2}[X^\cdot][X_2^{\cdot-}] - (k_{scav2} + k_{scav3})[X_2^{\cdot-}][HO_2] + k_{scav4}[X_2][HO_2] = 0 \quad (34)$$

$$\left(\frac{d[X_2]}{dt}\right) = k_{x3}[X^\cdot]^2 + k_{x2}[X^\cdot][X_2^{\cdot-}] + k_{scav2}[X_2^{\cdot-}][HO_2] - k_{scav4}[X_2][HO_2] - k_{diff2}[X_2] = 0 \quad (35)$$

5 Chapter 5

Influence of humidity and iron (III) on photodegradation of atmospheric secondary organic aerosol particles

Pablo Corral Arroyo^{1,2}, Kurtis Malecha³, Markus Ammann¹, Sergey Nizkorodov³

1. Paul Scherrer Institute, Laboratory of Environmental Chemistry, 5232 Villigen PSI, Switzerland.
2. Department of Chemistry and Biochemistry, University of Bern, 2012 Bern, Switzerland.
3. Department of Chemistry, University of California, Irvine, California 92697, United States.

The experiments described in this chapter were performed during a research visit at the University of California at Irvine, CA, USA, under the supervision of Prof. Sergey Nizkorodov, from 1.11 to 1.12, 2017. The sections from 5.1 to 5.6 are the reproduction of the article of “Influence of humidity and iron (III) on photodegradation of atmospheric secondary organic aerosol particles” by P. Corral-Arroyo, K. Malecha, M. Ammann, S. Nizkorodov submitted to *Physical Chemistry Chemical Physics*.

5.1 Abstract

The absorption of solar actinic radiation by atmospheric secondary organic aerosol (SOA) particles drives condensed-phase photochemical processes, which lead to particle mass loss by the production of CO, CO₂, hydrocarbons, and various oxygenated volatile organic compounds (OVOCs). We examined the influence of relative humidity (*RH*) and Fe(III) content on the OVOC release and subsequent mass loss from secondary organic aerosol material (SOM) during UV irradiation. The samples were generated in a flow tube reactor from the oxidation of limonene by ozone. The SOM was collected with a Micro Orifice Uniform Deposit Impactor (MOUDI) on CaF₂ windows. To selected samples, a variable amount of FeCl₃ was added before irradiation. The resulting SOM samples, with or without added FeCl₃, were irradiated with a 305 nm light-emitting diode and the release of several OVOCs, including acetic acid, acetone, formic acid and acetaldehyde, was measured with a Proton Transfer Reaction Time-of-Flight Mass Spectrometer (PTR-ToF-MS). The release of OVOCs from photodegradation of SOM at mid-values of *RH* (30 – 70 %) was 2 – 4 times higher than under dry conditions. The release of OVOCs was slightly enhanced in the presence of low concentrations of iron (0.04 Fe molar ratio) but it was suppressed at higher concentrations (0.50 Fe molar ratio) of iron indicating the existence of a complicated radical chemistry driving the photodegradation of SOM. Our findings suggest that the presence of iron in atmospheric aerosol particles will either increase or decrease release of OVOCs due to the photodegradation of SOM depending on whether the relative iron concentration is low or high, respectively. At atmospherically relevant *RH* conditions, the expected fractional mass loss induced by these photochemical processes from limonene SOA particles would be between 2 and 4 % of particle mass per hour. Therefore, photodegradation is an important aging mechanism for this type of SOA.

5.2 Introduction

Organic compounds constitute a substantial fraction of atmospheric aerosol particles. They are present at an overall mass concentration that is comparable to that of major inorganic species such as sulfates, nitrates, sea salt and mineral dust components²⁰⁸. These organic compounds come from primary organic aerosol (POA), which is emitted directly by various sources, or from secondary organic aerosol (SOA), which derive from by reactions of volatile organic compounds (VOCs) with oxidants²⁰⁸. The distinction between the primary and secondary particles blurs as particles are aged by physical changes, such as gas-particle partitioning, particle coagulation or phase transitions within particles, and chemical processes such as reactive uptake of gas-phase oxidants by the particles⁶⁷. Recent studies have shown that multiphase chemistry and photochemistry may significantly contribute to aging and particle growth^{67,68,120}.

Particle phase photochemistry contributes to aerosol aging by multiple mechanisms. Energy-transfer or charge-transfer reactions driven by triplet states of organic compounds^{10,70,71}, photolysis of nitrate and nitrite resulting in free radicals⁷², photochemistry of iron carboxylate or free iron²⁰, and photolysis of carbonyls^{73,74} are some of the examples of these processes. The condensed-phase photochemical reactions may not only change the SOA composition, but also change the volatility distribution of the SOA compounds resulting from photo-induced fragmentation or oligomerization of SOA compounds into more or less volatile

products^{79,80}. The direct photolysis of organic compounds⁶⁶ or the secondary oxidation by HO_x radicals (HO₂ and OH) deriving from photolysis⁶⁹ explain the mass loss or decrease in particle size as well as the VOCs release observed in several studies related to photochemical processing of SOA^{297–300}. For example, in our previous work we have shown that secondary organic material (SOM) is efficiently degraded by exposure to UV radiation producing CO, CO₂, small hydrocarbons⁷⁴, as well as various oxygenated VOCs (OVOCs)^{299,301,302}. (In this paper, we are using “SOA” to refer to airborne particles, and “SOM” to the material formed by collecting bulk quantities of SOA particles on a substrate.)

It has been well established that SOA particle viscosity depends strongly on *RH*^{11,64,199}. Related to that, *RH* has a strong influence on diffusion-limited processes in SOA particles such as uptake or evaporation of chemical compounds or chemical reactions. For example, Ye and coworkers³⁰³ found that SOA particles from toluene oxidation resist exchange of semivolatile compounds at low relative humidity, but lose that resistance above 20 % *RH*. Shiraiwa et al.⁶ showed that the uptake coefficient of ozone to protein films varies with relative humidity due to the increase of the ozone diffusion coefficient with *RH*. Similarly, Steimer et al.²¹² demonstrated a strong relationship between the steady state reactivity of ozone with shikimic acid and the estimated diffusivity of ozone as a function of relative humidity. Slade and Knopf showed that increasing *RH* enhances the OH uptake in levoglucosan particles due to the faster diffusion³⁰⁴. *RH* also is a key parameter controlling the rate of evaporation of OVOCs from SOA particles as shown by Yli-Juuti et al.³⁰⁵. The *RH* was found to influence the photodegradation of 2,4-dinitrophenol through its effect on viscosity in several types of SOM including that generated by oxidation of d-limonene by ozone^{206,247}. They observed a faster photodegradation at high *RH* due to the increase of the efficiency in the second-order degradation reactions, which are likely to be affected by the diffusion limitations of the excited state, and therefore, by the viscosity²⁴⁷. Global atmospheric chemical models should take viscosity dependence into consideration because aerosol particles can be liquid, semisolid or solid depending on the latitude, altitude and conditions as predicted by Shiraiwa et al.²¹⁹ Our first goal is to understand the effect of *RH* on the photodegradation of SOA compounds. The results suggest that the photodegradation rate estimates based on previous measurements under dry conditions may be too conservative²⁹⁹.

Iron is emitted into the troposphere as minerals, as amorphous hydroxides, such as Fe(OH)₃, adsorbed on clay minerals, organic matter, or carbonaceous particles or bound in salts. It may be released from the particulate form by complexation or acidic dissolution into the aqueous phase^{94,138}. Dissolved iron is present in the atmosphere in two oxidation states, (II) and (III), which interconvert by various redox processes. Depending on chemical parameters such as ionic strength, pH and concentration of involved compounds, iron is present in the form of complexes with the organic and inorganic compounds in the aerosol particles and cloud droplets⁹⁴. Some of these complexes have strong ligand-to-metal charge transfer (LMCT) bands in the UV and visible ranges of the solar spectrum. Excitation of these LMCT bands in Fe(III) complexes leads to photoreduction of iron to Fe(II) and decomposition of the ligands by free radical chemistry. Fe(III)-carboxylate complexes are well-known photoactive compounds in atmospheric aerosol particles which drive LMCT reactions leading to the decarboxylation of the ligands, being the major particle phase sink of carboxylate groups in the atmosphere²⁰. The degradation of the carboxylic groups is followed by the production of OVOCs and CO₂^{95,168}, which contribute to the particle mass loss. Iron can cycle

actually suppressed at higher Fe(III) concentration demonstrating a potentially complicated role of Fe(III) on SOA photochemistry.

5.3 Experimental Section

SOA was generated by oxidation of d-limonene (Sigma-Aldrich, 98 %) with ozone in a ~ 20 L Plexiglas flow cell in the absence of seed particles. Pure oxygen at 0.5 L/min was sent through an ozone generator and into the flow cell. Limonene was evaporated in a separate 4.5 L/min air flow using a syringe pump at 25 $\mu\text{L}/\text{hour}$ liquid flow rate. The flow of air containing limonene was mixed with the O_3/O_2 flow at the entrance of the flow cell. The starting mixing ratios of ozone and limonene were about 20 ppm and 10 ppm, respectively, and the reaction time in the flow cell was about 4 min. Particles were collected with a Micro-Orifice Uniform-Deposit Impactor (MOUDI, MSP Corp. model 110-R) equipped with custom-made metal supporting rings to accommodate 2.54 cm diameter CaF_2 windows as substrates instead of Teflon or foil filters. We typically collected hundreds of micrograms of SOM per window; the largest amount was typically found on stages 8 (0.18 – 0.32 μm particle size range) and 9 (0.10 – 0.18 μm particle size range). The window was then placed in a laboratory oven overnight at 40 C with ~ 10 L/min of purge air flowing over it in order to drive off higher volatility species and help anneal the collected SOA particles into a more uniform SOM film on the window. For the *RH* dependent experiments, we used the sample immediately after annealing without further adjustments. For the experiments with variable amounts of Fe(III), a certain volume ranging from 50 μL to 2000 μL of a solution of FeCl_3 in water (0.001M, pH = 5) was dropped on the window surface, and the sample was placed again in the laboratory oven overnight under the same conditions as before. For larger volumes from 1000 μL up to 2000 μL , the solution was applied in two additions to avoid spilling over the edges of the window. For volumes lower than 500 μL , an additional droplet of water was

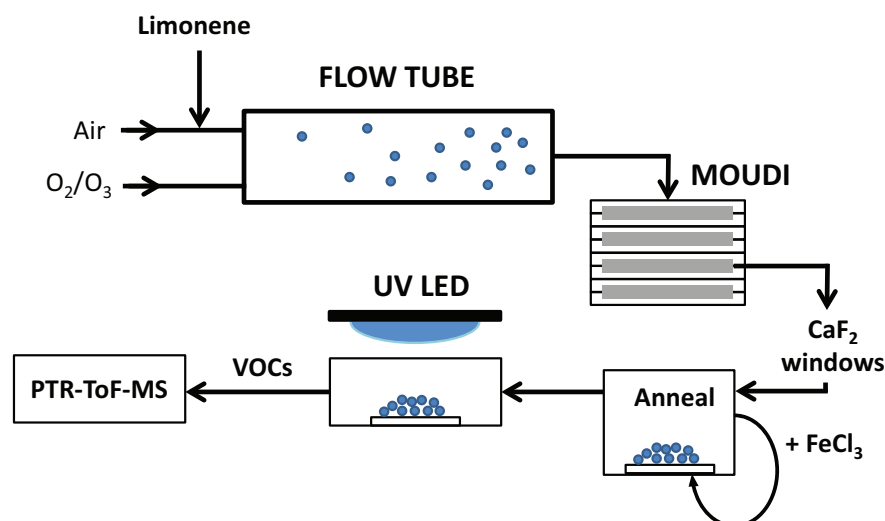


Figure 5.2: Diagram illustrating SOM preparation and UV exposure steps. SOA particles are produced by mixing a flow of air and O_2/O_3 with limonene in a flow tube. The particles are collected on CaF_2 windows located in a MOUDI, and the particles are annealed. FeCl_3 is added for the iron content dependence experiments. After annealing at 40°C, samples are irradiated with a 305 nm UV-LED, and the OVOCs released are analyzed by a PTR-ToF-MS.

added up to 500 μL to be sure that the solution covered the entire window. For the control experiments, 500 μL of nanopure water was used instead of the Fe-containing solution. The addition of liquid resulted in a redistribution of SOM on the CaF_2 window, resulting in a reduction in the film thickness in the center and a build-up of the material on the edges. The material was redistributed due to an outflow created within the droplet while it was evaporating due to the different evaporation rate in the edge compared with the one on the top of the deposited droplet³¹⁰. Because the CaF_2 window was always fully covered by the deposited droplet, we assume that the fraction exposed to UV light was always the same for every experiment and that the ratio Fe(III)/SOM is homogeneous through the sample after drying. Experiments with identical conditions of Fe(III) concentration, irradiation and RH did not indicate a dependence of OVOCs release on the volume of solution used to deposit Fe(III). The window was then placed into a custom-made glass flow cell with 0.2 L/min of purge air flowing over the window. A UV-light emitting diode (Thorlabs, Inc. model M300L4) with a wavelength centered at ~ 305 nm, a full width half-maximum of ~ 10 nm, and a power of 26 mW at 350 mA current (measured with a Coherent Powermax PS19Q power sensor) was used to irradiate the particles on the CaF_2 window. For the experiments with variable iron content dependence, the exposures to UV light were made either under dry air conditions or at $55 \pm 2\%$ RH (measured with a Vaisala HMP330 humidity probe). For the experiments related to the RH dependence of SOM decomposition, in which no Fe(III) was added to the SOM sample, we exposed SOM to UV radiation under a wider range of RH values (Fig. 5.2).

OVOCs in the flow exiting the photolysis cell were detected by a Proton Transfer Reaction Time-of-Flight Mass Spectrometer (PTR-ToF-MS). The PTR-ToF-MS was calibrated with respect to several OVOCs, namely acetic acid, formic acid, acetone and formaldehyde by injecting known amounts of these compounds in a 5 m³ chamber, similar to a procedure described in Malecha and Nizkorodov²⁹⁹. For experiments at different RH the signal was normalized to take into account the RH dependence of the ion detection sensitivity. Specifically, we evaluated the variation of the ionizing agents (H_3O^+ and $\text{H}_3\text{O}^+(\text{H}_2\text{O})$) with respect to the experiments at dry conditions and we normalized the signal to those. We took into account the different reactivity that the two ionizing agents have with the VOCs^{311,312}. Additional details are provided in the SI section.

5.4 Results and discussion

Figure 5.3 shows PTR-ToF mass spectra of the air passing over the SOM before and during the UV irradiation. Upon irradiation, certain peaks increase indicating the production and release of the corresponding compounds from SOM. The major peaks that increase are detected at m/z 43.055 (ketene, ethynol, or oxirene), m/z 45.034 (acetaldehyde), m/z 47.013 (formic acid), m/z 59.050 (acetone, propanal, or allyl alcohol) and m/z 61.029 (acetic acid, glycoaldehyde, or methyl formate). Because of the inability of PTR-ToF-MS to distinguish structural isomers, the assignments cannot be made with certainty. However, because of chemical considerations about the possible mechanism of degradation, the m/z 45.034, 47.013, 59.050, and 61.029 peaks are assigned to acetaldehyde, formic acid, acetone and acetic acid, respectively. The peak at m/z 43.055 is likely a fragment of acetic acid³¹³. Photolysis processes such as bond cleavage into free rad-

icals, photoisomerization, H abstraction or photosensitization⁶⁷, together with HO_x radical reactions, are the processes controlling the OVOC production. For example, acetone could be a product of degradation by Norrish type-II mechanisms, i.e., splitting of methyl terminated ketones. Acetic acid and formic acid could be produced by direct photolysis or by reaction of organics with HO_x radicals, which will react with organics by hydrogen abstraction and oxidation reactions, which can lead to the cleavage of carbon chains. Additionally we rely on the LMCT reactions of iron complexes as additional source of CO₂ and OVOC by decarboxylation and further degradation of the organic radicals initially produced.

Effect of *RH* on samples without added Fe(III)

Figure 5.4a shows the signal of acetaldehyde normalized to the maximal steady-state signal achieved during irradiation. The signal was also normalized to the total mass of each sample. The release of acetaldehyde levels off after about 15 minutes for dry conditions but the time needed to achieve the steady state becomes shorter for the experiments at higher *RH* (4 minutes for 70 % *RH*). We attribute this faster time to establish steady state release of acetaldehyde at higher *RH* to an increased diffusion coefficient for acetaldehyde through SOM. The increased diffusivity would be caused by the decrease of viscosity with increasing water content in the film. Indeed, the viscosity of SOM prepared by oxidation of alpha-pinene²⁶⁴ and limonene²⁴⁷ has been shown to decrease with *RH*. The reported self-diffusion coefficients in SOM change widely with *RH*^{11,64,199} going from $10^{-22} - 10^{-20} \text{ cm}^2 \text{ s}^{-1}$ at dry conditions to $10^{-9} - 10^{-7} \text{ cm}^2 \text{ s}^{-1}$ at high *RH* while the diffusion coefficient of water in alpha-pinene SOA varies from $10^{-11} - 10^{-10} \text{ cm}^2 \text{ s}^{-1}$ at dry conditions to $10^{-8} - 10^{-6} \text{ cm}^2 \text{ s}^{-1}$ at high *RH*.

Figure 5.4b shows the dependence of release of several OVOCs on *RH* corrected for the *RH*-dependent ionization efficiency in the PTR as described in the SI. The signal is normalized by the total mass of the

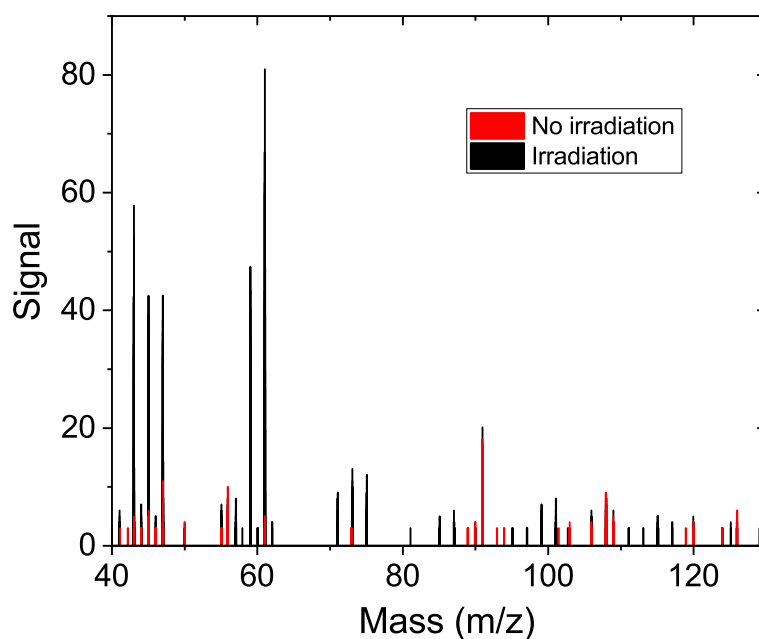


Figure 5.3: PTR-ToF-MS stick spectra of the OVOCs released from SOM before (red) and during (black) irradiation.

SOM and multiplied by the total gas flow through the sample in order to correct for the different gas flows used in different experiments (so the magnitude of the normalized signal is proportional to the OVOC flux out of the material). The data were taken from the time period where the release reaches the maximum which was different for different humidity conditions, as shown in Fig. 5.4a. The release of every compound shown in Fig. 5.4b increases with RH from 0 % to 40 – 55 % RH . There are two possible explanations for this. Firstly, certain photochemical reactions are suppressed in viscous SOA, especially the ones involving secondary reactions of long-lived electronically excited molecules²⁴⁷. Secondly, since it takes OVOCs longer to diffuse through the SOM at lower RH , the probability increases that they are degraded by secondary free-radical driven reactions before they get out of the material. From 55 % RH to 70 % RH the rate of OVOC release decreases by more than 25 %. This is attributable to a dilution effect: as the water activity in the SOM increases the concentrations of all other reactants decrease. Previous research has shown that oxygen solubility in organic solvents, such ethanol, propanol or carboxylic acids, is lower than in water²⁶⁶. Therefore, we assume that oxygen solubility also decreases upon increasing water activity meaning that HO_x radicals deriving from photolysis of SOM will be produced less efficiently since the precursor molecule (O_2) is less concentrated and subsequently OVOC production will be decreased. The decrease of the concentration

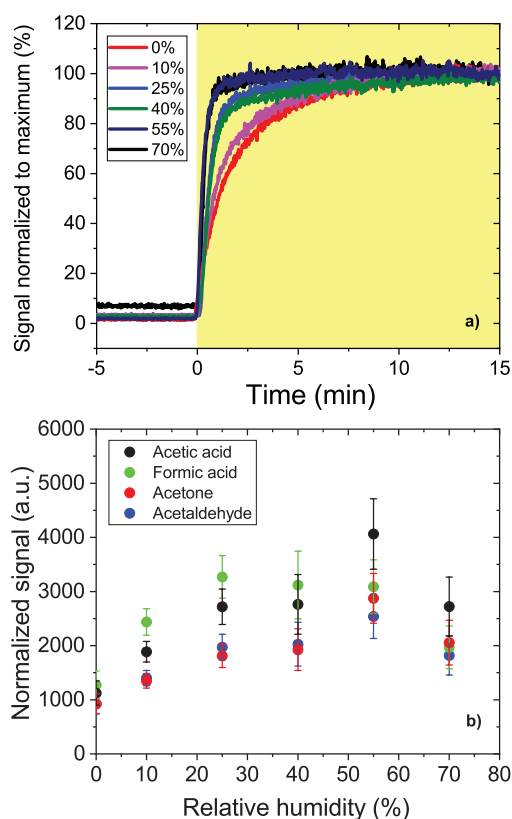


Figure 5.4: (a) Signal of acetaldehyde normalized to the maximum of the signal for each sample upon irradiation (shaded zone) at several values of RH . (b) Signal of OVOCs upon UV irradiation corresponding to the total OVOC flux and multiplied by the flow in mL/min for SOM samples versus relative humidity (%). The error bars represent the standard deviation resulting from 2 or 3 experiments.

of reactants at higher humidity should result in a decrease of second order reaction rates. Thus, the OVOC release is expected to get smaller with increasing RH . Similar dependence on RH , featuring a maximum at certain RH level, was observed in the HO_2 release in previous work¹²⁰. We estimated the diffusion coefficient of acetaldehyde at different values of RH based on the decay of its concentration in the flow after switching off the UV light (Figure 5.5). We developed a kinetic multi-layer model by means of the diffusion equation (Eq. 36), which provides a depth-resolved description of mass transport and release in films as a function of time, dividing our film in 30 equally thick layers. A detailed description of the model is provided in the SI. The diffusion is considered throughout the film by applying the diffusion equation to every layer. Since the gas flow over the film is fast (on the order of hundreds of mL per minute), we assume that the gas phase concentration of acetaldehyde next to the surface plays no role in the equilibrium between condensed and gas phase. Therefore, the release is described as the diffusion into a gas layer, where the concentration is negligible. We estimated the thickness of the sample assuming that the density of the SOM is 1.5 g/cm^3 ³¹⁴.

$$\frac{\partial C}{\partial t} = D \frac{\partial^2 C}{\partial x^2} \quad (36)$$

We optimized the values of the diffusion coefficients at different RH by fitting the release predicted by the model to the observed decay of acetaldehyde after switching off lights as shown in Fig. 5.5a. We note that the initial concentration profile in the film may change the release. Therefore, we tested the sensitivity of two initial concentration profiles on the diffusion coefficient parameter to reproduce our data: i) uniform initial concentration profile is flat throughout the film and ii) linear initial concentration profile where its maximum concentration is at the bottom of the film and zero at the surface. The two initial conditions represent two possible steady state concentration profiles during the irradiation. These two different scenarios should provide a lower (i) and upper (ii) limits of predicted diffusion coefficients, respectively.

The trend of the calculated diffusion coefficients follows the expected trend, i.e., diffusion coefficients increasing with RH . The calculated upper limit diffusion coefficients of acetaldehyde are two or three orders of magnitude lower at low RH and four or five orders of magnitude lower at high RH lower than the diffusion coefficients of water in alpha-pinene SOA measured previously by Lienhard et al.³¹⁵ The molecule of acetaldehyde is larger than the molecule of water, so, based on the Stokes-Einstein equation, we would expect water to diffuse only around two times faster than acetaldehyde. However, the Stokes-Einstein equation performs poorly for molecules of this size³¹⁶, so quantitative comparison is not possible. But as the upper limit values for the acetaldehyde diffusion coefficients in Figure 5.5b are closer to the reported values for water, they are probably more representative of the actual diffusion coefficients. The relative change of D between 0 and 70 % RH is a factor of 2 – 3 while a range of about one or two orders of magnitude is observed for $D_{\text{H}_2\text{O}}$ in SOA^{315,317} and a range of about 9 to 10 orders of magnitude is observed for D_{org} in sucrose³¹⁸. A possible explanation for this would be that the steady-state profile of the concentration of acetaldehyde in limonene SOA while irradiation is flat at low RH (lower limit prediction) and it will have a gradient at high RH (upper limit prediction), leading to a range of D of about two orders of magnitude as an upper limit. We also note that our analysis assumes that the acetaldehyde release is limited by diffusion only, and not by reaction kinetics, which may not be completely true.

Effect of added Fe(III)

Figure 5.6 shows the PTR-ToF-MS time-dependent signal of acetic acid released under irradiation under dry conditions (a) and at 55 % RH (b). The signal was normalized by the initial dry mass of SOM on the substrate (it was not corrected for the RH -dependent ionization efficiency because only signals at the same RH are compared to each other). Different traces correspond to different mole fractions of added Fe(III) (estimated assuming an average molar mass of 200 g/mol for SOM compounds). The release reaches a maximum around 30 minutes after the start of the irradiation, and after that the release drops slowly, and finally drops to the baseline level after several hours of UV exposure (not shown). At 55 % RH , the maximum signal is reached earlier than under dry conditions because the diffusion of the OVOCs through SOM is faster at higher RH , as discussed above, and the steady state release is reached earlier. The release of other compounds (acetaldehyde, formic acid, and acetone) shows the same trend as acetic acid. Figure 5.7 shows the average of the normalized signal of the 4 OVOCs under dry conditions (a) and at 55 % RH (b). To account for the faster appearance of the signal in humidified air, the averaging period is 2000 – 2500 s (33.3 – 46.7 min) for dry conditions, and 750 – 1000 s (12.5 – 16.7 min) at 55 % RH . Contrary to

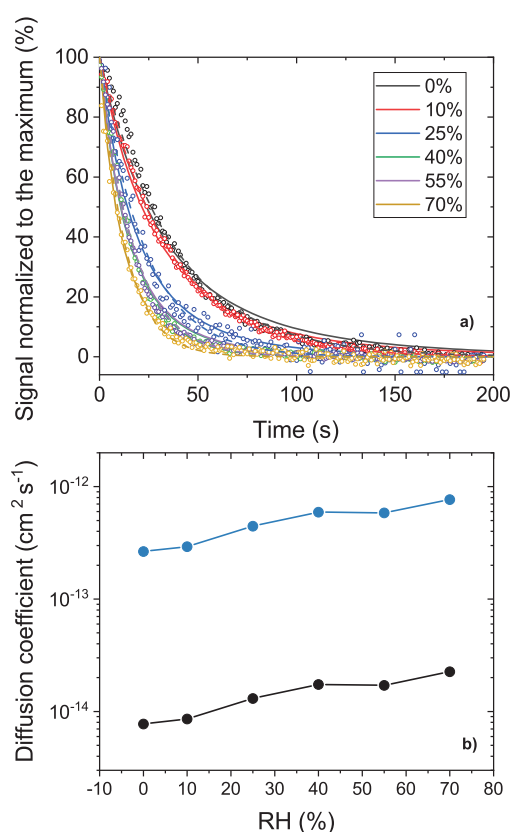


Figure 5.5: (a) Signal of acetaldehyde after irradiation background-subtracted and normalized to the maximum of the signal for each sample upon irradiation (symbols) as a function of RH . Predictions by the diffusion model with upper and lower limits for the diffusion coefficient are shown as dashed and solid lines, respectively. (b) Diffusion coefficients predicted by the model for acetaldehyde as a function of RH , with the upper (blue) and lower (black) limits shown as blue and black symbols, respectively.

our expectations that the presence of Fe should accelerate photodegradation of SOM, there is a general decreasing trend in the signal of OVOC photoproducts with the relative amount of added Fe. The trend is not linear, however. At 55 % *RH*, the release of all OVOCs is higher for samples with 4 % of Fe(III) compared to samples without added Fe. Above that fraction (and above 10 % for acetone and acetic acid), OVOC release drops below that of SOM without Fe added. Then, at higher Fe(III) concentrations, the release is strongly suppressed. Under dry conditions, acetic acid and perhaps acetone follow a similar trend with a maximum emission at 4 % Fe(III), and decreasing at higher Fe(III) concentrations. For acetaldehyde and formic acid there is a steady decrease of the signal as the Fe(III) concentration is increasing. At 55 % *RH*, all species exhibit first increased release with increasing Fe(III) content, and then a decrease for higher Fe(III) additions. We suspect that two competing effects maybe at work, one enhancing the OVOC release at low Fe(III) concentrations and suppressing it at high Fe(III) concentrations.

The enhancement in the release of OVOCs at low Fe(III) concentrations may result from increased OVOC production from the photolysis of iron carboxylate complexes likely produced after adding Fe(III) to SOM, as illustrated in Figure 5.1. This is in agreement with the work of Hems et al.³¹⁹ which found that the OH production from the photodegradation of SOA compounds by themselves is slower than the one promoted by iron carboxylate complexes formed between iron and SOA material at low Fe/SOA ratio (~ 0.3 %). The enhancement in OVOC release can be due to i) increase of the HO_x radical production inside SOM and

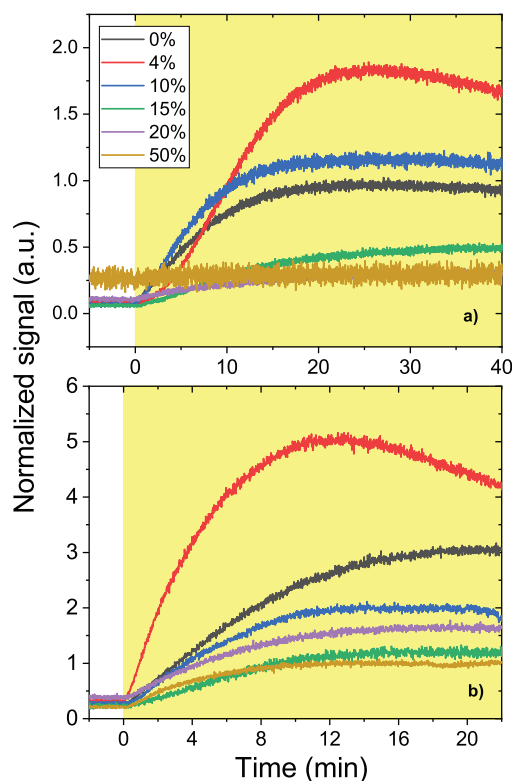


Figure 5.6: PTR-ToF-MS signal of acetic acid released upon UV irradiation for SOM samples versus time under dry conditions (a) and at 55 % *RH* (b) with varying mole fraction of added FeCl₃. The shaded zone indicates the irradiation time. Signals from different samples were normalized to the total mass of the sample.

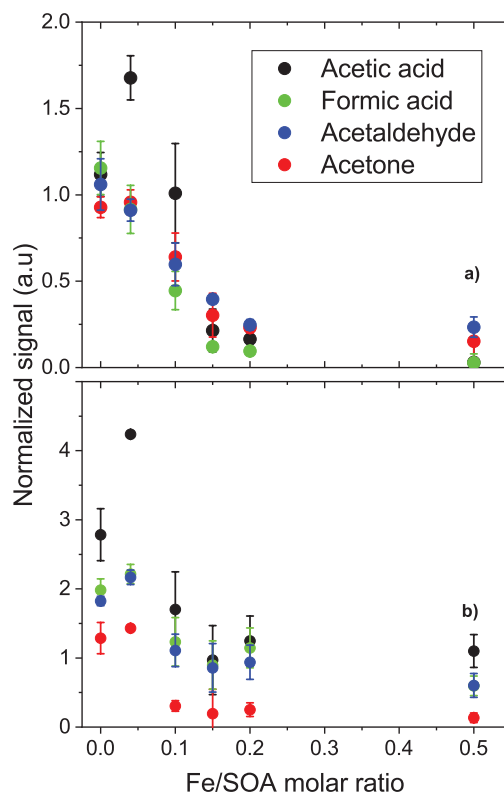


Figure 5.7: Peak intensities of signals from acetic acid, formic acid, acetaldehyde and acetone normalized to the total mass of the sample for SOM samples versus Fe/SOA molar ratio under dry conditions (a) and at 55 % *RH* (b). The error bars represent the standard deviation resulting from 2 or 3 repeated experiments.

ii) the direct photolysis of iron carboxylate complexes. Our experiments cannot differentiate between these possibilities.

The decrease of the OVOC release at high iron concentration may be the result of the presence of incompletely complexed Fe in the condensed phase, i.e., not with all coordination sites occupied by the SOA carboxylic ligands. Instead of driving LMCT transitions, incompletely complexed iron could be cycling between Fe(III) and Fe(II) (Fig. 5.1) turning HO_x radicals into water and oxygen and making them unavailable to oxidize SOA compounds into OVOCs.

5.5 Conclusions and atmospheric implications

This work reveals that *RH* plays an important role in the OVOC release from SOA induced by photolysis of the compounds presents in SOA. In the work of Malecha and Nizkorodov (2016)²⁹⁹, they estimated the emission of OVOC coming from the photolysis of several SOA under dry conditions and they predicted that SOA particles may lose at least $\sim 1\%$ of their mass over 24 hours during summertime conditions in Los Angeles, California. We claim that, under more realistic humidity conditions ($\sim 50\%$), the mass loss experienced by SOA particles may be up to 2 to 4 times higher than what was estimated in the work of Malecha and Nizkorodov²⁹⁹. We propose that all future photodegradation studies of SOA should be done

under humid conditions to more accurately estimate the rate of mass loss from the particles. Based on the analysis of the decay of the release signal after switching off lights, we suspect that OVOCs concentration gradients can take place over a range of hundreds of nanometers in aerosol particles while photolysis and persist for several minutes depending on the humidity conditions, nature of the SOM and nature of the diffusing molecule. The diffusion coefficient of acetaldehyde in limonene SOA is in the range from 10^{-14} to 10^{-12} $\text{cm}^2 \text{s}^{-1}$. The second conclusion of this work is that iron influences the OVOC generation and release during UV irradiation of SOA particles. For atmospherically relevant conditions of humidity and iron content (up to 2 % of iron concentration), OVOC release will be slightly enhanced likely due to the efficient photo-degradation of iron carboxylate complexes. The work of Wang et al.³²⁰ indicates that the iron can be highly concentrated in continental aerosol particles near the surface of the Earth. For instance, in Europe the observed concentrations of iron are between $0.1 - 1 \mu\text{g m}^{-3}$ ($\sim 0.8 - 8$ % in molar ratio in SOA). A study from Moffet et al. has shown that in urban outflow, all particles have organic matter dominated by carboxyl functionalities, and, among them, 5 % contain detectable Fe¹². In the technique they used, the detection limit was about 5 % of iron in molar ratio. Saharan dust, urban particles, coal fly ash and oil fly ash contain iron in the range from 3 to 9 % of weight mass⁹⁴. The fraction of soluble Fe in desert dust typically goes from values ~ 0.1 % to up to ~ 80 %³²¹⁻³²³. On the other hand, measurements of dissolved iron in rural or urban atmospheric waters indicate concentrations ranging from 10^{-7} down to 10^{-14} M. Overall, dissolved iron concentrations in aerosol particles vary broadly and range from micromolar up to an upper limit of about 10 %. Our findings point out that OVOC production and release is strongly influenced by iron in iron-containing particles, with the sign and magnitude of the effects being dependent on the concentration and conditions.

5.6 Supporting Information

5.6.1 PTR normalization for different RH

The relative abundance of $\text{H}_3^{18}\text{O}^+$ and $\text{H}_3\text{O}^+(\text{H}_2\text{O})$ in the PTR-ToF-MS ion source changes as a function of *RH* (Table 5). The detect organics react at different rates with H_3O^+ and with $\text{H}_3\text{O}^+(\text{H}_2\text{O})$, making their ionization efficiency *RH*-dependent. We define X_R as the ratio between the reaction rate of an organic molecule with $\text{H}_3\text{O}^+(\text{H}_2\text{O})$ and H_3O^+ . X_R is around 0.48 and 0.58 for acetaldehyde and acetone and in general is 0.5 for organics which do not contain aromatic rings^{311,312}. We consider X_R to be 0.5 for formic acid and acetic acid. Because we are only interested in relative concentrations, we normalized the signal observed at different *RH* to what it would have been at 0 % *RH*:

$$S'_{\text{VOC}}(\text{corrected}) = S'_{\text{VOC}}(\text{measured at } RH) \times \frac{(S_{\text{H}_3\text{O}^+} + X_R S_{\text{H}_3\text{O}^+(\text{H}_2\text{O})})_{0\%RH}}{(S_{\text{H}_3\text{O}^+} + X_R S_{\text{H}_3\text{O}^+(\text{H}_2\text{O})})_{RH}} \quad (37)$$

We checked for the presence of ionic clusters between protonated organic molecules and water. For formic acid, at 25 % *RH* and 40 % *RH* for the signal due to the $[\text{M}+\text{H}+\text{H}_2\text{O}]^+$ cluster was 2 % and 3 %, respectively, of the protonated ion $[\text{M}+\text{H}]^+$. For the rest of the ions, the cluster contribution was below 1 %. Therefore, we do not take clustering into account because it does not affect the signal significantly.

Table 5: Signal of $\text{H}_3^{16}\text{O}^+$ (derived from the signal of $\text{H}_3^{18}\text{O}^+$) and signal of the $\text{H}_3\text{O}^+(\text{H}_2\text{O})$ measured at different RH .

Relative humidity (%)	Signal H_3O^+	Signal $\text{H}_3\text{O}^+(\text{H}_2\text{O})$
0	2.05×10^6	8×10^4
10	2.25×10^6	1.2×10^5
25	2.35×10^6	2.7×10^5
40	2.35×10^6	3.5×10^5
55	2.25×10^6	1.5×10^5
70	2.25×10^6	2×10^5

5.6.2 Modelling

We developed a kinetic multi-layer model of release of volatile compounds from films that explicitly evaluate diffusion and release of volatile compounds from the films to the gas phase, resolving concentration gradients and diffusion throughout the film and release into the gas phase.

$$\frac{\partial C}{\partial t} = D \frac{\partial^2 C}{\partial x^2} \quad (38)$$

The bulk of the film is divided in n layers (numbered 1,2,3,... n) and m columns (numbered 1,2,3,... m) as shown in Fig. 5.8 leading to a mesh of compartments. Each of these compartments exchange mass with the four adjacent ones. For our system we defined the concentration in the gas phase as 0, leading just to release but not uptake. Another boundary condition was to make equal the concentration in the last layer in the three edges to the concentration in the second last layer to be able to apply Eq. 38 in every compartment:

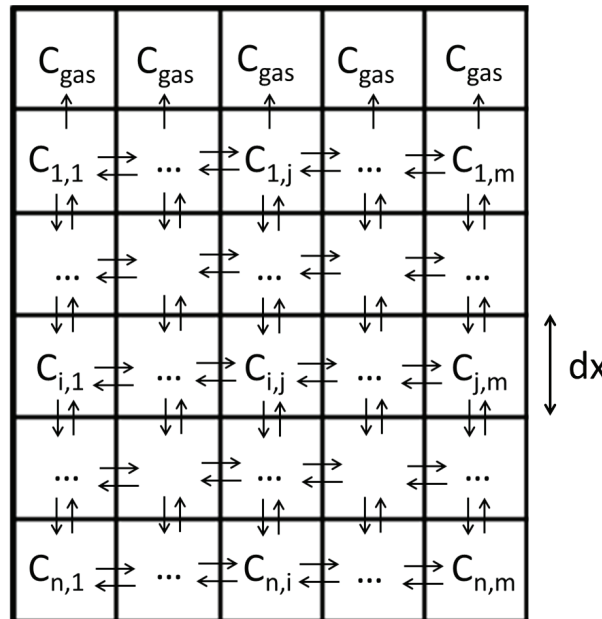


Figure 5.8: Model compartments and layers in which the film is divided. The arrows represent the diffusion that occur between different compartments. The dimension of the compartments is represented by dx .

$$C_{(n,j)} = C(n-1, j) \quad (39)$$

for $j=1,2,\dots,m$

$$C_{(i,1)} = C(i, 2) \quad (40)$$

for $i = 1,2,\dots,n$

$$C_{(i,m-1)} = C(i, m) \quad (41)$$

for $i = 1,2,\dots,n$

Following the diffusion equation Eq. 38, and assuming an initial profile, the mass transport is evaluated in the film by applying Eq. 42 to every cell for a certain number of time intervals which length is defined by dt :

$$C_{(i,t,t)} = C(i, j, t-1) + dt \times D \times (C(i+1, j, t-1) + C(i, j+1, t-1) - 4 \times C(i, j, t-1) + C(i-1, j, t-1) + C(i, j-1, t-1)) / dx/dx \quad (42)$$

We defined a system with $n = 30$ layers and $m = 50$ columns which led to a mesh of 150 compartments. The time interval used for the predictions was 0.1 s extending the predictions up to 200 seconds. We optimized the values of the diffusion coefficients (D) at different RH by fitting the release predicted by the model to the observed decay of acetaldehyde after switching off lights as shown in the main text. We tested the sensitivity of two initial concentration profiles on the diffusion coefficient parameter to reproduce our data: i) uniform initial concentration profile is flat throughout the film and ii) linear initial concentration profile where its maximum concentration is in the bottom of the film and zero at the surface.

6 Chapter 6

Aerosol aging driven by photochemistry of iron citrate

Pablo Corral Arroyo^{1,2}, Peter A. Alpert¹, Jing Dou³, Yanisha Manoharan²,
Saša Bjelić⁴, Josef Dommen⁵, Ulrich Krieger³, Markus Ammann¹

1. Paul Scherrer Institute, Laboratory of Environmental Chemistry, 5232 Villigen PSI, Switzerland.
2. Department of Chemistry and Biochemistry, University of Bern, 2012 Bern, Switzerland.
3. ETH Swiss Federal Institute of Technology Zürich, Institute for Atmospheric and Climate Science, 8006 Zürich, Switzerland.
4. Paul Scherrer Institute, Laboratory of Bioenergy and Catalysis, 5232 Villigen PSI, Switzerland.
5. Paul Scherrer Institute, Laboratory of Atmospheric Chemistry, 5232 Villigen PSI, Switzerland.

The sections from 6.1 to 6.5 are the reproduction of the report of “Aerosol aging driven by photochemistry of iron citrate” by Pablo Corral Arroyo, Peter A. Alpert, Jing Dou, Yanisha Manoharan, Kasia Arturi, Saša Bjelic, Josef Dommen, Ulrich Krieger and Markus Ammann

6.1 Abstract

Aerosol aging refers to oxidative processes that change the physical and chemical properties of atmospheric aerosol particles via a variety of chemical and physical processes both in the gas and in the condensed phase. These specifically also include several multiphase and heterogeneous chemical reactions. Photochemistry can trigger aerosol aging within aerosol particles by promoting production of radicals and more generally reactive oxygen species (ROS). The production of radicals leads to fragmentation, functionalization and oligomerization of organic molecules present in atmospheric aerosol particles, which induces changes in the physical properties such as viscosity and diffusion. We assess the contribution to aerosol aging initiated by the photolysis and degradation of iron carboxylate complexes. We observed changes in the carbon functionalities and in the iron oxidation state upon UV irradiation in single particles containing Fe(III) citrate by means of Scanning Transmission X-ray Microspectroscopy (STXM) experiments. We observed the production of a wide spectrum of compounds and their trend as a function of time upon irradiation in samples containing Fe(III) citrate by means of HPLC-MS analysis, which corroborates our observations in STXM. We measured the photochemical release of OVOCs (acetic acid, acetaldehyde and acetone) from mixtures of FeCit and CA in a Coated Wall Flow Tube reactor for several conditions of iron content and relative humidity by means of Proton Transfer Reaction Mass Spectrometry (PTR-MS). We suspect that oxygen diffusion limitation is occurring in our experiments leading to an anoxic chemistry in the bulk. This may be extremely relevant if it applies to atmospheric aerosol particles in general. We discuss the possible mechanism for some of the major compounds observed.

6.2 Introduction

Aerosol aging involves many processes by which atmospheric aerosol particles change their physical and chemical properties. An important set of contributions is related to oxidation processes driven by uptake of reactive species from the gas phase, gas-particle partitioning of oxidized compounds, and chemical processes initiated within the particle^{6,21,22,68,324}. Aging driven by chemistry within the particle phase include processes such as photochemistry⁶⁶⁻⁶⁸ or radical chemistry⁶⁹. The reactions that induce aging of organic compounds can be separated into fragmentation, oligomerization and functionalization⁵⁷. Over the past years many studies have pointed out the importance of heterogeneous and multiphase chemistry in aerosol aging^{67-69,89,120,171}. Particle phase photochemistry contributes to aerosol aging by multiple mechanisms. Energy-transfer or charge-transfer reactions driven by triplet states of aromatic organic compounds^{10,70,71}, photolysis of nitrate resulting in free radicals⁷², photochemistry of iron carboxylate or free iron²⁰, and photolysis of carbonyls^{73,74,325} are some of the examples of these processes.

Iron is the most abundant transition metal on Earth's continental ground surfaces. It may get mobilized from natural minerals or from anthropogenic materials and pollutants and incorporated into aquatic atmospheric systems such as aerosol particles³²⁶. Iron is emitted into the troposphere as minerals, as amorphous hydroxides, such as Fe(OH)₃, adsorbed on clay minerals, organic matter, or carbonaceous particles or bound in salts. Its release into the aqueous phase may be driven by complexation or acidic dissolution^{94,138}. Iron is well known to form complexes with organic or inorganic ligands, the stability of which depends on the

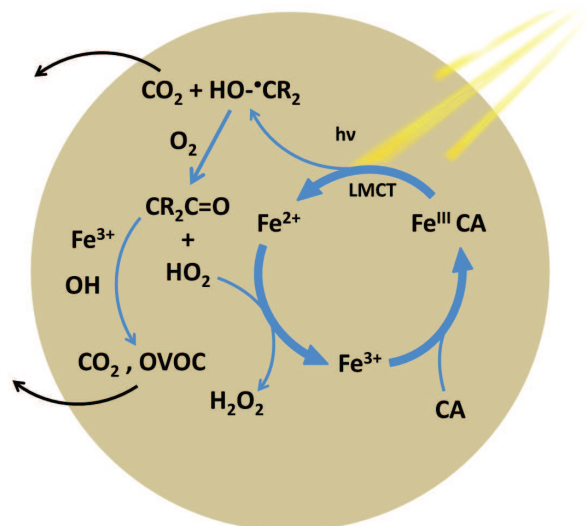


Figure 6.1: Photochemical catalytic cycle of iron-carboxylate complex in a particle. $\text{Fe}^{\text{III}}\text{CA}$ (iron citrate) is photolyzed leading to the reduction of iron to Fe^{2+} and the decarboxylation of the ligand and the production of an organic radical. The latter reacts with oxygen leading to HO_x and a new stable molecule, which can further react with HO_x or by cycling with Fe^{3+} , leading to the decomposition to oxygenated volatile organic compounds (OVOC). HO_2 reduces Fe^{2+} back into Fe^{3+} , which can be complexed again by citric acid.

pH, ionic strength and the concentration of ligands and iron⁹⁴. Dissolved iron is present in atmospheric aerosol particles mainly in the two oxidation states (II) and (III), which may interconvert by various redox processes¹². Some of these complexes are photoactive and allow ligand-to-metal charge transfer (LMCT) reactions. Iron-carboxylate complexes are well known photoactive complexes in atmospheric aerosol particles where they drive LMCT reactions leading to a reduction of Fe(III) to Fe(II) and to the decarboxylation of the ligand and further oxidation processes^{94,162}. These degradation processes are a major sink of carboxylate groups in the aerosol phase in the atmosphere and thus change the chemical composition and lead to the release of volatile organic compounds (VOC)^{20,95,168}. It has also been suggested that this photochemistry might be an important source of reactive oxygen species (ROS) in particulate matter^{94,169,170}. Apart from the health concerns related to ROS, ROS such as HO_2 and OH radicals are key to assess the condensed phase oxidative capacity in aerosols. The main sources of OH in aerosol particles are the reactions between Fe(II) or Cu(I) with H_2O_2 (Fenton reaction), photolysis of nitrate and photolysis of the complex FeOH^{2+} , while phase transfer of OH from the gas phase plays a minor role²². OH radicals react rapidly with organic compounds in the condensed phase producing a broad spectrum of oxidized compounds^{65,69,171}.

The degradation of organic compounds by reactive uptake of OH has recently been studied in some aerosol particles containing organic compounds such as squalene^{69,327}, or citric acid^{65,171}. Functionalization of the compounds in the condensed phase and a decrease in the particle mass due to OVOCs production and release was observed. At low OH exposure, the oxygen content of the organics increases, indicating that functionalization dominates, whereas for more oxidized organics the amount of carbon in the particles decreases, indicating the increasing importance of fragmentation processes. Once the organics are moderately oxidized ($\text{O}/\text{C} = 0.4$), fragmentation completely dominates, and the increase in O/C ratio upon further

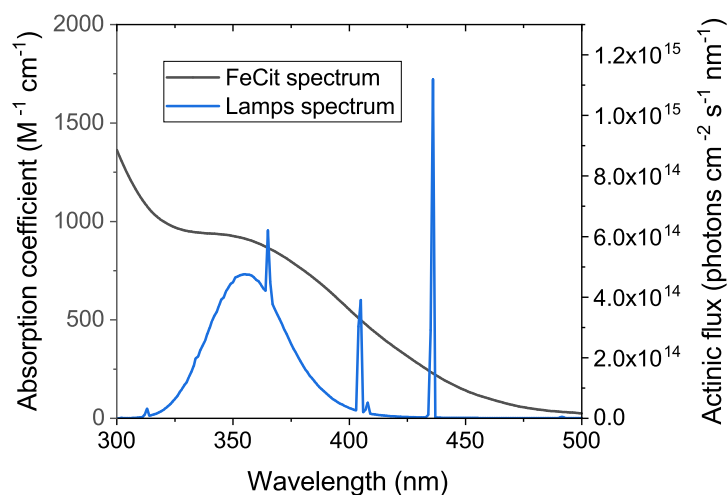


Figure 6.2: Spectrum of absorption of Fe(III) citrate and spectrum of irradiation of the lamps used.

oxidation is due to the loss of carbon rather than the addition of oxygen. The rate of degradation of CA initiated by reactive uptake of OH was observed to increase with RH due to the higher uptake coefficient.

The catalytic cycle of Fe(III) carboxylate complexes is represented in Fig. 6.1 using iron citrate as example. Initially iron complexes absorb radiation in the UV-VIS region and are thus photoreactive through ligand to metal charge transfer reactions (LMCT)¹⁶³, which is an inner sphere electron transfer from the carboxylate functionality to iron. The Fe(III) carboxylate complex is initially excited to a long lived radical complex¹⁶⁴⁻¹⁶⁶, which can dissociate producing Fe(II) and R-COO \cdot radical. The further decarboxylation of the ligand leads to the production of a carbon-centered radical, which reacts further with oxygen producing a peroxy radical (RO $_2\cdot$) (in presence of O $_2$). The peroxy radical may lead to production of HO $_2$ and a new stable carbonyl organic molecule (CR $_2$ C=O). HO $_2$, as well as H $_2$ O $_2$ and OH further produced, can re-oxidize Fe(II) to Fe(III) produced by consecutive iron oxidation steps, maintaining a catalytic cycle (in Fe) and providing an additional OH source. The subsequent degradation of CR $_2$ C=O by HO $_x$ radicals or iron photochemistry will lead to functionalization, oligomerization or fragmentation. The latter process leads to production and release of oxygenated volatile organic compounds (OVOCs) (e.g., acetone) and mass loss. If we take into account that oxygen diffuses in from the gas phase, two different cases may be considered by comparing the diffusion and reaction rates²¹⁶. In the first case, the diffusion of oxygen is much faster than the reaction rate with the reactant present in the bulk (organic radicals in our case), therefore oxygen remains well-mixed over the entire bulk. The second case applies when oxygen diffuses slowly in comparison with the rate of reaction between oxygen and organic radicals. If the second case applies, oxygen will not get throughout the entire bulk and the chemistry may get anoxic from a certain depth in the bulk. The organic radicals will tend to undergo intermolecular reactions or radical recombination. For organic mixtures RH and temperature control the diffusion rate throughout the bulk^{11,64}.

The photolysis of Fe(III) carboxylate complexes leads to direct degradation by radical production and

decarboxylation and additionally the HO_x radicals produced radical-driven degradation. In this work we assess the functionalization, fragmentation and oligomerization resulting from photochemistry of Fe(III) carboxylate complexes. We carry out photochemical experiments within single particles containing Fe-Cit and CA placed in an environmental cell in an X-ray microscope and we performed analysis of extractions of films containing Fe-Cit and CA before and after irradiation with HPLC-OrbiTrap-MS. We assess the OVOCs production by means of irradiating mixtures of FeCit and CA in a Coated Wall Flow Tube reactor and analyzing the outflow with PTR-MS.

6.3 Experimental

STXM/NEXAFS measurements were performed at the PolLux beam line (X07DA) of the Swiss Light Source (SLS) at Paul Scherrer Institute, Switzerland. The end station³²⁸ provides a focused (35 nm) monochromatic X-ray beam to perform chemically resolved imaging. Additional energy calibration of spectra beyond the routine calibration of the beam line was done by comparing the measured lowest energy peak of polystyrene with its literature value (285.18 eV)³²⁹. Raw data are converted from transmission to optical density (OD) by using the LambertBeer law ($OD = \ln(I/I_0) = d\mu$). Here μ is the linear absorption coefficient, d the thickness of the sample, I the transmitted light intensity through the particle and I_0 the incident light intensity. We measured X-ray absorption spectra at the carbon K-shell absorption edge (278 – 320 eV) by line scans and image stack mode, in which a series of images is taken at closely spaced energy steps, yielding spatially resolved spectra³³⁰. The step sizes for the present experiments were 0.6 eV in the range of 278 – 284 eV, 0.15 eV in the range of 284.2 – 292 eV and 0.5 eV in the range of 292.5 – 320 eV, with a dwell time of 2 ms for each energy. We measured X-ray absorption spectra at the iron L-edge absorption edge (700 – 720 eV). By using a parameterization described in Moffet et al¹² we were able to map the Fe(III) molar fraction (ϕ) in single FeCit/CA particles. For the stacks, the spatial resolution was 35 nm \times 35 nm pixels over a rectangular area typically 4 μm^2 . The line scans were made with a line resolution of 35 nm pixel. The UV irradiation was made by means of a LED inserted in the experimental chamber which provided an irradiation of 3 W m^{-2} at 375 nm (5.66×10^{14} photons $\text{cm}^2 \text{s}^{-1}$). Particles containing FeCit and CA (1:1) are exposed to UV light and the lights are then switched off, and then particles are analyzed in the dark during continuous O_2 and RH exposure. In these experiments we aimed to track simultaneously the oxidation state of iron and the carbon evolution. Quantitative analysis by STXM required a relatively high iron concentration.

For experiments related to the condensed phase oxidation processes, a solution of Fe-Cit and CA (1:1) was deposited on the top of a petri dish. This configuration, rather than the coated wall flow tube described further below, was chosen to assure a complete extraction of the sample and low blank values from contaminations. To compare the results with the ones of STXM, we used the same concentration of iron. The solutions were made from fresh solutions of Fe-Cit (0.0305 M) and 1.8 mg of CA in HPLC-MS grade water. The sample was then dried under a gentle flow of N_2/O_2 at 40 % RH . The resulting mixture equilibrated at 40 % RH was exposed to different times of UV light irradiation. The irradiation was made in a reactor with UV lamps (see Fig. 6.2). The extraction was made by a mixture acetonitrile:water (1:1) where vanillin was included as a standard at a fixed concentration. Prior to the analysis, the solutions were filtered (0.22

μm). Carry-over was assessed by a blank run in between each analysis. The injection volume was one μl . The time-resolved separation of the analytes was performed in a Thermo Scientific Dionex™ Ultimate 3000 Series RS system (Thermo Scientific™, Switzerland) including a pump, a column compartment, and an auto-sampler. The used column and pre-column were Thermo Scientific Acclaim™ Organic Acid (150 mm \times 2.1 mm, particle size 3 μm). The following program with mobile phase A (1 vol.% methanol, 1 vol.% acetonitrile and 0.2 vol.% HCOOH in high purity water) and mobile phase B (100 vol.% MeOH) was applied: 1 % B (0 – 1 min) 1 to 40 % B (1-6 min), 40 % B (6 – 8 min), followed by equilibration step and 40 to 1 % B (8 – 8.2 min), 1 % B (8.2 – 10 min). The flow was set to 0.25 ml/min, the temperature of the column was kept constant at $T = 40^\circ\text{C}$. A heated electrospray ionization (ESI) was used for the ionization of the analytes at +3.5 and -2.1 kV spray voltage in positive and negative mode, respectively. Data acquisition was performed using Thermo Scientific Q-Exactive hybrid quadrupole-orbitrap mass spectrometer controlled by Xcalibur 4.1 software. Mass spectra were acquired in full scan mode with an isolation window of 1 m/z from 50 – 750 m/z. The resolution was 70000 at m/z = 200. Raw mass spectral data files were collected in triplicate including a blank between each run. The UHPLC-HRMS data were imported into Compound Discoverer™ 2.1 software (Thermo Scientific, Switzerland) and processed with standard settings except for mass tolerance (set to 2.5 ppm). The composition was predicted based on exact mass and isotopic patterns and evaluated against MS/MS spectra.

The OVOCs release was measured by means of a Proton Transfer Reaction Mass Spectrometer (PTR-MS). Films containing Fe-Cit and CA were prepared in a coated wall flow tube (CWFT) by deposition of a solution of FeCit/CA in the inner part of the flow tube and a homogeneous film by rolling and tilting the flow tube while passing a gentle flow of nitrogen, which was humidified to the RH that was used in the following experiment. The coated tubes were 1.2 cm in inner diameter, 50 cm long (Duran glass) and fitted snugly into the reactor as inserts. The jacketed glass UV reactor held at $T = 25 \pm 1^\circ\text{C}$ was surrounded by 7 fluorescent lamps (UV-A range, Philips Cleo Effect 20 W: 300420 nm, 41 cm, 2.6cm o.d., see Fig. 6.2), leading to J_{NO_2} of 0.011 s^{-1} in the flow tube. Flows of N_2 and O_2 were set by mass flow controllers at 0.8 L/min and 0.2 L/min respectively. While irradiating the reactor, the OVOCs released in the films were analyzed with the PTR-MS (IONICON Analytik GmbH, Innsbruck, Austria).

Chemicals

The chemicals used were iron citrate tribasic (Sigma-Aldrich), citric acid (Sigma-Aldrich), acetonitrile (LC-MS Chromasolv, Aldrich), HPLC-MS grade water (VWR Prolabo Chemicals) and vanillin (Sigma-Aldrich).

6.4 Results

6.4.1 STXM results

Figure 6.3 shows X-ray absorption spectra at the C K-edge region (278 – 320 eV) of particles containing citric acid (black), iron citrate (red) and FeCit/CA (1:1) after 3 hours of UV irradiation in Helium (50 mbar) and oxygen (100 mbar) (blue) and in absence of oxygen (green) at 60 % RH . The background of the averaged pre-edge absorption at 278 – 282 eV was subtracted and all the spectra were normalized by the

averaged post-edge absorption at 305 – 320 eV. The main features are at 286.8 eV and at 288.6 eV, which indicate the absorption of carbonylic and carboxylic groups, respectively. Figure 6.4 shows X-ray absorption spectra at the C K-edge region at only 6 energies (278, 286.8, 288.6, 290.8, 298.4 and 320 eV) of particles containing FeCit/CA (1:1), freshly prepared and after different times of UV irradiation.

Figures 6.3a shows the absorption spectra of CA and Fe-Cit in comparison. The CA spectrum is dominated by the carboxyl peak at 288.6 eV, which appears broader in the Fe-Cit spectrum. Figure 6.3b shows the appearance of new features upon UV irradiation such as the feature at 286.8 eV, corresponding to carbonyl compounds, or the feature at 285.0 eV, corresponding to double bonds. The appearance of a feature at 290.8 eV is a consequence of the exposure of the particles to X-rays, which damages them and generates

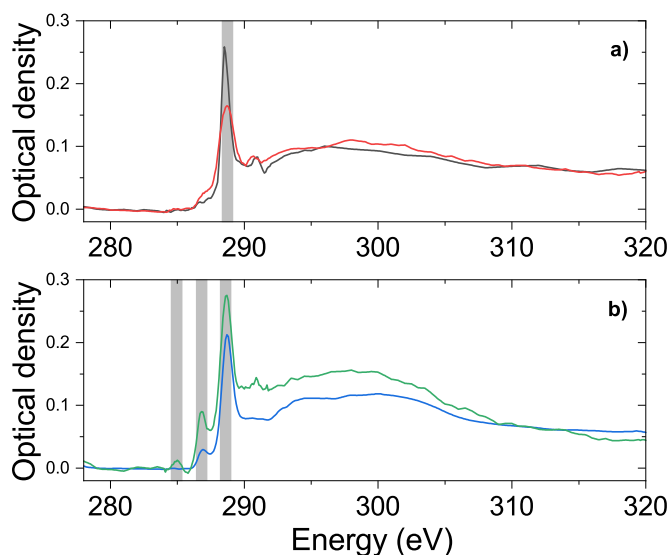


Figure 6.3: C-NEXAFS spectra from 278 eV to 320 eV of particles containing citric acid (black), iron citrate (red) and FeCit/CA (1:1) after 3 hours of UV irradiation in presence (blue) and absence (green) of oxygen. The shady zones correspond with the absorption of double bond, carbonyl and carboxyl compounds at 285.0 eV, 286.8 eV and at 288.6 eV respectively.

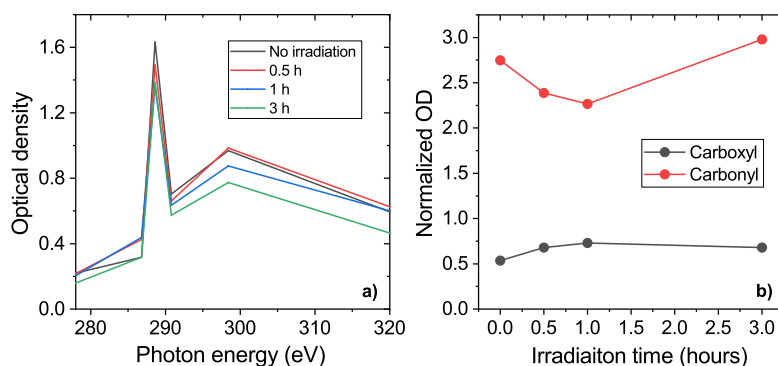


Figure 6.4: 6-Energy spectra of particles containing FeCit/CA (1:1) before (black) and after 0.5, 1 and 3 hours of irradiation (red, blue and green respectively) over the same particles. b) Optical density of the carbonyl (black) and carboxyl (red) peak to the optical density in the post edge (320 eV).

carbonate. Even so, the damage is very low so we do not consider it. We can first conclude that Fe-Cit photochemistry induces the production of new compounds by photolysis and further reaction. We observed that the concentration of carbonyl compounds is higher when the irradiation is made in absence of oxygen while the double bound compounds are only detectable in absence of oxygen. This can be understood by assuming that in presence of oxygen Fe-Cit cycling occurs several times, leading to further CA degradation and also leading to higher generation oxidation products, including OVOC, which can leave the particles. In absence of oxygen, the cycle (Fig. 6.1) presumably is occurring once, but cannot be maintained due to lack of oxidants for Fe(II), and thus later oxidation generations are not formed. Consequently, the organic radicals produced in the first step of photolysis of Fe-Cit can drive radical recombination or intramolecular reactions. The latter can be elimination reactions which may lead to the formation of double bounds³³¹.

Figure 6.4a shows that Fe-Cit photochemistry drives the degradation of citric acid over several hours. The decarboxylation produced by the initial photolysis or Fe^{III}Cit becomes apparent with the continuous depletion of the absorption at 288.6 eV, indicating lower concentration of carboxylate groups. The increase in the absorption at 286.8 eV indicates the production of carbonyl groups upon UV irradiation. The optical density in the post-edge decreases substantially after 3 hours of irradiation due to most likely the release of OVOCs and thus the decrease of mass and of total carbon of the particles. Figure 6.4b shows the optical density of the carbonyl (black) and carboxyl (red) peak normalized to the optical density at the post edge (320 eV). In the first hour of irradiation the main loss in terms of functionalities is driven by the loss of carboxylic compounds, presumably CO₂ and acetic acid, while the carbonyl content increases. From 1 hour to 3 hours of irradiation the carboxyl content increases due to the mass loss of the particles (dominated by release of OVOCs without carboxylic groups) while the carbonyl content decreases most likely due to the higher concentration of C₄ compounds which are precursors of OVOCs (acetone). This is in agreement with HPLC-MS results and OVOCs results shown later below. The decrease of the carbonyl signal after 3 hours of irradiation can be due to the decrease of the total carbon rather than an effective decrease of the carbonyl concentration.

Figure 6.5 shows a map of Fe(III) fraction (ϕ) of particles containing FeCit/CA (1:1 molar ratio) after illumination with UV light (375 nm) over 15 minutes in an atmosphere of 110 mbar of oxygen and 40 % RH. Images of particles reveal that Fe(III) is highly depleted while it is still present near the surface as seen as the colour contrast from blue (more Fe²⁺) to red (more Fe³⁺). O₂ supply into the bulk can have been restricted only to surface layers with a small depth. We calculated the lower limit of the reacto-diffusive length by assuming that the rate coefficient of the reaction between oxygen and the organic radical is $\sim 10^6$ M⁻¹ s⁻¹¹⁵⁵, and that the diffusion coefficient of oxygen in citric acid at 40 % RH is 10⁻¹³ cm² s⁻¹¹¹. If every iron atom leads to a radical (potential concentration of ~ 1 M at the beginning) the reacto-diffusive length ($l = \sqrt{D/k}^{216}$), which is the distance over which O₂ is lost due to the reaction with radicals, would be 0.01 nm .

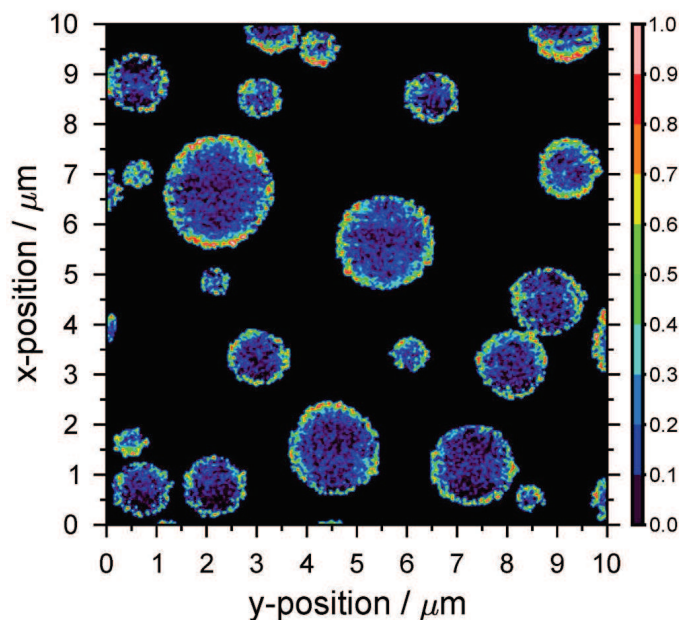


Figure 6.5: Map of FeCit/CA particles (1:1 molar ratio) after illumination with UV light over 15 minutes in an atmosphere of 110 mbar of oxygen and 40 % *RH*. The color scale indicates $(\text{Fe(III)})/(\text{Fe(II)}+\text{Fe(III)})$ and is generated by means of the parameterization described in Moffet et al.¹²

6.4.2 HPLC-MS results

Figure 6.6 shows the signal of CA normalized to vanillin of the extracts of the films containing Fe-Cit and CA (1:1) as a function of irradiation time in hours at 40 % *RH* and in presence of 20 % of oxygen. We observed the decay in the signal of CA upon UV irradiation indicating the degradation rate of CA by photolysis of Fe-Cit, which is in agreement with the depletion of the carboxylic signal observed in STXM.

The life time of iron citrate under our conditions is in the order of half a minute ($j = 0.068 \text{ s}^{-1}$, $\phi \approx 0.28^{168}$). We observed a decrease of approximately half of the initial CA at the first data point after light on, after 1 hour, while a much slower decrease is observed after the first hour. The fraction of CA decaying initially corresponds to the fraction that is attached to Fe(III) forming complexes. Therefore, we suspect that the citrate that is initially forming complexes with Fe(III) is rapidly photolyzed, presumably in the first minutes (taking into account the short life time of iron citrate under our conditions). The slow CA degradation observed afterwards can be explained taking into account that Fe(III) can produce complexes with many new species apart of CA, the equilibrium of Fe(III) - Fe(II) will be shifted to Fe(II) once lights are on, leading to less concentration of photoactive Fe(III) compound, and this equilibrium is depending on the diffusion rate of oxygen into the sample.

Figure 6.7a shows the appearance and temporal evolution of the signal of several products with smaller or equal number of carbon atoms than CA over several hours of UV irradiation. The C_6 compounds come from the functionalization of CA, and C_5 , C_4 and C_3 compounds come from the fragmentation and further reaction following decarboxylation of the citrate ligand after initial photolysis of iron citrate complexes or by the degradation of uncomplexed CA by HO_x radicals generated in the complex degradation. The general

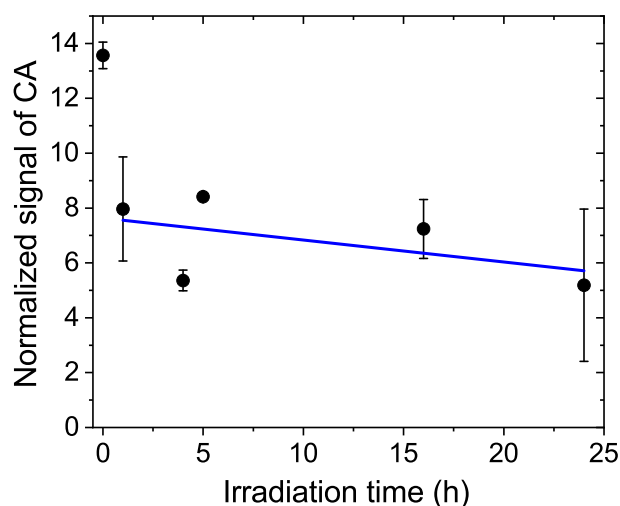


Figure 6.6: Signal normalized to the vanillin of citric acid before and after several hours of UV irradiation. Error bars indicate the standard deviation of 2 – 3 replica experiments. The blue line represents the linear decay from 1 hour to 24 hours of irradiation.

trend is an increase over the first 16 hours of irradiation and a decrease after that, most likely due to further degradation towards OVOCs that leave the sample. We noted that 6 and 5-carbon molecules arise generally earlier than the 4-carbon molecules, which supports the idea of decarboxylation as an important pathway. We detected the rise of compounds coming from one and two decarboxylations of CA, $C_5H_6O_5$ and $C_4H_6O_3$, respectively, which is in agreement with the proposed mechanism (Figure 6.1). As described later, we detected a significant release of acetic acid, which means that some of the C_4 compounds are produced by fragmentation of CA into a C_4 product and acetic acid. The appearance of $C_5H_6O_5$ indicates that the radical produced can be reduced to produce the alcohol. Additionally, other compounds are produced upon

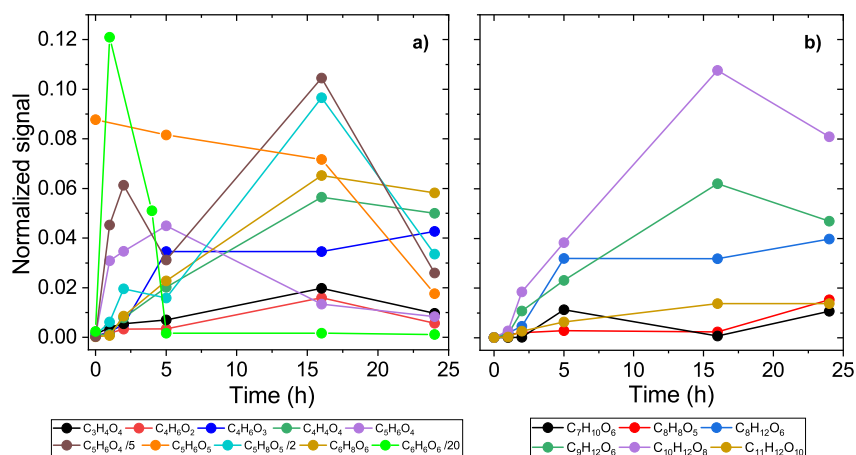


Figure 6.7: Signal normalized to vanillin signal before and after several hours of UV irradiation of a) several products of the decomposition of citric acid in positive mode and b) products bigger than CA.

UV irradiation most likely coming from the degradation of CA and the further degradation of first generation products by HO_x radicals³²⁷. The products of the direct degradation of CA by OH radicals tend to have a larger O:C ratio⁶⁵. We argue that in the degradation of CA observed by Davis and Wilson⁶⁵ the oxidation was mainly occurring at or close to the surface and exclusively initiated by OH radicals, but also in a region which remains accessible to oxygen. Therefore the O:C ratio in the products is expected to be larger than for our system, where radical production occurs throughout the particles, but oxygen is coming from the gas phase side only. The difference in the nature of the compounds can be due to oxygen diffusion limitations leading to a chemistry where HO_x do not play a major role. Therefore, we suspect that the main source of oxidation of the products we observed in this work is not the reaction with OH radicals but photolysis or reaction with HO_2 , H_2O_2 or peroxy radicals.

Because of the formation of certain compounds with double bonds observed in STXM experiments under irradiation in absence of oxygen and the presence of $\text{C}_6\text{H}_6\text{O}_6$ (likely a double bond compound) in the extracts of films exposed to radiation in presence of oxygen, we suspect that oxygen cannot enter and diffuse fast enough in the sample leading to anoxic conditions within the sample. This is supported by the presence of $\text{C}_4\text{H}_6\text{O}_2$ (see mechanism in Fig. 6.7). Diffusion limitation of oxygen is also supported by the fact that citric acid is not further degraded rapidly after one hour of irradiation (Fig. 6.2) because the lack of oxygen makes the catalytic cycle run slowly. The thin oxygen rich layer is of course also apparent from the Fe(III) fraction only being high at the outermost surface as observed by STXM.

Figure 6.7b shows the appearance and increase of the signal of several products larger than CA, which resemble oligomerization products (from accretion chemistry), over several hours of irradiation. These compounds most likely come from the recombination of radicals produced in the condensed phase. These oligomerization compounds tend to appear later than the smaller products, which can be explained by assuming that the whole range of smaller compounds must be produced first in order to produce larger compounds with 7 to 11 carbon atoms. The decrease after 24 hours of irradiation is not as relevant as for the degradation compounds. Though, the concentration of some compounds slightly decreases from 16 hours to 24 hours of irradiation. The radicals that presumably react in a termination reaction to produce these oligomerization products can react rapidly with oxygen. Therefore, the presence of these compounds is another indication of the presumably anoxic conditions in the bulk.

We detected the presence of poly-iron complexes such as $\text{Fe}_2\text{C}_{11}\text{H}_{16}\text{O}_{19}$ and $\text{Fe}_3\text{C}_{18}\text{H}_{19}\text{O}_{26}$ ¹⁶⁸. Higher viscosity possibly induced by these compounds may lead to lower diffusivity of oxygen and thus an even

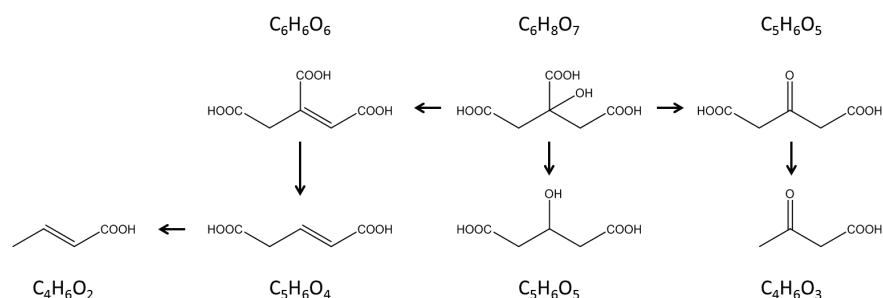


Figure 6.8: Proposed mechanism of degradation of citric acid by FeCit photochemistry.

smaller reacto-diffusive length, and thus an even larger volume fraction remaining under anoxic conditions. OVOCs measurements

6.4.3 PTR-MS results

We observed the release of several compounds, of which acetic acid, acetaldehyde and acetone were the ones with the largest release. We observed steady-state release for acetic acid and acetaldehyde during irradiation, while the release of acetone increased as a function of time for all the experiments. Figure 6.9a shows the steady state release of acetic acid and acetaldehyde from films loaded with FeCit and CA at 30 % RH and 20 % O_2 while irradiating with UV light as a function of FeCit. The content of CA was always 25 mg and the content of FeCit varied from 0 to 4 mg. We noted that the release of both OVOCs is not dependent on the iron concentration above a FeCit/CA ratio of 0.03. Figure 6.9b shows the steady-state release of acetic acid from films containing FeCit and CA (1 mg and 25 mg, respectively, with molar ratio of 0.03) upon UV irradiation as a function of RH . The release of acetic acid increases with RH from 10 % RH up to 60 % RH .

Because we observed steady-state behavior for the release of acetic acid and acetaldehyde we suspect that these are products of fragmentation by HO_x or by photolysis and not from the gradual degradation by Fe(III) carboxylate complexes photochemistry. In the latter case, we would have observed a gradual increase of the release of OVOCs. Therefore, the production of acetic acid and acetaldehyde depends on the HO_x produced and, thus, the oxygen content in the sample. Based on the results shown in Fig. 6.9a, we suspect that HO_x radicals can lead to the formation of OVOCs and react further with them, and therefore, the concentration of OVOCs is constant with increasing concentration of HO_x . The increase in the release rate of acetic acid with RH (Fig. 6.9b) can be explained by an increase in the diffusion coefficient of acetic acid. Figure 6.10 shows the release of acetone from films containing FeCit/CA at molar ratios of 0.03, 0.06, 0.09

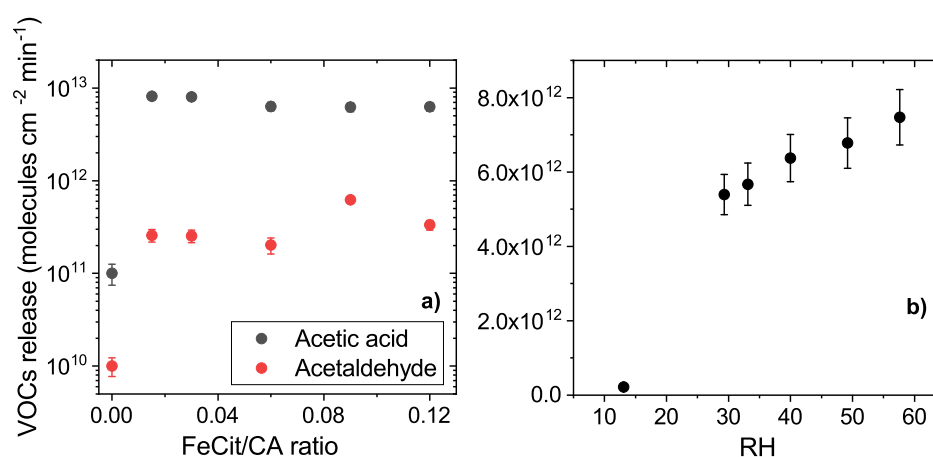


Figure 6.9: a) Steady state release of acetic acid and acetaldehyde from films loaded with FeCit and CA at 30 % RH while irradiating UV light as a function of FeCit content keeping constant the CA content. b) Steady state release of acetic for films containing FeCit and CA from films loaded with FeCit and CA ($\chi=0.03$) while irradiating UV light as a function of RH .

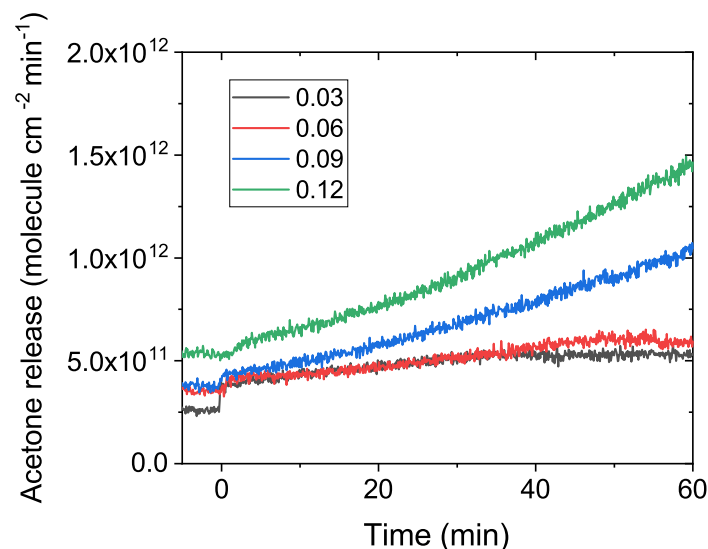


Figure 6.10: Acetone release from films containing FeCit/CA with different molar ratios as a function of time at 30 % *RH*.

and 0.12 at 30 % *RH*. Its release increases as a function of time and the increase is proportional to the concentration of FeCit in the sample. This indicates that acetone is a product of consecutive decarboxylations of CA. Because acetone is a third generation compound (three decarboxylations needed), the population of its second generation precursor ($C_4H_6O_3$) builds up in the films with time, and therefore the production and release of acetone also increases over time. This is in agreement with the findings in the HPLC-MS analysis, which indicate that the concentration of the C_4 compounds increase over several hours. This explains the increasing carbonyl loss observed in STXM experiments.

6.5 Conclusions

Our results reveal that iron carboxylate photochemistry induces aging by fragmentation, functionalization and oligomerization producing a wide spectrum of compounds. This chemical evolution of aerosol particles containing these compounds can potentially induce changes in the physical properties of the particles such as viscosity or absorption. We observed products of the photolysis of Fe(III) citrate but also products coming from radical chemistry and/or direct photolysis of the compounds produced. This photochemistry needs to be investigated in more detailed to better understand how it influences the physical properties of aerosol particles. We suggested that that the system can run into anoxic conditions in the bulk as a result of oxygen diffusion limitations changing the chemistry and the resulting compounds. When this applies to atmospheric aerosol particles, the chemistry driven in the bulk will extremely depend on the diffusion of oxygen within particles. The anoxic conditions lead to different chemical evolution of the particles such as the production of unsaturated compounds, as our HPLC and STXM results show, where HO_x chemistry plays a minor role. The release of OVOCs appears to be greater under humid conditions than under dry conditions due to the limitations of oxygen to get into the bulk and due to the changes in the diffusivity of the OVOCs themselves.

7 Conclusions and outlook

7.1 Conclusions

Brown carbon and iron carboxylate complexes are chromophores present in atmospheric aerosol particles that photochemically trigger radical reactions, which induce the production of HO_x radicals and the subsequent oxidation and secondary radical and non-radical processes, which contribute to aerosol aging. The products resulting from these processes include oxygenated volatile organic compounds (OVOCs), functionalization and oligomerization products. The overarching goal of this thesis has been to understand the feedbacks between indirect photochemical radical production and aging triggered by chromophores mentioned above within atmospheric aerosol particles and the physical properties of those particles such as diffusion or viscosity.

The HO₂ radical production and release photochemically induced by BrC have been assessed by HO₂ release measurements by using IC, BPh and BBA as proxies of photosensitizers forming excited triplet states, which act as oxidants towards organic aerosol components. Comparable HO₂ release was also observed from iron citrate initiated photochemistry. It has been demonstrated that the contribution of this photochemistry to the sources of HO₂ in the gas phase of the atmosphere is less relevant for polluted regions but it may be more important in unpolluted regions under biogenic influences, in twilight or at high latitudes when less UV for traditional radical production or direct photolysis is available and gas-phase radical production rates are lower.

It was demonstrated that the presence of triplet-scavenging, partially oxygenated organic H atom donors in the condensed phase can substantially contribute to the organic and HO₂ radical production, by scavenging triplet states of BrC faster than more oxidized organic compounds, such as citric acid. In a similar way, the excited triplet states act as a sink to drive reactive uptake of H atom donors, such as limonene, from the gas phase, and thereby promote the aerosol growth. The predicted OH production in the condensed phase by other, traditional, sources is around 15 M day⁻¹²². Uptake of HO_x radicals from the gas phase amounts to about 1 M day⁻¹. The upper limit of indirect photochemical HO₂ production is around 20 M day⁻¹. Therefore, the triplet induced radical production clearly outcompetes the traditional condensed phase radical sources and also radical uptake from the gas phase. Simultaneously, the HO₂ produced from triplet scavenging is in turn scavenged by the same organic compounds, hence preventing the release of HO₂ into the gas phase (as mentioned above), but keeping the oxidative capacity within aerosol particles.

In this thesis, also the influence of halides on the photosensitized chemistry of BrC was studied. It was established previously that halides act as electron donor towards triplet states¹⁹⁵. Therefore, halides can promote the organic and HO₂ radical production in a similar way as organic donors. Additionally, halogen radicals and molecular halogens are produced, which can be recycled into halides by HO₂ with an efficiency up to around 50 % therefore reducing the oxidative capacity in the aerosol phase. In turn, the other 50 % are released to the gas phase in the form of molecular halogen compounds. Using the example of iodine, it has been demonstrated that this photosensitized halogen activation is comparable to or larger than halogen activation by oxidation of iodide by ozone in aerosol particles, when the reactive uptake is low

due to diffusion limitations, as is the case in sea-spray derived organic-rich aerosol particles transported to the free troposphere.

A complex dependence of the photosensitized chemistry and radical production and release with RH was observed. This complexity comes from the interplay between the changes in diffusion, intersystem crossing, radical reaction rates and a possible photosensitized surface reaction upon water content changes. In all systems investigated, radical production increased from dry to medium RH conditions, reaching a maximum in the range 50 – 60 % RH , which was attributed to increasing diffusivity of all reactants and products. Also the release of OVOC products from iron citrate induced citric acid degradation and from iron doped limonene SOA increased similarly. The decrease of photochemical turnover at higher RH was generally larger than expected from the effect of dilution of reactions with increasing water activity and may be related to complex water activity-dependent reaction mechanisms not considered so far.

We observed the carbon chemical evolution and iron speciation under UV irradiation of samples containing Fe(III) citrate and citric acid including the degradation of carboxylate groups by direct photolysis of Fe(III) carboxylate complexes and the HO_x radical chemistry triggered by the photolysis of Fe(III) carboxylate complexes. We also observed gradients in the iron oxidation state in single particles after irradiation, which indicates the existence of oxygen diffusion limitations. We conclude that Fe(III) carboxylate photochemistry can contribute to aerosol aging and potentially to changes in the physical properties of aerosol particles such as diffusion, viscosity or absorption. The products detected together with the iron speciation maps after irradiation point out to oxygen diffusion limitations within atmospheric particles aerosol which would induce an anoxic region in the bulk beyond the reacto-diffusive length of oxygen. Generalizing from the special case of the study cases with either high photosensitizer or high iron citrate concentrations, we could use the assessment of OH production for well-established OH sources for aqueous tropospheric aerosol particles, 15 M/day from Tilgner et al. (2013)²². We could assume that each organic radical resulting from reaction with OH is able to scavenge oxygen. An upper limit concentration of oxygen in atmospheric aerosol particles is around 10^{-3} M. Then, the first order decay rate of oxygen would be 5.9 s^{-1} . Assuming a diffusion coefficient of about $10^{-12} \text{ cm}^2 \text{ s}^{-1}$ for oxygen¹¹, the reacto-diffusive length ($l = \sqrt{D/k^{216}}$) would be about 40 nm. By the support of our results, we claim the existence of anoxic region in the bulk of atmospheric aerosol particles in full sun light.

In order to address the impact of iron complex chemistry in a more realistic organic aerosol matrix, the OVOC release was measured, produced by photolysis and the subsequent HO_x chemistry, while irradiating SOA produced by the oxidation of limonene by ozone as a function of iron content and RH . We noted that the presence of iron in low concentrations (~ 4 %) can promote the OVOC production and release most likely due to the production of carboxylate complexes. On the other hand, high concentrations of iron produce a drop in the OVOC release. At high iron concentration, a larger fraction of iron may form less stable complexes in the SOA matrix. Therefore HO_x radical chemistry can be shut down by cycling between Fe(II) and Fe(III). The OVOC release increases from dry conditions to 55 % RH by a factor of 4 most likely due to the faster diffusion of oxygen inside the samples and the subsequent increase of the HO_x production due to photolysis. A diffusion model built by fitting the output of the model to the data demonstrates an increase of the diffusion coefficient of organic molecules along with the increase in the RH . We conclude

that the potential mass loss induced by photochemistry in SOA is around 4 % per day, which is a factor of 4 larger than the mass loss calculated by previous work at dry conditions²⁹⁹.

7.2 Outlook

In this work photosensitized HO₂ production has been identified as a relevant contribution to the gas and condensed phase radical sources. A better knowledge of the composition of atmospheric aerosol particles is required to better assess these contributions. The existence of radical recycling has been demonstrated to exist for photosensitized chemistry in presence of halides and the importance of the halogen activation deriving from it, especially in low-diffusion systems. Further experiments varying *RH* are required to better understand the influence of diffusion and viscosity on halogen activation. The dependence of photosensitized radical production and aerosol aging on relative humidity has been investigated. Even so, due to the complexity of the interplay of several properties changing upon change in relative humidity, further and simpler experiments are required. The aging induced by iron complex photochemistry in terms of OVOCs release, functionalization and oligomerization has been investigated as well as the changes in the iron oxidation state. The production of a broad spectrum of compounds and gradients in the iron oxidation state were observed, which indicates the existence of oxygen diffusion limitations. Further experiments are suggested below. The implications of the processes on human health should be considered, since the production of reactive oxygen species (ROS) in particles or their potential to produce them is relevant for the health effects of inhaled particles.

The main experiments in the chapters 2, 3 and 4 are HO₂ radical release measurements from mixtures containing photosensitizers and by evaluating this data and building a model, we could indirectly obtain information about the radical and triplet production in the condensed phase. In order to get a better and more systematic insight into that, we point out to the need of measurements of photochemical production of radicals within the condensed phase, for example with condensed-phase scavengers. Such experiments would be helpful to corroborate or adjust our models and to understand the atmospheric implications taken from them. In this work the HO₂ measurements have been done by scavenging of HO₂ by NO. In order to discard interferences coming from the reaction between RO₂ radicals with NO in the condensed phase or other radical processes involving NO³³², direct measurements of HO₂ radical such as the ones performed by Vincent et al.³³³ above titania samples in the gas phase could be attempted in the future.

In this thesis it has been shown that BrC photochemistry can contribute significantly to the aerosol growth. Even so, other studies point out that this contribution is tiny³³⁴. At the same time, it was observed that the photolysis of SOA material produces OVOC, the release of which induces mass loss. Further studies should be done to assess these two effects of photochemistry in SOA particles.

It has been shown that the dependence of photochemical radical production and release on *RH* is very complex, because diffusion, viscosity, oxygen solubility and water content change together while changing *RH*. Water content influences the rate coefficient of radical reactions and viscosity can influence the intersystem crossing efficiency. Oxygen plays an important role in photosensitized chemistry since it induces HO₂ radical production and deactivates triplet states. Changes in the oxygen diffusion and solubility induce

changes in HO₂ production and triplet states quantum yields. In terms of photochemistry, the interplay of these processes makes understanding the feedbacks between photochemistry and physical properties a challenging task. Therefore future studies should be focused on taking apart these effects to better understand each effect separately.

The model systems studied here are idealized systems with comparatively high photosensitizer concentrations. There are some studies about the concentration of triplets in environmental waters. The steady-state triplet states concentration in surface waters has been estimated by McNeill and Canonica (2016)¹¹⁷ from 10⁻¹⁴ to 10⁻¹². M. Kaur and Anastasio (2018)²⁷² showed that the steady-state triplet states concentration in bulk fog water goes up to 10⁻¹³ M. They also suggested that triplet excited states can be the dominant aqueous oxidants for organic compounds such as phenols from biomass combustion. The concentration of triplet states in the aerosol phase are so far unknown. Therefore, future studies should look at it, for example collecting natural samples of SOA and measuring the single oxygen production³³⁵. Field campaigns are also needed to assess the organic content of aerosol particles and its reactivity against triplet states and radicals. With this information we may become able to accurately predict the radical production and recycling within aerosol particles.

It has been showed that the efficiency in the release of photosensitized production of halogens is *RH* dependent due to the efficiency in the different release rate of HO₂ and X₂ at different diffusive properties. It has been also showed that photosensitized halogen activation can compete with non-photochemical halogen activation pathways triggered by reactive uptake of an oxidant at low enough *RH*. Since the measurements were performed just for iodine, future studies should assess bromine and chlorine activation from photosensitized chemistry in aerosol particles. I suggest that future studies should include this new photosensitized halogen activation pathway in atmospheric models to precisely assess the contribution of it as well as to better understand the halogen radical recycling that take place in aerosol particles. Additionally, we assessed the influence of *RH* on photosensitized halogen activation and recycling by means of the outcome of our model taking into account that just diffusion changes with *RH*. Since other aspects can change with *RH* apart from diffusion, I suggest to experimentally investigate the influence of *RH* on photosensitized halogen activation and recycling. I also suggest to assess the contribution of photosensitized halogen activation to the sources of reactive halogen species (RHS) and, therefore, to the climate. The iron-containing samples used in chapter 5 were made by adding a certain volume FeCl₃ solution to the SOM. We did not observe any indication of not well-mixed mixtures but we cannot ensure they were. Therefore, I suggest that future studies should be done by producing particles from solutions of SOM material and dissolved Fe(III) or using FeCl₃ seed particles and condense SOM on them.

We investigated the carbon evolution in iron citrate samples during irradiation by the analysis of the extracts of irradiated bulk samples with HPLC-MS. Performing these experiments online by using, for example, an Aerosol Mass Spectrometer (AMS) and irradiating iron citrate aerosols would provide better time resolution. Though the range of detectable species or species families depends on the ionization scheme.

It has been demonstrated that oxygen diffusion limitation occurs within our iron citrate aerosol particles just by the scavenging of oxygen by radicals in highly-viscous particles, which changes the chemical evolution by aging. Our discussion was focused on the difference in the iron oxidation state from the surface and the

bulk. Additionally we could detect products (HPLC) and new functionalities (STXM) coming presumably from anoxic chemistry. Changes in composition can alter the physical properties such as surface tension, hygroscopicity or size. It would be intriguing to study the influence of the presence of these compounds on condensation of clouds, ice nucleation or absorption. Radicals (organic or HO_x) may accumulate in the bulk since oxygen may not be present there, which can have a great impact on the internal chemical processes and potentially human health. I suggest to investigate the production of organic radicals and distribution within single particles by STXM as a direct confirmation of the oxygen diffusion limitations. This can be accomplished by magnetizing the sample and utilizing X-rays with variable polarity while observing differences in X-ray absorption, commonly known as circular dichroism. In addition, future STXM studies could be focused on the difference in the iron oxidation state profile at different humidities and its evolution as a function of time. Breathing illuminated particles containing chromophores can lead to the release of radicals in our lungs and subsequent oxidative stress. I suggest the study and assessment of this topic.

I also suggest to further explore the suggested feature of anoxic radical chemistry. The present experiments were dealing with fairly high radical production rates, which may indeed induce mass transport limitations for oxygen in viscous particles. Further experiments need to explore this further for example with natural samples to know whether and under which conditions oxygen transport limitations are possible. These goals can be achieved by measurement of environmental persistent radicals as a function of oxygen exposure or by carefully analyzing the composition of aerosol particles and recognize products coming from anoxic radical chemistry. Relative humidity in the atmosphere³³⁶ and the viscosity of atmospheric aerosol particles⁶ should be used to assess the oxygen diffusion limitation on atmospheric aerosol particles. The consequences of these findings should be assessed precisely in terms of aerosol aging and public health.

8 References

References

- [1] Q. Zhang, J. L. Jimenez, M. R. Canagaratna, J. D. Allan, H. Coe, I. Ulbrich, M. R. Alfarra, A. Takami, A. M. Middlebrook, Y. L. Sun, K. Dzepina, E. Dunlea, K. Docherty, P. F. DeCarlo, D. Salcedo, T. Onasch, J. T. Jayne, T. Miyoshi, A. Shimono, S. Hatakeyama, N. Takegawa, Y. Kondo, J. Schneider, F. Drewnick, S. Borrmann, S. Weimer, K. Demerjian, P. Williams, K. Bower, R. Bahreini, L. Cottrell, R. J. Griffin, J. Rautiainen, J. Y. Sun, Y. M. Zhang and D. R. Worsnop, *Geophys. Res. Lett.*, 2007, **34**, L13801.
- [2] IPCC, in *Climate Change 2013: The Physical Science Basis. Contribution of Working Group I to the Fifth Assessment Report of the Intergovernmental Panel on Climate Change*, ed. T. Stocker, D. Qin, G.-K. Plattner, M. Tignor, S. Allen, J. Boschung, A. Nauels, Y. Xia, V. Bex and P. Midgley, Cambridge University Press, Cambridge, United Kingdom and New York, NY, USA, 2013, pp. 1523–1535.
- [3] M. M. Galloway, P. S. Chhabra, A. W. H. Chan, J. D. Surratt, R. C. Flagan, J. H. Seinfeld and F. N. Keutsch, *Atmos. Chem. Phys.*, 2009, **9**, 3331–3345.
- [4] G. Yu, A. R. Bayer, M. M. Galloway, K. J. Korshavn, C. G. Fry and F. N. Keutsch, *Environ. Sci. Technol.*, 2011, **45**, 6336–6342.
- [5] C. J. Kampf, R. Jakob and T. Hoffmann, *Atmos. Chem. Phys.*, 2012, **12**, 6323–6333.
- [6] M. Shiraiwa, M. Ammann, T. Koop and U. Poschl, *P. Natl. Acad. Sci. USA*, 2011, **108**, 11003–11008.
- [7] T. Koop, J. Bookhold, M. Shiraiwa and U. Poschl, *Physical Chemistry Chemical Physics*, 2011, **13**, 19238–19255.
- [8] S. Canonica, U. Jans, K. Stemmler and J. Hoigné, *Environ. Sci. Technol.*, 1995, **29**, 1822–1831.
- [9] C. George, R. S. Strekowski, J. Kleffmann, K. Stemmler and M. Ammann, *Faraday Discuss.*, 2005, **130**, 195.
- [10] K. Z. Aregahegn, B. Nozière and C. George, *Faraday Discuss.*, 2013, **165**, 123.
- [11] D. M. Lienhard, A. J. Huisman, D. L. Bones, Y. F. Te, B. P. Luo, U. K. Krieger and J. P. Reid, *Phys. Chem. Chem. Phys.*, 2014, **16**, 16677–83.
- [12] R. C. Moffet, H. Furutani, T. C. Rdel, T. R. Henn, P. O. Sprau, A. Laskin, M. Uematsu and M. K. Gilles, *J. Geophys. Res. Atmos.*, 2012, **117**, n/a–n/a.
- [16] B. H. J. Bielski, D. E. Cabelli, R. L. Arudi and A. B. Ross, *J. Phys. Chem. Ref. Data*, 1985, **14**, 1041–1100.
- [13] D. M. Bartels and S. P. Mezyk, *J. Phys. Chem.*, 1993, **97**, 4101–4105.
- [14] D. L. Baulch, J. Duxbury, S. J. Grant and D. C. Montague, *J. Phys. Chem. Ref. Data*, 1981, **10**, 1–721.
- [15] R. Bianchini and C. Chiappe, *J. Org. Chem.*, 1992, **57**, 6474–6478.
- [17] K. Ishigure, H. Shiraiishi and H. Okuda, *Radiat. Phys. Chem.*, 1988, **32**, 593–597.
- [18] M. Morrison, G. S. Bayse and A. W. Michaels, *Anal. Biochem.*, 1971, **42**, 195–201.
- [19] I. Wagner and H. Strehlow, *Ber. Bunsen. Phys. Chem.*, 1987, **91**, 1317–1321.
- [20] C. Weller, A. Tilgner, P. Brauer and H. Herrmann, *Environ. Sci. Technol.*, 2014, **48**, 5652–9.

- [21] H. Herrmann, T. Schaefer, A. Tilgner, S. A. Styler, C. Weller, M. Teich and T. Otto, *Chem. Rev.*, 2015, **115**, 4259–4334.
- [22] A. Tilgner, P. Brauer, R. Wolke and H. Herrmann, *J. Atmos. Chem.*, 2013, **70**, 221–256.
- [23] O. Boucher, D. Randall, P. Artaxo, C. Bretherton, G. Feingold, P. Forster, V.-M. Kerminen, Y. Kondo, H. Liao, U. Lohmann, P. Rasch, S. K. Satheesh, S. Sherwood, S. B. and Z. X.-Y., in *Climate Change 2013: The Physical Science Basis. Contribution of Working Group I to the Fifth Assessment Report of the Intergovernmental Panel on Climate Change*, ed. S. Fuzzi, J. Penner, V. Ramaswamy and C. Stubenrauch, Cambridge University Press, Cambridge, United Kingdom and New York, NY, USA, 2013, ch. 8. Clouds and Aerosols, pp. 571–657.
- [24] D. Fowler, K. Pilegaard, M. A. Sutton, P. Ambus, M. Raivonen, J. Duyzer, D. Simpson, H. Fagerli, S. Fuzzi, J. K. Schjoerring, C. Granier, A. Neftel, I. S. A. Isaksen, P. Laaj, M. Maione, P. S. Monks, J. Burkhardt, U. Daemmgen, J. Neiryneck, E. Personne, R. Wichink-Kruit, K. Butterbach-Bahl, C. Flechard, J. P. Tuovinen, M. Coyle, G. Gerosa, B. Loubet, N. Altimir, L. Gruenhage, C. Ammann, S. Cieslik, E. Paoletti, T. N. Mikkelsen, H. Ro-Poulsen, P. Cellier, J. N. Cape, L. Horvath, F. Loreto, U. Niinemets, P. I. Palmer, J. Rinne, P. Misztal, E. Nemitz, D. Nilsson, S. Pryor, M. W. Gallagher, T. Vesala, U. Skiba, N. Brüeggemann, S. Zechmeister-Boltenstern, J. Williams, C. O’Dowd, M. C. Facchini, G. de Leeuw, A. Flossman, N. Chaumerliac and J. W. Erisman, *Atmos. Environ.*, 2009, **43**, 5193–5267.
- [25] WHO, *Review of evidence on health aspects of air pollution REVIHAAP project*, World Health Organisation, WHO, 2013.
- [26] A. Grini, C. S. Zender and P. R. Colarco, *Geophys. Res. Lett.*, 2002, **29**, 4.
- [27] A. S. Zakey, F. Solmon and F. Giorgi, *Atmos. Chem. Phys.*, 2006, **6**, 4687–4704.
- [28] Q. Han and C. S. Zender, *J. Geophys. Res-Atmos.*, 2010, **115**, 11.
- [29] L. Chao, M. N. M. and del Corral John, *J. Geophys. Res.*, 2003, **108**,.
- [30] J. M. Prospero, *Hum. Ecol. Risk Assess.*, 1999, **5**, 471–479.
- [31] H. Maring, D. L. Savoie, M. A. Izaguirre, L. Custals and J. S. Reid, *J. Geophys. Res-Atmos.*, 2003, **108**, 6.
- [32] P. Ginoux, M. Chin, I. Tegen, J. M. Prospero, B. Holben, O. Dubovik and S. J. Lin, *J. Geophys. Res-Atmos.*, 2001, **106**, 20255–20273.
- [33] A. Karanasiou, N. Moreno, T. Moreno, M. Viana, F. de Leeuw and X. Querol, *Environ. In.*, 2012, **47**, 107–114.
- [34] J. M. Prospero, P. Ginoux, O. Torres, S. E. Nicholson and T. E. Gill, *Rev. Geophys.*, 2002, **40**, 31.
- [35] F. Solmon, M. Mallet, N. Elguindi, F. Giorgi, A. Zakey and A. Konare, *Geophys. Res. Lett.*, 2008, **35**, 6.
- [36] C. Zhao, X. Liu and L. R. Leung, *Atmos. Chem. Phys.*, 2012, **12**, 3717–3731.
- [37] P. K. Quinn, D. B. Collins, V. H. Grassian, K. A. Prather and T. S. Bates, *Chem. Rev.*, 2015, **115**, 4383–4399.
- [38] J. W. Fitzgerald, *Atmos. Environ. A-Gen.*, 1991, **25**, 533–545.
- [39] D. C. Blanchard, *Science*, 1964, **146**, 396–397.
- [40] J. T. Hardy, *Prog. Oceanogr.*, 1982, **11**, 307–328.
- [41] R. Jaenicke, *Science*, 2005, **308**, 73–73.
- [42] N. Lang-Yona, K. Dannemiller, N. Yamamoto, N. Burshtein, J. Peccia, O. Yarden and Y. Rudich, *Atmos. Chem. Phys.*, 2012, **12**, 2681–2690.

- [43] F. Bianchi, J. Trostl, H. Junninen, C. Frege, S. Henne, C. R. Hoyle, U. Molteni, E. Herrmann, A. Adamov, N. Bukowiecki, X. Chen, J. Duplissy, M. Gysel, M. Hutterli, J. Kangasluoma, J. Kontkanen, A. Kurten, H. E. Manninen, S. Munch, O. Perakyla, T. Petaja, L. Rondo, C. Williamson, E. Weingartner, J. Curtius, D. R. Worsnop, M. Kulmala, J. Dommen and U. Baltensperger, *Science*, 2016, **352**, 1109–1112.
- [44] J. R. Odum, T. Hoffmann, F. Bowman, D. Collins, R. C. Flagan and J. H. Seinfeld, *Environ. Sci. Technol.*, 1996, **30**, 2580–2585.
- [45] M. Claeys, B. Graham, G. Vas, W. Wang, R. Vermeylen, V. Pashynska, J. Cafmeyer, P. Guyon, M. O. Andreae, P. Artaxo and W. Maenhaut, *Science*, 2004, **303**, 1173–1176.
- [46] S. Gao, M. Keywood, N. L. Ng, J. Surratt, V. Varutbangkul, R. Bahreini, R. C. Flagan and J. H. Seinfeld, *J. Phys. Chem. A*, 2004, **108**, 10147–10164.
- [47] M. L. Walser, Y. Desyaterik, J. Laskin, A. Laskin and S. A. Nizkorodov, *Physical Chemistry Chemical Physics*, 2008, **10**, 1009–1022.
- [48] H. J. L. Forstner, R. C. Flagan and J. H. Seinfeld, *Environ. Sci. Technol.*, 1997, **31**, 1345–1358.
- [49] J. D. Surratt, S. M. Murphy, J. H. Kroll, N. L. Ng, L. Hildebrandt, A. Sorooshian, R. Szmigielski, R. Vermeylen, W. Maenhaut, M. Claeys, R. C. Flagan and J. H. Seinfeld, *J. Phys. Chem. A*, 2006, **110**, 9665–9690.
- [50] R. J. Charlson, J. E. Lovelock, M. O. Andreae and S. G. Warren, *Nature*, 1987, **326**, 655–661.
- [51] S. Saarikoski, M. Sillanpaa, M. Sofiev, H. Timonen, K. Saarnio, K. Teinela, A. Karppinen, J. Kukkonen and R. Hillamo, *Atmos. Environ.*, 2007, **41**, 3577–3589.
- [52] H. Naoe, J. Heintzenberg, K. Okada, Y. Zaizen, K. Hayashi, T. Tateishi, Y. Igarashi, Y. Dokiya and K. Kinoshita, *Atmos. Environ.*, 2003, **37**, 3047–3055.
- [53] N. Schleicher, U. Kramar, V. Dietze, U. Kaminski and S. Norra, *Atmos. Environ.*, 2012, **48**, 113–121.
- [54] M. Kanakidou, J. H. Seinfeld, S. N. Pandis, I. Barnes, F. J. Dentener, M. C. Facchini, R. Van Dingenen, B. Ervens, A. Nenes, C. J. Nielsen, E. Swietlicki, J. P. Putaud, Y. Balkanski, S. Fuzzi, J. Horth, G. K. Moortgat, R. Winterhalter, C. E. L. Myhre, K. Tsigaridis, E. Vignati, E. G. Stephanou and J. Wilson, *Atmos. Chem. Phys.*, 2005, **5**, 1053–1123.
- [55] A. H. Goldstein and I. E. Galbally, *Environ. Sci. Technol.*, 2007, **41**, 1514–1521.
- [56] D. R. Hanson, *J. Phys. Chem. B*, 1997, **101**, 4998–5001.
- [57] J. L. Jimenez, M. R. Canagaratna, N. M. Donahue, A. S. H. Prevot, Q. Zhang, J. H. Kroll, P. F. DeCarlo, J. D. Allan, H. Coe, N. L. Ng, A. C. Aiken, K. S. Docherty, I. M. Ulbrich, A. P. Grieshop, A. L. Robinson, J. Duplissy, J. D. Smith, K. R. Wilson, V. A. Lanz, C. Hueglin, Y. L. Sun, J. Tian, A. Laaksonen, T. Raatikainen, J. Rautiainen, P. Vaattovaara, M. Ehn, M. Kulmala, J. M. Tomlinson, D. R. Collins, M. J. Cubison, E. J. Dunlea, J. A. Huffman, T. B. Onasch, M. R. Alfarra, P. I. Williams, K. Bower, Y. Kondo, J. Schneider, F. Drewnick, S. Borrmann, S. Weimer, K. Demerjian, D. Salcedo, L. Cottrell, R. Griffin, A. Takami, T. Miyoshi, S. Hatakeyama, A. Shimono, J. Y. Sun, Y. M. Zhang, K. Dzepina, J. R. Kimmel, D. Sueper, J. T. Jayne, S. C. Herndon, A. M. Trimborn, L. R. Williams, E. C. Wood, A. M. Middlebrook, C. E. Kolb, U. Baltensperger and D. R. Worsnop, *Science*, 2009, **326**, 1525–1529.
- [58] S. E. Schwartz and J. E. Freiberg, *Atmos. Environ.*, 1981, **15**, 1129–1144.
- [59] T. E. Ramabhadran, T. W. Peterson and J. H. Seinfeld, *Aiche J.*, 1976, **22**, 840–851.
- [60] M. A. Freedman, *Chem. Soc. Rev.*, 2017, **46**, 7694–7705.

- [61] A. Laskin, R. C. Moffet, M. K. Gilles, J. D. Fast, R. A. Zaveri, B. B. Wang, P. Nigge and J. Shutthanandan, *J. Geophys. Res-Atmos.*, 2012, **117**, 12.
- [62] S. S. Steimer, M. Lampimki, E. Coz, G. Gržinić and M. Ammann, *Atmos. Chem. Phys.*, 2014, **14**, 10761–10772.
- [63] B. Ervens, *Chem. Rev.*, 2015, **115**, 4157–4198.
- [64] T. Berkemeier, S. S. Steimer, U. K. Krieger, T. Peter, U. Poschl, M. Ammann and M. Shiraiwa, *Phys. Chem. Chem. Phys.*, 2016, **18**, 12662–74.
- [65] J. F. Davies and K. R. Wilson, *Chem. Sci.*, 2015, **6**, 7020–7027.
- [66] A. P. Bateman, S. A. Nizkorodov, J. Laskin and A. Laskin, *Physical Chemistry Chemical Physics*, 2011, **13**, 12199–12212.
- [67] C. George, M. Ammann, B. D'Anna, D. J. Donaldson and S. A. Nizkorodov, *Chem. Rev.*, 2015, **115**, 4218–4258.
- [68] M. Shiraiwa, L. D. Yee, K. A. Schilling, C. L. Loza, J. S. Craven, A. Zuend, P. J. Ziemann and J. H. Seinfeld, *P. Natl. Acad. Sci. USA*, 2013, **110**, 11746–11750.
- [69] J. H. Kroll, J. D. Smith, D. L. Che, S. H. Kessler, D. R. Worsnop and K. R. Wilson, *Physical Chemistry Chemical Physics*, 2009, **11**, 8005–8014.
- [70] C. M. Sharpless and N. V. Blough, *Environ. Sci. Process. Impacts*, 2014, **16**, 654–71.
- [71] J. Smith, V. Sio, L. Yu, Q. Zhang and C. Anastasio, *Environ. Sci. Technol.*, 2014, **48**, 1049–57.
- [72] H. Herrmann, B. Ervens, H. W. Jacobi, R. Wolke, P. Nowacki and R. Zellner, *J. Atmos. Chem.*, 2000, **36**, 231–284.
- [73] M. Krapf, I. El Haddad, E. A. Bruns, U. Molteni, K. R. Daellenbach, A. S. H. Prevot, U. Baltensperger and J. Dommen, *Chem*, 2016, **1**, 603–616.
- [74] S. A. Mang, D. K. Henricksen, A. P. Bateman, M. P. S. Andersen, D. R. Blake and S. A. Nizkorodov, *J. Phys. Chem. A*, 2008, **112**, 8337–8344.
- [75] J. Laskin, A. Laskin, P. J. Roach, G. W. Slysz, G. A. Anderson, S. A. Nizkorodov, D. L. Bones and L. Q. Nguyen, *Analytical Chemistry*, 2010, **82**, 2048–2058.
- [76] B. Nozière and W. Esteve, *Geophys. Res. Lett.*, 2005, **32**, 5.
- [77] J. P. S. Wong, A. Nenes and R. J. Weber, *Environ. Sci. Technol.*, 2017, **51**, 8414–8421.
- [78] V. Varutbangkul, F. J. Brechtel, R. Bahreini, N. L. Ng, M. D. Keywood, J. H. Kroll, R. C. Flagan, J. H. Seinfeld, A. Lee and A. H. Goldstein, *Atmos. Chem. Phys.*, 2006, **6**, 2367–2388.
- [79] K. M. Henry and N. M. Donahue, *J. Phys. Chem. A*, 2012, **116**, 5932–5940.
- [80] D. E. Romonosky, Y. Li, M. Shiraiwa, A. Laskin, J. Laskin and S. A. Nizkorodov, *J. Phys. Chem. A*, 2017, **121**, 1298–1309.
- [81] A. Nel, *Science*, 2005, **308**, 804–806.
- [82] G. Oberdörster and M. J. Utell, *Environ. Health Persp.*, 2002, **110**, A440–A441.
- [83] A. E. Nel, D. Diaz-Sanchez, D. Ng, T. Hiura and A. Saxon, *J. Allergy Clin. Immun.*, 1998, **102**, 539–554.
- [84] A. Peters, D. W. Dockery, J. E. Muller and M. A. Mittleman, *Circulation*, 2001, **103**, 2810–2815.
- [85] C. A. Pope, R. T. Burnett, M. C. Turner, A. Cohen, D. Krewski, M. Jerrett, S. M. Gapstur and M. J. Thun, *Environ. Health Persp.*, 2011, **119**, 1616–1621.

- [86] P. S. Monks, *Chem. Soc. Rev.*, 2005, **34**, 376–95.
- [87] P. M. Sheehy, R. Volkamer, L. T. Molina and M. J. Molina, *Atmos. Chem. Phys.*, 2010, **10**, 6993–7008.
- [88] R. Atkinson, D. L. Baulch, R. A. Cox, J. N. Crowley, R. F. Hampson, R. G. Hynes, M. E. Jenkin, M. J. Rossi and J. Troe, *Atmos. Chem. Phys.*, 2004, **4**, 1461–1738.
- [89] B. Ervens, B. J. Turpin and R. J. Weber, *Atmos. Chem. Phys.*, 2011, **11**, 11069–11102.
- [90] R. Zellner, M. Exner and H. Herrmann, *J. Atmos. Chem.*, 1990, **10**, 411–425.
- [91] R. Zhao, A. K. Y. Lee, R. Soong, A. J. Simpson and J. P. D. Abbatt, *Atmos. Chem. Phys.*, 2013, **13**, 5857–5872.
- [92] K. M. Badali, S. Zhou, D. Aljawhary, M. Antinolo, W. J. Chen, A. Lok, E. Mungall, J. P. S. Wong, R. Zhao and J. P. D. Abbatt, *Atmos. Chem. Phys.*, 2015, **15**, 7831–7840.
- [93] H. J. H. Fenton, *J. Chem. Soc. Trans.*, 1894, **65**, 899–910.
- [94] L. Deguillaume, M. Leriche, K. Desboeufs, G. Mailhot, C. George and N. Chaumerliac, *Chem. Rev.*, 2005, **105**, 3388–3431.
- [95] C. Weller, S. Horn and H. Herrmann, *J. Photoch. Photobio. A*, 2013, **268**, 24–36.
- [96] C. Weller, S. Horn and H. Herrmann, *J. Photoch. Photobio. A*, 2013, **255**, 41 – 49.
- [97] B. Ervens, S. Gligorovski and H. Herrmann, *Phys. Chem. Chem. Phys.*, 2003, **5**, 1811–1824.
- [98] T. C. Bond and R. W. Bergstrom, *Aerosol Sci. Technol.*, 2006, **40**, 27–67.
- [99] Y. Feng, V. Ramanathan and V. R. Kotamarthi, *Atmos. Chem. Phys.*, 2013, **13**, 8607–8621.
- [100] T. C. Bond, S. J. Doherty, D. W. Fahey, P. M. Forster, T. Berntsen, B. J. DeAngelo, M. G. Flanner, S. Ghan, B. Karcher, D. Koch, S. Kinne, Y. Kondo, P. K. Quinn, M. C. Sarofim, M. G. Schultz, M. Schulz, C. Venkataraman, H. Zhang, S. Zhang, N. Bellouin, S. K. Guttikunda, P. K. Hopke, M. Z. Jacobson, J. W. Kaiser, Z. Klimont, U. Lohmann, J. P. Schwarz, D. Shindell, T. Storelvmo, S. G. Warren and C. S. Zender, *J. Geophys. Res-Atmos.*, 2013, **118**, 5380–5552.
- [101] A. Hoffer, A. Gelencsr, P. Guyon, G. Kiss, O. Schmid, G. P. Frank, P. Artaxo and M. O. Andreae, *Atmos. Chem. Phys.*, 2006, **6**, 3563–3570.
- [102] T. W. Kirchstetter and T. L. Thatcher, *Atmos. Chem. Phys.*, 2012, **12**, 6067–6072.
- [103] A. Laskin, J. Laskin and S. A. Nizkorodov, *Chem. Rev.*, 2015, **115**, 4335–82.
- [104] R. Duarte, E. B. H. Santos and A. C. Duarte, *Water Res.*, 2003, **37**, 4073–4080.
- [105] H. Sun, L. Biedermann and T. C. Bond, *Geophys. Res. Lett.*, 2007, **34**, L17813.
- [106] R. K. Chakrabarty, H. Moosmuller, L. W. A. Chen, K. Lewis, W. P. Arnott, C. Mazzoleni, M. K. Dubey, C. E. Wold, W. M. Hao and S. M. Kreidenweis, *Atmos. Chem. Phys.*, 2010, **10**, 6363–6370.
- [107] M. Zhong and M. Jang, *Atmos. Chem. Phys.*, 2014, **14**, 1517–1525.
- [108] C. Song, M. Gyawali, R. A. Zaveri, J. E. Shilling and W. P. Arnott, *J. Geophys. Res-Atmos.*, 2013, **118**, 11741–11749.
- [109] M. Zhong and M. Jang, *Atmos. Environ.*, 2011, **45**, 4263–4271.
- [110] A. Gelencser, A. Hoffer, G. Kiss, E. Tombacz, R. Kurdi and L. Bencze, *J. Atmos. Chem.*, 2003, **45**, 25–33.
- [111] Y. L. Sun, Q. Zhang, C. Anastasio and J. Sun, *Atmos. Chem. Phys.*, 2010, **10**, 4809–4822.

- [112] C. J. Kampf, A. Filippi, C. Zuth, T. Hoffmann and T. Opatz, *Phys Chem Chem Phys*, 2016, **18**, 18353–64.
- [113] E. L. Shapiro, J. Szprengiel, N. Sareen, C. N. Jen, M. R. Giordano and V. F. McNeill, *Atmos. Chem. Phys.*, 2009, **9**, 2289–2300.
- [114] A. T. Lambe, C. D. Cappa, P. Massoli, T. B. Onasch, S. D. Forestieri, A. T. Martin, M. J. Cummings, D. R. Croasdale, W. H. Brune, D. R. Worsnop and P. Davidovits, *Environ. Sci. Technol.*, 2013, **47**, 6349–6357.
- [115] R. Saleh, C. J. Hennigan, G. R. McMeeking, W. K. Chuang, E. S. Robinson, H. Coe, N. M. Donahue and A. L. Robinson, *Atmos. Chem. Phys.*, 2013, **13**, 7683–7693.
- [116] H. J. Lee, P. K. Aiona, A. Laskin, J. Laskin and S. A. Nizkorodov, *Environ. Sci. Technol.*, 2014, **48**, 10217–10226.
- [117] K. McNeill and S. Canonica, *Environ. Sci. Process. Impacts*, 2016, **18**, 1381–1399.
- [118] S. Canonica, *CHIMIA International Journal for Chemistry*, 2007, **61**, 641–644.
- [119] S. Canonica, B. Hellrung and J. Wirz, *J. Phys. Chem. A*, 2000, **104**, 1226–1232.
- [120] L. González Palacios, P. Corral Arroyo, K. Z. Aregahegn, S. S. Steimer, T. Bartels-Rausch, B. Nozière, C. George, M. Ammann and R. Volkamer, *Atmos. Chem. Phys.*, 2016, **16**, 11823–11836.
- [121] J. D. Smith, H. Kinney and C. Anastasio, *Phys. Chem. Chem. Phys.*, 2015, **17**, 10227–37.
- [122] J. D. Smith, H. Kinney and C. Anastasio, *Atmos. Environ.*, 2016, **126**, 36–44.
- [123] L. Yu, J. Smith, A. Laskin, C. Anastasio, J. Laskin and Q. Zhang, *Atmos. Chem. Phys.*, 2014, **14**, 13801–13816.
- [124] M. Teich, D. van Pinxteren, S. Kecorius, Z. Wang and H. Herrmann, *Environ. Sci. Technol.*, 2016, **50**, 1166–73.
- [125] R. I. Olariu, I. Barnes, K. H. Becker and B. Klotz, *Int. J. Chem. Kinet.*, 2000, **32**, 696–702.
- [126] J. A. Roger Atkinson, *Environ. Health Perspect.*, 1994, **102**, 117–126.
- [127] S. Decesari, M. C. Facchini, E. Matta, M. Mircea, S. Fuzzi, A. R. Chughtai and D. M. Smith, *Atmos. Environ.*, 2002, **36**, 1827–1832.
- [128] B. Graham, *J. Geophys. Res.*, 2002, **107**, 8047.
- [129] J. Ofner, H. U. Kruger, H. Grothe, P. Schmitt-Kopplin, K. Whitmore and C. Zetzsch, *Atmos. Chem. Phys.*, 2011, **11**, 1–15.
- [130] C. J. Weschler, M. L. Mandich and T. E. Graedel, *J. Geophys. Res-Atmos.*, 1986, **91**, 5189–5204.
- [131] C. Guieu, S. Bonnet, T. Wagener and M. D. Loye-Pilot, *Geophys. Res. Lett.*, 2005, **32**, 5.
- [132] S. O. Pehkonen, R. Siefert, Y. Erel, S. Webb and M. R. Hoffmann, *Environ. Sci. Technol.*, 1993, **27**, 2056–2062.
- [133] S. Weber, P. Hoffmann, J. Ensling, A. N. Dedik, S. Weinbruch, G. Miehe, P. Gutlich and H. M. Ortner, *J. Aerosol Sci.*, 2000, **31**, 987–997.
- [134] S. Lafon, J. L. Rajot, S. C. Alfaro and A. Gaudichet, *Atmos. Environ.*, 2004, **38**, 1211–1218.
- [135] C. Rodriguez-Navarro, F. di Lorenzo and K. Elert, *Atmos. Chem. Phys.*, 2018, **18**, 10089–10122.
- [136] B. Kopcewicz and M. Kopcewicz, *Atmos. Environ.*, 2001, **35**, 3739–3747.
- [137] C. R. Usher, A. E. Michel, D. Stec and V. H. Grassian, *Atmos. Environ.*, 2003, **37**, 5337–5347.

- [138] D. M. Cwiertny, G. J. Hunter, J. M. Pettibone, M. M. Scherer and V. H. Grassian, *J. Phys. Chem. C*, 2009, **113**, 2175–2186.
- [139] X. R. Zhu, J. M. Prospero, F. J. Millero, D. L. Savoie and G. W. Brass, *Mar. Chem.*, 1992, **38**, 91–107.
- [140] D. M. Cwiertny, J. Baltrusaitis, G. J. Hunter, A. Laskin, M. M. Scherer and V. H. Grassian, *J. Geophys. Res-Atmos.*, 2008, **113**, 18.
- [141] C. Luo, N. M. Mahowald, N. Meskhidze, Y. Chen, R. L. Siefert, A. R. Baker and A. M. Johansen, *J. Geophys. Res-Atmos.*, 2005, **110**, 23.
- [142] C. Brandt and R. Vaneldik, *Chem. Rev.*, 1995, **95**, 119–190.
- [143] H. Hofmann, P. Hoffmann and K. H. Lieser, *Fresen. J. Anal. Chem.*, 1991, **340**, 591–597.
- [144] A. Chebbi and P. Carlier, *Atmos. Environ.*, 1996, **30**, 4233–4249.
- [145] K. Kawamura, L. L. Ng and I. R. Kaplan, *Environ. Sci. Technol.*, 1985, **19**, 1082–1086.
- [146] R. L. Siefert, A. M. Johansen, M. R. Hoffmann and S. O. Pehkonen, *J. Air Waste Ma.*, 1998, **48**, 128–143.
- [147] J. D. Willey, R. J. Kieber, K. H. Williams, J. S. Crozier, S. A. Skrabal and G. B. Avery, *J. Atmos. Chem.*, 2000, **37**, 185–205.
- [148] P. Behra and L. Sigg, *Nature*, 1990, **344**, 419–421.
- [149] B. J. Majestic, J. J. Schauer and M. M. Shafer, *Atmos. Chem. Phys.*, 2007, **7**, 2475–2487.
- [150] H. B. Dunford, *Coordin. Chem. Rev.*, 2002, **233**, 311–318.
- [151] W. G. Barb, J. H. Baxendale, P. George and K. R. Hargrave, *Transactions of the Faraday Society*, 1951, **47**, 462–500.
- [152] W. C. Bray and M. H. Gorin, *J. Am. Chem. Soc.*, 1932, **54**, 2124–2125.
- [153] L. Deguillaume, M. Leriche and N. Chaurnerliac, *Chemosphere*, 2005, **60**, 718–724.
- [154] F. Gozzo, *J. Mol. Catal. A-Chem.*, 2001, **171**, 1–22.
- [155] S. J. Hug and O. Leupin, *Environ. Sci. Technol.*, 2003, **37**, 2734–2742.
- [156] M. L. Kremer, *J. Phys. Chem. A*, 2003, **107**, 1734–1741.
- [157] S. Enami, Y. Sakamoto and A. J. Colussi, *P. Natl. Acad. Sci. USA*, 2014, **111**, 623–628.
- [158] F. R. Kameel, F. Riboni, M. R. Hoffmann, S. Enami and A. J. Colussi, *J. Phys. Chem. C*, 2014, **118**, 29151–29158.
- [159] L. Deguillaume, M. Leriche, A. Monod and N. Chaumerliac, *Atmos. Chem. Phys.*, 2004, **4**, 95–110.
- [160] L. Emmenegger, R. R. Schonenberger, L. Sigg and B. Sulzberger, *Limnol. Oceanogr.*, 2001, **46**, 49–61.
- [161] F. Wu and N. S. Deng, *Chemosphere*, 2000, **41**, 1137–1147.
- [162] Z. H. Wang, C. C. Chen, W. H. Ma and J. C. Zhao, *J. Phys. Chem. Lett.*, 2012, **3**, 2044–2051.
- [163] P. Ciesla, P. Kocot, P. Mytych and Z. Stasicka, *J. Mol. Catal. A-Chem.*, 2004, **224**, 17–33.
- [164] W. Feng, D. Nansheng, E. M. Glebov, I. P. Pozdnyakov, V. P. Grivin, V. F. Plyusnin and N. M. Bazhin, *Russ. Chem. B+*, 2007, **56**, 900–903.

- [165] E. M. Glebov, I. P. Pozdnyakov, V. P. Grivin, V. F. Plyusnin, X. Zhang, F. Wu and N. S. Deng, *Photoch. Photobio. Sci.*, 2011, **10**, 425–430.
- [166] X. Zhang, Y. Gong, F. Wu, N. Deng, I. P. Pozdnyakov, E. M. Glebov, V. P. Grivin, V. F. Plyusnin and N. M. Bazhin, *Russ. Chem. B+*, 2009, **58**, 1828–1836.
- [167] B. C. Faust and R. G. Zepp, *Environ. Sci. Technol.*, 1993, **27**, 2517–2522.
- [168] H. B. Abrahamson, A. B. Rezvani and J. G. Brushmiller, *Inorg. Chim. Acta*, 1994, **226**, 117–127.
- [169] Y. G. Zuo and Y. W. Deng, *Chemosphere*, 1997, **35**, 2051–2058.
- [170] Y. G. Zuo and J. Hoigné, *Atmos. Environ.*, 1994, **28**, 1231–1239.
- [171] S. H. Kessler, T. Nah, K. E. Daumit, J. D. Smith, S. R. Leone, C. E. Kolb, D. R. Worsnop, K. R. Wilson and J. H. Kroll, *J Phys Chem A*, 2012, **116**, 6358–65.
- [172] L. J. Carpenter, S. M. MacDonald, M. D. Shaw, R. Kumar, R. W. Saunders, R. Parthipan, J. Wilson and J. M. C. Plane, *Nature Geosci.*, 2013, **6**, 108–111.
- [173] S. Y. Wang and K. A. Pratt, *J. Geophys. Res-Atmos.*, 2017, **122**, 11991–12007.
- [174] S. N. Wren, D. J. Donaldson and J. P. D. Abbatt, *Atmos. Chem. Phys.*, 2013, **13**, 9789–9800.
- [175] H. Hepach, B. Quack, S. Tegtmeier, A. Engel, A. Bracher, S. Fuhlbrugge, L. Galgani, E. L. Atlas, J. Lampel, U. Friess and K. Kruger, *Atmos. Chem. Phys.*, 2016, **16**, 12219–12237.
- [176] R. Vogt, R. Sander, R. Von Glasow and P. J. Crutzen, *J. Atmos. Chem.*, 1999, **32**, 375–395.
- [177] W. R. Simpson, S. S. Brown, A. Saiz-Lopez, J. A. Thornton and R. Glasow, *Chem. Rev.*, 2015, **115**, 4035–62.
- [178] T. Sherwen, J. A. Schmidt, M. J. Evans, L. J. Carpenter, K. Gromann, S. D. Eastham, D. J. Jacob, B. Dix, T. K. Koenig, R. Sinreich, I. Ortega, R. Volkamer, A. Saiz-Lopez, C. Prados-Roman, A. S. Mahajan and C. Ordez, *Atmos. Chem. Phys.*, 2016, **16**, 12239–12271.
- [179] A. Saiz-Lopez, J. M. Plane, A. R. Baker, L. J. Carpenter, R. von Glasow, J. C. Martin, G. McFiggans and R. W. Saunders, *Chem. Rev.*, 2012, **112**, 1773–804.
- [180] W. J. Bloss, J. D. Lee, G. P. Johnson, R. Sommariva, D. E. Heard, A. Saiz-Lopez, J. M. C. Plane, G. McFiggans, H. Coe, M. Flynn, P. Williams, A. R. Rickard and Z. L. Fleming, *Geophys. Res. Lett.*, 2005, **32**, 4.
- [181] W. L. Chameides and D. D. Davis, *J. Geophys. Res. Oceans*, 1980, **85**, 7383–7398.
- [182] D. J. Lary, *J. Geophys. Res-Atmos.*, 1996, **101**, 1505–1516.
- [183] A. Saiz-Lopez and R. von Glasow, *Chem. Soc. Rev.*, 2012, **41**, 6448–72.
- [184] R. Sommariva, W. J. Bloss and R. von Glasow, *Atmos. Environ.*, 2012, **57**, 219–232.
- [185] R. von Glasow, R. von Kuhlmann, M. G. Lawrence, U. Platt and P. J. Crutzen, *Atmos. Chem. Phys.*, 2004, **4**, 2481–2497.
- [186] A. S. Mahajan, M. Sorribas, J. C. G. Martin, S. M. MacDonald, M. Gil, J. M. C. Plane and A. Saiz-Lopez, *Atmos. Chem. Phys.*, 2011, **11**, 2545–2555.

- [187] G. McFiggans, C. S. E. Bale, S. M. Ball, J. M. Beames, W. J. Bloss, L. J. Carpenter, J. Dorsey, R. Dunk, M. J. Flynn, K. L. Furneaux, M. W. Gallagher, D. E. Heard, A. M. Hollingsworth, K. Hornsby, T. Ingham, C. E. Jones, R. L. Jones, L. J. Kramer, J. M. Langridge, C. Leblanc, J. P. LeCrane, J. D. Lee, R. J. Leigh, I. Longley, A. S. Mahajan, P. S. Monks, H. Oetjen, A. J. Orr-Ewing, J. M. C. Plane, P. Potin, A. J. L. Shillings, F. Thomas, R. von Glasow, R. Wada, L. K. Whalley and J. D. Whitehead, *Atmos. Chem. Phys.*, 2010, **10**, 2975–2999.
- [188] T. Hoffmann, C. D. O’Dowd and J. H. Seinfeld, *Geophys. Res. Lett.*, 2001, **28**, 1949–1952.
- [189] G. McFiggans, H. Coe, R. Burgess, J. Allan, M. Cubison, M. R. Alfarra, R. Saunders, A. Saiz-Lopez, J. M. C. Plane, D. J. Wevill, L. J. Carpenter, A. R. Rickard and P. S. Monks, *Atmos. Chem. Phys.*, 2004, **4**, 701–713.
- [190] R. W. Saunders and J. M. C. Plane, *J. Aerosol Sci.*, 2006, **37**, 1737–1749.
- [191] T. M. Sherwen, M. J. Evans, D. V. Spracklen, L. J. Carpenter, R. Chance, A. R. Baker, J. A. Schmidt and T. J. Breider, *Geophys. Res. Lett.*, 2016, **43**, 10012–10019.
- [192] A. Saiz-Lopez and J. M. C. Plane, *Geophys. Res. Lett.*, 2004, **31**, 4.
- [193] L. J. Carpenter, *Chem. Rev.*, 2003, **103**, 4953–4962.
- [194] S. Pechtl, G. Schmitz and R. von Glasow, *Atmos. Chem. Phys.*, 2007, **7**, 1381–1393.
- [195] A. Jammoul, S. Dumas, B. D’Anna and C. George, *Atmos. Chem. Phys.*, 2009, **9**, 4229–4237.
- [196] C. Marcolli, B. P. Luo and T. Peter, *J. Phys. Chem. A*, 2004, **108**, 2216–2224.
- [197] S. T. Martin, *Chem. Rev.*, 2000, **100**, 3403–3453.
- [198] S. Bastelberger, U. K. Krieger, B. P. Luo and T. Peter, *Atmos. Chem. Phys.*, 2017, **17**, 8453–8471.
- [199] Y. C. Song, A. E. Haddrell, B. R. Bzdek, J. P. Reid, T. Bannan, D. O. Topping, C. Percival and C. Cai, *J. Phys. Chem. A*, 2016, **120**, 8123–8137.
- [200] R. M. Power, S. H. Simpson, J. P. Reid and A. J. Hudson, *Chem. Sci.*, 2013, **4**, 2597.
- [201] A. Virtanen, J. Joutsensaari, T. Koop, J. Kannosto, P. Yli-Pirila, J. Leskinen, J. M. Makela, J. K. Holopainen, U. Poeschl, M. Kulmala, D. R. Worsnop and A. Laaksonen, *Nature*, 2010, **467**, 824–827.
- [202] C. D. Cappa and K. R. Wilson, *Atmos. Chem. Phys.*, 2011, **11**, 1895–1911.
- [203] T. D. Vaden, C. Song, R. A. Zaveri, D. Imre and A. Zelenyuk, *P. Natl. Acad. Sci. USA*, 2010, **107**, 6658–6663.
- [204] M. Kalberer, D. Paulsen, M. Sax, M. Steinbacher, J. Dommen, A. S. H. Prevot, R. Fisseha, E. Weingartner, V. Frankevich, R. Zenobi and U. Baltensperger, *Science*, 2004, **303**, 1659–1662.
- [205] E. Mikhailov, S. Vlasenko, S. T. Martin, T. Koop and U. Poeschl, *Atmos. Chem. Phys.*, 2009, **9**, 9491–9522.
- [206] H. Lignell, M. L. Hinks and S. A. Nizkorodov, *P. Natl. Acad. Sci. USA*, 2014, **111**, 13780–13785.
- [207] K. Nagarajan, A. R. Mallia, K. Muraleedharan and M. Hariharan, *Chem. Sci.*, 2017, **8**, 1776–1782.
- [208] U. Poeschl, *Angew. Chem. Int. Ed. Engl.*, 2005, **44**, 7520–40.
- [209] A. Sadezky, H. Muckenhuber, H. Grothe, R. Niessner and U. Poeschl, *Carbon*, 2005, **43**, 1731–1742.
- [210] A. Vlasenko, T. Huthwelker, H. W. Gaggeler and M. Ammann, *Physical Chemistry Chemical Physics*, 2009, **11**, 7921–7930.

- [211] G. Gržinić, T. Bartels-Rausch, T. Berkemeier, A. Trler and M. Ammann, *Atmos. Chem. Phys.*, 2015, **15**, 13615–13625.
- [212] S. S. Steimer, T. Berkemeier, A. Gilgen, U. K. Krieger, T. Peter, M. Shiraiwa and M. Ammann, *Phys. Chem. Chem. Phys.*, 2015, **17**, 31101–9.
- [213] P. S. J. Lakey, T. Berkemeier, M. Krapf, J. Dommen, S. S. Steimer, L. K. Whalley, T. Ingham, M. T. Baeza-Romero, U. Pschl, M. Shiraiwa, M. Ammann and D. E. Heard, *Atmos. Chem. Phys.*, 2016, **16**, 13035–13047.
- [214] C. Anastasio and M. Mozurkewich, *J. Atmos. Chem.*, 2002, **41**, 135–162.
- [215] Q. Shi, J. T. Jayne, C. E. Kolb, D. R. Worsnop and P. Davidovits, *J. Geophys. Res-Atmos.*, 2001, **106**, 24259–24274.
- [216] M. Ammann, R. A. Cox, J. N. Crowley, M. E. Jenkin, A. Mellouki, M. J. Rossi, J. Troe and T. J. Wallington, *Atmos. Chem. Phys.*, 2013, **13**, 8045–8228.
- [217] M. M. IvkovicJensen and N. M. Kostic, *Biochemistry-US*, 1997, **36**, 8135–8144.
- [218] S. Mitroka, S. Zimmeck, D. Troya and J. M. Tanko, *J. Am. Chem. Soc.*, 2010, **132**, 2907–2913.
- [219] M. Shiraiwa, Y. Li, A. P. Tsimpidi, V. A. Karydis, T. Berkemeier, S. N. Pandis, J. Lelieveld, T. Koop and U. Poschl, *Nat. Comm.*, 2017, **8**, 7.
- [220] J. G. Calvert and Pitts, *Photochemistry*, Wiley, 1966.
- [221] S. Sander, J. Abbatt, J. R. Barker, J. B. Burkholder, R. R. Friedl, D. M. Golden, R. E. Huie, C. E. Kolb, M. J. Kurylo, G. K. Moortgat, V. L. Orkin and P. H. Wine, *JPL Publication*, 2011, 10–6.
- [222] W. M. Draper and D. G. Crosby, *J. Agr. Food Chem.*, 1983, **31**, 734–737.
- [223] B. C. Faust, in *Aquatic Photochemical Reactions in Atmospheric, Surface, and Marine Waters: Influences on Oxidant Formation and Pollutant Degradation*, ed. P. Boule, Springer Berlin Heidelberg, Berlin, Heidelberg, 1999, pp. 101–122.
- [224] R. P. Schwarzenbach, P. M. Gschwend and D. M. Imboden, *Environmental Organic Chemistry*, Wiley-Interscience, 2002.
- [225] J. Yi, C. Bahrini, C. Schoemaeker, C. Fittschen and W. Choi, *J. Phys. Chem. C*, 2012, **116**, 10090–10097.
- [226] Y. Dupart, S. M. King, B. Nekat, A. Nowak, A. Wiedensohler, H. Herrmann, G. David, B. Thomas, A. Miffre, P. Rairoux, B. D’Anna and C. George, *P. Natl. Acad. Sci. USA*, 2012, **109**, 20842–20847.
- [227] B. Nozière, P. Dziedzic and A. Cordova, *J. Phys. Chem. A*, 2009, **113**, 231–237.
- [228] A. Maxut, B. Nozière, B. Fenet and H. Mechakra, *pCcp*, 2015, **17**, 20416–20424.
- [229] N. Sareen, A. N. Schwier, E. L. Shapiro, D. Mitroo and V. F. McNeill, *Atmos. Chem. Phys.*, 2010, **10**, 997–1016.
- [230] M. Trainic, A. A. Riziq, A. Lavi, J. M. Flores and Y. Rudich, *Atmos. Chem. Phys.*, 2011, **11**, 9697–9707.
- [231] A. J. Sumner, J. L. Woo and V. F. McNeill, *Environ. Sci. Technol.*, 2014, **48**, 11919–11925.
- [232] M. E. Monge, T. Rosenorn, O. Favez, M. Mueller, G. Adler, A. A. Riziq, Y. Rudich, H. Herrmann, C. George and B. D’Anna, *P. Natl. Acad. Sci. USA*, 2012, **109**, 6840–6844.
- [233] S. Rossignol, K. Z. Aregahegn, L. Tinel, L. Fine, B. Nozière and C. George, *Environ. Sci. Technol.*, 2014, **48**, 3218–3227.
- [234] R. Kaur, C. Anastasio, K. T. Valsaraj, H. S. Vempati and M. Vaitilingom, *AGU Fall Meeting Abstracts*, 2014, A53S–07.
- [235] R. Jacob, *PhD thesis*, Johannes Gutenberg-Universitaet Mainz, 2015.

- [236] R. Thalman and R. Volkamer, *Atmos. Meas. Tech.*, 2010, **3**, 1797–1814.
- [237] J. Heland, J. Kleffmann, R. Kurtenbach and P. Wiesen, *Environ. Sci. Technol.*, 2001, **35**, 3207–3212.
- [238] J. Kleffmann, J. Heland, R. Kurtenbach, J. Lorzer and P. Wiesen, *Environ. Sci. Pollut. R.*, 2002, 48–54.
- [239] J. Kleffmann, J. C. Loerzer, P. Wiesen, C. Kern, S. Trick, R. Volkamer, M. Rodenas and K. Wirtz, *Atmos. Environ.*, 2006, **40**, 3640–3652.
- [240] R. Thalman, K. J. Zarzana, M. A. Tolbert and R. Volkamer, *J. Quant. Spectrosc. Ra.*, 2014, **147**, 171–177.
- [241] R. A. Washenfelder, A. O. Langford, H. Fuchs and S. S. Brown, *Atmos. Chem. Phys.*, 2008, **8**, 7779–7793.
- [242] R. Thalman, M. T. Baeza-Romero, S. M. Ball, E. Borrás, M. J. S. Daniels, I. C. A. Goodall, S. B. Henry, T. Karl, F. N. Keutsch, S. Kim, J. Mak, P. S. Monks, A. Muñoz, J. Orlando, S. Peppe, A. R. Rickard, M. Rodenas, P. Sanchez, R. Seco, L. Su, G. Tyndall, M. Vazquez, T. Vera, E. Waxman and R. Volkamer, *Atmos. Meas. Tech.*, 2015, **8**, 1835–1862.
- [243] R. Thalman and R. Volkamer, *pCcP*, 2013, **15**, 15371–15381.
- [244] A. C. Vandaele, C. Hermans, S. Fally, M. Carleer, R. Colin, M.-F. Mrienne, A. Jenouvrier and B. Coquart, *J. Geophys. Res. Atmos.*, 2002, **107**, ACH 3–1–ACH 3–12.
- [245] P. S. J. Lakey, I. J. George, L. K. Whalley, M. T. Baeza-Romero and D. E. Heard, *Environ. Sci. Technol.*, 2015, **49**, 4878–4885.
- [246] A. A. Zardini, S. Sjogren, C. Marcolli, U. K. Krieger, M. Gysel, E. Weingartner, U. Baltensperger and T. Peter, *Atmos. Chem. Phys.*, 2008, **8**, 5589–5601.
- [247] M. L. Hinks, M. V. Brady, H. Lignell, M. J. Song, J. W. Grayson, A. K. Bertram, P. Lin, A. Laskin, J. Laskin and S. A. Nizkorodov, *Physical Chemistry Chemical Physics*, 2016, **18**, 8785–8793.
- [248] K. Stemmler, M. Ammann, C. Donders, J. Kleffmann and C. George, *Nature*, 2006, **440**, 195–198.
- [249] K. Stemmler, M. Ndour, Y. Elshorbany, J. Kleffmann, B. D’Anna, C. George, B. Bohn and M. Ammann, *Atmos. Chem. Phys.*, 2007, **7**, 4237–4248.
- [250] A. Jammoul, S. Gligorovski, C. George and B. D’Anna, *J. Phys. Chem. A*, 2008, **112**, 1268–1276.
- [251] R. Volkamer, F. S. Martini, L. T. Molina, D. Salcedo, J. L. Jimenez and M. J. Molina, *Geophys. Res. Lett.*, 2007, **34**, L19807.
- [252] G. Li, W. Lei, M. Zavala, R. Volkamer, S. Dusanter, P. Stevens and L. T. Molina, *Atmos. Chem. Phys.*, 2010, **10**, 6551–6567.
- [253] R. Volkamer, P. Sheehy, L. T. Molina and M. J. Molina, *Atmos. Chem. Phys.*, 2010, **10**, 6969–6991.
- [254] B. Ervens and R. Volkamer, *Atmos. Chem. Phys.*, 2010, **10**, 8219–8244.
- [255] D. M. Lienhard, D. L. Bones, A. Zuend, U. K. Krieger, J. P. Reid and T. Peter, *J. Phys. Chem. A*, 2012, **116**, 9954–9968.
- [256] P. M. Medeiros and B. R. T. Simoneit, *Environ. Sci. Technol.*, 2008, **42**, 8310–8316.
- [257] C. G. Nolte, J. J. Schauer, G. R. Cass and B. R. T. Simoneit, *Environ. Sci. Technol.*, 2001, **35**, 1912–1919.
- [258] J. J. Schauer, M. J. Kleeman, G. R. Cass and B. R. T. Simoneit, *Environ. Sci. Technol.*, 2001, **39**, 1716–1728.
- [259] M. Ammann, E. Rossler, R. Strekowski and C. George, *Phys. Chem. Chem. Phys.*, 2005, **7**, 2513–2518.

- [260] M. J. Kurylo, P. A. Ouellette and A. H. Laufer, *J. Phys. Chem.*, 1986, **90**, 437–440.
- [261] A. A. Lamola and G. S. Hammond, *J. Chem. Phys.*, 1965, **43**, 2129–2135.
- [262] A. K. Bertram, S. T. Martin, S. J. Hanna, M. L. Smith, A. Bodsworth, Q. Chen, M. Kuwata, A. Liu, Y. You and S. R. Zorn, *Atmos. Chem. Phys.*, 2011, **11**, 10995–11006.
- [263] L. Renbaum-Wolff, M. J. Song, C. Marcolli, Y. Zhang, P. F. F. Liu, J. W. Grayson, F. M. Geiger, S. T. Martin and A. K. Bertram, *Atmos. Chem. Phys.*, 2016, **16**, 7969–7979.
- [264] L. Renbaum-Wolff, J. W. Grayson, A. P. Bateman, M. Kuwata, M. Sellier, B. J. Murray, J. E. Shilling, S. T. Martin and A. K. Bertram, *P. Natl. Acad. Sci. USA*, 2013, **110**, 8014–8019.
- [265] P. Jacques, X. Allonas, M. Von Raumer, P. Suppan and E. Haselbach, *J. Photoch. Photobio. A*, 1997, **111**, 41–45.
- [266] R. Battino, T. R. Rettich and T. Tominaga, *J. Phys. Chem. Ref. Data*, 1983, **12**, 163–178.
- [267] N. Kanno, K. Tonokura, A. Tezaki and M. Koshi, *J. Phys. Chem. A*, 2005, **109**, 3153–3158.
- [268] A. S. Tatikolov, V. I. Sklyarenko, V. A. Kuzmin and M. A. Alperovich, *Bull. Acad. Sci. USSR, Div. Chem. Sci.*, 1989, **38**, 1597–1601.
- [269] A. Kunze, U. Muller, K. Tittes, J. P. Fouassier and F. MorletSavary, *J. Photoch. Photobio. A*, 1997, **110**, 115–122.
- [270] M. D. Dave and U. C. Pande, *J. Chem. Pharm. Res.*, 2012, **4**, 4721–4730.
- [271] S. Dusanter, D. Vimal, P. S. Stevens, R. Volkamer, L. T. Molina, A. Baker, S. Meinardi, D. Blake, P. Sheehy, A. Merten, R. Zhang, J. Zheng, E. C. Fortner, W. Junkermann, M. Dubey, T. Rahn, B. Eichinger, P. Lewandowski, J. Prueger and H. Holder, *Atmos. Chem. Phys.*, 2009, **9**, 6655–6675.
- [272] R. Kaur and C. Anastasio, *Environ. Sci. Technol.*, 2018, **52**, 5218–5226.
- [273] L. Tinel, S. Dumas and C. George, *C. R. Chimie*, 2014, **17**, 801–807.
- [274] B. Maillard, K. U. Ingold and J. C. Scaiano, *J. Am. Chem. Soc.*, 1983, **105**, 5095–5099.
- [275] Y. X. Tang, G. S. Tyndall and J. J. Orlando, *J. Phys. Chem. A*, 2010, **114**, 369–378.
- [276] X. Shi, S. Mandel and M. Platz, *J. Am. Chem. Soc.*, 2007, **129**, 4542–4550.
- [277] K. U. Ingold, *Acc. Chem. Res.*, 1969, **2**, 1–9.
- [278] R. Sander and P. J. Crutzen, *J. Geophys. Res-Atmos.*, 1996, **101**, 9121–9138.
- [279] J. A. Schmidt, D. J. Jacob, H. M. Horowitz, L. Hu, T. Sherwen, M. J. Evans, Q. Liang, R. M. Suleiman, D. E. Oram, M. Le Breton, C. J. Percival, S. Wang, B. Dix and R. Volkamer, *J. Geophys. Res-Atmos.*, 2016, **121**, 11819–11835.
- [280] M. J. Molina and F. S. Rowland, *B. Am. Meteorol. Soc.*, 1974, **55**, 491–491.
- [281] J. C. Farman, B. G. Gardiner and J. D. Shanklin, *Nature*, 1985, **315**, 207–210.
- [282] A. Saiz-Lopez, J. M. C. Plane, A. S. Mahajan, P. S. Anderson, S. J. B. Bauguitte, A. E. Jones, H. K. Roscoe, R. A. Salmon, W. J. Bloss, J. D. Lee and D. E. Heard, *Atmos. Chem. Phys.*, 2008, **8**, 887–900.
- [283] D. Stone, T. Sherwen, M. J. Evans, S. Vaughan, T. Ingham, L. K. Whalley, P. M. Edwards, K. A. Read, J. D. Lee, S. J. Moller, L. J. Carpenter, A. C. Lewis and D. E. Heard, *Atmos. Chem. Phys.*, 2018, **18**, 3541–3561.

- [284] H. Herrmann, Z. Majdik, B. Ervens and D. Weise, *Chemosphere*, 2003, **52**, 485–502.
- [285] D. I. Reeser, C. George and D. J. Donaldson, *J. Phys. Chem. A*, 2009, **113**, 8591–8595.
- [286] A. Cincinelli, P. G. Desideri, L. Lepri, L. Checchini, M. Del Bubba and R. Udisti, *Int. J. Environ. A. Ch.*, 2001, **79**, 283–299.
- [287] E. J. Hoffman and R. A. Duce, *J. Geophys. Res. Oc. Atm.*, 1976, **81**, 3667–3670.
- [288] K. A. Hunter and P. S. Liss, *Mar. Chem.*, 1977, **5**, 361–379.
- [289] C. D. O’Dowd and G. de Leeuw, *Philos. Trans. A Math. Phys. Eng. Sci.*, 2007, **365**, 1753–74.
- [290] A. R. Baker, *Geophys. Res. Lett.*, 2004, **31**, 4.
- [291] A. R. Baker, *Environ. Chem.*, 2005, **2**, 295–298.
- [292] S. Pechtl, G. Schmitz and R. von Glasow, *Atmos. Chem. Phys.*, 2007, **7**, 1381–1393.
- [293] E. De Laurentiis, M. Minella, V. Maurino, C. Minero, G. Mailhot, M. Sarakha, M. Brigante and D. Vione, *Sci. Total Environ.*, 2012, **439**, 299–306.
- [294] P. Corral-Arroyo, T. Bartels-Rausch, P. A. Alpert, S. Dumas, S. Perrier, C. George and M. Ammann, *Environ. Sci. Technol.*, 2018, **14**, 7680–7688.
- [295] B. C. Gilbert, J. K. Stell, W. J. Peet and K. J. Radford, *J. Chem. Soc. Farad. T. 1*, 1988, **84**, 3319–3330.
- [296] L. Magi, F. Schweitzer, C. Pallares, S. Cherif, P. Mirabel and C. George, *J. Phys. Chem. A*, 1997, **101**, 4943–4949.
- [297] K. E. Daumit, A. J. Carrasquillo, R. A. Sugrue and J. H. Kroll, *J. Phys. Chem. A*, 2016, **120**, 1386–1394.
- [298] S. A. Epstein, S. L. Blair and S. A. Nizkorodov, *Environ. Sci. Technol.*, 2014, **48**, 11251–11258.
- [299] K. T. Malecha and S. A. Nizkorodov, *Environ. Sci. Technol.*, 2016, **50**, 9990–7.
- [300] J. P. S. Wong, S. M. Zhou and J. P. D. Abbatt, *J. Phys. Chem. A*, 2015, **119**, 4309–4316.
- [301] X. Pan, J. S. Underwood, J. H. Xing, S. A. Mang and S. A. Nizkorodov, *Atmos. Chem. Phys.*, 2009, **9**, 3851–3865.
- [302] M. L. Walser, J. Park, A. L. Gomez, A. R. Russell and S. A. Nizkorodov, *J. Phys. Chem. A*, 2007, **111**, 1907–1913.
- [303] Q. Ye, E. S. Robinson, X. Ding, P. Ye, R. C. Sullivan and N. M. Donahue, *Proc. Natl. Acad. Sci. USA*, 2016, 12649–12654.
- [304] J. H. Slade and D. A. Knopf, *Geophys. Res. Lett.*, 2014, **41**, 5297–5306.
- [305] T. Yli-Juuti, A. Pajunoja, O. P. Tikkanen, A. Buchholz, C. Faiola, O. Vaisanen, L. Q. Hao, E. Kari, O. Perakyla, O. Garmash, M. Shiraiwa, M. Ehn, K. Lehtinen and A. Virtanen, *Geophys. Res. Lett.*, 2017, **44**, 2562–2570.
- [306] G. R. Wentworth and H. A. Al-Abadleh, *Physical Chemistry Chemical Physics*, 2011, **13**, 6507–6516.
- [307] T. B. Nguyen, M. M. Coggon, R. C. Flagan and J. H. Seinfeld, *Environ. Sci. Technol.*, 2013, **47**, 4307–4316.
- [308] D. A. Thomas, M. M. Coggon, H. Lignell, K. A. Schilling, X. Zhang, R. H. Schwantes, R. C. Flagan, J. H. Seinfeld and J. L. Beauchamp, *Environ. Sci. Technol.*, 2016, **50**, 12241–12249.
- [309] S. A. Styler and D. J. Donaldson, *Environ. Sci. Technol.*, 2012, **46**, 8756–8763.
- [310] R. D. Deegan, O. Bakajin, T. F. Dupont, G. Huber, S. R. Nagel and T. A. Witten, *Nature*, 1997, **389**, 827–829.

- [311] J. de Gouw and C. Warneke, *Mass Spectrom. Rev.*, 2007, **26**, 223–257.
- [312] J. A. de Gouw, P. D. Goldan, C. Warneke, W. C. Kuster, J. M. Roberts, M. Marchewka, S. B. Bertman, A. A. P. Pszenny and W. C. Keene, *J. Geophys. Res-Atmos.*, 2003, **108**, 18.
- [313] M. Baasandorj, D. B. Millet, L. Hu, D. Mitroo and B. J. Williams, *Atmos. Meas. Tech.*, 2015, **8**, 1303–1321.
- [314] E. Kostenidou, R. K. Pathak and S. N. Pandis, *Aerosol Sci. Technol.*, 2007, **41**, 1002–1010.
- [315] D. M. Lienhard, A. J. Huisman, U. K. Krieger, Y. Rudich, C. Marcolli, B. P. Luo, D. L. Bones, J. P. Reid, A. T. Lambe, M. R. Canagaratna, P. Davidovits, T. B. Onasch, D. R. Worsnop, S. S. Steimer, T. Koop and T. Peter, *Atmos. Chem. Phys.*, 2015, **15**, 13599–13613.
- [316] H. C. Price, B. J. Murray, J. Mattsson, D. O’Sullivan, T. W. Wilson, K. J. Baustian and L. G. Benning, *Atmos. Chem. Phys.*, 2014, **14**, 3817–3830.
- [317] H. C. Price, J. Mattsson, Y. Zhang, A. K. Bertram, J. F. Davies, J. W. Grayson, S. T. Martin, D. O’Sullivan, J. P. Reid, A. M. J. Rickards and B. J. Murray, *Chem. Sci.*, 2015, **6**, 4876–4883.
- [318] Y. Chenyakin, D. A. Ullmann, E. Evoy, L. Renbaum-Wolff, S. Kamal and A. K. Bertram, *Atmos. Chem. Phys.*, 2017, **17**, 2423–2435.
- [319] R. F. Hems, J. S. Hsieh, M. A. Slodki, S. Zhou and J. P. D. Abbatt, *Environ. Sci. Technol.*, 2017, **4**, 439–443.
- [320] R. Wang, Y. Balkanski, O. Boucher, L. Bopp, A. Chappell, P. Ciais, D. Hauglustaine, J. Peuelas and S. Tao, *Atmos. Chem. Phys.*, 2015, **15**, 6247–6270.
- [321] E. Journet, K. V. Desboeufs, S. Caquineau and J. L. Colin, *Geophys. Res. Lett.*, 2008, **35**, 5.
- [322] N. M. Mahowald, S. Engelstaedter, C. Luo, A. Sealy, P. Artaxo, C. Benitez-Nelson, S. Bonnet, Y. Chen, P. Y. Chuang, D. D. Cohen, F. Dulac, B. Herut, A. M. Johansen, N. Kubilay, R. Losno, W. Maenhaut, A. Paytan, J. A. Prospero, L. M. Shank and R. L. Siefert, *Annu. Rev. Mar. Sci.*, 2009, **1**, 245–278.
- [323] Z. Shi, M. D. Krom, T. D. Jickells, S. Bonneville, K. S. Carslaw, N. Mihalopoulos, A. R. Baker and L. G. Benning, *Aeolian Res.*, 2012, **5**, 21 – 42.
- [324] A. L. Robinson, N. M. Donahue, M. K. Shrivastava, E. A. Weitkamp, A. M. Sage, A. P. Grieshop, T. E. Lane, J. R. Pierce and S. N. Pandis, *Science*, 2007, **315**, 1259–1262.
- [325] A. E. Reed Harris, A. Pajunoja, M. Cazaunau, A. Gratien, E. Pangui, A. Monod, E. C. Griffith, A. Virtanen, J. F. Doussin and V. Vaida, *J. Phys. Chem. A*, 2017, **121**, 3327–3339.
- [326] H. Matsui, N. M. Mahowald, N. Moteki, D. S. Hamilton, S. Ohata, A. Yoshida, M. Koike, R. A. Scanza and M. G. Flanner, *Nat. Comm.*, 2018, **9**, 10.
- [327] J. D. Smith, J. H. Kroll, C. D. Cappa, D. L. Che, C. L. Liu, M. Ahmed, S. R. Leone, D. R. Worsnop and K. R. Wilson, *Atmos. Chem. Phys.*, 2009, **9**, 3209–3222.
- [328] J. Raabe, G. Tzvetkov, U. Flechsig, M. Boge, A. Jaggi, B. Sarafimov, M. G. Vernooij, T. Huthwelker, H. Ade, D. Kilcoyne, T. Tyliczszak, R. H. Fink and C. Quitmann, *Rev. Sci. Instrum.*, 2008, **79**, 113704.
- [329] O. Dhez, H. Ade and S. Urquhart, *J. Electron Spectrosc.*, 2003, **128**, 85–96.
- [330] J. C., W. C., F. G. and Z. C., *J. Microsc. Oxford*, 2000, **197**, 173–184.
- [331] N. Grassie and W. W. Kerr, *J. Chem. Soc. Faraday Trans.*, 1957, **53**, 234–239.

- [332] N. K. Richards-Henderson, A. H. Goldstein and K. R. Wilson, *J. Phys. Chem. Lett.*, 2015, **6**, 4451–4455.
- [333] G. Vincent, A. Aluculesei, A. Parker, C. Fittschen, O. Zahraa and P.-M. Marquaire, *J. Phys. Chem. C*, 2008, **112**, 9115–9119.
- [334] W. G. Tsui, Y. Rao, H. L. Dai and V. F. McNeill, *Environ. Sci. Technol.*, 2017, **51**, 7496–7501.
- [335] E. Appiani and K. McNeill, *Environ. Sci. Technol.*, 2015, **49**, 3514–3522.
- [336] J. Peixoto and A. Oort, *J. Climate*, 1996, **9**, 3443–3463.

9 Acknowledgements

The development of the thesis would not have been possible without the help and support of many colleagues, friends, and family. I would like to thank all who directly participated and indirectly supported this thesis. First and foremost, I would like to thank Markus Ammann for being an excellent mentor and supervisor, for giving me the fantastic opportunity of working at the Surface chemistry group and, furthermore, for all the inspiration, guidance, scientific inputs and innumerable discussions. I feel really fortunate to have had as a supervisor such a great scientist and person. I would like to truly thank Andreas Türlér for accepting me as a PhD student, for the helpful evaluation and suggestions and for the interesting discussions about the thesis. I would like to thank my friend Peter A. Alpert for being the best work mate I could ever imagine, for all the interesting discussions, for all the good times spent together, for all what I have learnt from him (including how to operate STXM) and for all the things he did for me. I truly thank Christian George for accepting to be a referee of my thesis, for all the fruitful collaborations, for all the interesting discussions and furthermore the nice hosting at Lyon. I truly thank Sergey Nizkorodov and Kurtis Malecha for accepting me as visiting student in UC Irvine, for our fruitful collaboration, for the very interesting discussions and for the nice hosting in Irvine. I would also like to thank our colleagues at ETH Zürich, Jing Dou, Ulrich Krieger, Beiping Luo and Thomas Peter, for being excellent collaborators and for all the interesting (and long) discussions. I thank Laura González and Rainer Volkamer for the fruitful collaborations and for all the interesting discussions. I also thank the whole group of surface chemistry, past and present. I would like to thank Luca Artiglia for being such a nice work mate in liquid jet beam times and for the nice times spent out of work, Fabrizio Orlando for all the times we passed together at PSI and out of work, for the interesting discussions in the liquid jet beam times and specially for being the first friend I made in Switzerland, Thorsten Bartels-Rausch for the office atmosphere and the support in daily work as well as for the interesting discussions, Sarah Steimer, Goran Gržinić, Astrid Waldner, Xiangrui Kong, Jacinta Edebeli, Shuzhen Chen, Huanyu Yang, Anthony Boucly and Jérôme Gabathuler for the helpful support in daily work at the lab and the office, for all the nice experiments performed together in the lab, for being such nice mates, for all the interesting scientific discussions and all the great times spent together out of work. I thank as well Mario Birrer and Andres Laso, our fantastic technicians, for all the help received these years and for the good moments spent together. I thank the whole group of Analytical Chemistry at LUC laboratory (PSI), Anna Dal Farra, Dimitri Osmont, Sven E. Avak, Anja Eichler, Ling Fang, Theo Jenk, Silvia Köchli, Michael Sigl and Jonas Stegmaier for the pleasant working atmosphere and for all the nice time we spent together at work, out of it or even floating in the Aare. I would like to specially thank Margit Schwikowski, head of the Laboratory of Environmental Science, for being so nice with all of us. I truly thank Benjamin Watts and Simone Finizio, at PolLux beamline, for teaching me and advising me about STXM as well as for all the help received from them (including phone calls at 4 am). I thank Thomas Huthwelker, Jacinta Xto, Katja D. Henzler and Camelia N. Borca for our collaborations at PolLux beamline and the nice times spent there. I thank Josef Dommen and his group for letting me use their PTR-MS and advising me about it. I thank Saša Bjelić for analyzing my samples with HPLC-MS and our nice collaboration and discussions. I thank Nønne Prisle, Jack Lin and Marco Huttula for our nice experiments at UVSOR in

Japan. I truly thank Angela Blattmann and Doris Böhler for helping me with all the administrative stuff. I would like to truly thank all the friends I made in PSI along these years, specially to the Spanish-Italian community (Marc Raventos, Henar Rojo, María Victoria Manzi, Daniela Leanza, Debora Foppiano, Eibar Flores, Michele Zendri, Pablo Carmona, Marc Hüppin, Joanna Gałczyńska, Samy Hocine, Laura Maurel, Juan Cabrera, Pablo Villanueva, Ignasi Villacampa, Ainara Irastorza, etc.) for having been my best group of friends in Switzerland, for all the support and all the experiences lived together. I will never forget you, guys! I also thank all the members of our rock'n'roll band at PSI (PSIchedellics) for all the fun we have had together in practices, concerts and events out of PSI. I would also like to thank the people from the football club at PSI (Tine Celder, Goran Lovric, Raoult Ngayam, Cedric Cozzo, etc), for all the fun time we spent together in trainings and tournaments. I thank my friends from my village (Lumbrales) for having always been great in my times spent there and being always a friendly support. I would like to thank all the teachers and professors I have had from high school to college for transmitting so much knowledge to us and lifting us to the place where we are today.

My deepest gratitude goes to my beloved family, my parents, my siblings, my nephew and godson, my three nieces and my extended family, for their love and constant support. Without you in my life, nothing of this would have been possible.

Erklärung

gemäss Art. 28 Abs. 2 RSL 05

Name/Vorname: Corral Arroyo, Pablo

Matrikelnummer: 14-139-711

Studiengang: Chemie und Molekulare Wissenschaften

Bachelor Master Dissertation

Titel der Arbeit: Impacts of indirect photochemistry of Brown Carbon and iron carboxylate complexes on gas and aerosol chemistry

LeiterIn der Arbeit: Prof. Dr. Andreas Türlér

Ich erkläre hiermit, dass ich diese Arbeit selbständig verfasst und keine anderen als die angegebenen Quellen benutzt habe. Alle Stellen, die wörtlich oder sinngemäss aus Quellen entnommen wurden, habe ich als solche gekennzeichnet. Mir ist bekannt, dass andernfalls der Senat gemäss Artikel 36 Absatz 1 Buchstabe r des Gesetzes vom 5. September 1996 über die Universität zum Entzug des auf Grund dieser Arbeit verliehenen Titels berechtigt ist. Ich gewähre hiermit Einsicht in diese Arbeit.

Bern, 9.8.2018

Ort/Datum



Unterschrift

Pablo Corral Arroyo

Curriculum Vitae

Place of birth: Salamanca
Date of birth: September 10th 1991
Citizenship: Spanish

Education

- Chemistry BS/MS at the Faculty of Chemical Sciences at University of Salamanca (Salamanca, Spain). From September of 2009 to June of 2014
- PhD in Chemistry at the Department of Chemistry and Biology at University of Bern (Bern, Switzerland) and at Paul Scherrer Institut (PSI Villigen, Switzerland). "Impacts of indirect photochemistry of Brown Carbon and iron carboxylate complexes on gas and aerosol chemistry". From November of 2014 to 2018.

Conferences contributions

- International Conference on Chemistry and the Environment (Leipzig, 2015). ORAL. "Radical production from photosensitization of imidazoles"
- American Geophysical Union General Assembly (San Francisco, 2015). POSTER. "Radical production from photosensitization of imidazoles"
- European Geophysical Union General Assembly (Vienna, 2016). ORAL. "Radical production from photosensitization of imidazoles, benzophenone and 4-benzoylbenzoic acid"
- European Aerosol Conference (Tours, 2016). POSTER. "Radical production from photosensitization of imidazoles, benzophenone and 4-benzoylbenzoic acid"
- International Conference of the Aerosol Cycle (Lille, 2017). POSTER. "Radical production and aerosol aging sustained by photosensitizers within atmospheric particles"
- European Geophysical Union General Assembly (Vienna, 2017). ORAL. "Photochemistry of iron citrates initiated by UV-VIS light"

- European Aerosol Conference (Zurich, 2017). ORAL “Molecular diffusion limitations during photochemical aging of iron citrate aerosols”
- American Association for Aerosol Research Conference (Raleigh, 2017), POSTER “Feedbacks between atmospheric aerosol microphysics and photochemistry of iron complexes”
- International Aerosol Conference (Saint Louis, 2018), POSTER, “Molecular Diffusion Limitations Coupled with Aerosol Aging Initiated by Iron Citrate Photochemistry

Awards

- Prize “San Alberto Magno” to the best academic records in the Faculty of Chemical Sciences (2014).
- ACS “Certificate of Merit” awarded for a contribution at the 254th ACS Meeting (Washington DC, August of 2017)
- Scholarship granted by Deutsche Akademische Austauschdienst (DAAD) to participate in an internship program in Kekule Institut at University of Bonn (Bonn, Germany) in the Summer of 2013.
- Scholarship by Spanish Catalyst Society (SECAT) with the “Beca SECAT de introducción a la catálisis” to make an internship in the Institute of Catalysis and Petrochemistry (ICP) of CSIC.

Invited symposia and talks

- Talk at Rowland Hall at University of California Irvine (UCI, Irvine, November 16th of 2017), “Feedbacks between atmospheric aerosol microphysics and aerosol aging induced by photochemistry of iron complexes”
- Talk at Institute of physical chemistry at Rocasolano (CSIC, Madrid, February 17th of 2017) “Indirect photochemical processes and radical production in aerosol particles”

Publications

- González Palacios, L., Corral Arroyo, P., Aregahegn, K.Z., Steimer, S.S., Bartels-Rausch, T., Nozière, B., Ammann, M., George, C., Volkamer, R. Heterogeneous photochemistry of imidazole-2-carboxaldehyde: HO₂ radical formation and aerosol growth. *Atmospheric Chemistry and Physics* 16, 18, 11823-11836 (2016)
- Artiglia, L., Edebeli J., Orlando F., Chen S., Lee M., Corral-Arroyo P., Gilgen A., Bartels-Rausch T., Kleibert A., Vazdar M, Carignano M., Francisco J., Shepson P., Gladich I., Ammann M. A surface-stabilized ozonide triggers bromide oxidation at the aqueous solution-vapor interface *Nature Communications* 8, 700, 2017

- Corral Arroyo, P., Bartels-Rausch, T., Alpert, P.A., Dumas, S., Perrier, S., George, C.; Ammann, M. Particle phase photosensitized radical production and aerosol aging. *Environmental Science and Technology* 52, (14), 7680-7688, 2018
- Corral Arroyo, P., Malecha K., Ammann, M., Nizkorodov, S.; Influence of iron (III) and humidity on OVOC release induced by photochemistry in atmospheric secondary organic aerosol particles. Submitted to *Physical Chemistry Chemical Physics*

Workshops

- The Second Sino-European School on Atmospheric Chemistry (Shanghai, 2015)

Teaching

- Teaching assistant at University of Bern for practical courses in physical chemistry (courses of 2015/2016, 2016/2017 and 2017/2018).